Magnetic, Dielectric and Microwave Absorption Properties of Transition Metal based Ferrite Nanostructures

Thesis submitted for the degree of

Doctor of Philosophy (Science)

in

Physics (Experimental)

by

Dipika Mandal

Department of Physics

Jadavpur University

2020

CENTRE FOR BASIC SCIENCES 1986
S.N. BOSE NATIONAL
1894-1974
विज्ञानेन परिपश्यन्ति धीराः

सत्येन्द्र नाथ बसु राष्ट्रीय मौलिक विज्ञान केन्द्र
SATYENDRA NATH BOSE NATIONAL
CENTRE FOR BASIC SCIENCES
সত্যেন্দ্র নাথ বসু জাতীয় মৌল বিজ্ঞান কেন্দ্র

CERTIFICATE FROM THE SUPERVISOR

This is to certify that the thesis entitled "**Magnetic, Dielectric and Microwave Absorption Properties of Transition Metal based Ferrite Nanostructures**" submitted by **Ms. Dipika Mandal** who got her name registered on **09th May, 2016** for the award of Ph. D. (Science) degree of Jadavpur University, is absolutely based upon her own work under the supervision of **Prof. Kalyan Mandal** and that neither this thesis nor any part of it has been submitted for either any degree/diploma or any other academic award anywhere before.

Kalyan Mandal
24-12-2020

(Signature of the Supervisor with official seal and date)

डॉ. कल्याण मण्डल / Dr. Kalyan Mandal
वरिष्ठ प्राध्यापक / Senior Professor
संघनित पदार्थ भौतिकी एवं सामग्री विज्ञान विभाग
Dept. of Condensed Matter Physics and Material Sciences
सत्येंद्र नाथ बसु राष्ट्रीय मौलिक विज्ञान केंद्र
S. N. Bose National Centre for Basic Sciences
ब्लॉक-जे.डी., सेक्टर-III, सॉल्ट लेक, कोलकाता-700106, भारत
Block-JD, Sector-III, Salt Lake, Kolkata-700106, India

Dedicated to Maa and Baba.....

Abstract

In the present scenario, electromagnetic wave (EM) pollution becomes endangerous to human health due to rapid development of technology and hence EM wave absorbers (EMA) are in serious need to shield the unwanted waves. This EM wave Interference (EMI) also interrupts smooth operation of electronic devices and hence frequency selective EM shielding is required. Also in stealth technology and to construct emerging metamaterials, presence of ferrite absorbers with their synergistic dielectric and magnetic properties is inevitable. Preference of light-weight, size-efficient, low-cost yet efficient EMA materials influences us to focus on nano-structures among which nano-hollow spheres (NHS) are a new drift. To achieve an efficient broad-band EMA material, several techniques such as doping of cations, hybridization of materials, morphology and size control are introduced in this thesis. In-detail study of magnetic, dielectric and microwave (MW) absorption properties of earth-abundant transition metal based ferrites, TFe_2O_4 (T = transition metal ions) nanostructures indicate that ferrites in the form of low density hollow structures equipped with interesting properties such as multiple internal reflections of EM wave, are therefore much more efficient than their bulk and solid counterparts. Optimization of EM wave absorption properties in the frequency range from 1 to 20 GHz is executed and divalent cation substitution on traditional magnetite is found to effectively increase the Reflection loss (RL). $MnFe_2O_4$ NHS displays most promising results and therefore the following investigations by tuning its filler concentration and NHS sizes are performed. $MnFe_2O_4$ NHS shows a gradual increase in RL values from 0 wt% to 50 wt% loading content and an excellent RL of about -45.6 dB at thickness $\sim$ 4.2 mm is obtained for 50 wt% composite with a total effective bandwidth (BW) ($RL < -10$ dB i.e. absorption $> 90\%$) of $\sim$ 3.6 GHz. Further, a thickness dependent study on optimized 450 nm NHS composites reveals that maximum RL reached to ~ -55.4 dB (i.e. shielding $\sim 99.9997\%$) at 9.6 GHz for $t =$ 5.1 mm with a broad BW of $\sim$ 3.7 GHz, at much lower filler concentration (only 20 wt% in epoxy resin matrix) due to the best impedance matching, $|Z_{in}/Z_0| \sim 1$ in it, along with significant dielectric and magnetic losses. In a morphology dependent MW absorption study in widely used X-Band (8 – 12 GHz) with rectangular waveguide, Nickel ferrite

NHS showed a better performance than its bulk and solid counterparts. Moreover, analysis of quarter-wavelength model for best matching thickness (t_m) displays a good agreement between experimental and simulated matching thickness (t_m) values. Further, to explore possible applications of ferrite nanostructures, an in-depth magnetic characterization of Dioctyl sodium sulfosuccinate (AOT) functionalized cobalt-ferrite nanoparticles with average size sets from 12 nm to 22 nm, is carried out and an improvement in EM wave absorption is observed due to surface modification through surface spin pinning and charge transfer. Here, studies on tunable dielectric and magnetic properties with substitution of different cations and modulating sizes provide a map to select an efficient material for applications from high-frequency devices to bio-medical field.

List of Publications

(Included in thesis)

1. **D. Mandal**, M.M. Goswami and K. Mandal, 'Magnetic properties of AOT functionalized cobalt-ferrite nanoparticles in search of hard-soft marginal magnet', *IEEE Trans. Magn.* 54 (2018) 1–6

2. **D. Mandal**, M. Alam and K. Mandal, '$NiFe_2O_4$ nano-hollow spheres with improved magnetic and dielectric properties', *Physica B Condens. Matter* 554 (2019) 51-56

3. **D. Mandal**, A. Gorai and K. Mandal, 'Electromagnetic wave trapping in $NiFe_2O_4$ Nano-Hollow Spheres: an Efficient Microwave Absorber', *J. Magn. Magn. Mater.* 485 (2019) 43-48

4. **D. Mandal** and K. Mandal, 'Tuning of Structural, Magnetic and Dielectric Properties of TFe_2O_4 (T = Mn, Fe, Co, Ni, Cu, and Zn) Nano-Hollow Spheres: Effect of Cation Substitution', *J. Alloys Compd.* 851 (2021) 156898

5. **D. Mandal** and K. Mandal, 'Electromagnetic wave attenuation properties of MFe_2O_4 (M = Mn, Fe, Co, Ni, Cu, Zn) Nano-Hollow spheres in search of an Efficient Microwave Absorber' **(Under Communication)**

6. **D. Mandal** and K. Mandal, 'Enhancement of Electromagnetic Wave Absorption in $MnFe_2O_4$ Nano-hollow spheres' **(Under Communication)**

(Not included in thesis)

7. S. Talukdar, **D. Mandal**, K. Mandal, 'Surface Modification of Cobalt Ferrite NanoHollowspheres for Inherent Multiple Photoluminescence and Enhanced Photoatalytic Activities', *Chem. Phys. Lett.* 672 (2017) 57-62

8. R. Rakshit, E. Khatun, M. Pal, S. Talukdar, **D. Mandal**, P. Saha, and K. Mandal, 'Influence of functional group of dye on the adsorption behaviour of $CoFe_2O_4$ nano–hollow spheres', *New J. Chem.* 41 (2017) 9095-9102

9. I. Chakraborty, U. Saha, **D. Mandal**, S. Mukherjee, N. Joardar, S. P. S. Babu, G. S. Kumar and K. Mandal, 'Effect of Bovine Serum Albumin on Tartrate Modified Manganese Ferrite Nano Hollow Spheres: Spectroscopic and Toxicity Study', *Phys. Chem. Chem. Phys.* 21 (2019) 10726

10. **D. Mandal** and K. Mandal, 'Magnetite Nano Hollow Spheres: Efficient and Tunable Electro- Magnetic wave Absorber', *2019 IEEE MTT-S International Microwave and RF Conference (IMARC)*

11. D. Maity, K. Karmakar, **D. Mandal**, D. Pal, G. G. Khan and K. Mandal, 'Earth abundant transition metal ferrite nanoparticles anchored ZnO nanorods as efficient and stable photoanodes for solar water splitting', *Nanotechnology* 31 (2020) 475403

12. A. Dutta, A. Gorai, **D. Mandal**, K. Mandal, 'Dielectric and microwave absorption properties of $Na_{0.5}Bi_{0.5}TiO_3$-$SrTiO_3$ system' **(Submitted)**

Acknowledgement

First of all, I would like to express my sincere gratitude to my PhD supervisor Prof. Kalyan Mandal for his continuous support, motivation and guidance throughout these years of research. He always encouraged me to think research plans independently and took care of smooth and successful execution of the research ideas. He always inspired me to build new experimental set-up, work hard in laboratory, think scientifically and study thoroughly. Important and valuable research related discussions with him improved my conception and enriched my research. I am really grateful to him for his suggestions, constant encouragement, kind gesture and I must convey that it would not be possible to bring out my dissertation without his help.

I am extremely thankful to Prof. M. Jaleel Akhtar, IIT Kanpur and his group, for helping in my works related to microwave measurements. I would like to thank especially Mr. Rakesh Roshan, Vishal and Moitreya Da from group of Akhtar sir and Amartya da, Jadavpur University for their efforts, valuable discussions and friendly assistance. A part of my thesis work involved measurements that are performed in SAMEER (Society for Applied Microwave Electronics Engineering & Research), Kolkata and I am really thankful to Dr. Dipankar Dan and Mr. Partha Pratim Sardar for their active participation in discussion related to waveguides and microwaves.

I feel blessed as a PhD fellow in S. N. Bose National Centre for Basic Sciences (SNBNCBS), Kolkata, loaded with advanced instrumental facilities, surrounded by a beautiful, lively campus with a favorable research environment. I am extremely thankful to the Council of Scientific and Industrial Research (CSIR), Government of India, for providing me the financial support (CSIR Award No.: 09/575(0113)/2016-EMR-I) during the tenure of my research work.

I would like to thank all of my labmates from bottom of my heart, Madhuri di, Arup da, Rupali di, Souvanik da, Mahebub da, Keshab da, Indranil da, Chaitali di, Deblina di, Subrata, Dipanjan, Priyanka, Anupam, Swarnali, Saheli and Alo di for their cheerful company, love, help and support in my colorful lab days. Madhuri di amazed me with

her enthusiasm in work which inspired me a lot. Mahebub da, Subrata, Dipanjan, Keshab da, Indranil da were always ready to help whenever needed even in my personal difficulties. I will surely miss the late night chit-chats and funs with our 'Picnic' group. Subrata's dedication towards research and science always motivated me to work better. Anupam is a wonderful junior who assisted me multiple times. I would also like to thank some dear juniors, Priya, Smriti, Rupam, Saurav, Nopu and Kaliprasanna, who joined our lab for their projects and filled lives with joy. My former seniors in lab, Arko da, Rajasree di, Debasish da, Ashu da, Monalisa di remained supportive, informative and gifted some cherishable memories.

I would like to acknowledge every staffs of SNBNCBS including academic, accounts, purchase and technical departments. The cleaners, gardeners, cook and security, I would like to thank everyone. Their well-wishes for me made me feel more alive. I also would like to thank my SNB friends including 'Social wing', 'Cultural group', 'Hostel' and specially Piya di, Supriyo da, Anuvab da, Juriti di, Sucheta di, Kajal di, Sudip (Kumar Saha), Pabi, Subhrasish, Subhadip, Didhiti, Rafiqul and Tania for a happy and memorable stay here. Last but not the least, Fuchi and Puchkum are my dearest ones who always brought smile on my face after a tiring day at work.

I am extremely grateful to all of my teachers specially Sudipa didimoni, Farzana madam, SKM sir, Krishnacharya sir and Verma sir for their constant support and encouragement. I am thankful to my dear friends and well-wishers, Puja, Dora, Rayeesa, Gaurab, Prachi, Sumana di, Monalisa (Ghosh) di who always loved and admired me.

Finally, I want to express my love, respect and deepest gratitude to Maa and Baba (Tapati Mandal & Dr. Joydev Mandal) for their sacrifice, support, love, affection and guidance. Vai (Partha Sarathi Mandal) and my dear cousins Smritu, Rumu, Iti and Achintya always remained as my backbone and pillar of happiness.

Dipika Mandal

S. N. Bose National Centre for Basic Sciences

List of abbreviation:

A	Area
AOT	Dioctyl Sodium Sulfosuccinate
B	Bloch constant
BW	Bandwidth
C	Capacitance
CFSE	Crystal field splitting energy
d	Diameter
D	Crystallite size
dc	Direct current
DOS	Density of States
DSC	Differential Scanning Calorimetry
E	Energy
EDX	Energy Dispersive X-ray analysis
EDS	Energy Dispersive Spectroscopy
EM	Electromagnetic
EMA	EM wave absorbing materials
EMI	EM wave interference
FC	Field cooled
fcc	Face centered cubic
FESEM	Field Emission Scanning Electron Microscope
FWHM	Full width at half maxima
g	Grain
gb	Grain boundary

H_C	Coercivity
H_{ex}	Exchange Hamiltonian
HRTEM	High Resolution Transmission Electron Microscope
J_{AB}	Inter-site exchange constant
J_e	Isotropic exchange integral
K	Anisotropy Constant
K_V	Volume Anisotropy Constant
K_S	Surface Anisotropy Constant
LAS	Law of approach to magnetic saturation
LFT	Ligand field theory
LMCT	Ligand-metal charge transfer
MLCT	Metal-ligand charge transfer
MD	Multi domain
M_R	Remanent magnetization
M_S	Saturation magnetization
NHS	Nano-hollow spheres
NMs	Nanomaterials
NPs	Nano particles
NSs	Nanostructures
PSD	Pseudo Single domain
PVP	Polyvinylpyrrolidone
R	Resistance
r	Radius
RL	Reflection Loss

S	Spin operator
SAED	Selected Area Electron Diffraction
SD	Single domain
SE	Shielding efficiency
SEM	Scanning Electron Microscope
t_N	Neel relaxation time
t_B	Brown relaxation time
t	Thickness
T	Transition metal ion
t_m	Matching thickness
T_B	Blocking temperature
T_C	Curie temperature
TE	Transverse electric mode
TEM	Transverse electromagnetic mode
TG	Thermogram
T_N	Neel temperature
TM	Transition metal
V	Volume
VSM	Vibrating sample magnetometer
XRD	X-ray diffraction or diffractometer
Z	Complex Impedance
ZFC	Zero field cooled

List of symbols:

a	Lattice constant
B	Magnetic flux density
C	Heat capacity
d	Inter-planner spacing
e	Elementary charge ($=1.602\times10^{-19}$ C)
α	Attenuation Constant
k	Wavenumber
γ	gyromagnetic ratio
H	Magnetic field
I	Current
k_B	Boltzmann constant ($=1.3806488\times10^{-23}$J/K)
λ	Wave length
M	Magnetization
μ_B	Bohr magnetron ($= 9.274096\times10^{-24}$J/T)
μ_0	Permeability of free space
Φ	Magnetic flux
μ	Permeability
ε	Permittivity
Γ	Reflection Co-efficient
T	Temperature

$tan\delta$	Loss tangent
τ	Time
θ	Angle
V	Voltage
ρ	Resistivity
σ	Conductivity
χ	Susceptibility

Contents

List of Figures

Chapter 1 | Introduction

This introductory chapter consists of a detailed literature review, theoretical background and motivation to work in this particular field with a brief outline of the entire work.

1.1 Significance of Nano

The idea of nanotechnology was first unveiled by Physicist Richard P. Feynman in his lecture titled 'There is plenty of room at the bottom' where he emphasized necessity of nanoscale materials for the need of better and miniature devices. The term 'nanotechnology', first introduced by Norio Taniguchi in 1974, refers to the science that deals with properties and applications of various materials having extremely low dimension, in the range of 1 to 100 nm. These size constraints appeared in case of nanostructures (NSs) often produce qualitatively new behavior in comparison to their bulk counterpart. For example, Cox and his co-workers found that bare Rhodium (Rh) clusters display a non-zero magnetic moment for less than 60 atoms in it, which is an indication of either ferro- or ferrimagnetic ordering even though the bulk Rh is Pauli paramagnet at all temperatures [1]. These unique properties arise in these functional nanomaterials (NMs) when their size becomes comparable to certain physical length scales such as carrier mean free path, superconducting coherence length, magnetic domain wall width, spin diffusion length, etc. [2]. Moreover, reduction in size of materials restricts them into confinement zones where quantum phenomena play a huge role and this leads to density of states (DOS) of electrons in the material, changing from a continuous function ($D \propto E^{1/2}$) to delta function as we move from bulk to nanoscale, as shown in Fig. 1.1 [3]. Since the surface area (A) to volume (V) ratio in nanoscale highly increases with reduction in sizes ($A/V \propto 1/r$ for spherical particles), a greater amount of material can come into contact with surrounding materials, thus affecting properties such as transition temperatures, fluorescence, electronic excitation, electrical conductivity, magnetic permeability and chemical reactivity [4–8].

The properties and characteristic parameters of engineered nanomaterials can be tuned and manipulated which makes them even more interesting as such variation in nanoscale lead to their versatile applications [5,9–16]. In this context, tailoring size, morphology, composition of nanomaterials and functionalization are introduced as promising strategies [12,17,18]. The fabrication as well as characterization of nanostructures of different functional materials is important and also challenging because defect states and structure induced in nanoscale and thus their properties are

to be finely controlled [19]. For instance, reduction of size to a certain level introduces superparamagnetism in ferrites that make them more suitable as bio-sensors [4,20]. Though Iron (Fe), Cobalt (Co), Nickel (Ni) all are ferromagnetic, but Co or Ni cation substitution in traditional magnetite produces hard magnetic and soft magnetic substances respectively [8,21]. Also magnetic or non-magnetic layer capping on nanostructures sustain a pronounced effect on their properties due to surface modification and charge transfer [22,23].

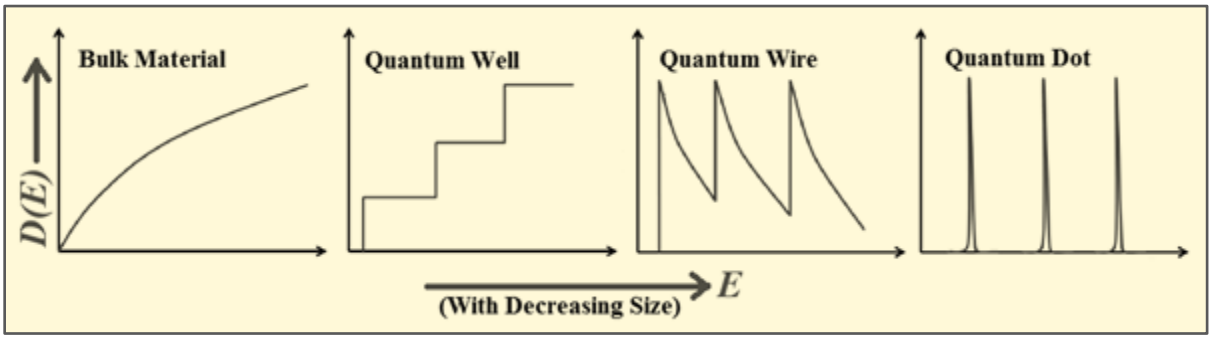

Figure 1.1. Change in density of states (DOS) with reducing size: from bulk to quantum dot

Nanotechnology is helping to considerably improve, even revolutionize, many sectors such as information technology, medicine, transportation, energy and environmental science, among many others. From components in high frequency devices to the bio-medical field, even from formation of 'smart fabrics' to 'anti-friction fluids' nanomaterials are used everywhere [10,24–26]. Moreover, their light-weight, size-efficient, low-cost yet effective nature craft better and fruitful devices. Figure 1.2 schematically represents the tuning and applications of nanomaterials in various fields. Though several commercial applications are successfully executed, researches on nanoscale materials are not saturated at all and still remain highly enthusiastic. For instance; Liu et al. prepared yolk-shell Fe_3O_4@Mesoporus SiO_2 heterostructures to enhance absorption of unwanted electromagnetic (EM) wave pollution [27]. Green energy production through water splitting by 2D–1D nano-heterostructure is performed by Karmakar et al. to quench the demand for alternate energy resources [17].

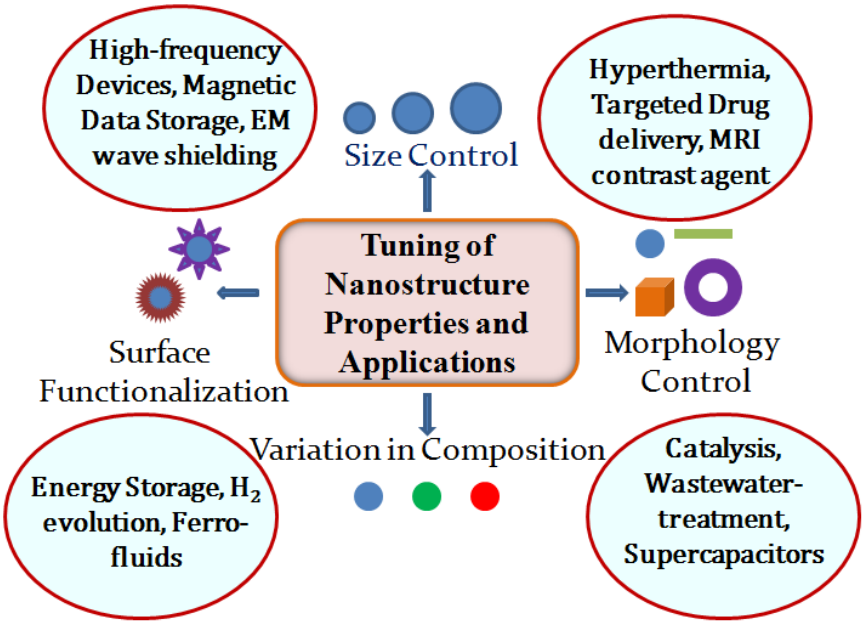

Figure 1.2. Schematic representation of some possible tuning procedures of nanostructures and their applications

1.2 Nanostructures

Nanomaterials of polymer, carbon, ferrites and so on possess different morphologies including nanoparticles (NPs), nanorods, nanowires, nanotubes, disc, cube, film, flower etc., as shown in Fig. 1.3 [28–30]. In spite of having building blocks with same composition, these nanostructures exhibit different thermodynamics, physical and mechanical properties due to change in boundary constraints, defect states etc. applicable to them [3,19,31]. For example, two-dimensional (2D) Y_2NiMnO_6 films are found to exhibit unexpected room temperature ferromagnetism and spontaneous ferroelectricity which their NPs counterpart does not illustrate [32].

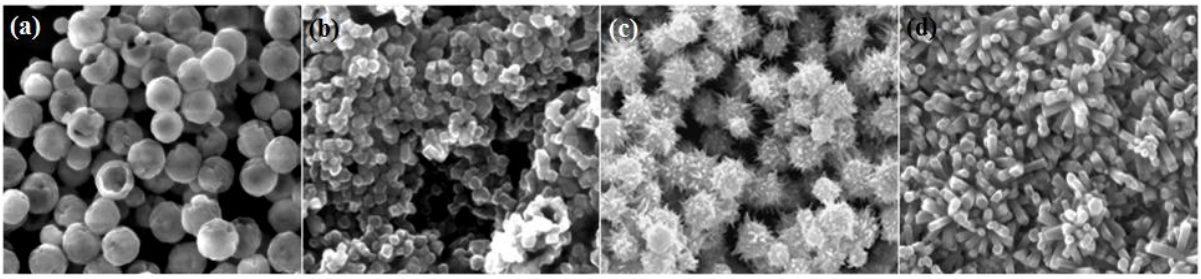

Figure 1.3. Different morphologies of nanostructures (a) nano-hollow spheres (b) nanocubes (c) etching core-shell structure (d) nanorods

1.2.1 Nano-Hollow Spheres

Among the nanostructures, in last few years, researchers are drifted in fabricating nano hollow spheres (NHSs) because of its hollow interior which further enhances its effective surface area while the density is much lower than that of their dense solid counterparts [31,33]. NHSs are found to be very promising because of their high saturation magnetization (M_S), large surface area and pore volume, low density, ability to withstand volume changes due to temperature and pressure which enable them to be used in wide varieties of applications in the fields of biomedical research [5], high frequency magnetic devices [34], energy storage [11], ferro-fluids [10], Hydrogen evolution reaction [17], supercapacitors [12] and chemical sensors [14]. Large void space and outer interface of NHSs can be used for encapsulating drugs and their controlled release [35,36]. Moreover, repeated internal reflections of EM wave in inner hollow core of NHS increases total path length of it and absorbs it to a greater extent promoting EM wave shielding [37,38].

Though by definition, nanomaterials should have dimension $\leq$100 nm, NHS with size $>$100 nm also behave like nano because of their shell thickness less than 100 nm and this fact relaxes their nanoscale range thus also increases their area of applications [23,39]. Possibilities of various configurations of hollow spheres such as single-shell, multi-shell, yolk-shell, rattle-type etc. also boost this morphology as a growing research topic [33].

1.2.2 Transition Metal based Ferrite Nanostructures

It is well-known that the traditional iron oxide, Fe_3O_4, also named as 'loadstone' from old age, is a versatile compound immensely used as MRI contrast agent for early stage cancer detection to formation of metamaterials [40,41]. Ferrites are also useful in high frequency components as they possess a very high dc electrical resistivity, hence low loss [42]. Moreover, newly observed phenomena like giant magneto-resistance are also dependent on magnetic nanomaterials. To enhance the chemical stability and tune properties such as magneto-crystalline anisotropy, magnetostriction, M_S, relaxation

times (Neel relaxation time, t_N, Brown relaxation time, t_B), and blocking temperature (T_B) of ferrites, substitution of divalent cation to Fe_3O_4 is a renowned strategy [21]. For example, Co^{2+} substitution in place of Fe^{2+} in Fe_3O_4 increases its coercivity (H_C) making $CoFe_2O_4$ a hard magnet whereas $NiFe_2O_4$ is a soft magnetic material. In general, empirical formula for transition metal (TM) based ferrite is TFe_2O_4 (T = transition metal ion) where transition metals include 3d elements such as Fe, Co, Ni etc. and 4f elements, such as Nd, Sm, Gd, Dy etc. Possible replacement of permanent magnets made up of Sm-Co, Nd-Fe-B alloys by TM based ferrites makes the applications cost-effective. Also usage of largely available elements like 3d transition metals cut down the expenses while simple structures can be tuned easily without compromising their necessary properties [43]. Therefore, considering suitability in practical applications, low cost, earth-abundant, non-toxic ferrites with simple crystal structure will be focused further.

In addition, ferrites with combination of relatively better permittivity (ε) and permeability (μ) ensures wider bandwidth (BW), higher impedance matching and EM wave absorption in comparison to traditional EM wave absorbing materials, such as carbon-based materials and metal powders [44,45]. In present scenario, EM wave absorbing materials (EMA) are in serious need to shield the unwanted waves and for their tunable absorption bands, they are widely used in military and civil fields, such as stealth technology, anti-radiation sheets and anechoic chambers. Both dielectric and magnetic losses are key sources and high ε and μ values lessen the required thickness (t) of EMA making it size-efficient [46]. Hence a detailed study on structural, magnetic, dielectric and microwave absorption properties on 3d transition metal based ferrite (magnetic) nanostructures become extremely important.

1.3 Crystal Structure

The structural classification of ferrites includes three types, generally, (i) Spinels (ii) Garnets and (iii) Hexaferrites. 3d transition metal based ferrites with formula TFe_2O_4 (T= transition metal ion) are spinel ferrites that belong to space group Fd3m. The cubic unit cell is formed by 56 atoms, 32 oxygen anions distributed in a cubic close-packed structure, and cations occupying 8 of the 64 available in tetrahedral sites (A sites) and

16 of the 32 available in octahedral sites (B sites) as shown in Fig. 1.4. The limit of atomic radii contained in A-site is ~ 0.30 Å and in B-site ~ 0.55 Å. Depending on the cationic radii placed in the sites, the structure can get expanded or contracted. Moreover, in such oxygen closed pack configuration constituted of intervening face-centered cubic (fcc) lattices, anions are occupied at the corners of a cube and the cation is at the center of the void created by these anions. The structural formula for a basic spinel compound TFe_2O_4 can be written as [47]

$$[T_{(1-i)}\,Fe_i]^A\,[T_iFe_{(2-i)}]^BO_4 \qquad 1.1$$

where the amounts in brackets represent the average occupancy of A sites and B sites and i is the inversion parameter.

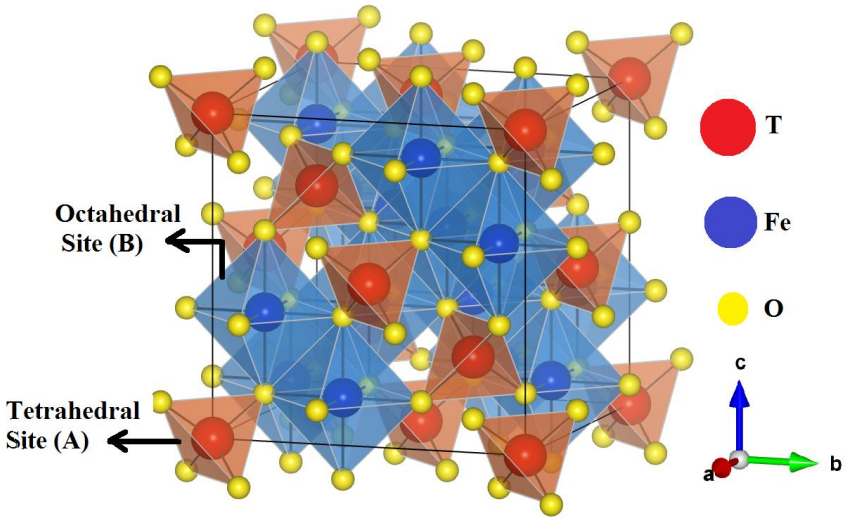

Figure 1.4. Crystal structure of a spinel ferrite, TFe_2O_4

The cation distribution in A- and B sites mainly depends on crystal field stabilization energy (CFSE) and relative size of the cations. The higher value of CFSE of constituent cations decides their preference for higher co-ordination site i.e. B-site and accordingly Fe_3O_4, $CoFe_2O_4$, $NiFe_2O_4$ and $CuFe_2O_4$ are of inverse spinel structure [48]. However, in $ZnFe_2O_4$, Zn^{2+} with d^0 configuration and in $MnFe_2O_4$, both cations Fe^{3+} and Mn^{2+} with states d^5, have no specific preference of sites. Therefore $MnFe_2O_4$ and $ZnFe_2O_4$ have possibilities of forming normal, inverse or mixed spinel structure. Along with CFSE,

reduction of the grain size to below 6.8 nm resulted in a transformation of most of the inverted spinel ferrite molecules to the normal spinel structure due to an abnormal lattice contraction [49]. The change in cation distribution among tetrahedral (A) and octahedral (B) sites can affect their structural properties which in turn vary their magnetic and dielectric properties. Like in Zn-doped Fe_3O_4, at a certain doping concentration of non-magnetic element Zn, cation distribution varies in such a way that magnetic exchange interaction in B-site increases the total magnetic moment of the ferrite [50].

1.3.1 Normal Spinel Ferrite

On the basis of cation distribution, a spinel ferrite can be of types normal, inverse, or mixed. In a normal spinel structure, 8 divalent cations are all located in tetrahedral sites and 16 trivalent cations are all located in octahedral sites, hence the inversion parameter (i) becomes 0 (schematically illustrated in Fig. 1.5(a)). In general, this type of distribution takes place in bulk zinc ferrites, $Zn^{2+}[Fe^{3+}Fe^{3+}]O_4^{2-}$.

1.3.2 Inverse Spinel Ferrite

Unlike normal spinels, the T^{2+} ions occupy the octahedral voids, whereas one half of Fe^{3+} ions occupy the tetrahedral voids and the other half occupies B sites. Therefore, the inversion parameter (i) leads to 1. It can be represented as: $Fe^{3+}[T^{2+}Fe^{3+}]O_4^{2-}$. Fe_3O_4, $CoFe_2O_4$, and $NiFe_2O_4$ are some examples of inverse spinel structure. In this kind of ferrites, magnetic contribution from Fe^{3+} ions gets compensated by inter-lattice super-exchange and that from T^{2+} ions only persists. This kind of spinel is schematically illustrated in Figure 1.5(b).

1.3.3 Mixed Spinel Ferrite

Mixed spinel structure or partly inverse spinel arises when cations T^{2+} and Fe^{3+} are distributed in both A- sites and B- sites and the structural formula of this ferrite becomes $T_{(1-i)}^{2+}Fe_i^{3+}[T_i^{2+}Fe_{(2-i)}^{3+}]O_4^{2-}$, where i is the degree of inversion (schematically illustrated in Fig. 1.5(c)). $MnFe_2O_4$ generally represents this kind of

structure and has an inversion degree of $i = 0.2$ with structural formula: $Mn_{0.8}^{2+}Fe_{0.2}^{3+}[Mn_{0.2}^{2+}Fe_{1.8}^{3+}]O_4^{2-}$ [51].

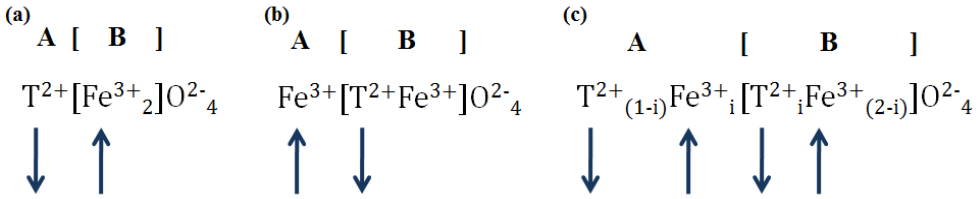

Figure 1.5. Cations distribution in (a) normal, (b) inverse, (c) mixed spinel ferrites

1.4 Surface Functionalization

Modification of nanostructure surfaces often employed not only for controlled synthesis of nanostructures but also for prevention in agglomeration of small magnetic NPs, increase in biocompatibility and biodegradability of materials, tune morphology and functional properties such as magnetic, electric, optical properties etc. of nanomaterials [39,52]. Thus, surface functionalization is worth to discuss as they enhance potentiality of NSs. During synthesis, surfactants like oleylamine, Polyvinylpyrrolidone (PVP) are used for controlled fabrication of nanoparticles and manipulation of shapes of nanostructures [39]. General classification of surfactants includes hydrophilic or water-soluble type such as citric, tartaric, salt etc. and hydrophobic or oil-soluble type like fatty acid, alkyl phenol but inorganic materials such as silica, metals and oxides also serve as an important class of surface modifiers [52,53]. Fabrication of oil-soluble type NPs is very important for obtaining mono-disperse NPs whereas dispersion in either aqueous or organic solvent can be performed choosing either polar or non-polar ligands respectively. Inorganic material coatings can induce several different properties such as high electron density and strong optical absorption (e.g. by noble metal particles, in particular Au and Ag), fluorescence (by semiconductor quantum dots, e.g. CdSe or CdTe) or magnetic moment (e.g. by Fe, Mn, Ni, Co or their oxide NPs).

The surface of NPs contains numerous uncompensated coordination spheres due to broken bonds. The ligand molecules get bound to the NPs surface by attractive

interactions, such as chemisorptions, electrostatic interaction, most commonly, provided by head group of the ligand molecule and follows Ligand Field Theory (LFT). In case of ferrite structures, LFT describes bonding interaction between ligands and valence atomic orbitals of 3d transition metal ion and their orbital arrangement. In octahedral field (B-site), as ligands approach from the direction of axes, the three t_{2g} orbital states d_{xz}, d_{yz} and d_{xy}, will be lower in energy than the two e_g states $d_{x^2-y^2}$ and d_{z^2} whereas in tetrahedral symmetry (A-site), inverse arrangement is observed, as depicted in Fig. 1.6. Interactions between ligand and metal cause splitting of the d-orbitals (Δ) primarily depends on type of ligands and also metal ions (Δ increases with increasing oxidation number). For example, π-donor ligands having occupied p-orbitals tend to donate π and σ electrons to the metal ions, exhibiting stronger metal-ligand interactions and an effective decrease of Δ, whereas π-acceptor ligands lead to a large value of Δ and are called strong- or high-field ligands.

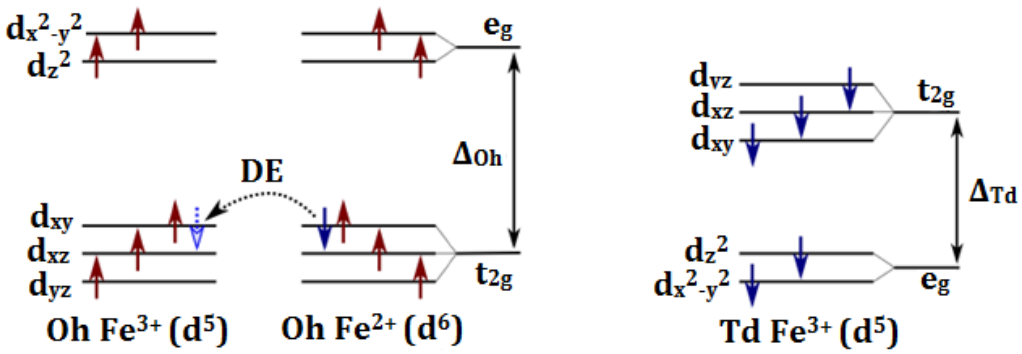

Figure 1.6. Schematic representation of electron occupation of octahedral (Oh) Fe^{2+} and Fe^{3+} as well as tetrahedral (Td) Fe^{3+} 3d states in Fe_3O_4

1.4.1 Ligand to Metal and Metal to Ligand Charge Transfer

Ligands normally possess σ, σ*, π, π*, and non-bonding molecular orbitals. If the ligand molecular orbitals are full, charge transfer possibly occur from the ligand orbitals to the empty or partially filled metal d-orbitals in ferrites. The intense absorptions arising from this process are called ligand-to-metal charge-transfer transitions (LMCT) (shown in Fig. 1.7) [22]. On the other side, if the metal is in a low oxidation state (electron rich) and the ligand possesses low-lying empty orbitals (e.g. CO- or CN- having π* orbitals)

then a metal-to-ligand charge transfer (MLCT) transition may occur. MLCT transitions are common for coordination compounds having π-acceptor ligands. Moreover, along with the head groups, length of the tail part i.e. ligand chain-length also has importance in tuning properties of the material as it is associated with steric hindrance of the compound. For instance, Giri et al. reported that although Mn_3O_4 NPs is paramagnetic at room temperature, it becomes ferromagnetic upon co-ordination with π-donor ligand [54].

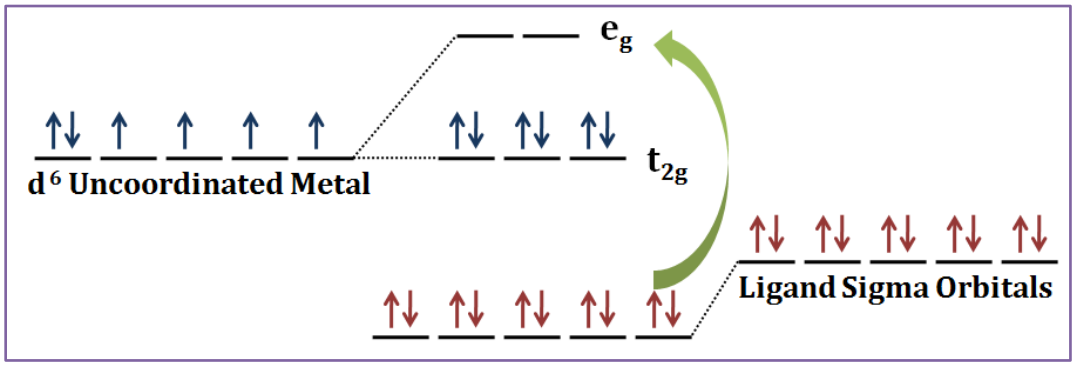

Figure 1.7. Ligand to Metal Charge Transfer (LMCT) involving an octahedral d^6 complex

1.5 Magnetic Properties

This section will be devoted to magnetic properties of nanostructures specifically of spinels, in dc and ac magnetic fields, their important and related consequences. The origin of magnetism is intimately related to the spin and orbital angular momentum of electrons and nuclei. Types of magnetism include paramagnetism, which is due to spin and angular momentum of individual electrons, diamagnetism which has its origin in the orbital angular momentum of the electron, and ferromagnetism originates from the formation of domains with each domain containing a large number of aligned spins. Figure 1.8 shows magnetic behavior of the materials under influence of an applied field showing the characteristic positions, saturation magnetization (M_S, maximum induced magnetization), remanent magnetization (M_R, remaining magnetization after an applied field is removed), and coercivity (H_C, magnetic field needed to demagnetize the sample). In terms of susceptibility (χ) of a material, ferromagnets have $\chi >> 0$. Spinel

ferrites with anti-parallel distribution of divalent and trivalent cations in A- and B-sites are generally ferrimagnetic in nature and if the magnetic moment of cations in anti-parallel distribution becomes equal, the material shows anti-ferromagnetism. In tetrahedral and octahedral sites individually, spins have direct exchange interaction between them. Exchange Hamiltonian can be expressed as, $H_{ex} = -2J_e \sum_j S_i . S_j$, S is the spin operator and J_e is the isotropic exchange integral [55]. Apart from this direct exchange, there are systems with indirect exchange, e.g. (1) Ruderman–Kittel–Kasuya–Yosida (RKKY) exchange, where the metallic ions are coupled via itinerant electrons, (2) super-exchange, here the exchange is mediated via different non-magnetic ions, (3) anisotropic exchange interaction (also known as Dzyaloshinskii-Moriya interaction), where the spin-orbit interaction plays a major role and often leads to canting of spins by small angle [55]. In spinels, the unpaired spins of inter-site cations are coupled through shared oxygen ions by super exchange process. This exchange constant (J) between A- and B-sites can be determined from Bloch's theorem which will be discussed later [42]. Therefore, for inverse spinel ferrites, TFe_2O_4 (T^{2+} = divalent ions like Fe, Co, Ni), a resultant ferromagnetic interaction get produced for the ferrites where T^{2+} ions have unpaired electrons.

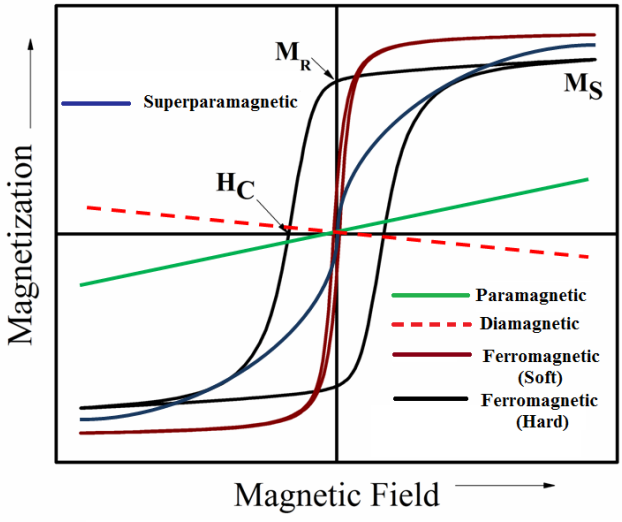

Figure 1.8. Magnetic behavior of materials under the influence of an applied field

Size of the NSs has an enormous effect on their magnetic behavior. M_S can be reduced in nanoparticles than their bulk counterpart due to surface spin canting [56]. Moreover, for bulk sizes, temperature dependence of M_S is found to obey Bloch's $T^{3/2}$ law, where the small nanoparticles show a deviation from this $T^{3/2}$ nature trending towards T^2 [42,57]. In general, magnetic domains (10-1000 nm) in ferromagnetic materials are separated by domain walls, which have energy associated with their formation and existence. The domain-wall widths (wall energies) extend from 5nm ($50mJ/m^3$) for hard magnetic materials and 100 nm ($0.1mJ/m^3$) for soft magnetic materials [58]. Analysis of magnetic hysteresis behavior of ferro/ferrimagnets becomes simpler if the magnetic domain structure is well-known. The possible domain structures can be investigated in terms of Day plot which is a graphical mapping of M_{RS}/M_S vs. H_{CR}/H_C, where H_{CR} is the value of the field under which the $M - H$ loop shows a remanence $M_R = 0.5M_{RS}$ [59]. Naturally occurring hard magnets with larger exchange interaction constant possess high magnetostriction and magnetocrystalline anisotropy [21]. In contrast, when crystal grains are comparable to the size of the magnetic domains, then the magnetic domains are pinned by crystal grain boundaries and show high inertia to the applied magnetic field. Along with this, when the crystal size just reaches to the single domain (SD) dimension from multi-domain (MD) upon scaling down the particle size of ferromagnetic material, all the spins get aligned to each other and only rotation of spins can take place, so the demagnetization becomes difficult increasing the H_C value [42]. Further decrease in particle size leads to superparamagnetic nature of ferro/ferrimagnetic NPs. In this case, without application of field, the NPs behave like paramagnets, and with magnetic field, they behave as strong ferromagnets without hysteresis loss and this property of NPs is highly used in switching devices and bio-medicine [28].

Furthermore, magnetic properties are dependent on temperature. With increasing temperature ferromagnetic crystals expand and the spin-spin exchange becomes weaker. Above a certain characteristic temperature, Curie temperature (T_C), super-exchange vanishes completely and the material becomes paramagnetic [60]. At lowering temperature, spins tend to freeze on the surface of nanostructures, which

increase both the coercivity and magnetization values of the material. For antiferromagnetism, the characteristic temperature is known as Neel temperature (T_N). Above the temperature known as Blocking temperature (T_B), both ferro and ferrimagnetic nanoparticles exhibit superparamagnetic behavior manifested by rapid and random magnetization reversals leading to a zero time-average magnetic moment [4]. The parameters of magnetic properties largely depend on anisotropy of the material, exchange interactions, and even frequency of the measurement. Therefore, elaborate discussions on these phenomena are depicted hereafter.

1.5.1 Magnetic Anisotropy

In absence of any external magnetic field, sometimes there is an energetically favorable direction for spontaneous magnetization depending on exchange interactions and crystal axis called the 'easy axis' and this directional dependence of the material's magnetic moment is known as 'Magnetic Anisotropy'. In a material, the magnetic anisotropy may arise due to the symmetry of the crystalline lattice and even from specific shape of the nano-structured material.

1.5.1.1 Magnetocrystalline Anisotropy

The magnetocrystalline anisotropy is an intrinsic property of the material and the most prominent contribution to the magnetic anisotropy, which is caused by the spin-orbit interaction of the electrons. The spatial arrangement of the electron orbitals is strongly linked to the crystallographic structure. Consequently, when the electron spins interact, they force each other to align along unidirectional well-defined crystallographic axes. The two models to describe the magnetic anisotropy are: (a) Neel model which says that magnetic anisotropy arises due to the magnetic spin pair interactions and (b) Single-ion or crystal field model that describes crystal field interactions with atoms which are not essentially magnetic [55,56]. As the magnetocrystalline energy is associated with the relative orientation of the total magnetization with respect to the magnetic easy axis of the crystal, i.e. θ, the magnetocrystalline anisotropy energy can be expressed as,

$$E_k = V(K_0 + K_1 \sin^2\theta + K_2 \sin^4\theta) \quad 1.2$$

Where, K_n ($n = 0, 1, 2 \ldots$) are the magnetocrystalline anisotropy constants. For a single crystallite, considering small θ value, from magnetocrystalline anisotropy energy expression, magnetization (M_H) at any applied magnetic field (H) can be written (neglecting higher order terms) as,

$$M_H = M_S[1 - (a/H) - (b/H^2)] + \chi H \quad 1.3$$

Neel attributed constant a to the effect of inhomogeneity and defects inside the crystallites or grain boundary and b is with stress due to anisotropy in the material [61]. The b value is experimentally determined to be ($0.07619K^2/H^2M^2$) and this law of approach to magnetic saturation (LAS) is used most effectively for measurement of the magnetocrystalline anisotropy on polycrystalline specimens [61,62].

1.5.1.2 Shape Anisotropy

The magnetic dipolar anisotropy, or shape anisotropy, is mediated by the dipolar interaction of free magnetic poles causing stray or demagnetization fields. This interaction tends to direct magnetic moments parallel to the surfaces to minimize the magneto-static energy. The interaction is long range and hence its contribution is dependent upon the shape of the sample. Shape anisotropy becomes important in thin films and often produces in-plane alignment of moments. For shape anisotropy, demagnetization factor is 0 for long cylinders, 1/3 for spheres and 1 for plates [56].

1.5.1.3 Surface Anisotropy

Surface anisotropy, first introduced by Neel, is related to surface and interfaces of nanostructures and it is mainly observed in case of materials having complicated structures and morphologies such as metal films, multilayer, rough surfaces and especially in smaller particles. Generally surface anisotropy in nanoparticles is found to be much higher than the bulk value which is due to larger fraction of surface ions in smaller particle [63]. This superficial spins are disordered because they resides within

an uncompensated coordination sphere due to broken bonds, vacancies and also due to the bond formation with some organic molecules. Thus the surface anisotropy makes the surface layer magnetically harder than the core region of a fine nanoparticle. For a spherical particle the effective anisotropy energy (K_{eff}) can be written as, $K_{eff} = K_V + \frac{6}{D}K_S$, where K_V and K_S are the bulk (or, volume) and surface anisotropy constants respectively and D is the diameter of the particle.

1.5.2 Super-exchange interaction and Bloch's theorem

In spinel ferrites, the intra-site interactions (A-A and B-B) are direct exchange type and inter-site interaction i.e. A-B interaction is of super-exchange type where the interaction between 3d cations mediates through 2p spins of non-magnetic oxygen anions. The exchange constant (J_{AB}) between tetrahedral (A) and octahedral (B) sites can be calculated experimentally from the fitting of Bloch's law in temperature vs. M_S curves.

According to the spin wave theory, demagnetization of ferromagnetic substance from $M_S(0)$(M_S at T = 0 K) with temperature, is due to the excitation of spin waves of long wavelengths and the excitation energy $\mathcal{E}_k$ of the spin waves can be written as [20,42],

$$\mathcal{E}_k = Dk^2 + Ek^4 + g\mu_B(H_0 + H_A + H_D) \quad 1.4$$

Here D is the spin-wave stiffness co-efficient, H_0, H_A and H_D is the externally applied field, anisotropy field and demagnetization field respectively. In general, at temperatures well below T_C, the temperature dependence of saturation magnetization follows the Bloch's law,

$$M_S(T) = M_S(0)(1 - BT^b) \quad 1.5$$

where B is the Bloch constant proportional to the inverse of exchange constant (J) and b is the Bloch exponent which is 3/2 for a three dimensional system [63,64]. In small nanoparticles, a clear deviation from Bloch's law can be observed at low temperature,

which is due to the presence of magnons having wavelength larger than the particle dimension, and hence cannot be excited. Bloch exponent is found to be strongly dependent on size of the particles, their chemical composition and synthesis route but independent of structure of the nanoparticles. From the B values, exchange constant between A and B sites (J_{AB}) can be calculated using the equation as given below [20,42],

$$J_{AB} = \frac{16 k_B (S_{B1} + S_{B2} - S_B)}{11 S_A (S_{B1} + S_{B2})} \left[\frac{0.05864}{4B(S_{B1} + S_{B2} - S_A)}\right]^{2/3} \quad 1.6$$

where for magnetite, S_A and S_{B1} are the spins of Fe^{3+} and equal to $5/2$. $S_{B2} = 2$ is the spin of Fe^{2+} ions in octahedral site of Fe_3O_4 lattice.

1.5.3 Superparamagnetism

Single domain ferromagnetic substance below a certain critical diameter (d_c) becomes superparamagnetic. In terms of K, anisotropy constant, J, exchange constant, μ_0, the free-space permeability and M_S, d_c can be calculated from, $d_c \approx \frac{\sqrt{JK}}{\mu_0 M_S^2}$. In single domain, the magnetostatic energy becomes equal to the domain wall energy and also to magnetic anisotropy energy. Below d_c and above T_B, thermal energy is sufficient enough to invert the spin direction by overcoming the anisotropy barrier [4]. With presence of external applied field, superparamagnetic nanoparticle magnetic moments attain rapid random saturated magnetization. Therefore, superparamagnetic NPs allow better control over the application of their magnetic properties as they provide a strong response to the field.

1.5.4 Magnetic Relaxation

For small nanosized particles, after removal of magnetic field, spin flips to retain a random position and reversal time depends on external parameters such as temperature and measurement frequency and internals like anisotropy energy, striction etc. The average time between magnetization reversals is given by Arrhenius like Neel-Brown expression, $\tau = \tau_0 e^{(\frac{KV}{k_B T})}$, where τ_0 is from 10^{-9} to 10^{-13} s, K, the anisotropy constant and V is volume of the particle [65]. The magnetic relaxation curves

(M versus time) are interesting to study for permanent magnetic materials to observe their ability to store the magnetization in time duration. From Brownian and Neel spin-spin relaxation, magnetization is found to decay exponentially with time, $M(t) = M_0 e^{-\frac{t}{\tau}}$, where $M(t)$ and M_0 are magnetizations of sample at time t and $t = 0$ and τ is the relaxation time constant [66].

1.5.5 Dynamic Magnetization

Ferrites are non-conducting oxides and therefore allow total penetration of electromagnetic fields in it unlike metals and these have an increasing demand in high-frequency applications such as telecommunications and radar systems [43]. At such high frequencies, domain walls are unable to follow the field (dispersion of domain walls typically occurs at ~ 10 GHz) and absorption of microwave power takes place by spin dynamics [18]. The magnetic spins precess around their equilibrium orientation under a torque at the frequency of external field to minimize the Zeeman energy (as shown in Fig. 1.9). The net behavior of dynamic magnetization is explained by the Landau-Lifshitz-Gilbert (LLG) equation of motion [67]. From a semi-classical approach, torque (T) associated with an electron spin (S) is, $\frac{dS}{dt} = T = M \times H_{eff}$, where $M(= -\gamma S)$ is the magnetic moment of an electron and H_{eff} is the effective applied magnetic field. The equation of motion of the magnetization with additional damping terms takes the form as,

$$\frac{dM}{dt} = -\gamma(M \times H_{eff}) + \frac{\alpha}{M_S}(M \times \frac{dM}{dt}) \qquad 1.7$$

Here, α is the Gilbert damping coefficient, $\gamma = ge/2mc$, gyromagnetic ratio and H_{eff}, total field on the spins (external and internal). The resultant solution of this equation of motion reproduces Globus' relation for the static case and further shows that the dispersion frequency (f_r) varies as $\sim D^{-1}$ (D = diameter of grains) for small grains and $\sim D^{-2}$ for large grain sizes [68].

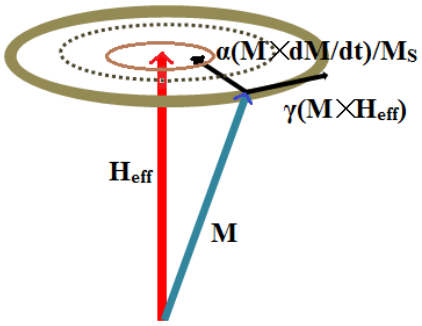

Figure 1.9. The precessional motion of the magnetization around the effective magnetic field direction when damping is included

1.6 Dielectric Properties

In order to design high frequency circuits, it is essential to have vital understanding of the electrical properties of materials especially the dielectric constant and loss tangent at the operating conditions. Generally, materials can be classified into conductors, semiconductors and insulators depending on their conductivity and into dielectric, paraelectric and ferroelectric in terms of their polarizibility [69]. Ferrites normally belong to semiconductor and dielectric range. The measurement of complex dielectric properties of materials at radio frequency (RF) and microwave frequency is very relevant especially in the research fields, such as material science, communication, microwave circuit design and biological research [6]. Moreover, measurements in ac frequency provide insights to the microscopic nature of the ionic conducting process whereas technically more difficult dc measurements give less information of the entire dynamic behavior of the sample. Hence, ac techniques are adopted to measure the material properties such as bulk conductivity, surface, grain boundary effect, ionic transport and double layer formation at the electrode/sample interface etc. [7]. Dielectric properties related to the polarization behavior, conduction and relaxation mechanisms of a material vary with both external and internal parameters such as frequency, temperature, pressure and also with the orientation, mixture and molecular structure of the sample. For instance, Verway [5] attributed high conductivity in Fe_3O_4 due to the presence of Fe^{2+} and Fe^{3+} ions on equivalent sites (octahedral sites) whereas high resistivity in ferrites such as $NiFe_2O_4$ or, $CoFe_2O_4$ etc is attributed to the occupation

of B-sites by other divalent metal ions and trivalent Fe ions. Therefore, in the following section, important topics related to dielectric properties of a material are discussed.

1.6.1 Impedance Spectroscopy and Permittivity

It is well-known that impedance spectroscopy is a powerful technique in the investigation of dielectric properties of materials, such as conductivity (σ), dielectric constant (ε), transport phenomena, interfacial capacitance, mobility of charges and their equilibrium concentration etc [70]. When an ac signal with electric field strength far less than breakdown voltage, is applied to a system, the impedance of the system obeys Ohm's law, as ratio of voltage (V) to current (I) in the time domain,

$$V(t) = V_0 exp(j\omega t) \text{ and } I(t) = I_0 exp(j\omega t - \theta) \quad 1.8$$

$$Z^*(\omega) = |Z|\cos\theta - j|Z|\sin\theta = Z' - jZ'' = \frac{1}{j\omega C^*} \quad 1.9$$

Here, Z' and Z'' are the real and imaginary parts of complex impedance (Z^*), ω ($=2\pi f$), angular frequency of the signal and C^* is the complex capacitance of the dielectric sample. As the relative dielectric constant or, permittivity (ε^*) of the material is related to the capacitance in a way, $\varepsilon^* = C^*/C_0$, from impedance it can be calculated from,

$$\varepsilon^* = \frac{1}{j\omega C_0 Z^*} = \varepsilon' - j\varepsilon'' \quad 1.10$$

Where, capacitance of free space, $C_0 = \frac{\varepsilon_0 A}{d}$, ε_0, A and d are free space permittivity (8.854×10^{-12} F/m), area and thickness of the sample respectively. Expanding Eq. (1.10), real and imaginary parts of dielectric constant in terms of impedance parts are,

$$\varepsilon' = \frac{Z''}{\omega C_0 (Z'^2 + Z''^2)} \text{ and } \varepsilon'' = \frac{Z'}{\omega C_0 (Z'^2 + Z''^2)} \quad 1.11$$

Moreover, real part of conductivity can be found as $\sigma = \omega\varepsilon_0\varepsilon''$. Permittivity values show the interaction of an external field with electric dipole moments of the sample. The ε' represents the amount of dipole or charge alignment (both induced and permanent) due to polarization and ε'' measures the energy required to align the dipoles or move ions. Loss tangent ($\tan\delta_\varepsilon = \frac{\varepsilon''}{\varepsilon'}$) is expressed as measure of energy loss from the material

due to an external electric field. Generally, with rising temperatures, ε^* increases in dielectric material with an increase in participating dipoles or ions. Frequency dependence of ε′ according to ideal Debye's dispersion equation is,

$$\varepsilon' = \varepsilon'_{\infty} + \frac{(\varepsilon'_0 - \varepsilon'_{\infty})}{(1+(\omega\tau)^2)} \text{ and } \varepsilon'' = \frac{(\varepsilon'_0 - \varepsilon'_{\infty})\omega\tau}{(1+(\omega\tau)^2)} \quad 1.12$$

Where, ε'_{∞} and ε'_0 are the permittivity values at high and at low frequency respectively and τ is relaxation time constant. With increasing frequency ε' falls as the polarizing dipoles started lagging behind the field whereas ε″ exhibits a maximum at $\omega = 1/\tau$, where the oscillating charges are coupled with the oscillating field and absorbs a maximum electrical energy. Many materials show a non-Debye dielectric behavior characterized by a broader asymmetric loss peak where greater than one ions are responsible for dielectric dispersion. Cole-Cole, Davidson-Cole and empirical expression proposed by Havriliak-Negami could describe the non-Debye behavior of the material [71]. Electric modulus (M), defined as the inverse of relative permittivity, comes into play for analyzing dielectric behavior at relatively higher temperatures, where ε usually becomes very high due to electrode polarization and carrier transport.

1.6.2 Polarization

In ferrites, the cations are surrounded by close packed oxygen anions and can be treated as isolated from each other. Therefore, the electrons or holes associated with particular ion will remain localized creating a potential well. For a carrier charge, trapped at a lattice site in such deep well, its transition to a neighboring lattice site may get activated by thermal activation or at higher frequency. This trapped charge is called small polaron which is consequence of defect in the crystal lattice and gives rise to polarization when an electric field is applied [72]. The migration of the charge carriers as well as the characteristic features in dielectric properties largely depends on the cation placement in A or B sites of ferrites. Moreover, the interaction of hopping of electrons between cations through the following process gives rise to dipole pairs in ferrites which make contribution in dipolar polarization [6]:

$$T^{2+} + Fe^{3+} \leftrightarrow T^{3+} + Fe^{2+} + E_a \quad 1.13$$

where E_a is the activation energy, required for transfer of electron from T^{2+} to Fe^{3+} and vice versa. This polarization originates from a number of sources:

Electronic: Electron cloud displaces relative to nucleus while external field is applied. The required time for this type is the lowest ($\sim 10^{-15}$ s) and hence its small contribution becomes prominent at optical frequencies.

Atomic: Atomic polarization occurs when adjacent positive and negative ions 'stretch' under an applied electric field. This is also a fast process as time required for response is 10^{-13} s and this kind of polarization is effective at THz and microwave frequencies. Along with dielectric relaxation, at high frequency, resonance-type dielectric response takes place in the dielectric system inertial effects in charge movement or anomalous dispersion is considered [73].

Dipolar: Alignment through orientation of dipoles in electric field is known as dipolar or orientation polarization. This orientation polarization typically requires 10^{-9} s.

Space charge: Interfacial polarization is due to space charge accumulation at the structural interfaces of an inhomogeneous dielectric material. The trapped charge carriers participate in this process and with increasing temperature, this kind of polarization enhances as thermal agitation makes more carriers active. Its operating frequency range is less than 10^7 Hz and takes place between microwave and radio-wave frequency range at room temperature.

As frequency increases, the slow mechanisms drop out leaving the faster ones to contribute in ε values. A dielectric constant versus frequency curve showing different types of polarization is schematically presented in Fig. 1.10. This dielectric relaxation can be described through Maxwell-Wagner grain-grain boundary model for ferrites and visualized in Cole-Cole plot.

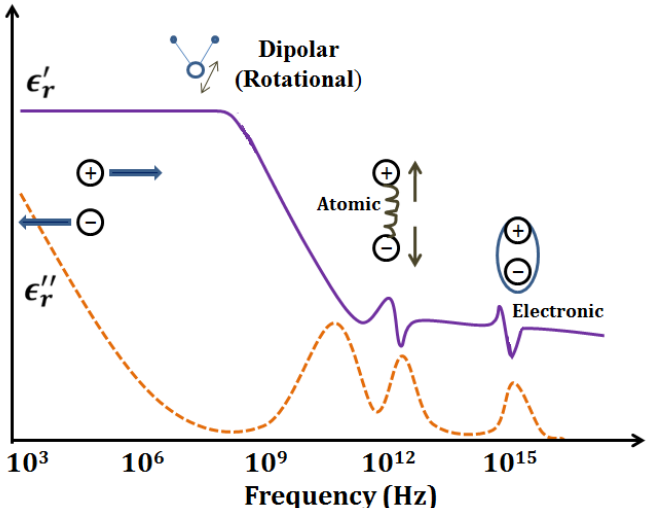

Figure 1.10. Dielectric response with frequency

1.6.3 Maxwell-Wagner Model and Cole-Cole Plot

Koops [74] suggested a theory in which conducting grains and insulating grain boundary layers of ferrite material can be understood as inhomogeneous polycrystalline dielectric structure, which is introduced by Maxwell and Wagner [75]. When an external electric field is applied, the charge carriers easily migrate from the grain and get accumulated (space charge) at the resistive grain boundaries. This process can produce large polarization and high ε' at low frequencies. The presence of inertia to the charge movement would cause a relaxation of dipoles to the polarizing field which causes a finite phase difference with the field. After a sufficiently high characteristic cut off frequency, the phase lag in the carriers becomes prominent and hence ε' decays. At such frequencies, conductive grains become more active and electron hopping takes place, thereby increasing the conduction in the material.

Cole-Cole plot is basically simple real part of impedance (Z') vs. imaginary part of impedance (Z'') plot that can portray Maxwell-Wagner two layer model and represent the electrical processes taking place within the system and the relaxation mechanism happening. A Cole-Cole plot for two layer model is described in Fig. 1.11. At a particular temperature, a Debye type material shows a perfect semi-circular plot, for

non-Debye type it is a distorted semi-circle and electrode-sample interface shows an inclined line plot. The resistive and capacitive components of complex Z of grain and grain boundary can be analyzed as shown in Fig. 1.11.

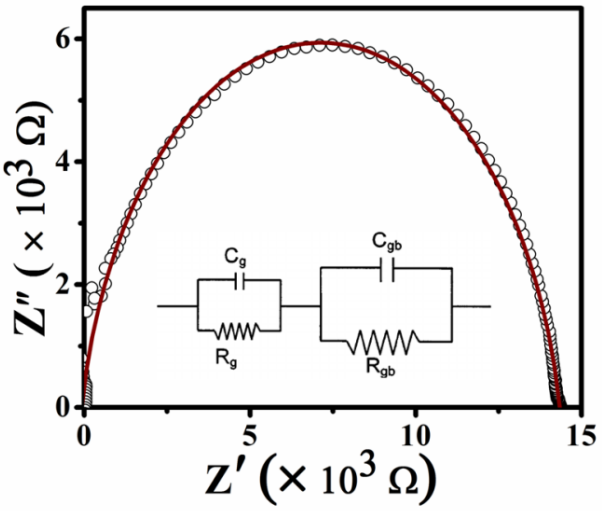

Figure 1.11. An illustration of Cole-Cole plot fitted with equivalent circuit for dielectric properties of grain and grain boundaries

1.6.4 Conduction

In dielectric ferrites, as the frequency of the applied field increases, the conductive grains become more active by promoting the hopping of electrons and holes between Fe^{2+} and T^{3+} ions and vice-versa, thereby increasing the hopping rate. Thus, a gradual increase in conductivity with applied field frequency can be observed with a simultaneous decay in polarization. The frequency dependence of conductivity is related by a simple expression given by Jonscher's power law [76]

$$\sigma_{ac}(\omega, T) = \sigma_{dc}(T) + A\omega^{s}(T) \qquad 1.14$$

Here, σ_{dc} is the dc conductivity of the material, A is material dependent and s is the temperature dependent parameter, varies within $0 < s < 1$ depending on the mechanism of conduction. Though the grain boundaries are resistive and may act as a hindrance to the ionic transport, but the presence of large defect density in the interfacial region contributes to the high conduction path. Thermal excitation facilitates

hopping of charges by increasing mobility of charge carriers and carrier concentration. Activation energy (taking it also as thermally activated) for dc conduction (E_{dc}) is found by fitting Arrhenius equation of conductivity to $\ln\sigma_{ac}$ vs. $1/k_BT$ plot at low frequency.

1.7 Microwave Absorption Properties

Approximate Band Designations	
High frequency (HF)	3 MHz–30 MHz
Very high frequency (VHF)	30 MHz–300 MHz
Ultra high frequency (UHF)	300 MHz–3 GHz
L band	1–2 GHz
S band	2–4 GHz
C band	4–8 GHz
X band	8–12 GHz
Ku band	12–18 GHz
K band	18–26 GHz
Ka band	26–40 GHz
U band	40–60 GHz
V band	50–75 GHz
E band	60–90 GHz
W band	75–110 GHz
F band	90–140 GHz

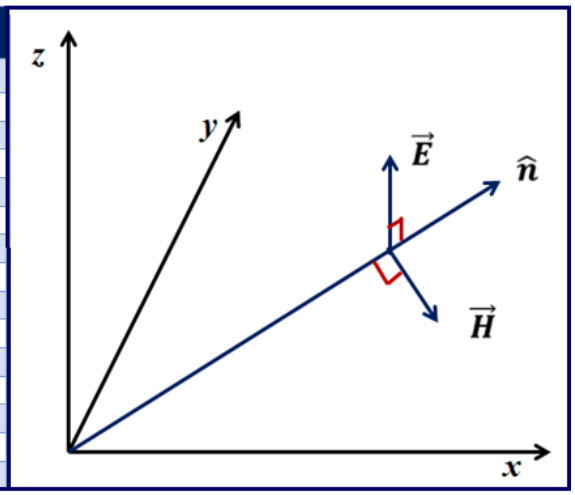

Figure 1.12. (a) Frequency band designations over EM wave spectra (b) Orientation of the $\vec{E},\vec{H},\vec{k} = k\hat{n}$ vectors for a general plane wave

With the widespread evolution of technology, from wireless information transfer, global navigation to radar (radio detection and ranging) communication, the demand of ferrites is increasing rapidly for high-frequency applications [9,44,77]. Frequency band designations over EM wave spectra are tabulated in Fig. 1.12(a). A recent survey shows researches on ferrites in engineering is around 23% and as an effect on application, this enhances the production quantity lowering the cost of microwave devices [78]. Ferrites are ferrimagnetic oxides of iron which combine the properties of a magnetic material with that of an electrical insulator [43]. Unlike highly conductive metals, they allow penetration of electromagnetic (EM) waves into the material and due to high resistivity; they lessen eddy current loss increasing scope of applications in high-frequency devices. In non-reciprocal devices like circulators, fast sensors ferrite properties such as high anisotropy, low FMR (ferro-magnetic resonance) bandwidth and low loss are needed [43,79,80]. In contrast, for microwave absorbers, lossy material with broad

resonance bandwidth and a proper matching of relative permittivity ($\varepsilon = \varepsilon' - j\varepsilon''$) and permeability ($\mu = \mu' - j\mu''$) is essential.

In recent years, the unwanted side-effects from usage of high-frequency devices, such as Electromagnetic Interference (EMI) became a serious issue [34,44]. Interference of EM waves from different sources results in misinterpretation of carried information, noise and hence, slow down of devices. Moreover, this undesired wave pollution is hazardous to environment also. Not only it is harmful to birds but it can even deteriorate human health. Therefore, Electromagnetic absorbers (EMA) are in serious need to suppress and shield unwanted EM waves [38,81]. EMA materials can be implied in form of films in circuit components as frequency-selective band pass filters. Further, in military field, from 19th century, there is huge use of EMA materials in 'stealth technology' to make the aircrafts or ships invisible towards radar detection [82,83]. In spite of the ferrite domination in high-frequency devices, the main drawback relies on their heavy weight because thin, light-weight, inexpensive yet efficient microwave absorbers are most expected for practical applications [9,15,84]. To achieve this purpose, NHSs of ferrites can be an interesting morphology as they are light-weight and can enhance both dielectric and magnetic losses. Ferrite based EMA materials prevent reflection of EM wave and transform most of it as heat energy. In relation with this dissipation of heat and rise in temperature of the material, ferrites due to their lower thermal co-efficient and stability can act fairly up to 200°C [85]. For the study and application purposes, ferrite fillers are usually dispersed into a favorable polymer matrix and precisely to a shape. Over the years, there are numerous methods developed for measuring permeability and permittivity. These techniques include free-space methods, open-ended coaxial probe techniques, cavity resonators, full-body resonance techniques, and transmission-line techniques [86]. Each method has its range of applicability and its own inherent limitations. For example, techniques based on cavities are accurate, but not broadband [86]. Among these, transmission line techniques are the simplest and relatively accurate ways of measuring characteristic properties of materials. In the following sections, detailed outline of transmission line technique with EM wave theory related to microwave absorption is described.

1.7.1 Related Electromagnetic Theory

Electric and magnetic phenomena, electromagnetic wave propagation at the macroscopic level are described by Maxwell's equations, as published by Maxwell in 1873 and that provided a foundation for practical applications of guided waves and transmission lines. Maxwell's equations in a material are,

$$\vec{\nabla} \cdot \vec{\mathrm{D}} = \rho \qquad 1.15(a)$$

$$\vec{\nabla} \cdot \vec{\mathrm{B}} = 0 \qquad 1.15(b)$$

$$\vec{\nabla} \times \vec{\mathrm{E}} = -\frac{\partial \vec{\mathrm{B}}}{\partial t} \qquad 1.15(c)$$

$$\vec{\nabla} \times \vec{\mathrm{H}} = \vec{\mathrm{J}} + \frac{\partial \vec{\mathrm{D}}}{\partial t} \qquad 1.15(d)$$

Here, $\vec{\mathrm{D}} = \varepsilon_0 \vec{\mathrm{E}} + \vec{\mathrm{P}} = \varepsilon \vec{\mathrm{E}}$, is electric flux density, $\vec{\mathrm{B}} = \mu_0 (\vec{\mathrm{H}} + \vec{\mathrm{M}}) = \mu \vec{\mathrm{H}}$, magnetic flux density, ρ, free charge density and $\vec{\mathrm{J}} = \sigma \vec{\mathrm{E}}$, current density in the material. Orientation of the $\vec{E}, \vec{H}, \vec{k} = k\hat{n}$ vectors for a general plane wave is schematically represented in Fig. 1.12(b). $\vec{\mathrm{H}}$ can be written in terms of $\vec{\mathrm{E}}$ as,

$$\vec{\mathrm{H}} = -\frac{1}{j\omega\,\mu_0} \vec{\nabla} \times \left(\vec{\mathrm{E}}_0 e^{-j\vec{\mathrm{k}} \cdot \vec{\mathrm{r}}} \right) \qquad 1.16(a)$$

$$= \frac{1}{\omega\,\mu_0} \vec{\mathrm{k}} \times \vec{\mathrm{E}}_0 e^{-j\vec{\mathrm{k}} \cdot \vec{\mathrm{r}}} \qquad 1.16(b)$$

$$= \sqrt{\frac{\varepsilon_0}{\mu_0}} \left(\hat{n} \times \vec{\mathrm{E}} \right) \qquad 1.16(c)$$

Considering wave equation, $\vec{\mathrm{E}} = E_0 \cos(\omega t + \varphi)\hat{x}$, Maxwell's equations are in phasor form,

$$\vec{\nabla} \cdot \vec{\mathrm{D}} = \rho \qquad 1.17(a)$$

$$\vec{\nabla} \cdot \vec{\mathrm{B}} = 0 \qquad 1.17(b)$$

$$\vec{\nabla} \times \vec{\mathrm{E}} = -j\omega \vec{\mathrm{B}} \qquad 1.17(c)$$

$$\vec{\nabla} \times \vec{\mathrm{H}} = j\omega\vec{\mathrm{D}} + \vec{\mathrm{J}} \qquad 1.17(\mathrm{d})$$

Propagation of ac EM wave suggests permittivity of a material to be complex. In that case, Eq. 1.17(d) takes the form below and dielectric loss tangent is defined again.

$$\vec{\nabla} \times \vec{\mathrm{H}} = j\omega(\varepsilon^{'} - j\varepsilon^{''})\vec{\mathrm{E}} + \sigma\vec{\mathrm{E}} \qquad 1.18$$

$$tan\delta_{\varepsilon} = \frac{(\sigma + \omega\,\varepsilon^{''})}{\varepsilon^{'}} \qquad 1.19$$

Solving for $\mathbf{E}$ or $\mathbf{H}$ from 1.17(c) and 1.17(d) gives Helmholtz wave equations.

$$\vec{\nabla} \times \vec{\nabla} \times \vec{\mathrm{E}} = -j\omega\mu\vec{\nabla} \times \vec{\mathrm{H}} = \omega^2\mu\varepsilon\vec{\mathrm{E}} \qquad 1.20(\mathrm{a})$$

$$\nabla^2\vec{\mathrm{E}} + \omega^2\mu\varepsilon\vec{\mathrm{E}} = 0 \qquad 1.20(\mathrm{b})$$

A constant $k = \omega\sqrt{\mu\varepsilon}$ is defined as the propagation constant (also known as the phase constant, or wave number) of the medium. For plane waves in a general lossy (with a finite conductivity σ) medium, the resulting wave equation for $\mathbf{E}$ becomes,

$$\nabla^2\vec{\mathrm{E}} + \omega^2\mu\varepsilon\left(1 - j\frac{\sigma}{\omega\varepsilon}\right)\vec{\mathrm{E}} = 0 \qquad 1.21$$

Then a complex propagation constant for the medium is defined as,

$$\gamma = \alpha + j\beta = j\omega\sqrt{\varepsilon\mu}\sqrt{1 - j\frac{\sigma}{\omega\varepsilon}} \qquad 1.22$$

where α is the attenuation constant and β is the phase constant. When an incident wave enters in absorbing material, the wave exponentially decays with distance z, by the factor, $e^{-\alpha z}$ and for low conductive material like ferrites, α is expanded as,

$$\alpha + j\beta = j\frac{2\pi f}{c}\sqrt{(\mu'\varepsilon' - \mu''\varepsilon'') - j(\mu'\varepsilon'' + \mu''\varepsilon')} \qquad 1.23(\mathrm{a})$$

$$\alpha = \frac{\sqrt{2}\pi f}{c}\sqrt{(\mu''\varepsilon'' - \mu'\varepsilon') + \sqrt{(\mu''\varepsilon'' - \mu'\varepsilon')^2 + (\mu^{''}\varepsilon^{'} + \mu'\varepsilon'')^2}} \qquad 1.23(\mathrm{b})$$

From 1.16(b) and considering modified Helmholtz equation, relation between magnetic and electric field transforms to,

$$\vec{\mathrm{H}} = \frac{\gamma}{j\omega\mu}\vec{\mathrm{E}} \qquad 1.24$$

Here, $\eta = \frac{j\omega\mu}{\gamma}$ is the intrinsic impedance of the conducting medium. For highly conducting media like metal (high σ), EM wave does not penetrate into material as the skin-depth, $\delta = 1/\alpha = \sqrt{\frac{2}{\omega\mu\sigma}}$ becomes much lower. The average power (P_l) dissipated in the volume V of a lossy medium due to conductivity, dielectric, and magnetic losses is

$$P_l = \frac{\sigma}{2}\int E^2\, dv + \frac{\omega}{2}\int(\varepsilon'' E^2 + \mu'' H^2)dv \qquad 1.25$$

However, the contribution from magnetic hysteresis and domain wall resonance turns out to be less important in low field and at high frequencies ($f > 100\ MHz$ for ferrites) whereas characteristic FMR and eddy current loss are much prominent in the GHz region [18,87].

An EM wave propagating along the z-direction, when incidents on a media interface, some part of it reflects and some passes through the material. Considering normal incidence (as shown in Fig. 1.13), the expressions for incident waves ($\mathbf{E_i}$, $\mathbf{H_i}$), reflected ($\mathbf{E_r}$, $\mathbf{H_r}$) and transmitted ($\mathbf{E_t}$, $\mathbf{H_t}$) will be,

(at $z < 0$)

$$\vec{\mathrm{E}}_i = \hat{x}E_0 e^{-jk_0 z} \qquad 1.26(a)$$

$$\vec{\mathrm{H}}_i = \hat{y}\frac{1}{\eta_0}E_0 e^{-jk_0 z} \qquad 1.26(b)$$

$$\vec{\mathrm{E}}_r = \hat{x}\Gamma E_0 e^{jk_0 z} \qquad 1.26(c)$$

$$\vec{\mathrm{H}}_r = -\hat{y}\frac{\Gamma}{\eta_0}E_0 e^{jk_0 z} \qquad 1.26(d)$$

(at $z > 0$)

$$\vec{\mathrm{E}}_t = \hat{x}TE_0 e^{-\gamma z} \qquad 1.26(e)$$

$$\vec{\mathrm{H}}_t = \hat{y}\frac{T}{\eta}E_0 e^{-\gamma z} \qquad 1.26(f)$$

Here, Γ is the reflection coefficient, T, the transmission coefficient and η_0, intrinsic impedance of free space ($\sim$ 377 Ω). Since the tangential field components must be continuous at $z = 0$, applying boundary conditions, obtained equations are

$$1 + \Gamma = T \qquad 1.27(a)$$

$$1 - \frac{\Gamma}{\eta_0} = \frac{T}{\eta} \qquad 1.27(b)$$

Solving the equations, Γ and T can be expressed as,

$$\Gamma = \frac{\eta - \eta_0}{\eta + \eta_0} \qquad 1.28(a)$$

$$T = \frac{2\eta}{\eta + \eta_0} = 1 + \Gamma \qquad 1.28(b)$$

Reflection loss (RL) related to reflected power of EM wave from a material is defined from Γ value as, RL (in dB) $= -20\log|\Gamma|$. In this thesis, the sign for RL is taken negative ($-$) as per convention.

The EM wave when gets confined to a waveguide, optical fiber or resonator, different transverse modes are associated considering the boundary conditions of transmission lines. The discussion is continued in the following section.

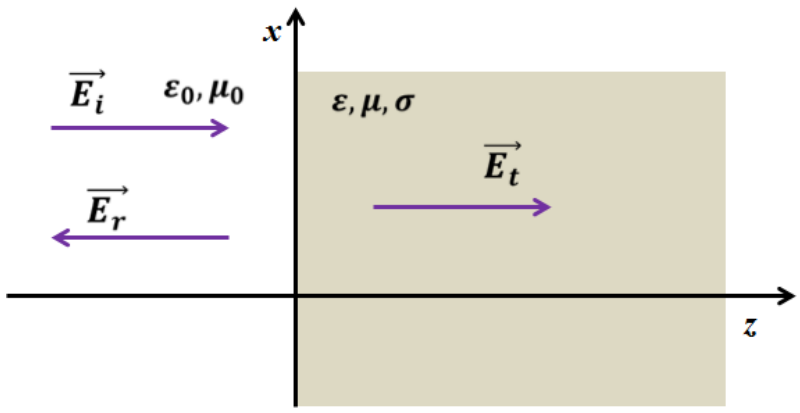

Figure 1.13. Plane wave reflection from an arbitrary medium: normal incidence

1.7.2 Transmission Line Analogy

Transmission lines are generally consisted of one or more conducting lines. The circuit elements related to such lines are series resistance (R) for their length, series inductance (L) from conductors, shunt capacitance (C) from parallel placed lines and an additional shunt conductance (G) from added load [88]. Thus a transmission line is a distributed parameter network, where voltages and currents can vary appreciably in magnitude and phase over its length. Such transmission lines are compact, low in cost and capable of being easily integrated with active circuit devices and therefore are of significant importance in the analysis of microwave circuits and devices [89]. Transmission lines that consist of two or more conductors can only support transverse electromagnetic (TEM) waves, characterized by the lack of longitudinal field components. On the other hand, waveguides consisting of a single conductor, support transverse electric (TE) and/or transverse magnetic (TM) waves, characterized by the presence of longitudinal magnetic or electric field components respectively. From Maxwell equations, fields with their transverse components are [90],

$$\vec{\mathrm{E}}(x,y,z) = \left[\vec{\mathrm{E}}_0(x,y) + \hat{z}E_z(x,y)\right]e^{-j\beta z} \qquad 1.29(a)$$

$$\vec{\mathrm{H}}(x,y,z) = \left[\vec{\mathrm{H}}_0(x,y) + \hat{z}H_z(x,y)\right]e^{-j\beta z} \qquad 1.29(b)$$

and

$$H_x = \frac{j}{k_c^2}\left(\omega\epsilon\frac{\partial E_z}{\partial y} - \beta\frac{\partial H_z}{\partial x}\right) \qquad 1.29(c)$$

$$H_y = -\frac{j}{k_c^2}\left(\omega\epsilon\frac{\partial E_z}{\partial x} + \beta\frac{\partial H_z}{\partial y}\right) \qquad 1.29(d)$$

$$E_x = -\frac{j}{k_c^2}\left(\beta\frac{\partial E_z}{\partial x} + \omega\mu\frac{\partial H_z}{\partial y}\right) \qquad 1.29(e)$$

$$E_y = \frac{j}{k_c^2}\left(-\beta\frac{\partial E_z}{\partial y} + \omega\mu\frac{\partial H_z}{\partial x}\right) \qquad 1.29(f)$$

where $k_c = \sqrt{k^2 - \beta^2}$, is cut-off wave number. Solution for TE mode characterized by $E_z = 0$ and $H_z \neq 0$, from $H_z(x,y,z) = h_z(x,y)e^{-j\beta z}$ and reduced Helmholtz wave equation,

$$\left(\frac{\partial^2}{\partial x^2} + \frac{\partial^2}{\partial y^2} + k_c^2\right) h_z = 0 \qquad 1.30$$

For rectangular waveguide with breadth 'a' and width 'b', general solution of 1.30 gives,

$$h_z(x,y) = X(x)Y(y) \qquad 1.31(a)$$

$$h_z(x,y) = (A\ \cos k_x x + B\ \sin k_x x)\left(C\ \cos k_y y + D\ \sin k_y y\right) \qquad 1.31(b)$$

Considering the following boundary conditions on the electric field components tangential to the waveguide walls,

$$e_x(x,y) = 0\ at\ y = 0, b \qquad 1.32(a)$$

$$e_y(x,y) = 0\ at\ x = 0, a \qquad 1.32(b)$$

The final solution for H_z is then,

$$H_z(x,y,z) = A_{mn}\ \cos\frac{m\pi x}{a}\cos\frac{n\pi y}{b}\, e^{-j\beta z} \qquad 1.33$$

Where, the propagation constant for TE_{mn} mode is $\beta = \sqrt{k^2 - \pi^2\left[\left(\frac{m}{a}\right)^2 + \left(\frac{n}{b}\right)^2\right]}$. The associated cut-off frequency is given by $f_{c_{mn}} = \frac{1}{2\pi\sqrt{\mu\varepsilon}}\pi^2\left[\left(\frac{m}{a}\right)^2 + \left(\frac{n}{b}\right)^2\right]$. The mode with the lowest cutoff frequency is called the dominant mode which is here TE_{10} mode. At a given operating frequency f only those modes having $f > f_c$ will propagate, modes with $f < f_c$ will lead to an imaginary β (or real α), that means all field components will decay exponentially from the source of excitation. Such modes are referred to as evanescent modes that can cause overmoding; hence noise can originate in the signal.

Transverse electromagnetic (TEM) waves are characterized by $E_z = H_z = 0$. Here, from 1.29, both k and β equals to $\omega\sqrt{\mu\varepsilon}$. The cutoff wave number, $k_c = \sqrt{k^2 - \beta^2}$, is thus zero for TEM waves. When a gradient of a scalar potential, $\varphi(x,y)$ arises between

two conductors in a waveguide, TEM mode can propagate. Solving Laplace's equation between the two conductors,

$$\nabla_t^2 h(x,y) = 0 \qquad 1.34(a)$$

$$\vec{E}(x,y) = \overrightarrow{\nabla_t}\Phi(x,y) \qquad 1.34(b)$$

With the knowledge of possible wave mode propagation in transmission lines, to get voltage (v) and current (i) definations of a two-wire line, circuit analysis is described. The schematic reperesentation of a tranmission line with its components is shown in Fig. 1.14.

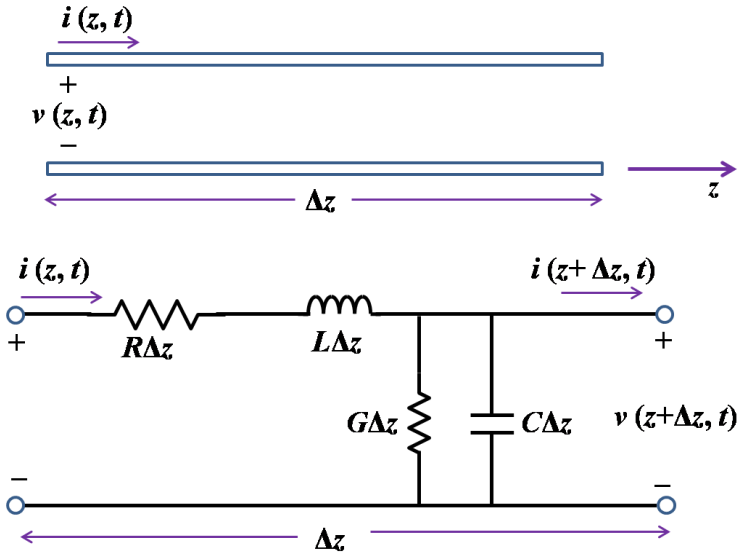

Figure 1.14. (a) Voltage and current definitions and (b) equivalent circuit for an incremental length of transmission line

From the circuit diagram, Kirchhoff's voltage and current laws can be applied to give

$$v(z,t) - R\Delta z i(z,t) - L\Delta z \frac{\partial i(z,t)}{\partial t} - v(z+\Delta z,t) = 0 \qquad 1.35(a)$$

$$i(z,t) - G\Delta z v(z+\Delta z,t) - C\Delta z \frac{\partial v(z+\Delta z,t)}{\partial t} - i(z+\Delta z,t) = 0 \qquad 1.35(b)$$

For the steady-state condition, the 1.35 equations can be simplified into their phasor forms,

$$\frac{dV(z)}{dz} + (R + j\omega L)I(z) = 0 \qquad 1.36(a)$$

$$\frac{dI(z)}{dz} + (G + j\omega C)V(z) = 0 \qquad 1.36(b)$$

Comparing these with wave equations for *V(z)* and *I(z)*, with propagation constant, $\gamma = \sqrt{(R + j\omega L)(G + j\omega C)}$,

$$V(z) = V_0^+(e^{-\gamma z} + \Gamma e^{\gamma z}) \qquad 1.37(a)$$

$$I(z) = \frac{V_0^+}{Z_0}(e^{-\gamma z} - \Gamma e^{\gamma z}) \qquad 1.37(b)$$

where the $e^{-\gamma z}$ term represents wave propagation in the +z direction, and the $e^{\gamma z}$ term, wave propagation in the –z direction. Characteristic impedance (Z_0) of the circuit is defined as,

$$Z_0 = \frac{V_0^+}{I_0^+} = \sqrt{\frac{R + j\omega L}{G + j\omega C}} \qquad 1.38$$

For a coaxial line with inner diameter (a) and outer diameter (b), geometry dependent characteristic impedance is related to intrinsic or wave impedance in the way,

$$Z_0 = \frac{E_\rho \ln(b/a)}{2\pi H_\varphi} = \sqrt{\frac{\mu}{\varepsilon}}\frac{\ln(b/a)}{2\pi} = \eta\frac{\ln(b/a)}{2\pi} \qquad 1.39$$

When transmission line is terminated in an arbitrary load impedance Z_L, at load point, $Z_L = \frac{V}{I} = \frac{V_0^+ + V_0^-}{V_0^+ - V_0^-} Z_0$. Therefore, solving for V_0^- gives,

$$\frac{V_0^-}{V_0^+} = \frac{Z_L - Z_0}{Z_L + Z_0} = \Gamma \qquad 1.40$$

At a distance $z = -l$ from the load, the input impedance (Z_{in}) seen looking toward the load is (from 1.37 and 1.40),

$$Z_{in} = \frac{V(-l)}{I(-l)} = Z_0\frac{Z_L + Z_0 \tanh \gamma l}{Z_0 + Z_L \tanh \gamma l} \qquad 1.41$$

As a special case of this transmission line impedance equation, a line is terminated in a short circuit, i.e. $Z_L = 0$, input impedance takes the form,

$$Z_{in} = Z_0 \tanh \gamma l \qquad 1.42$$

1.7.2.1 Rectangular Waveguide

The simplest and dominant propagation mode in rectangular waveguide with breadth (a) and width (b) (a > b) is the so-called TE_{10} mode and depends on longer side 'a'. Though TM mode can also propagate through this wave guide, its cut-off frequency is much higher than TE mode. Being a closed conductor, it cannot support TEM waves since the corresponding static potential in such a region would be zero or a constant. Rectangular waveguides are used generally to transfer large amounts of microwave power at high frequencies and material properties can be obtained accurately while using this kind of waveguide. A schematic diagram of a rectangular waveguide and field propagation in it is described in Fig. 1.15.

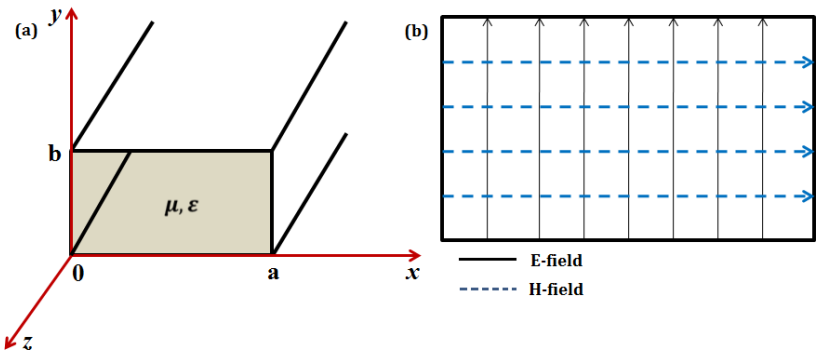

Figure 1.15. Geometry of a rectangular waveguide and field lines for TE_{10} mode

1.7.2.2 Coaxial Airline

Though TE and TM modes can propagate through coaxial airline, but TEM mode with its no cut-off frequency remains the dominant propagation mode. As coaxial airline has no restrictions in frequency, it is a broad band waveguide. Further, coaxial line is also shielded like rectangular waveguide and can be used at high-frequencies. Geometry of a coaxial line and field lines are shown in Fig. 1.16.

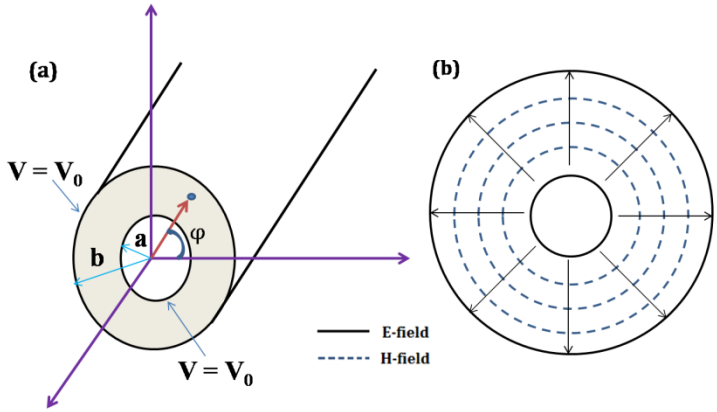

Figure 1.16. Geometry of a coaxial line and field lines for TEM mode

1.7.3 Scattering Parameters

Microwave network analysis is more practical and simple procedure that interconnects both the EM field theory and circuit analysis. At microwave frequencies as the measurement of voltage or current is difficult, a clearly defined terminal pair is needed. Impedance, admittance, scattering matrices of circuit theory are usually used as these terminal or port quantities. This type of representation leads to the development of equivalent circuits of arbitrary networks, which will be quite helpful in design of passive components such as couplers and filters. For a multiple port network, impedance, admittance and scattering parameters in matrix form are respectively,

$$[V] = [Z][I] \qquad 1.43(a)$$

$$[I] = [Y][V] \qquad 1.43(b)$$

$$[V^-] = [S][V^+] \qquad 1.43(c)$$

For transmission line, at high RF and microwave frequencies direct measurement of Y or Z parameters is difficult due to unavailability of equipment to measure port current and voltage directly and difficulty of obtaining perfect opens/shorts. Under this situation, direct measurements with the ideas of incident, reflected, and transmitted waves are given by the scattering matrix. A specific element of the scattering matrix can be determined as,

$$S_{ij} = \frac{V_i^-}{V_j^+}\Big|_{V_k^+=0, k\neq j} \qquad 1.44(a)$$

In words, 1.43 says that S_{ij} is the ratio of the reflected or transmitted wave amplitude V_i^- coming out of port i while the incident wave at port j is voltage V_j^+. For a two-port device the four S-parameters are S_{11}, S_{21}, S_{12}, and S_{22}. A schematic representation of a 2-port network defining its S-parameters is shown in Fig. 1.17. Here S_{11} and S_{22} are the forward and reverse reflection coefficients and S_{21} and S_{12} are the forward and reverse gains respectively.

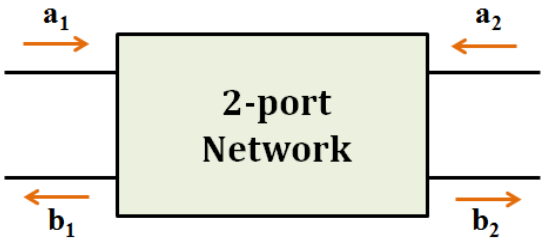

Figure 1.17. Schematic representation of a 2-port network

The expression for 2-port S-parameters is shown below,

$$\begin{bmatrix} b_1 \\ b_2 \end{bmatrix} = \begin{bmatrix} S_{11} & S_{12} \\ S_{21} & S_{22} \end{bmatrix} \begin{bmatrix} a_1 \\ a_2 \end{bmatrix} \qquad 1.44(b)$$

1.7.4 Nicholson-Ross-Weir Algorithm

In cases we have a material under test (MUT) inside a wave guide or a coaxial airline, the phenomena of reflection and transmission of incident wave is shown in Fig. 1.18(a). Measurement using the Transmission/Reflection line method involves placing a sample in a section of waveguide or coaxial line and measuring the two port complex scattering parameters with a vector network analyzer (VNA). The conversion of S-parameters to complex permittivity and permeability is computed by solving equations using different algorithms. Nicholson-Ross-Weir (NRW) method is the most commonly used one for measuring both μ and ε values of a magnetic material like ferrite. The determination of

μ and ε values usually proceeds by solving a transcendental equation that involves the sample length, sample position, and reflection coefficient [91]. The detailed steps of NRW method are described hereafter.

The first step will be to obtain relations of μ and ε values with Γ. Some parameter expressions such as γ, k_c, η are recalled, $\gamma^2 = k_c^2 - k^2$, $k_c = \frac{2\pi}{\lambda_c}$ (λ_c = cut-off wavelength), $k = \omega\sqrt{\varepsilon\mu}$ and $\eta = \frac{j\omega\mu}{\gamma}$. Reflection co-efficient Γ is written as,

$$\Gamma = \frac{\eta - \eta_0}{\eta + \eta_0} = \frac{\frac{\gamma_0}{\gamma}\mu - 1}{\frac{\gamma_0}{\gamma}\mu + 1} \tag{1.45}$$

Where, γ_0 is the complex propagation constant in the air. Solving for μ,

$$\mu = \left(\frac{1+\Gamma}{1-\Gamma}\right)\frac{\gamma}{\gamma_0} \tag{1.46}$$

$$\frac{\gamma}{\gamma_0} = \frac{j\sqrt{\frac{\omega^2\varepsilon\mu}{c^2} - \left(\frac{2\pi}{\lambda_c}\right)^2}}{j\sqrt{\left(\frac{\omega}{c}\right)^2 - \left(\frac{2\pi}{\lambda_c}\right)^2}} = \frac{\gamma}{j2\pi\sqrt{\frac{1}{\lambda_0^2} - \frac{1}{\lambda_c^2}}} \tag{1.47}$$

Defining $\frac{1}{\Lambda} = \frac{\gamma}{j2\pi}$ and from 1.45 and 1.46,

$$\mu = \left(\frac{1+\Gamma}{1-\Gamma}\right)\frac{1}{\Lambda\sqrt{\frac{1}{\lambda_0^2} - \frac{1}{\lambda_c^2}}} \tag{1.48}$$

From $\gamma^2 = (2\pi)^2\left[\frac{1}{\lambda_0^2} - \frac{\mu\epsilon}{\lambda_c^2}\right]$, solving for ε gives,

$$\varepsilon = \frac{{\lambda_0}^2\left[\frac{1}{\lambda_c^2} - \left(\frac{\gamma}{2\pi}\right)^2\right]}{\mu} = \frac{{\lambda_0}^2}{\mu}\left[\frac{1}{\lambda_c^2} + \frac{1}{\Lambda^2}\right] \tag{1.49}$$

The next step aims at clarifying the relationship between Γ, γ and the scattering matrix, which carries the information of the incident, reflected and transmitted waves (as shown in Fig. 1.18(b)). Assuming normal incidence in an isotropic material ($S_{12} = S_{21}$), the sum of reflected fields at the interface with the sample (Γ_{in}) is given by,

$$\Gamma_{in} = \Gamma_{12} + T_{12}\Gamma_{in}T_{21}e^{-2\gamma L} + T_{12}\Gamma_{21}\Gamma_{23}^2T_{21}e^{-4\gamma L} + \cdots \tag{1.50(a)}$$

$$\Gamma_{in} = \Gamma_{12} + \frac{T_{12}T_{21}\Gamma_{23}e^{-2\gamma L}}{1-\Gamma_{21}\Gamma_{23}e^{-2\gamma L}} \quad 1.50(b)$$

Here Γ_{ij} and T_{ij} are the reflection coefficient and transmission coefficient of the wave respectively that propagates from material 'i' to material 'j'. At the traditional setup, material 1 and material 3 are air. Based on 1.44, we can conclude that

$$\Gamma_{12} = -\Gamma_{21} = -\Gamma_{23} \quad 1.51$$

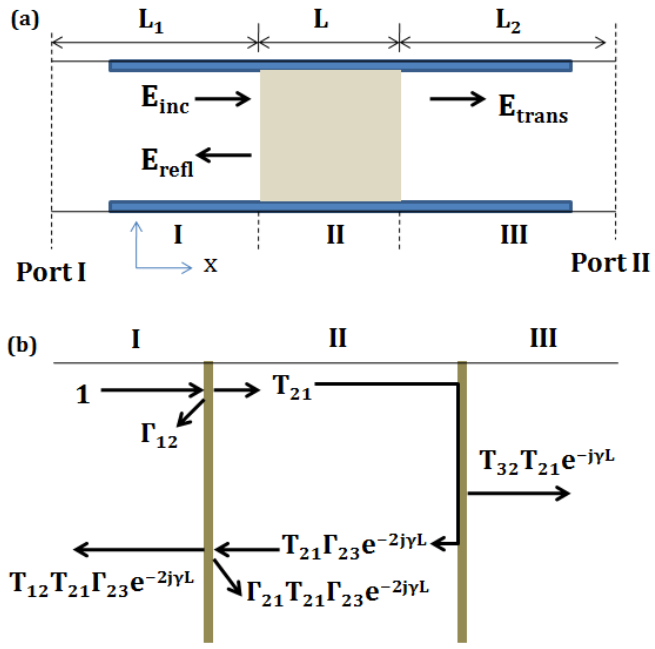

Figure 1.18. (a) Electromagnetic waves transmitting and reflecting from a sample in a transmission line (b) Multiple reflection at three materials interfaces

Further, applying the boundary condition of continuality for tangential component of electric fields across the interface,

$$T_{12} = 1 + \Gamma_{21} \quad 1.52$$

Defining $z = e^{-\gamma L}$ and $\Gamma = \Gamma_{12}$, we obtain from 1.49(b),

$$\frac{\sum E_{Reflected}}{E_{incident}} = S_{11} = \frac{\Gamma(1-z^2)}{1-\Gamma^2 z^2} \quad 1.53$$

In a similar manner, the transmission co-efficient results in,

$$\frac{\sum E_{transmitted}}{E_{incident}} = \frac{T_{32}\,T_{21}\,e^{-\gamma L}}{1-\Gamma_{21}\,\Gamma_{23}\,e^{-2\gamma L}} = \frac{(1-\Gamma^2)z}{1-\Gamma^2 z^2} = S_{21} \qquad 1.54$$

To obtain expression of Γ and z in terms of S_{11} and S_{21},

$$K = \frac{S_{11}-S_{21}+1}{2S_{11}} \qquad 1.55(a)$$

$$\Gamma^2 - 2\Gamma K + 1 = 0 \qquad 1.55(b)$$

$$\Gamma = K \pm \sqrt{K^2-1} \qquad 1.55(c)$$

The quadratic equation of Γ has two solutions. To determine the correct solution for a passive medium, the physical restriction $|\Gamma| < 1$ is used. From 1.52, 1.53 and 1.55(c),

$$z = \frac{S_{11}+S_{21}-\Gamma}{1-(S_{21}+S_{11})\Gamma} = e^{-\gamma L} \qquad 1.56$$

While solving 1.55 for γ, the phase ambiguity problem arises. The measurements of phase of S_{11} and of S_{21} are ambiguous since the network analyzer is only able to detect a phase between $-\pi$ and $+\pi$. Moreover, a limitation in length of the sample $l < \lambda/2$ also exists. The possible corrections for the ambiguities in this method are discussed in the following section.

1.7.5 Corrections and Polynomial Fit Model

The phase ambiguity is the main problem of the NRW method which makes the solution not entirely analytical [91]. Difficulties arise with these transmission line techniques for magnetic materials such that numerical singularities can occur at frequencies corresponding to integral multiples of one half wave length (λ/2). The most common is to use a very thin sample to solve this problem. Furthermore, air gaps and over-moding are two major problems encountered in transmission line measurements [86]. The imperfections can cause evanescent waves near sample-material interface and hence noise in the outcome. Among the possible ways to rectify the problems, two-sample technique has disadvantage that it needs two samples of different lengths at a time. The polynomial fitting technique is a newer method which assumes a functional

relationship between the material properties and the measurement frequency. The functional relationship is assumed to be an n[th] order polynomial [92],

$$y_n = \sum_{n=0}^{n=\infty} a_n x^n \qquad 1.57$$

Here the a_i terms are constants; n is the order of the polynomial and the initial values and order of the polynomial are guessed before fitting.

Gaps between the sample holder and sample either may be corrected with gap-correction formulas or a conducting paste can be applied to external surfaces of the sample that are in contact with the sample holder. Air gap in between interfaces can be considered as layered capacitors [86]. This approach assumes that the gaps between transmission line and sample are effectively modeled by a set of capacitors in series.

$$\frac{1}{C_m} = \frac{1}{C_1} + \frac{1}{C_2} + \frac{1}{C_3} \qquad 1.58(a)$$

For a coaxial line,

$$C = \frac{2\pi\varepsilon l}{\ln\frac{R_2}{R_1}} \qquad 1.58(b)$$

Solving for ε provides,

$$\varepsilon_c^{'} = \varepsilon_m^{'} \frac{L_2}{L_3 - \varepsilon_m^{'} L_1} \qquad 1.59(a)$$

$$\varepsilon_c{}'' = (\varepsilon_c{}' \times \frac{\varepsilon_m{}''}{\varepsilon_m{}'}) \frac{L_3}{L_3 - L_1 \varepsilon_m{}' (1 + [\frac{\varepsilon_m{}''}{\varepsilon_m{}'}]^2)} \qquad 1.59(b)$$

Modeling transmission line as a series of inductors for the E-field gap,

$$L_c = L_m - L_{air}$$

where c, m, and air denote corrected value, measured value and air space. For a coaxial line,

$$L = \frac{1}{2\pi} \mu' \ln({}^{D_3}/_{D_2}) \qquad 1.60$$

Therefore we can write for the corrected permeability,

$$\mu_c{}' = \mu_m{}' \frac{L_3 - L_1}{L_2} \quad 1.61(a)$$

$$\mu_c{}'' = \mu_m{}'' \frac{L_3}{L_2} \quad 1.61(b)$$

Where,

$$L_1 = \ln \frac{D_2}{D_1} + \ln \frac{D_4}{D_3} \quad 1.62(a)$$

$$L_2 = \ln \frac{D_3}{D_2} \quad 1.62(b)$$

$$L_3 = \ln \frac{D_4}{D_1} \quad 1.62(c)$$

These gap correction formulas can be derived directly from Maxwell's equations. At higher frequencies, a frequency dependent term should be included with this correction. For, rectangular waveguide, considering same models and H-field gap, the corrected values for μ and ε are,

$$\varepsilon_c{}' = \varepsilon_m{}' \frac{d}{b-(b-d)\varepsilon_m{}'} \quad 1.63(a)$$

$$\varepsilon_c{}'' = \varepsilon_c{}' \left(\frac{\varepsilon_m{}''}{\varepsilon_m{}'}\right) \frac{b}{b-(b-d)\varepsilon_m{}'} \quad 1.63(b)$$

$$\mu_c{}' = \mu_m{}' \left(\frac{b}{d}\right) - \left(\frac{b-d}{d}\right) \quad 1.63(c)$$

$$\mu_c{}'' = \mu_m{}'' \frac{b}{d} \quad 1.63(d)$$

Possible positions of air gaps after a sample inserted are depicted in Fig. 1.19 for coaxial line and rectangular waveguide respectively.

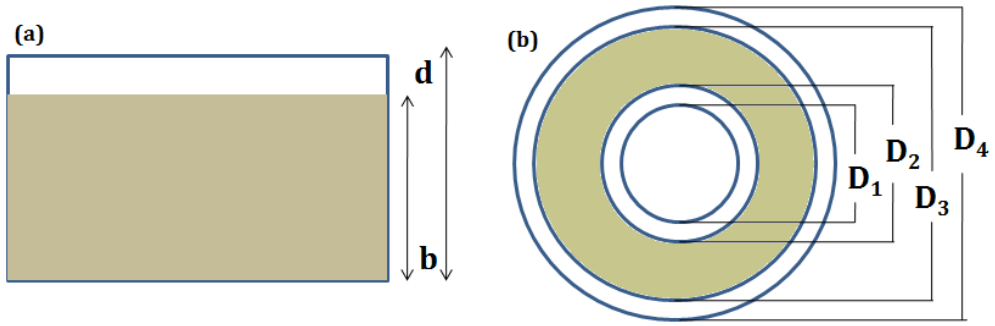

Figure 1.19. Air gaps after a sample inserted in a (a) rectangular waveguide and (b) coaxial line

1.7.6 EMI Shielding for Single Layer Absorber

The diagram of an electromagnetic wave normally incident on an absorber and possible interactions with the material is shown in Fig. 1.20. Shielding efficiency (*SE*) is defined as a parameter that measures amount of EM energy obstructed by an absorbing material slab while passing through it. A normally incident EM wave (E_I) is usually partially reflected at the air-absorber interface, labeled as E_R which can be detected by $S_{11\text{-OPEN}}$, partially penetrates through the layer, denoted as E_T (S_{21}), and partially attenuated in the absorber, E_A. Therefore, three different processes namely reflection, absorption and multiple internal reflections contribute to the whole attenuation, corresponding to shielding effectiveness SE_R, SE_A and SE_M, respectively [38,78]. Total shielding efficiency (*SE*) can be expressed as sum of contributions from reflection (SE_R), absorption (SE_A) and multiple internal reflections (SE_M).

$$SE\ (dB) = 10\log\left(P_t/P_I\right) = SE_A + SE_R + SE_M \qquad 1.64$$

Here, P_t is the transmitted power, and P_I is the incident power of EM wave. The SE components are defined as,

$$SE_R\ (dB) = 10\log(1-R)\,,[\text{where},R = |S_{11}|^2] \qquad 1.65(a)$$

and

$$SE_A\ (dB) = 10\log[(T/(1-R)]\,,[\text{where},T = |S_{21}|^2] \qquad 1.65(b)$$

Neglecting minute effects from multiple reflections ($SE_M = 20log[1 - 10^{\frac{SE_A}{10}}]$) in a slab and putting 1.64 in 1.63, total SE results in,

$$SE\ (dB) = 20\log|S_{21}| \qquad 1.66$$

SE_R is related to the relative impedance mismatching between surface of the shielding material and the EM waves whereas absorption loss results from ohmic losses and heating of the material due to the currents induced in the medium.

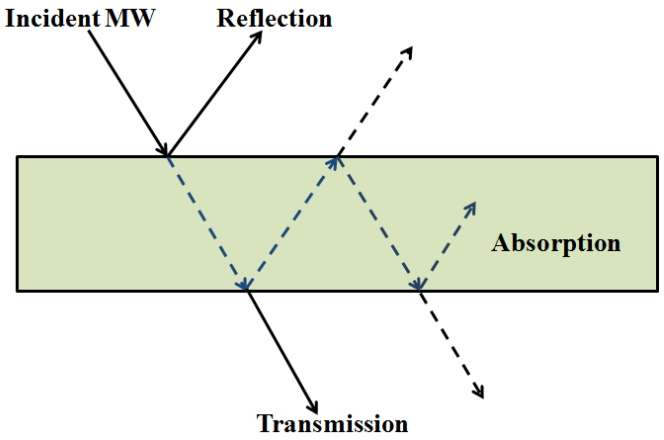

Figure 1.20. Schematic diagram of reflected and transmitted waves when an EM wave is incident on a material

Absorber slab with a conducting metal backing follows Eq. 1.42 for impedance and instead of transmission; EM wave gets totally reflected from absorber-metal surface. The RL properties can then be directly measured by $S_{11\text{-SHORT}}$, which is coincident with the calculated value from the transmission line theory [93]. At a quarter wavelength thickness of this system, EM waves reflected from the first and second interfaces of the absorber are 180 degrees out of phase, resulting in destructive interference. This matching thickness (t_m) is important for designing proper thickness of the absorber for maximum shielding and it can be interpreted from quarter wavelength ($\lambda/4$) model as,

$$t_m = \frac{nc}{4f_m\sqrt{|\varepsilon_r\mu_r|}}\ (n = 1,3,5,\dots) \qquad 1.67$$

where for odd values of *n*, reflected waves from two interfaces of the absorber become out of phase. Therefore, optimizing the material parameters and thickness, *RL* can be tuned for particular frequencies.

1.7.7 Brief Review on Available EMA

Recent advances on electromagnetic wave absorbing material show the evolution of EMA materials from dielectric carbon based ones to complex ferrite-dielectric quaternary compounds. Throughout the years, materials such as carbons, metal powders, ferrites, oxides or polymers are merged, coated, doped into each other to get required features and even different synthesis procedures are tested to vary their characteristic parameters. For instance, Qiu et al. studied microwave absorbing materials based on light-weight walnut shell-derived nano-porous carbon and a maximum reflection loss of −42.4 dB at 8.88 GHz is obtained arising from dielectric relaxation loss [45]. Liu et al. characterized ZnO coated Fe nano-capsules and found an optimal RL of −57.1dB at 7.8 GHz [82]. A brief review is attempted in a form of table summarizing the microwave absorption properties of different kinds of EMA materials.

Table 1.1. Microwave absorption properties of different possible EMA materials

Materials	Thickness (mm)	RL (dB)	Peak Frequency (GHz)	Reference
$Ba_1Co_{0.9}Zn_{1.1}Fe_{16}O_{27}$	2.0	−33.6	12.0	[94]
FeSiAl	4.0	−39.7	1.4	[95]
$SrZnCoFe_{16}O_{17}$	2.6	−33.4	10.4	[96]
rGO/MoS_2	2.0	−33.2	13.0	[97]
Fe_3O_4/C	3.0	−34.7	11.6	[98]
PEO/graphene	2.5	−37.8	16.4	[83]
D1.43μm Carbon fibers	3.0	−22.9	7.6	[99]
Ni/MWNT 5 wt%	4.0	−23.1	8.0	[100]
$PPy/Fe_3O_4/PVDF$	2.5	−21.5	16.8	[101]
Porous flower like Fe_3O_4	2.0	−28.31	13.2	[102]
Fe nanowire/epoxy	2.0	−47.0	9.4	[103]
FeNi@C	2.0	−47.6	3.17	[104]
$Fe_3O_4/ SiO_2/PVDF$ rod	2.5	−28.6	8.1	[105]

$Fe@NiFe_2O_4$	1.5	−27.0	13	[106]
Fe nanoflake@SiO_2	3.6	−20.0	7.3	[81]
Graphene/Fe_3O_4@C@MnO_2	1.8	−38.8	15	[107]
RGO/Fe_3O_4	2	−27.1	5.4	[108]
$CoFe_2O_4$/rGO	2.5	−37.2	11.6	[109]

1.8 Motivation of the Thesis

In the present scenario, electro-magnetic (EM) wave pollution become endangerous to human health due to rapid development of technology and hence EM wave absorbers (EMA) are in serious need to shield the unwanted waves. In this context, ferrites for their synergistic magnetic and dielectric properties are superior choice over traditional dielectrics like carbon based materials or magnetic ultrafine metal powders. Though there are several advantages, high density of ferrites make them heavy weight and difficult to use them in practical applications. Preference of light-weight and size-efficient EMA materials influences us to focus on nano-structures among which nano-hollow spheres (NHS) are a new drift. Moreover, nano-structures possess unique properties than their bulk counterparts and become significant for easy tuning of their properties. To achieve an efficient broad-band EMA material, several techniques such as chemical doping, hybridization of materials, morphology and size control are introduced in this thesis.

The sizes and also magnetic nature of cobalt ferrite nanoparticles are varied in order to explore different possible applications from bio-medicine to permanent magnets of ferrites. Considering the scope of $NiFe_2O_4$ in high-frequency devices for its high resistivity, the detail study of magnetic, dielectric and microwave absorption properties of $NiFe_2O_4$ is performed which indicate that ferrites in the form of hollow structures are much more efficient than their bulk and solid counterparts. Further, study on tunable dielectric and magnetic properties of low-density NHS morphology of transition metal based ferrites with substitution of different cations provides a map to select a proper material for various applications. Motivated by the application of ferrites as EMA material, further studies on ferrite NHSs are performed to find the best

one for it. $MnFe_2O_4$ NHS is found to be most suitable for high-frequency applications as an efficient low-cost microwave absorber. Therefore, a size-dependent microwave absorption study on $MnFe_2O_4$ NHSs is executed and that results highest value of reflection loss (*RL*) in 450 nm NHS with only 20 wt% filler loading content.

1.9 Thesis Organization

The entire thesis is divided into nine chapters. A brief outline of the chapters is given below.

Chapter 1 gives a brief introduction about ferrite nano-structures with their crystal structure, magnetic, electric and microwave absorption properties. Here we have also discussed about surface modification of NSs and its consequences. Frequency dependence of magnetic and electric properties, their origin and applications are described here. Moreover, the motivation of thesis work and the outline of work performed are also included.

Chapter 2 focuses on synthesis procedures, various instrumental techniques for characterization and measurements.

Chapter 3 shows from the detail morphology dependent studies, nano-hollow spheres of $NiFe_2O_4$ are found to exhibit favorable magnetic and dielectric properties compared to their nanoparticles and bulk counterparts.

Chapter 4 presents a comparative study of permittivity, permeability, Reflection Loss and Shielding efficiency on $NiFe_2O_4$ (NFO) nano hollow spheres with its nano particles and bulk counterpart for widely used X-Band (8-12 GHz) on composites filled (25 wt% and thickness of 2 mm) with each sample. Interestingly, light-weight NFO NHSs are found to be highly efficient material towards microwave attenuation.

Chapter 5 describes detail studies on structural, magnetic and dielectric properties of TFe_2O_4 nano-hollow spheres substituting different divalent cations. This study on tunable dielectric and magnetic properties with substitution of different cations

provides a map to select an efficient material for applications from high-frequency devices to bio-medical field.

Chapter 6 demonstrates investigation of electromagnetic wave attenuation properties of as-synthesized low-density TFe_2O_4 [T = Mn, Fe, Co, Ni, Cu, Zn] nano-hollow spheres (20 wt% filled in epoxy resin matrix) within widely-used frequency range of 1 - 20 GHz. Excellent *RL* and broad *BW* observed in $MnFe_2O_4$ NHS (50 wt%) makes it a cost-effective promising EMA material towards mass-efficient high-frequency applications.

Chapter 7 exhibits EM wave attenuation properties of as-synthesized low density MnFe2O4 NHSs in-detail, varying their sizes [mean diameter (nm) of sample sets = 100, 220, 300, 450 and 550 nm within frequency range of 1 – 20 GHz in order to obtain light-weight, stable and cost-effective yet efficient EM wave absorbing material. This study presents that the performance of $MnFe_2O_4$ NHS is optimized at 450 nm.

Chapter 8 reports the study of AOT-functionalized magnetic $CoFe_2O_4$ nanoparticles by a modified wet-chemical method with the size range of 12–22 nm. This size variation is found to vary their magnetic properties specially coercivity. Obtained high H_C ensure the permanent magnetic characteristic of the material which have the potential to replace the expensive rare-earth-transition metal-based permanent magnetic materials. On the other hand, materials with comparatively low value of H_C will be useful for biomedical applications. Among the applications, surface functionalization on NPs is found to enhance the EM wave absorption properties.

Chapter 9 draws the conclusion of this thesis and gives an idea about the scope for future work.

References

[1] A. J. Cox, J. G. Louderback, S. E. Apsel, and L. A. Bloomfield, Phys. Rev. B 49, 12295 (1994).

[2] J. I. Martín, J. Nogués, K. Liu, J. L. Vicent, and I. K. Schuller, J. Magn. Magn. Mater. 256, 449 (2003).

[3] A. V. Krasavin, P. V. Borisyuk, O. S. Vasiliev, Y. V. Zhumagulov, V. A. Kashurnikov, U. N. Kurelchuk, and Y. Y. Lebedinskii, Rev. Sci. Instrum. 89, (2018).

[4] A. G. Kolhatkar, A. C. Jamison, D. Litvinov, R. C. Willson, and T. R. Lee, *Tuning the Magnetic Properties of Nanoparticles* (2013).

[5] C.-Y. Wen, H.-Y. Xie, Z.-L. Zhang, L.-L. Wu, J. Hu, M. Tang, M. Wu, and D.-W. Pang, Nanoscale 8, 12406 (2016).

[6] G. Datt and A. C. Abhyankar, J. Appl. Phys. 122, 34102 (2017).

[7] C. V. Ramana, Y. D. Kolekar, K. Kamala Bharathi, B. Sinha, and K. Ghosh, J. Appl. Phys. 114, 183907 (2013).

[8] S. Sun, H. Zeng, D. B. Robinson, S. Raoux, P. M. Rice, S. X. Wang, and G. Li, J. Am. Chem. Soc. 126, 273 (2004).

[9] F. Wang, J. Liu, J. Kong, Z. Zhang, X. Wang, M. Itoh, and K. Machida, J. Mater. Chem. 21, 4314 (2011).

[10] J. S. An, W. J. Han, and H. J. Choi, Colloids Surfaces A Physicochem. Eng. Asp. 535, 16 (2017).

[11] B. Guo, K. Yu, H. Li, H. Song, Y. Zhang, X. Lei, H. Fu, Y. Tan, and Z. Zhu, ACS Appl. Mater. Interfaces 8, 5517 (2016).

[12] P. Liu, M. Yang, S. Zhou, Y. Huang, and Y. Zhu, Electrochim. Acta 294, 383 (2019).

[13] C. C. Li, Q. H. Li, L. B. Chen, and T. H. Wang, ACS Appl. Mater. Interfaces 4, 1233 (2012).

[14] J. W. Yoon, Y. J. Hong, Y. C. Kang, and J. H. Lee, RSC Adv. 4, 16067 (2014).

[15] Z. Yang, Z. Li, Y. Yang, and Z. J. Xu, ACS Appl. Mater. Interfaces 6, 21911 (2014).

[16] Z. Yang, Z. Li, Y. Yang, and Z. J. Xu, ACS Appl. Mater. Interfaces 6, 21911 (2014).

[17] K. Karmakar, D. Maity, D. Pal, K. Mandal, and G. G. Khan, ACS Appl. Nano Mater. 3, 1223 (2020).

[18] P. Liu, Y. Zhang, J. Yan, Y. Huang, L. Xia, and Z. Guang, Chem. Eng. J. 368, 285 (2019).

[19] A. Farajpour, M. H. Ghayesh, and H. Farokhi, Int. J. Eng. Sci. 133, 231 (2018).

[20] V. B. Barbeta, R. F. Jardim, P. K. Kiyohara, F. B. Effenberger, and L. M. Rossi, J. Appl. Phys. 107, 73913 (2010).

[21] H. L. Andersen, M. Saura-Múzquiz, C. Granados-Miralles, E. Canévet, N. Lock, and M. Christensen, Nanoscale 10, 14902 (2018).

[22] R. Rakshit, M. Mandal, M. Pal, and K. Mandal, Appl. Phys. Lett. 104, 2 (2014).

[23] S. Talukdar, D. Mandal, and K. Mandal, Chem. Phys. Lett. 672, (2017).

[24] Q. A. Pankhurst, J. Connolly, J. S. K, and J. Dobson, J. Phys. D. Appl. Phys. 36, R167 (2003).

[25] X. Zhou, Z. Jia, A. Feng, S. Qu, X. Wang, X. Liu, B. Wang, and G. Wu, J. Colloid Interface Sci. 575, 130 (2020).

[26] W. L. Song, L. Z. Fan, Z. L. Hou, K. L. Zhang, Y. Ma, and M. S. Cao, J. Mater. Chem. C 5, 2432 (2017).

[27] J. Liu, W. You, J. Yu, X. Liu, X. Zhang, J. Guo, and R. Che, ACS Appl. Nano Mater. 2, 910 (2019).

[28] C. Dey, K. Baishya, A. Ghosh, M. M. Goswami, A. Ghosh, and K. Mandal, J. Magn. Magn. Mater. 427, 168 (2017).

[29] D. Maity, K. Karmakar, and K. Mandal, J. Alloys Compd. 791, 739 (2019).

[30] Y. Yang, M. Li, Y. Wu, B. Zong, and J. Ding, RSC Adv. 6, 25444 (2016).

[31] J. Liu and D. Xue, Adv. Mater. 20, 2622 (2008).

[32] M. Alam, K. Mandal, and G. G. Khan, J. Alloys Compd. 822, 153540 (2020).

[33] S. F. Soares, T. Fernandes, A. L. Daniel-da-Silva, and T. Trindade, Proc. R. Soc. A Math. Phys. Eng. Sci. 475, 20180677 (2019).

[34] W. Ruan, C. Mu, B. Wang, A. Nie, C. Zhang, X. Du, J. Xiang, F. Wen, and Z. Liu, Nanotechnology 29, 405703 (2018).

[35] P. Chen, B. Cui, X. Cui, W. Zhao, Y. Bu, and Y. Wang, J. Alloys Compd. 699, 526 (2017).

[36] Y. Li, N. Li, W. Pan, Z. Yu, L. Yang, and B. Tang, ACS Appl. Mater. Interfaces 9, 2123 (2017).

[37] M. Han, X. Yin, L. Kong, M. Li, W. Duan, L. Zhang, and L. Cheng, J. Mater. Chem. A 2, 16403 (2014).

[38] R. Panigrahi and S. K. Srivastava, Sci. Rep. 5, 7638 (2015).

[39] M. Mandal Goswami, Sci. Rep. 6, 35721 (2016).

[40] W. Hou, T. B. Toh, L. N. Abdullah, T. W. Z. Yvonne, K. J. Lee, I. Guenther, and E. K. H. Chow, Nanomedicine Nanotechnology, Biol. Med. 13, 783 (2017).

[41] S. Sutradhar, S. Saha, and S. Javed, ACS Appl. Mater. Interfaces 11, 23701 (2019).

[42] D. Sarkar, M. Mandal, and K. Mandal, J. Appl. Phys. 112, 64318 (2012).

[43] R. Valenzuela, Phys. Res. Int. 2012, (2012).

[44] Y. Ding, Q. Liao, S. Liu, H. Guo, Y. Sun, G. Zhang, and Y. Zhang, Sci. Rep. 6, 32381 (2016).

[45] X. Qiu, L. Wang, H. Zhu, Y. Guan, and Q. Zhang, Nanoscale 9, 7408 (2017).

[46] F. Qin and C. Brosseau, J. Appl. Phys. 111, (2012).

[47] K. E. Sickafus, J. M. Wills, and N. W. Grimes, J. Am. Ceram. Soc. 82, 3279 (1999).

[48] Z. Szotek, W. M. Temmerman, D. Ködderitzsch, A. Svane, L. Petit, and H. Winter, Phys. Rev. B 74, 174431 (2006).

[49] S. Chakraverty, S. Mitra, K. Mandal, P. M. G. Nambissan, and S. Chattopadhyay, Phys. Rev. B - Condens. Matter Mater. Phys. 71, 1 (2005).

[50] J. Liu, Y. Bin, and M. Matsuo, J. Phys. Chem. C 116, 134 (2012).

[51] K. Vamvakidis, M. Katsikini, D. Sakellari, E. C. Paloura, O. Kalogirou, and C. Dendrinou-Samara, Dalt. Trans. 43, 12754 (2014).

[52] W. Wu, Q. He, and C. Jiang, Nanoscale Res. Lett. 3, 397 (2008).

[53] A. López-Ortega, M. Estrader, G. Salazar-Alvarez, A. G. Roca, and J. Nogués, Phys. Rep. 553, 1 (2015).

[54] A. Giri, N. Goswami, M. Pal, M. T. Zar Myint, S. Al-Harthi, A. Singha, B. Ghosh, J. Dutta, and S. K. Pal, J. Mater. Chem. C 1, 1885 (2013).

[55] A. H. Morrish, *The Physical Principles of Magnetism* (2001).

[56] S. Gangopadhyay, G. C. Hadjipanayis, B. Dale, C. M. Sorensen, K. J. Klabunde, V. Papaefthymiou, and A. Kostikas, Phys. Rev. B 45, 9778 (1992).

[57] D. Sarkar, M. Mandal, R. Das, and K. Mandal, in *IEEE Trans. Magn.* (2011), pp. 3163–3166.

[58] R. Skomski, *Simple Models of Magnetism* (2010).

[59] R. Day, M. Fuller, and V. A. Schmidt, Phys. Earth Planet. Inter. 13, 260 (1977).

[60] C. Kittel, Wiley Sons, New York, NY (2004).

[61] H. Zhang, D. Zeng, and Z. Liu, J. Magn. Magn. Mater. 322, 2375 (2010).

[62] E. du Trémolet de Lacheisserie, D. Gignoux, and M. Schlenker, *Magnetism: Fundamentals, Materials and Applications* (2002).

[63] G. Xiong, Z. Mai, M. Xu, S. Cui, Y. Ni, Z. Zhao, X. Wang, and L. Lu, Chem. Mater. 13, 1943 (2001).

[64] L. Patron, G. Marinescu, and I. Mindru, in *Dekker Encycl. Nanosci. Nanotechnology, Second Ed. - Six Vol. Set (Print Version)* (CRC Press, 2008), pp. 1968–1984.

[65] J. B. Weaver and E. Kuehlert, Med. Phys. 39, 2765 (2012).

[66] E. M. Markink, 99 (2012).

[67] M. Lakshmanan, Philos. Trans. R. Soc. A Math. Phys. Eng. Sci. 369, 1280 (2011).

[68] B. K. Das and P. Chaudhari, J. Mater. Sci. 13, 84 (1978).

[69] R. Dorey, in *Ceram. Thick Film. MEMS Microdevices* (Elsevier, 2012), pp. 85–112.

[70] K. Morikawa, Y. Kazoe, K. Mawatari, T. Tsukahara, and T. Kitamori, MicroTAS 2012 1 (2012).

[71] A. K. Jonscher, J. Phys. D. Appl. Phys. 32, R57 (1999).

[72] K. Vasundhara, S. N. Achary, S. K. Deshpande, P. D. Babu, S. S. Meena, and A. K. Tyagi, J. Appl. Phys. 113, 194101 (2013).

[73] R. Tang, C. Jiang, W. Qian, J. Jian, X. Zhang, H. Wang, and H. Yang, Sci. Rep. 5, 1 (2015).

[74] C. G. Koops, Phys. Rev. 83, 121 (1951).

[75] I. W. McAllister, IEEE Trans. Electr. Insul. 26, 498 (1991).

[76] N. Ponpandian, P. Balaya, and A. Narayanasamy, J. Phys. Condens. Matter 14, 3221 (2002).

[77] P. Liu, Y. Huang, J. Yan, Y. Yang, and Y. Zhao, ACS Appl. Mater. Interfaces 8, 5536 (2016).

[78] V. Shukla, Nanoscale Adv. 1, 1640 (2019).

[79] M. Green and X. Chen, J. Mater. 5, 503 (2019).

[80] M. Pardavi-horvath, J. Magn. Magn. Mater. 216, 171 (2000).

[81] L. Yan, J. Wang, X. Han, Y. Ren, Q. Liu, and F. Li, Nanotechnology 21, 95708 (2010).

[82] X. G. Liu, D. Y. Geng, H. Meng, P. J. Shang, and Z. D. Zhang, Appl. Phys. Lett. 92, 173117 (2008).

[83] X. Bai, Y. Zhai, and Y. Zhang, J. Phys. Chem. C 115, 11673 (2011).

[84] J. Liu, R. Che, H. Chen, F. Zhang, F. Xia, Q. Wu, and M. Wang, Small 8, 1214 (2012).

[85] H.-I. Hsiang, W.-S. Chen, Y.-L. Chang, F.-C. Hsu, and F.-S. Yen, Am. J. Mater. Sci. 1, 40 (2011).

[86] J. Baker-Jarvis, M. D. Janezic, J. H. Grosvenor, and R. G. Geyer, *NIST Technical Note 1355-R*

(1993).

[87] J. Z. He, X. X. Wang, Y. L. Zhang, and M. S. Cao, J. Mater. Chem. C 4, 7130 (2016).

[88] D. M. Pozar, *Microwave Engineering, 4th Edition* (2012).

[89] R. E. Collin, *Foundations for Microwave Engineering* (2010).

[90] D. J. Griffiths, *Introduction to Electrodynamics* (2017).

[91] A. N. Vicente, G. M. I. Dip, and C. Junqueira, in *SBMO/IEEE MTT-S Int. Microw. Optoelectron. Conf. Proc.* (2011), pp. 738–742.

[92] P. G. Bartley and S. B. Begley, in *2010 IEEE Int. Instrum. Meas. Technol. Conf. I2MTC 2010 - Proc.* (2010), pp. 54–57.

[93] T. Wang, R. Han, G. Tan, J. Wei, L. Qiao, and F. Li, J. Appl. Phys. 112, (2012).

[94] L. Deng, L. Ding, K. Zhou, S. Huang, Z. Hu, and B. Yang, J. Magn. Magn. Mater. 323, 1895 (2011).

[95] Y. Feng, C. Tang, and T. Qiu, Mater. Sci. Eng. B Solid-State Mater. Adv. Technol. 178, 1005 (2013).

[96] P. Azizi, S. M. Masoudpanah, and S. Alamolhoda, J. Alloys Compd. 739, 211 (2018).

[97] Y. Wang, D. Chen, X. Yin, P. Xu, F. Wu, and M. He, ACS Appl. Mater. Interfaces 7, 26226 (2015).

[98] X. Liu, H. Guo, Q. Xie, Q. Luo, L.-S. Wang, and D.-L. Peng, J. Alloys Compd. 649, 537 (2015).

[99] Z. Chu, H. Cheng, W. Xie, and L. Sun, Ceram. Int. 38, 4867 (2012).

[100] T. Zou, H. Li, N. Zhao, and C. Shi, J. Alloys Compd. 496, (2010).

[101] L. S. Fu, J. T. Jiang, C. Y. Xu, and L. Zhen, CrystEngComm 14, 6827 (2012).

[102] X. Li, B. Zhang, C. Ju, X. Han, Y. Du, and P. Xu, J. Phys. Chem. C 115, 12350 (2011).

[103] J. R. Liu, M. Itoh, M. Terada, T. Horikawa, and K. I. MacHida, Appl. Phys. Lett. 91, (2007).

[104] C. Feng, X. Liu, Y. Sun, C. Jin, and Y. Lv, RSC Adv. 4, 22710 (2014).

[105] X. Liu, Y. Chen, X. Cui, M. Zeng, R. Yu, and G. S. Wang, J. Mater. Chem. A 3, 12197 (2015).

[106] H. Lv, H. Zhang, G. Ji, and Z. J. Xu, ACS Appl. Mater. Interfaces 8, 6529 (2016).

[107] L. Wang, Y. Huang, C. Li, J. Chen, and X. Sun, Compos. Sci. Technol. 108, 1 (2015).

[108] X. Sun, J. He, G. Li, J. Tang, T. Wang, Y. Guo, and H. Xue, J. Mater. Chem. C 1, 765 (2013).

[109] M. Zong, Y. Huang, H. Wu, Y. Zhao, Q. Wang, and X. Sun, Mater. Lett. 114, 52 (2014).

Chapter 2 | Experimental Details

The current chapter briefly describes different techniques to synthesize bulk and nanostructure (such as nanoparticles, nano hollow spheres) of transition metal based ferrites. Various characterization techniques to investigate their structural, magnetic, electric and microwave properties are also discussed here.

2.1 Preamble

In this chapter, we will describe an overview about different experimental techniques such as wet-chemical, co-precipitation, solvothermal procedures which are used to synthesize bulk, different nanostructures and even AOT modified NPs of ferrites. Moreover, the following characterization techniques which are employed in this thesis work are also briefly demonstrated.

The structural phase and parameters of the samples are studied by powder X-ray diffraction (XRD) pattern using Rikagu MiniFlex II diffractometer and PANalytical X'Pert PRO equipped with Cu Kα radiation at the scanning rate of 1° per minute in the 2θ range of 20°–80°. A FEI QUANTA FEG 250 field-emission scanning electron microscope (FESEM) (0.2–30 kV) and a FEG high-resolution transmission electron microscope (HRTEM) (80–200 kV) are used to study the size and morphology of nanostructures. The Energy-dispersive X-ray (EDX) spectrum is recorded for elemental analysis of the samples. Spectroscopic analyses are carried out using a Fourier Transformed Infrared Spectrometer (JASCO FTIR-6300) in the range of 400–4000 cm^{-1}. Differential Scanning Calorimetry (DSC) and thermal gravimetric analysis (TGA) measurements are performed using Q-2000 unit in the temperature range 300–500 K. All the relevant magnetic measurements are carried out using a Vibrating Sample Magnetometer (VSM) (Lakeshore Cryotronics-7407). AC dielectric properties of NHSs are investigated using NF ZM2376 LCR meter (upto 5.5 MHz) and Agilent 4294A Impedance Analyzer (upto 110 MHz). A pressure ~25 MPa is applied to pelletize the powder sample for dielectric measurement using a Riken Pressure Gauge. Microwave properties of the samples for the frequency range 1–20 GHz are measured using Anritsu MS46122B Vector Network Analyzer (VNA). Each composite sample is properly inserted in port-1 end of a coaxial airline (Maury Microwaves−8043S6) and set-up calibration is performed using TOSLKF50A-20 kit for the measurements. Further analysis from measured 2-port scattering (S)-parameters is executed with polynomial fit model of Nicholson-Ross-Weir (NRW) algorithm based on transmission line technique [1].

2.2 Synthesis Techniques

There are varieties of techniques that are devised to create nanomaterials with specific structures and thus unique properties. These methods can be summarized as top-down (i.e. bulk to nanoparticle) and bottom-up (i.e. atom to nanoparticle) approaches [2]. The biggest drawback of the top-down process is the imperfection in surface structures of NSs that can have significant effect on their physical properties and surface chemistry. On the other hand, bottom-up approach ensures better chance to produce NSs with fewer defects, more homogeneity in chemical composition and more control in placement of individual atoms.

Nanostructures are formed usually via two steps, nucleation and growth (as illustrated in Fig. 2.1(a)) [3]. Homogeneous nucleation occurs when nuclei form uniformly whereas, heterogeneous nucleation forms at structural inhomogeneity. The parent phase condition for nucleation called supersaturation, can be achieved through rational control of reaction conditions such as solvent, capping agents, temperature etc. In a chemical reaction, study of overall free energy changes (ΔG) associated with the homogeneous nucleation process, corresponds to the minimum size of a stable particle [4]. For a spherical particle of radius r, the surface energy γ and the free energy of the bulk crystal ΔG_v, giving a total free energy ΔG, Eq. 2.1(a). The crystal free energy itself, ΔG_v is dependent upon the temperature (T), Boltzmann's constant (k_B), the supersaturation of the solution (S), and its molar volume (v), as defined in 2.1(b).

$$\Delta G = 4\pi r^2 \gamma + \frac{4}{3}\pi r^3 \Delta G_v \qquad 2.1(a)$$

$$\Delta G_v = -\frac{k_B T \ln(S)}{v} \qquad 2.1(b)$$

Due to the surface free energy always being positive and the crystal free energy negative (as shown in Fig. 2.1(b)), it is possible to find a maximum free energy which a nucleus will pass through to form a stable nucleus by differentiating ΔG with respect to r and setting it to zero, $d\Delta G / dr = 0$, which gives a critical free energy and also a critical radius. Therefore above some critical radius, the particles will form and grow, whereas below this radius, the particles will redissolve. The growth of NPs is dependent on

diffusion of small particles into the solution and surface of other particles. This growth mechanism of NPs is popularly known as Ostwald ripening that happens due to the change in solubility of NPs depending on their size [5]. Due to the high solubility and the surface energy of smaller particles within solution, they redissolve and in turn allow the larger particles to grow even more. For shape control, the widely acknowledged Gibbs–Curie–Wulff theorem suggests that the shape of a crystal is determined by the surface free energy of individual crystallographic faces and the final crystal shape is decided in a way such that the total free energy of the system is minimized [4].

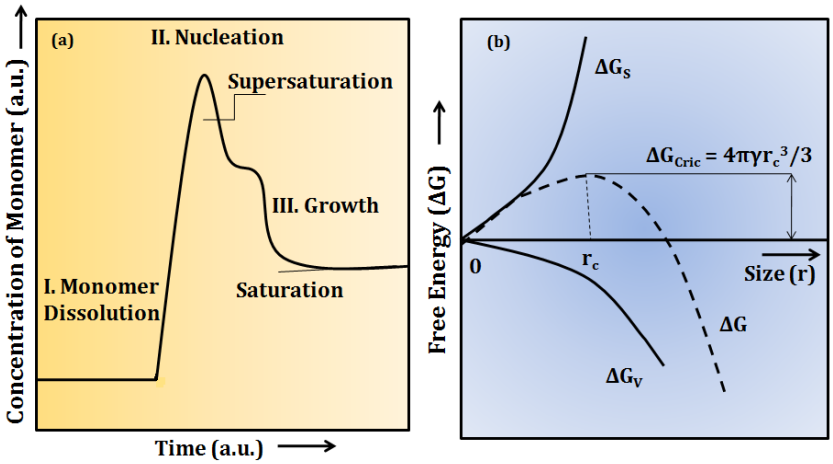

Figure 2.1. (a) Nucleation and growth step in a classical synthesis (b) Free-energy diagram for nucleation process

2.2.1 Wet Chemical Method

Wet chemical method is mainly a 'bottom-up' process to synthesize nanoparticles by chemical reduction of metal salts, electrochemical procedure or through controlled decomposition of different meta-stable organic and metallic compounds [3]. This method refers to an approach consisting of aqueous or non-aqueous solutions. This simple, inexpensive, modular and scalable process used to have better control over nanostructure and it can be used to produce even metal oxides in micrometer range. Here, in Chapter 3 and 4, bulk $NiFe_2O_4$ is synthesized using this procedure.

2.2.2 Chemical Co-precipitation Method

Co-precipitation is basically a modified version of wet chemical method with much precise control in size and distribution of nanoparticles. The co-precipitation setup used in our laboratory for fabrication of various oxide nanoparticles is shown in Fig. 2.2(a). This method is employed extensively in material science and industry to synthesize complex oxides with high crystallinity, compositional homogeneity and better stoichiometry [6]. In the co-precipitation technique, at first, precursor salts of the constituent materials are dissolved in aqueous medium and magnetically stirred to make it a completely homogeneous mixture. The solution temperature can be in the range between 0˚C to 80˚C depending on the materials dissolved in the solution. When the desired temperature of the primary solution is achieved, another solution of dissolved precipitating alkaline agent such as ammonium oxide (NH_4OH), potassium hydroxide (KOH) or sodium hydroxide (NaOH) is added into it. After completion of the reaction, the precipitation of the desired oxides is then filtrated and dried to make NPs powder of the product. Colloidal chemistry plays an important role to produce these powder oxides from the solution phase. After nucleation of the particles, they come close together due to their inter-particle interaction to form larger agglomerates and also to reduce their surface energy. During this time the agglomeration rate largely depends on the rate of collisions between nucleates due to Brownian motion, convection and also sheer forces caused by magnetic stirring. Net balance of these forces determines whether the freshly prepared nucleates adhere to form bigger size grains or not. Moreover, by controlling pH of the solution, surface charges can be made zero which stops the agglomeration and hence controls size of NPs. The mean size of the particles can also be controlled by adjusting the solution temperature and the rate of addition of precipitating agent in the precursor solution.

Micelle assisted co-precipitation is carried out by dissolving one or more salts containing the constituent elements with proper ratio in aqueous solvent in presence of suitable micelle in a burette, followed by its drop by drop addition into the aqueous solution of co-precipitating agent. A typical micelle in aqueous solution forms an aggregate with the hydrophilic ‘head’ regions in contact with surrounding solvent,

forcing the hydrophobic single tail regions in the micelle centre confining the NPs as shown in Figure 2.2(b). With the increase in surfactant concentration, micelles can be deformed and can change into different shapes, which make it possible to synthesize different shapes of NPs [7].

The micelle assisted wet chemical technique is utilized to synthesize the AOT functionalized $CoFe_2O_4$ NPs which is elaborately described in Chapter 8 of the thesis.

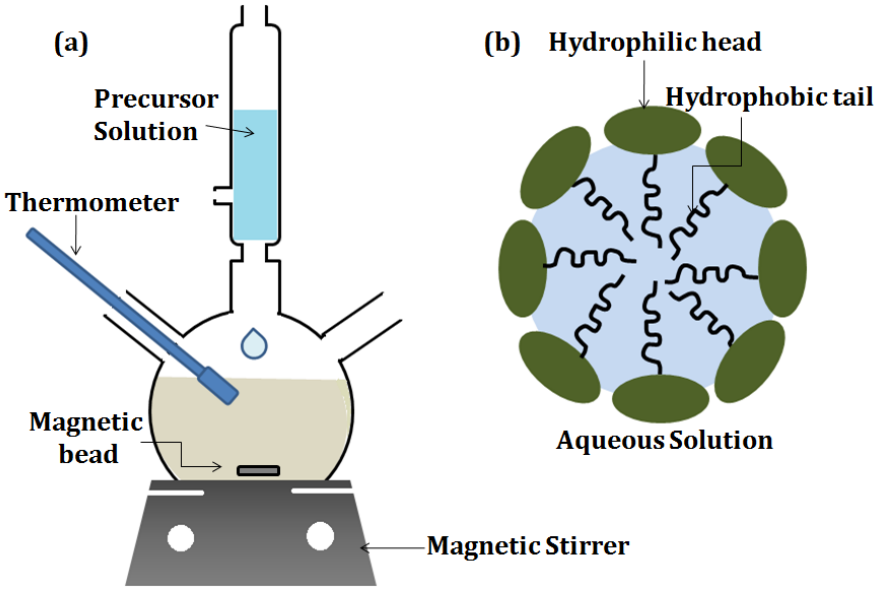

Figure 2.2. (a) Set-up for co-precipitation technique (b) Surfactant micelle dispersed in aqueous solution

2.2.3 Solvothermal Method

Solvothermal technique is an approach for fabrication of various nanostructures of metals, semiconductors, ceramics and polymers from aqueous or non-aqueous medium by controlling pressure, temperature, surfactant, chemical composition and duration of reaction [2,4]. This process involves different polar (such as water, ethanol etc.) or non-polar solvents (like benzene, ethylene glycol etc.) under high pressure and temperature (generally above the boiling point of solvent) to facilitate the interaction of different precursor molecules during the synthesis procedure. This method is much similar to hydrothermal route except here the precursor solution is usually non-aqueous.

In this procedure, a sealed reaction vessel is used and at temperature above the boiling point of the solvent, an autogeneous pressure (i.e. self-developing and not externally applied) is developed [2,6]. This pressure within the sealed container increases with temperature and also depends on other experimental factors, such as the percentage fill of the vessel, dissolved salts and amount of capping agents. Mobility of ions, viscosity of solvent, dielectric properties are greatly affected by pressure and temperature and this factor also changes the solubility and activity of the reactants. This technique starts with the dissolution of the precursors solutes in the solvent by magnetic stirring at room temperature. Then the homogeneous mixture is transferred into Teflon lined stainless steel autoclave chamber, as shown in Fig. 2.3. The precursor solution is poured to fill 70% volume of the chamber and the autoclave is then sealed and heated to a certain temperature in an oven. This method can be used to prepare various types of nanostructures such as cubes, hollow spheres, wires, rods, single crystals and many more. Not only that, the nanostructures formed in this procedure can be easily controlled by changing the solvent supersaturation, concentration and also through kinetic control. This technique can also be employed to prepare different thermodynamically stable or meta-stable states of novel materials that cannot be formed easily through other methods. Formation of NSs in solvothermal method is greatly influenced by different thermodynamic and crystallographic effects such as oriented attachment at phases, selective adsorption of ligand molecules, molecular template mechanism etc.

Here, from Chapter 3 to Chapter 7, the nano hollow spheres and NPs are synthesized by this particular method. The formation of hollow core is performed through one-pot soft-templating approach as it is faster, easier and cost-effective than hard-templating procedure [8]. A discussion of the synthesis and growth mechanism of $NiFe_2O_4$ NHSs is described in Chapter 3 of the thesis.

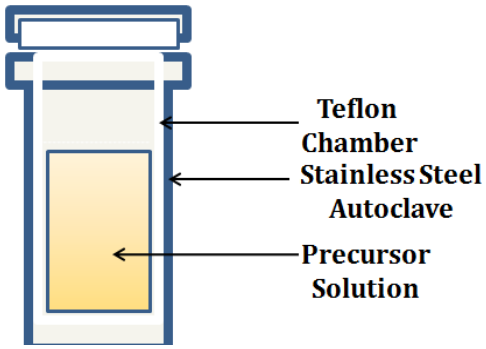

Figure 2.3. Schematic diagrams of an autoclave and a Teflon chamber used in solvothermal synthesis

2.3 Fabrication of Samples for Measurements

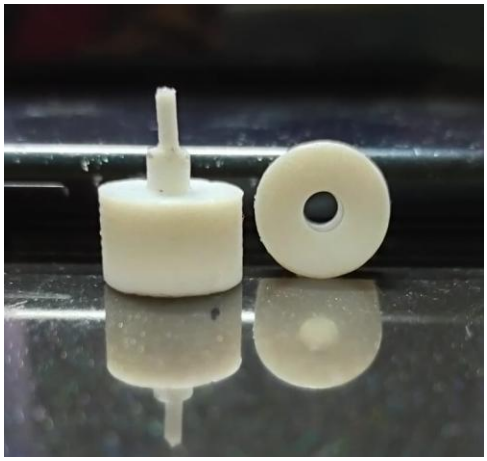

Figure 2.4. Teflon mould for sample preparation for study of Microwave properties

The as-synthesized powder ferrite samples should be given required shapes and forms for different measurements. For the dielectric measurements, the powder samples are pressed into a pellet and connected to wires with conductive silver paste. Powder samples are also needed to be pelletized for FTIR spectroscopy where potassium bromide (KBr, spectroscopic grade) is typically used as the window material. To pelletize the powder sample, pressure is applied around 25 MPa using a Riken Pressure Gauge. For microwave measurements using coaxial airline and VNA, the material should be of toroidal shape with outer diameter 3.5 mm and inner diameter 1.5 mm according

to the dimension of coaxial line. The composite samples for microwave measurements are prepared by loading powder samples in different wt% s in Epoxy Resin matrix and molding this mixture in a precisely fabricated self-made Teflon mould, as shown in Fig. 2.4.

2.4 Characterization Techniques

2.4.1 X-ray diffraction (XRD)

X-ray diffraction (XRD) is a well-known technique to investigate the crystal structures, phases, preferred crystal orientations, chemical compositions and other structural parameters such as average grain size, lattice strain and crystal defects of a material. A schematic representation of X-ray diffraction measurement is shown in Fig. 2.5. X-rays are produced by a cathode ray tube then, filtered to produce monochromatic radiation and subsequently, collimated to concentrate, and finally directed towards the sample. When, the monochromatic beam of X-rays (Cu-K_α, $\lambda \sim 1.54$ Å) falls on the crystalline sample, these X-rays are scattered elastically by the electrons within the crystal planes and form outgoing spherical waves. These scattered waves will interfere constructively in certain directions according to the Bragg's law [9],

$$2d \sin\theta = n\lambda \qquad 2.1$$

where, d, θ, n, λ stand for the inter-planer spacing in the crystal, the angle of diffraction, integer for order of diffraction and wavelength of the incident X-ray beam respectively. During measurement, the incident angle of X-ray beam with respect to the sample is varied for a small constant step in a wide range of angle and the diffracted beams of X-ray are recorded electronically using a detector. The presence of elements in the sample with their crystalline nature can be identified from the conversions of diffraction peaks to the d spacing. The peak positions provide the detail information about the crystal plane. The diffraction peaks can be identified from the Joint Committee on Powder Diffraction Standard (JCPDS) database. Moreover, by performing the Rietveld analysis

on the XRD data, the structure, lattice parameters, disorder, etc. of the material can be revealed.

We have used RIGAKU MiniFlex II (θ–2θ system) and PANalytical X'Pert Pro (θ–θ system) X-ray diffractometer using Cu-K_α radiation ($\lambda = 1.54$ Å) to characterize the samples for the present studies [10]. In θ–2θ system, X-ray source is fixed and the sample rotates at θ˚/min while the detector moves at 2θ˚/min whereas, in θ–θ system, the sample stage is fixed while X-ray source and the detector rotate simultaneously at an angular speed of θ˚/min.

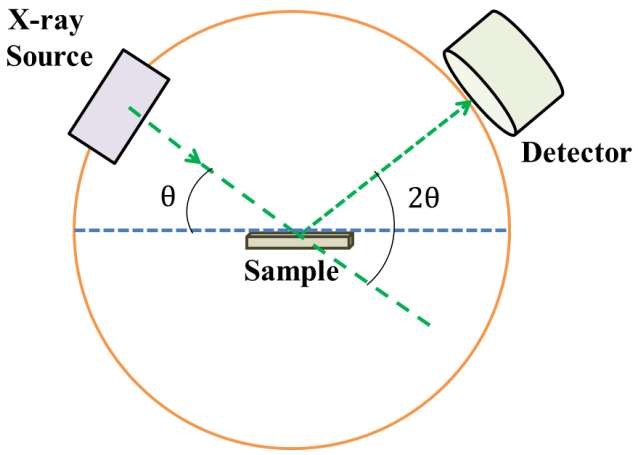

Figure 2.5. Schematic representation of X-ray diffraction measurement

2.4.2 Scanning electron microscope (SEM)

Scanning electron microscope (SEM) is a key technology for morphological characterization of a material. A schematic representation of a SEM is shown in Fig. 2.6. Here, thermionically or field emitted electron beam from the electron gun is confined and focused to irradiate the surface of the sample in vacuum. The beam of electrons passes through positively charged electrodes, condenser lenses, scan coils and objective lens. The objective lens is crucial for the final focusing of the beam to scan the sample's surface. These lenses are magnetic that deflect the electrons and focus them properly. The electron beam is now swept across the area over the sample with raster scanning. The highly energetic electrons interact with surface of the sample and the incident

electrons decelerate through the dissipation of their energy due to inelastic collision at the surface of the sample [11]. As a result, it produces a variety of signals. This signal contains low energy secondary electrons which are generated due to inelastic scattering of incident ones with the outer shell electrons of the atoms of the specimen. Those secondary electrons are attracted towards a positively biased detector and finally converted into a signal. Beside the secondary electrons, the SEM signal includes high energy backscattered electrons, diffracted backscattered electrons, characteristic X-rays produced by inelastic collisions of the incident electrons with the inner shell electrons of the sample atoms and visible light (cathode-luminescence). Comparing the mapped intensity produced by emitted secondary electrons during this process to the primary electron beam, a SEM micrograph of the sample surface is constructed.

We have used SEM with field emitted (FE) mode to characterize the investigated samples. In general, SEM works on a voltage range between 2 to 50 kV and its electron beam diameter varies between 5 nm to 2 μm.

2.4.2.1 Energy Dispersive X-ray Spectroscopy (EDX)

Energy dispersive analysis of X-ray (EDX) is a technique to analyze the elemental composition of a material. In this process, the sample is bombarded by high energy electrons and the bombarding electrons interact with the sample electrons. During this process, it can excite the electrons from inner shell of the atoms, to higher energy levels or, the electrons from the inner shell are ejected and hence, there is an electron deficiency in that inner shell (hole). Eventually, the hole is occupied by the electrons from the higher energy levels of the outer shell. As a result, the energy difference between these two energy levels is emitted in form of an X-ray from the material. In general, a Si (or Li) detector is used as an energy dispersive spectrometer to count the number of emitted X-rays. A schematic presentation of the fundamental process for both FESEM and EDX is shown in Fig. 2.6. However, the atom of each element releases the X-rays with unique amounts of energy. Hence, the elements present in the sample can be recognized by evaluating the amounts of energy present in the emitted X-rays from the sample. Usually, a characteristic EDX spectrum shows the peaks

corresponding to the energy levels for which the most X-rays are received. These peaks are distinctive to an atom and hence define a single element. From the relative intensities of these peaks, the atomic percentage of the elements in the sample can be measured.

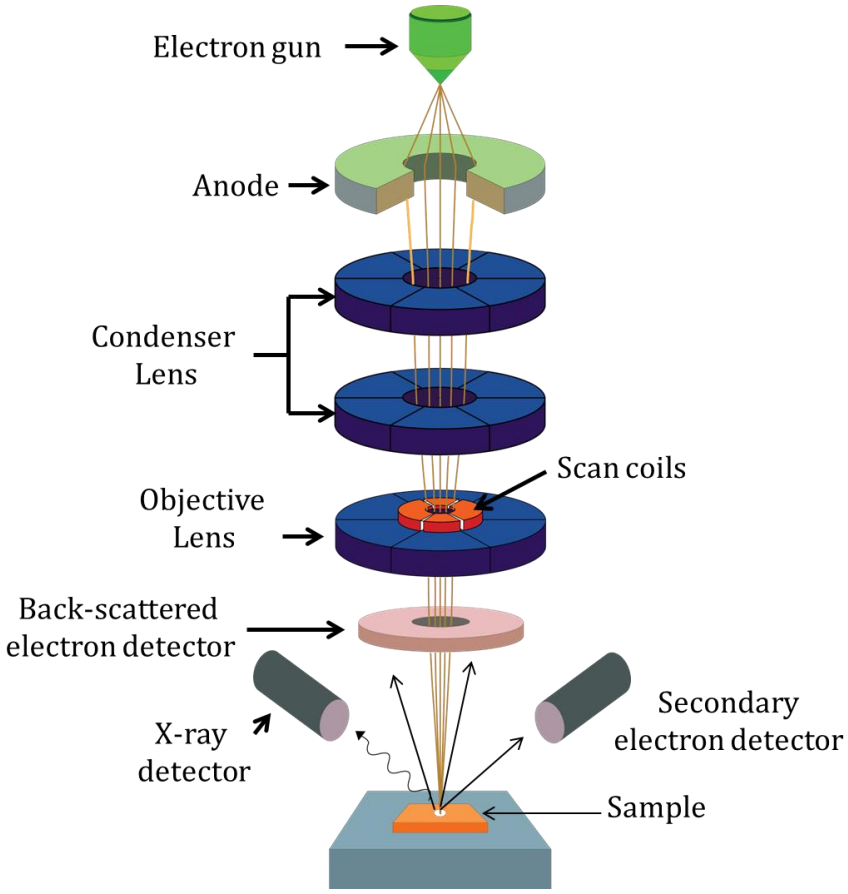

Figure 2.6. Schematic presentation of the fundamental process for both FESEM and EDX

2.4.3 Transmission Electron Microscope (TEM)

Transmission Electron Microscope (TEM) is a versatile instrument to characterize the internal structure of materials with a wide range of imaging. TEM was first developed in 1931. A schematic diagram of a TEM is shown in Fig. 2.7. In this electronic microscope, a beam of electrons originated from electron gun and having usual wavelength of less than 1 Å transmitted through a thin sample specimen without occurring any interaction inside it. During this process, a fraction of the beam electrons scattered by the electrons

of atoms in the specimen elastically (diffracted beams) and others are un-scattered electrons (transmitted beams). Thus, in case of crystalline samples, the electron beam undergoes diffraction according to Bragg's law when it is passed through the sample specimen. All the incident electrons have the same energy and they enter the sample normal to its surface. Here, all electrons that are scattered by the same atomic spacing will have same scattering angle. These scattered electrons are collated using magnetic lenses to form a pattern of spots and each spot corresponds to a specific atomic spacing or crystalline plane. Eventually, the pattern can yield information about the orientation, atomic arrangements and phases present in the area of the sample being investigated.

The transmitted beams produce a two-dimensional image of the sample. The transmission of these un-scattered electrons is inversely proportional to the thickness of the sample specimen. Moreover, if the area of the specimen becomes thicker, it will have fewer transmitted un-scattered electrons and as a result, the image will appear darker. Conversely the thinner areas will have more transmitted un-scattered electrons and thus, will appear lighter. This mode of operation to create contrast in image is known as bright field imaging mode.

In high resolution TEM (HRTEM) mode, one can achieve a resolution about 0.2 nm which is very efficient in observing the lattice fringes of the specimen. Energy filtered TEM (EFTEM) is a technique where electrons of particular energies are used to form an image or diffraction pattern. It gives information about the elemental composition of the investigated material. Further, another technique performed in TEM is electron energy loss spectroscopy (EELS) where a material is irradiated with the electron beam with a known narrow range of kinetic energy. These electrons undergo inelastic scattering while interacting with the atomic electrons in the specimen. Hence, the electron beam loses certain amount energy which is measured using an electron spectrometer. The energy distribution of all the inelastically scattered electrons yields the information about the local environment atomic electrons which is related to the physical and chemical properties of the sample specimen.

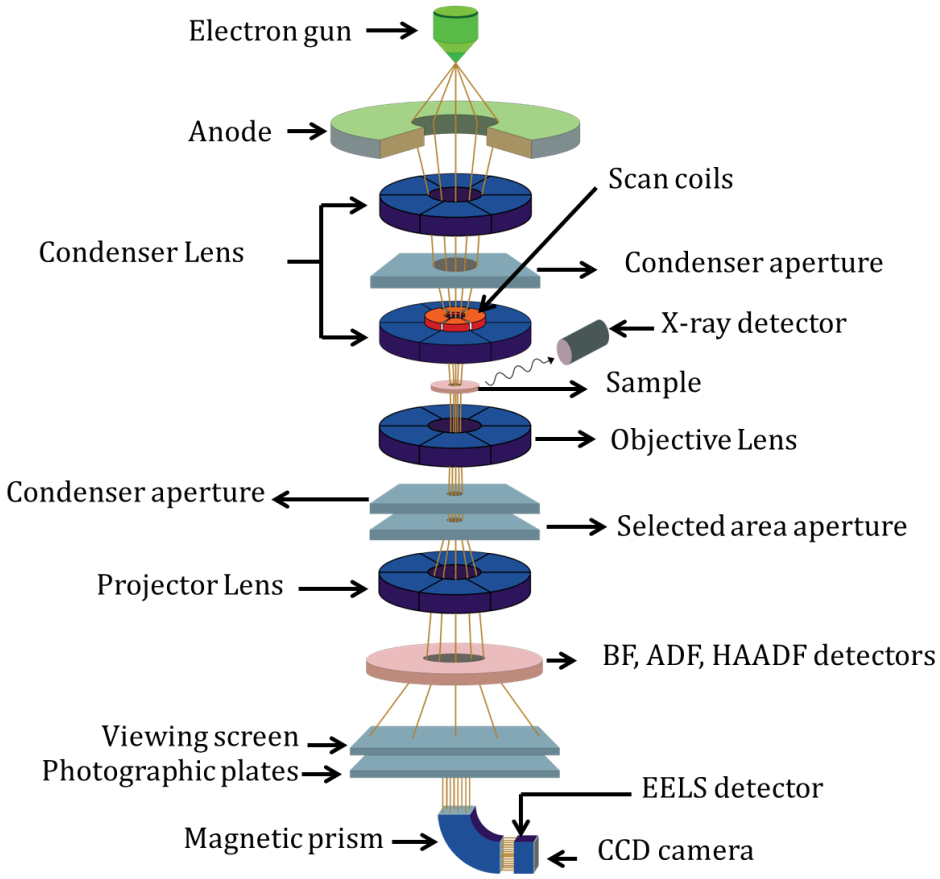

Figure 2.7. Operation of basic components in a TEM

2.4.4 Differential Scanning Calorimetry (DSC) and Thermo Gravimetric Analysis (TGA)

Differential Scanning Calorimetry (DSC) measures change is temperature and heat flow associated with transitions in materials as a function of time and temperature in a controlled atmosphere. These measurements provide quantitative and qualitative information about physical and chemical changes that involve endothermic (heat absorption), exothermic (heat evolution) processes or changes in heat capacity [12]. With linear heating, corresponding TGA measures the amount and the rate of weight change of a material with respect to temperature. Here, thermal analysis from DSC and TGA provides information about stability of the material over temperature, their chemical constituents, transitions and reaction kinetics. Figure 2.8 describes the

schematics for DSC and TGA respectively and a brief operation mechanism is depicted hereafter.

A functional DSC system has three major components: the instrument which contains the system electronics, the cell that monitors differential heat flow and temperature and a cooling accessory. In a typical DSC, the sample material is encapsulated in a conductive metal pan (such as Al, Pt etc.) and an empty reference pan also sits on a thermoelectric disk surrounded by a furnace. As the temperature of the furnace is varied (usually by heating at a linear rate), heat is transferred to the sample and reference through the thermoelectric disk. The differential heat flow (q) to the sample and reference is measured by area thermocouples, made up of alumel and chromel wires, using the thermal equivalent of Ohm's Law i.e. $q = \Delta T/R$, where R represents the thermal resistance of the disc and ΔT; the temperature difference proportional to the voltage difference (ΔV) between the thermocouple junctions. The required Refrigerated Cooling Systems (RCS) are used to perform DSC cooling experiments using liquid nitrogen.

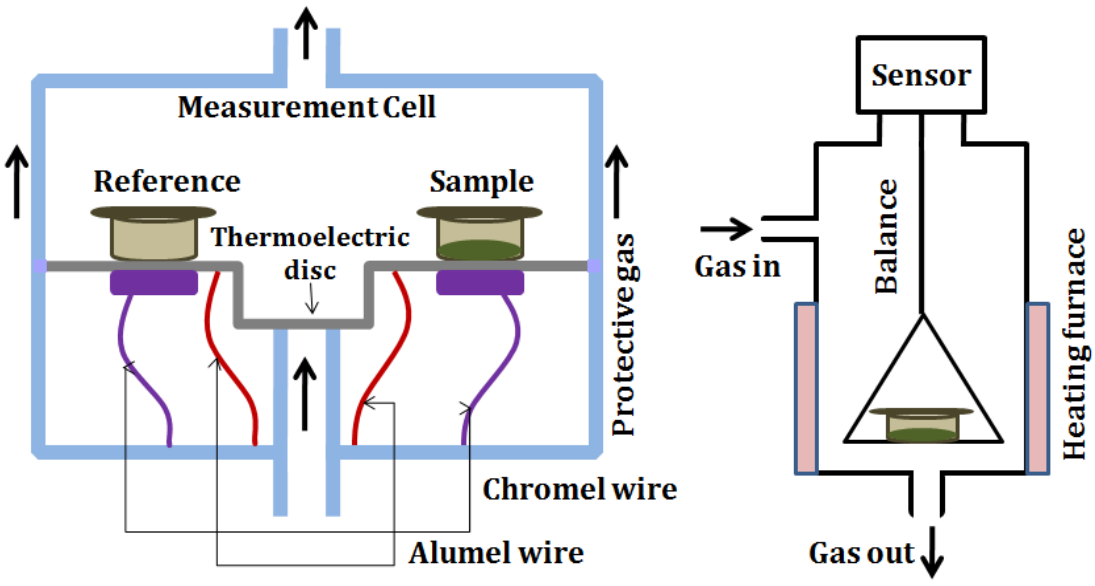

Figure 2.8. Schematic presentation of DSC and TGA

A TGA consists of a sample pan that is supported by a precision micro-balance. That pan resides in a furnace and is heated or cooled during the experiment. The mass of the sample is monitored during the whole experiment. A sample purge gas flows in the sample chamber and controls the sample environment.

2.4.5 Fourier Transformed Infrared Spectroscopy (FTIR)

FTIR is called molecular fingerprint as it is a powerful tool to identify the functional groups and chemical bonds within a molecule. The mid-infrared, approximately 4000−400 cm^{-1} (30–1.4 μm) is usually applied to study the fundamental rotational-vibrational structure of molecules. When an infra-red wave incident on a sample, absorption and transmission happens and this absorption energy at resonant frequency is composed of translational, vibrational, rotational and electric energies. These resonant frequencies are characteristic features of molecules and the intensity of absorption peaks is related to the change of dipole moment and the possibility of the transition of energy levels. Therefore, addition of surfactant, isotope effects or doping of cations can easily be detected from shifting or broadening of FTIR peaks [13].

A FTIR is typically based on the Michelson Interferometer Experimental Setup. The interferometer consists of a beam splitter, a fixed mirror and a moving mirror that translates back and forth very precisely. The most common source of IR spectrometer is Nernst glower which consists of a rod made up of the oxides of Zirconium, Ytterbium, and Erbium. The rod is electrically heated up to 1773 K to produce IR radiations. Potassium Bromide or other alkali metal halides are best window material as they are transparent in IR region. The interference caused by the beams from stationary and moving mirrors results in interferogram. This interferogram signal is digitized by FTIR spectrometer performing a Fourier Transform (FT) on the interferogram to obtain the spectrum. Therefore, X-axis of the signal transforms from optical path difference to wavenumber and the signal shifts to frequency domain. Thus, FTIR spectrometer is better and more accurate than dispersive spectrometers for higher signal to noise ratio and presence of wide range wavenumbers.

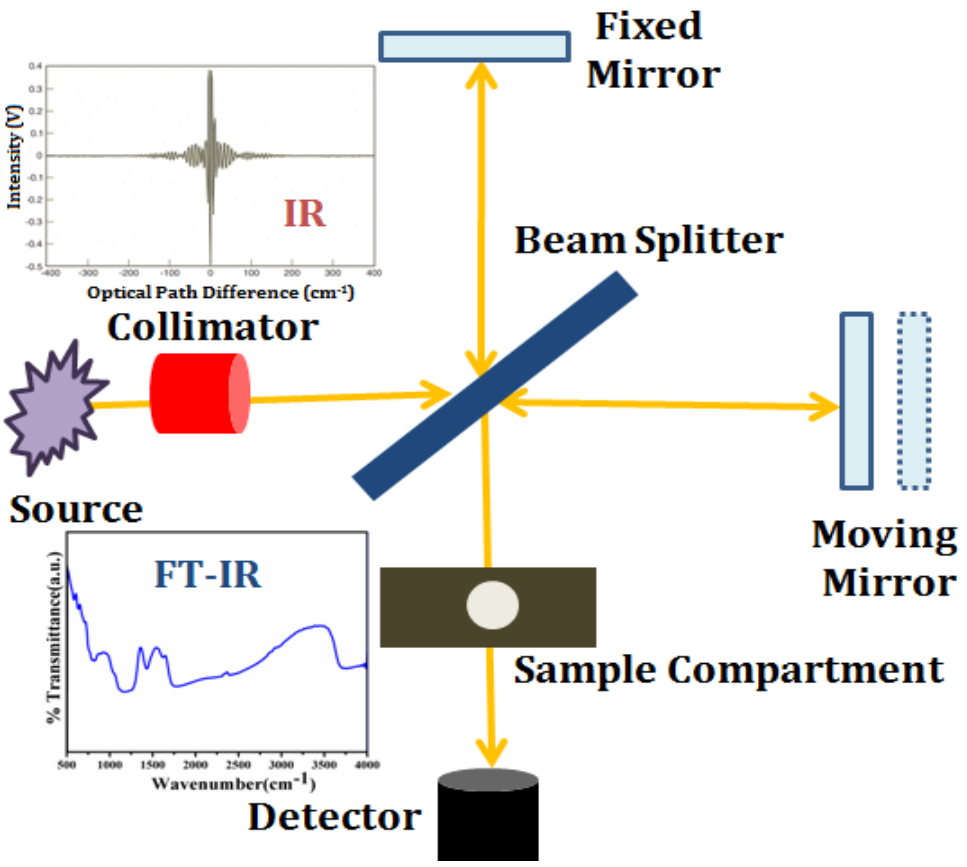

Figure 2.9. Schematic diagram of FTIR spectrometer

2.4.6 Vibrating Sample Magnetometer (VSM)

Vibrating Sample Magnetometer (VSM) measures magnetic behavior of a material. VSM is a sensitive magnetometer which can measure very low magnetic moment up to order of 10^{-5}-10^{-6} emu [14]. Working principle of VSM is based on Faraday's law of induction which states that, an electromotive force i.e. emf will be induced in a coil if there is a change in magnetic flux linking with the coil.

The schematic diagram of a VSM is shown in Fig. 2.10. Here, an electromagnet is used to apply a constant magnetic field to magnetize the sample. Two identical but oppositely wounds pick-up coils are mounted on two poles of electromagnet. The sample is mounted at the center region between the poles of the electromagnet. A thin vertical non-magnetic rod, usually made of plastic or quartz, connects the sample

holder to the transducer assembly which is placed above the magnet. The oscillator generates a sinusoidal signal that is converted by the transducer assembly into a vertical vibration of the sample. A constant external magnetic field from electromagnet magnetizes the sample. As the sample vibrates mechanically, according to Faraday's law of induction, the change in magnetic flux density that links with pick-up coils will produces an emf (V) as,

$$V = -d\Phi/dt \tag{2.2}$$

where, Φ is the magnetic flux. For the pick-up coils with cross-sectional area A and N number of turns,

$$V = -(\mathrm{NA})dB/dt \tag{2.3}$$

where, $B = \mu_0 H$, is the magnetic flux density, μ_0, permeability of free space and H, constant magnetic field.

Now, as the sample is placed between pick-up coils in a constant magnetic field, the sample will be magnetized and have a magnetization M. Therefore, the corresponding change in magnetic flux density (ΔB) is given by,

$$\Delta B = \mu_0 M \tag{2.4}$$

Then the induced emf in the pick-up coils can be expressed as,

$$V\mathrm{dt} = -\mu_0(\mathrm{NA})M \tag{2.5}$$

Thus the output signal is proportional to the magnetization of the sample but independent of the applied magnetic field in which the magnetization of the sample has to be determined. This signal goes through the lock-in amplifier as an input. The mechanical vibrator's frequency is set to the reference of the lock-in amplifier to eliminate the noise of the environment and to find the magnetic moment of the sample only. However, though the induced emf signal in the pick-up coils is proportional to the magnitude of the magnetic moment generated in the sample, it also depends on other factors such as frequency and amplitude of the vibration. In order to eliminate these issues, a vibrating capacitor is used to generate the reference signal which varies with

the vibrational frequency and amplitude following which, signal forms in the pick-up coils.

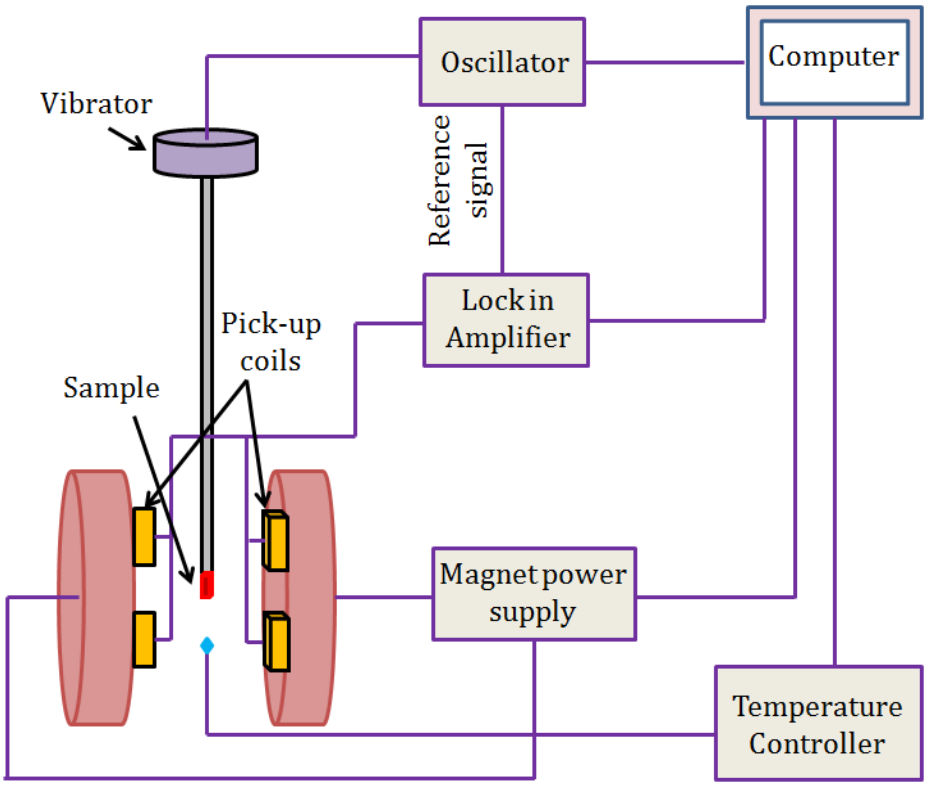

Figure 2.10. Working module of a VSM

2.4.7 LCR Meter and Impedance Analyzer

Dielectric properties of the pelletized samples are measured here using a LCR (Inductor-Capacitor-Resistor) meter within a frequency (*f*) range of 10 Hz – 5.5 MHz in Chapter 5, an Impedance Analyzer within a frequency (*f*) range of 40 Hz – 110 MHz in Chapter 3 and in Vector Network Analyzer beyond 1 GHz. Further, temperature modulation while investigating dielectric properties is performed through an oven. In general, for higher accuracy and simplicity in measurement, impedance analyzers are used in low frequency ranges and network analyzers in higher frequency ranges. Different electrical circuits that are applicable to these devices are Auto- Balancing Bridge, RF I-V and Network parameter analysis etc. These models are dependent mainly

on material impedance, connections, test frequency, required measurement parameters and accuracy etc.

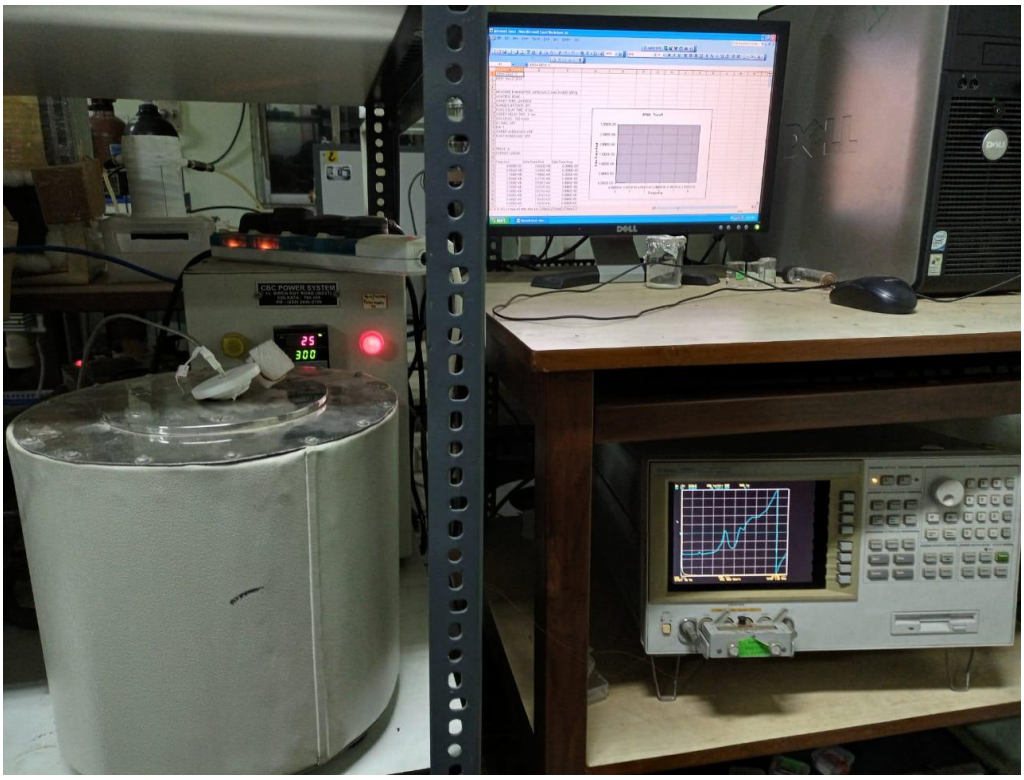

Figure 2.11. Dielectric properties measurement set-up in laboratory with impedance analyzer Agilent 4294A

Every circuit element components are sum of resistors, inductors and capacitors in series, parallel or combination connections. Impedance analyzer or an LCR meter (Inductance (L), Capacitance (C), and Resistance (R)) is very important equipment used to measure these parameters of a sample. Both in cases of LCR meter and Impedance analyzer basically auto-balancing bridge model works covering a wide impedance region and here the experimental sample is subjected to an AC voltage source [15]. The experimental setup in our laboratory is shown in Fig. 2.11 and a schematic diagram of LCR meter is illustrated in Fig. 2.12. The analyzer measures the voltage and current through the sample. From the ratio of these, the magnitude and

phase of the complex impedance are determined by the device. The impedance (Z) takes the form,

$$Z^* = R - jX = Z\angle\theta \qquad 2.6$$

A LCR meter can measure impedance at spot frequencies or in a wide range of frequencies and the capacitance, inductance and resistance parts can be deduced separately considering relation of series and parallel connections components to the net impedance. In the present instrumental setup, the LCR meter or impedance analyzer is interfaced with a computer and the data is collected as a function of frequency at different temperatures. From Z-θ plots, material properties such as permittivity (ε), loss-tangent, Q (quality)-factor can be easily calculated.

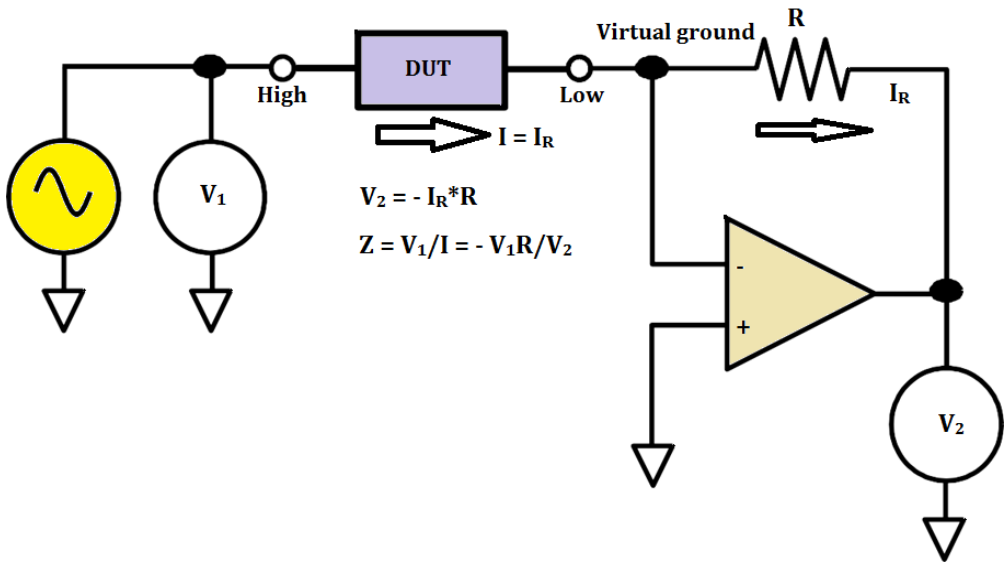

Figure 2.12. Schematic presentation of working principle of LCR meter and impedance analyzer

2.4.8 Vector Network Analyzer

A network analyzer is an instrument for measuring parameters of electrical networks and in this context, vector network analyzer (VNA) is very important as it measures both amplitude and phase properties. Now-a-days, network analyzers commonly measure S–parameters because reflection and transmission of electrical networks are

easy and accurate to measure at high frequencies. VNAs can be used on networks with an arbitrary number of ports but herein a 2-port network system will be discussed.

VNA which is an automatic network analyzer is widely used for radio frequency (RF) and microwave design applications and characterizations for both passive and active networks in terms of network scattering parameters i.e. S parameters [16].

A simplified block diagram of a vector network analyzer is shown in the accompanying figure, Fig. 2.13. This diagram depicts the essential parts of a typical 2-port VNA. The two ports of the device under test (DUT) are denoted as port 1 (P1) and port 2 (P2). The precision cables, PC1 and PC2 are attached to ports P1 and P2 from VNA respectively.

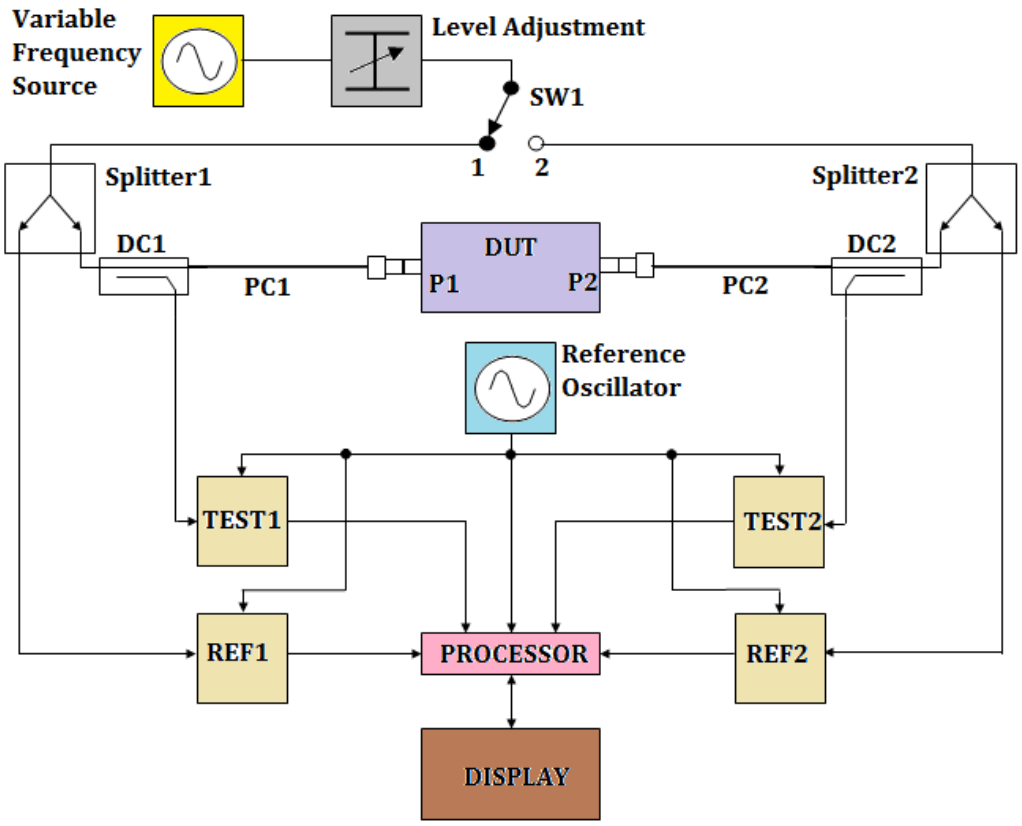

Figure 2.13. Simplified schematic presentation of a vector network analyzer

The RF test frequency is generated by a variable frequency source and its power level is set using a variable attenuator. The orientation of switch SW1 decides the direction at which the test signal passes through the DUT. Initially consider that SW1 is at position 1 so that the test signal is incident on the DUT at P1 which is appropriate for measuring S_{11} and S_{21}. The test signal is led to the common port of splitter 1, one part (the reference channel) feeding a reference receiver for P1 (REF1) and the other (the test channel) connecting to P1 via the directional coupler DC1 and cable PC1. The third port of DC1 couples off the power reflected from P1 via PC1, then, this moves to the test receiver 1 (TEST1). Similarly, signals leaving P2 pass via PC2 and DC2 goes to TEST2. REF1, TEST1, REF2 and TEST2 are known as coherent receivers as they share the same reference oscillator and they are capable of measuring the amplitude and phase of test signal at a certain frequency. All of the complex receiver output signals are fed to a processor which does the mathematical processing and displays the chosen parameters and format on the display. Though the instantaneous value of phase includes both the temporal and spatial parts, but the former is removed by virtue of using 2 test channels, one as a reference and the other for measurement. The quantities such as standing wave ratio (SWR), return loss, group delay, impedance etc. can be readily derived from this instrument and VNA also has the ability to determine the time-domain response of the network. Microwave properties measurement set-up in our laboratory with all necessary equipments is shown in Fig. 2.14.

Errors caused by directional coupler mismatch, imperfect directivity, loss in the cables, and variations in the frequency response of the analyzer system are rectified by a calibration procedure. The simplest one for this purpose is 'SOLT' i.e. 'Short', 'Open', 'Load' and 'Through'. Modern network analyzers have data stored about the devices in a suitable calibration kit.

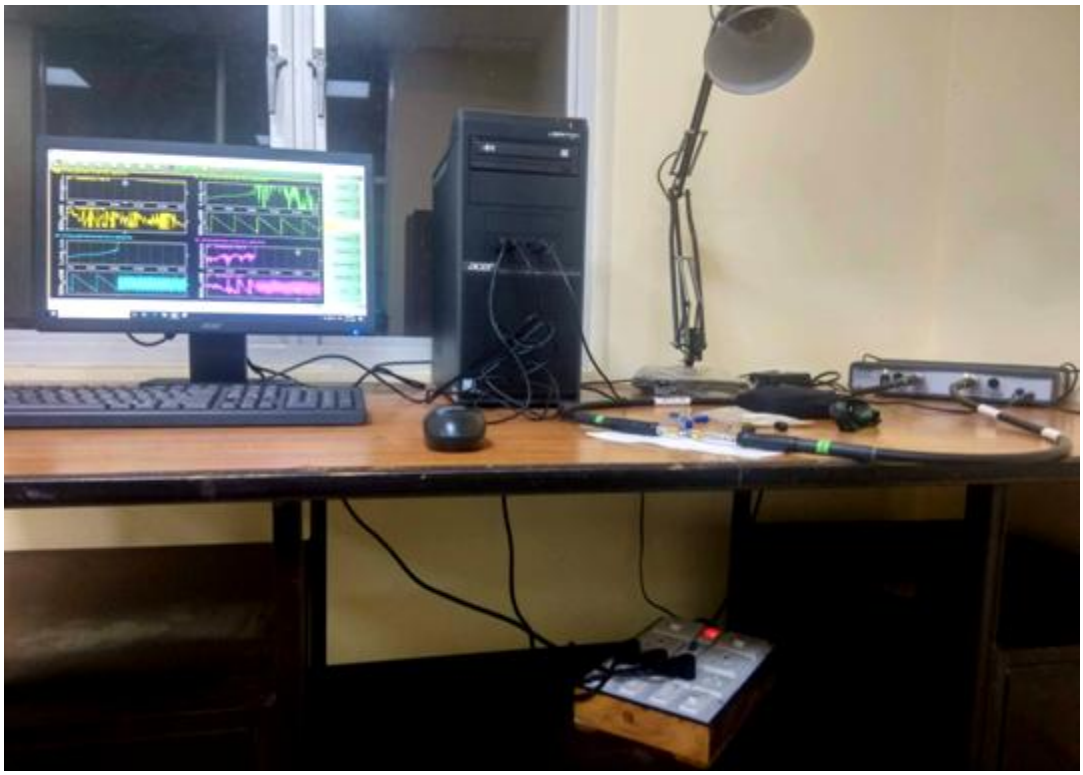

Figure 2.14. Microwave properties measurement set-up in our laboratory

References

[1] O. Luukkonen, S. I. Maslovski, and S. A. Tretyakov, IEEE Antennas Wirel. Propag. Lett. 10, 1295 (2011).

[2] N. T. K. Thanh, N. Maclean, and S. Mahiddine, Chem. Rev. 114, 7610 (2014).

[3] A. V. Nikam, B. L. V. Prasad, and A. A. Kulkarni, CrystEngComm 20, 5091 (2018).

[4] S. Kumar and T. Nann, Small 2, 316 (2006).

[5] C. Burda, X. Chen, R. Narayanan, and M. A. El-Sayed, *Chemistry and Properties of Nanocrystals of Different Shapes* (2005).

[6] D. Nunes, A. Pimentel, L. Santos, P. Barquinha, L. Pereira, E. Fortunato, and R. Martins, in *Met. Oxide Nanostructures* (2019), pp. 21–57.

[7] R. Rakshit, M. Mandal, M. Pal, and K. Mandal, Appl. Phys. Lett. 104, (2014).

[8] S. F. Soares, T. Fernandes, A. L. Daniel-da-Silva, and T. Trindade, Proc. R. Soc. A Math. Phys. Eng. Sci. 475, 20180677 (2019).

[9] C. Kittel, Wiley Sons, New York, NY (2004).

[10] N. W. Gregory, J. Am. Chem. Soc. 79, 1773 (1957).

[11] J. Goldstein, D. Newbury, D. Joy, C. Lyman, P. Echlin, E. Lifshin, L. Sawyer, and J. Michael, *Scanning Electron Microscopy Microanalysis and X-Ray Microanalysis* (2003).

[12] P. Gabbott, *Principles and Applications of Thermal Analysis* (2008).

[13] H. N. Hsieh, Public Domain 6 (2008).

[14] S. Foner, Rev. Sci. Instrum. 30, 548 (1959).

[15] X. M. Liu, H. Huang, and H. Xu, in *77th ARFTG Microw. Meas. Conf.* (IEEE, 2011), pp. 1–3.

[16] D. M. Pozar, *Microwave Engineering, 4th Edition* (2012).

Chapter 3

$NiFe_2O_4$ Nano-Hollow Spheres with Improved Magnetic and Dielectric Properties

In this chapter, three morphologies (bulk, nanoparticles and nano-hollow spheres) of Nickel ferrite are synthesized and their dc magnetic properties along with frequency (40 Hz – 110 MHz) and temperature (30˚C – 300˚C) dependent electric properties are studied in detail.

3.1 Preamble

Recently, research on transition metal oxide (TM) based magnetic nanomaterials are getting popular for their low cost, physical and chemical stability, unusual optical behavior, electronic and magnetic properties which differ significantly from their bulk counterpart [1,2]. $NiFe_2O_4$ (NFO) is one of the most significant spinel ferrites due to its specific qualities such as low coercivity (H_C), high saturation magnetization (M_S), Curie temperature (T_C) and electrical resistivity, low eddy current loss and remarkable thermal and chemical stability [3].

Among the various morphologies of magnetic nanomaterials, nano-hollow spheres (NHS) are found to be very promising because of their high M_S, large surface area and pore volume, low density, ability to withstand volume changes due to temperature and pressure which enable them to be used in wide varieties of applications in the fields of biomedical research [4], high frequency magnetic devices [5], energy storage [2], ferro-fluids [6], Hydrogen evolution reaction [7], super capacitors [8], Li ion battery [9] and chemical sensors [10]. The inner cavity and large surface area enhance their capability of capturing and delivering drugs and also repeated internal reflections increase their applicability as microwave absorbers [11]. Though by definition, the nanomaterials should have dimensions $\leq$100 nm, NHS, with size > 100 nm, also behave like nanomaterials because of their shell thickness less than 100 nm [12].

During the past decade, a number of efforts were made to increase the dielectric properties of ferrites with large magnetization to enhance their applicability in high frequency devices such as radars, isolators, circulators and so on [13,14]. For instance, Raghavender et al. analyzed those of Al substituted $CoFe_2O_4$ and got a maximum value of permittivity ~ 200 for 40% doping of Al [3]. Yadav et al. and Vasundhara et al. reported magnetic and dielectric studies on NFO nanoparticles (NPs) and $CoFe_2O_4$ NPs respectively prepared in gel combustion method and showed their changes with grain size [15,16]. Gul et al. used NFO/MWCNT nano-hybrid to achieve high value of dielectric constant of ~ 6.17×10^3 [17]. Grubbs et al. had tried to correlate the origin of magnetic

and dielectric properties for Fe- and Nb- doped $CaCu_3Ti_4O_{12}$ [18]. Moreover, Yang et al. [11] and Li et al. [19] had optimized the efficiencies of $ZnFe_2O_4$ NHS and $NiFe_2O_4$ NPs respectively as microwave absorbing and electromagnetic shielding materials. Further, a detail study towards magnetic/spintronic device applications of ferrites had been traced out by Hirohata et al. [20].

In this report, from the detail morphology dependent studies, NHS of $NiFe_2O_4$ are found to exhibit better magnetic and dielectric properties compared to their nanoparticles and bulk counterparts. Prepared by solvothermal method, these NHS with diameter of ~ 228 nm and much lower tap density of ~ 3.91 g/cc, show excellent magnetic properties with M_S and H_C, 63.5 emu/g and 122 Oe respectively. Variation of dielectric properties such as permittivity (ε), dielectric loss ($tan\delta$) and ac conductivity (σ_{ac}) of these NHS with frequency and temperature is explained on the basis of Maxwell-Wagner two layer model for space charge and hopping of charges from Fe^{3+} to Fe^{2+} as well as Ni^{2+} to Ni^{3+} ions at B (octahedral)-sites. The complex impedance spectroscopy study indicates the presence of grain and grain boundary effects in NHS and the conduction mechanism is explained by Jonscher's power law. A comparatively low value of the activation energy (E = 0.325 eV) is found for these NHS. Improved magnetic and dielectric properties of these light-weight NHS ensure their suitability for frequency dependent applications. Moreover, higher values of saturation magnetization and dielectric constant, observed in NFO NHS, give rise to high phase shift, which can be very effective in high-frequency devices and components such as circulators, antennas of smaller dimension [21].

3.2 Experimental

3.2.1 Synthesis Procedure

NFO NHS is synthesized by a template free solvothermal process using oleylamine as capping agent. Precursors, $NiCl_2$, $6H_2O$ (0.36 g) and $FeCl_3$, $6H_2O$ (0.819 g) are taken in 1:2 molar weight ratios with Urea (0.53 g) as reducing agent. Ethylene Glycol (20 ml)

and Ethyl Alcohol (10 ml) are taken in 2:1 ratios as solvents. Taking all the components in a 100 ml beaker, 1 ml oleylamine is added while stirring it. The clear homogeneous solution, after 30 min of stirring, is poured in a 50 ml Teflon lined stainless steel autoclave followed by continuous heating at 200°C for 24 h in an oven. Then the as-prepared NFO NHS is washed by ethanol and collected through magnetic separation and after that heating at 60°C for 30 min. During the reaction, urea helps to precipitate Ni^{2+} and Fe^{3+} ions of the precursor salts to their corresponding hydroxides and after the heat treatment, NFO phase is developed. The anticipated mechanism for the synthesis of NHS is Ostwald ripening [12,22] which involves a gradual re-crystallization of larger particles from the smaller ones to reduce their surface free energy. In addition, self-templating with the help of gas bubbles formed by urea, under the effect of oleylamine, ensures controlled formation of stable hollow spheres [5]. The schematic illustration of the formation mechanism of $NiFe_2O_4$ nano-hollow spheres is shown in Fig. 3.1 and the possible chemical reactions are as follows:

$$Ni(NH)_2 \rightarrow NH_3 + HCNO$$

$$NH_3 + H_2O \rightarrow NH_4^+ + OH^-$$

$$Ni^{+2} + 2OH^- \rightarrow Ni(OH)_2$$

$$Fe^{+3} + 3OH^- \leftrightarrow FeOOH + H_2O$$

$$Ni(OH)_2 + 2FeOOH \rightarrow NiFe_2O_4 + 2H_2O + H^+$$

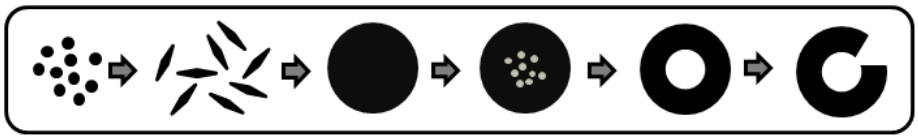

Figure 3.1. The schematic illustration of the formation mechanism of $CoFe_2O_4$ nano-hollow sphere

NFO NPs are prepared using the same method except the heating time of 15 h. Bulk NFO is synthesized in a wet-chemical combustion method. A 100 ml aqueous

solution of $NiCl_2$, $6H_2O$ and $FeCl_3$, $6H_2O$ taken in 1:2 molar weight ratios is continuously heated and stirred at 100°C for 1 h. Then the sample is annealed at 900°C for 4 h, crushed in mortar-pestle to a fine powder and collected.

Chemicals, having purity > 98%, were brought from Sigma-Aldrich and Loba Chemic for the above preparation.

3.2.2 Characterizations

The structural phase and crystallite size of as-prepared NFO NHS are studied by powder X-ray diffraction (XRD) using Rikagu MiniFlex II diffractometer equipped with Cu K_α radiation at the scanning rate of 1° per minute in the 2θ range of 20°–80°. A FEI QUANTA FEG 250 field-emission scanning electron microscope (FESEM) (0.2–30 kV) and a FEG high-resolution transmission electron microscope (HRTEM) (80–200 kV) are used to study the size, shape and morphology of NHS. The Energy-dispersive X-ray (EDX) spectrum is recorded for elemental analysis of the NFO NHS. All the relevant magnetic measurements are carried out using a vibrating sample magnetometer (VSM) (Lake Shore). AC dielectric properties of NHS are studied using Agilent 4294A Impedance Analyzer. To pelletize the powder samples, pressure is applied around 25 MPa using a Riken Pressure Gauge. The tap density (ρ) for bulk and NHS of NFO is calculated measuring the volume (V) and mass (m) of their respective pellets made from as-synthesized powder sample and using the equation $\rho = {}^{m}/_{V}$.

3.3 Results and Discussion

3.3.1 Crystallography and Morphology

Figure 3.2 shows the X-Ray Diffraction plots of NFO NHS and NFO Bulk indexing the crystal planes present. This graph confirms the single phase inverse spinel face centered cubic structure of NHS, as reported in the literature (JCPDS file no. 22–1086). Average crystallite size is calculated from the XRD peaks and found to be 23.6 nm for NHS and 42.5 nm for bulk using Scherrer formula, $D = \frac{k.\lambda}{\beta.\cos\theta}$, where D is the crystallite

size, k, the Scherrer constant (here ~ 0.94), λ, the working wave length, β, the FWHM of the selected peak in radians and θ, the XRD peak angle in degrees. Lattice constant is found to be 8.362 Å for NHS and 8.373 Å for Bulk as estimated from XRD using Bragg's law. The theoretical XRD density (ρ_t) for NFO NHS is calculated as 5.37 g/cc from the equation, $\rho_t = \frac{8M}{N_A V}$, where M is the molar mass of NFO, N_A is the Avogadro number, and V is the unit cell volume [3].

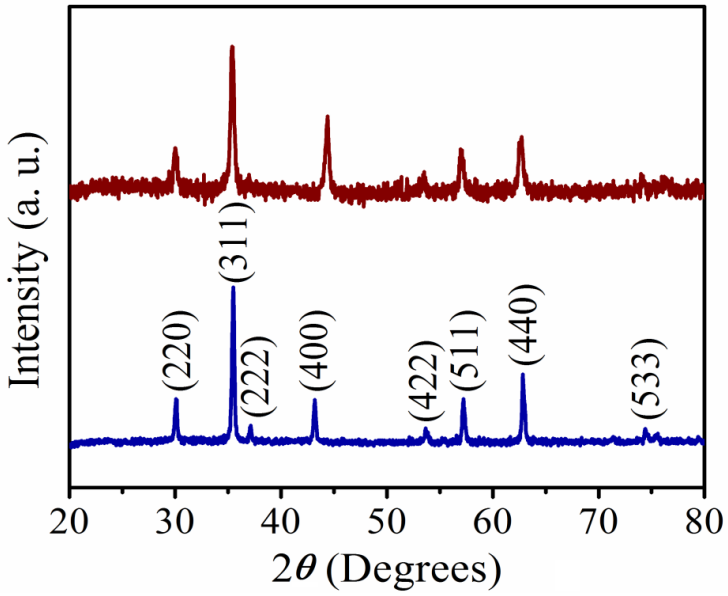

Figure 3.2. X-Ray Diffraction plots of NFO NHS and Bulk NFO

The morphologies of prepared NFO samples are shown in Fig. 3.3. The size and spherical shape of NFO NHS with a hollow center is clearly visible from the FESEM micrograph (Fig. 3.3(a)) having an average size of 228 nm with an outer shell width of ~ 55 nm. Bulk NFO is in μm size range and NFO NPs are of around 100 nm. The tap density of NHS and bulk NFO are found to be 3.91 g/cc and 4.78 g/cc respectively. Low density and light weight of NHS is obvious for it's scraped out hollow core which also make it more convenient for applications.

TEM image (Fig. 3.4(a)) also confirms hollow sphere nanostructures of the samples. Separation between the parallel diffraction planes (0.31 nm for (220), 0.25 nm for (311)) from HRTEM micrographs (Fig. 3.4(b)) matches well with the values

calculated from XRD data. The SAED pattern (Fig. 3.4(d)) shows the single crystal nature of NHS. EDX spectrum (Fig. 3.4(c)) is consistent with the composition (Ni, Fe and O) of the sample.

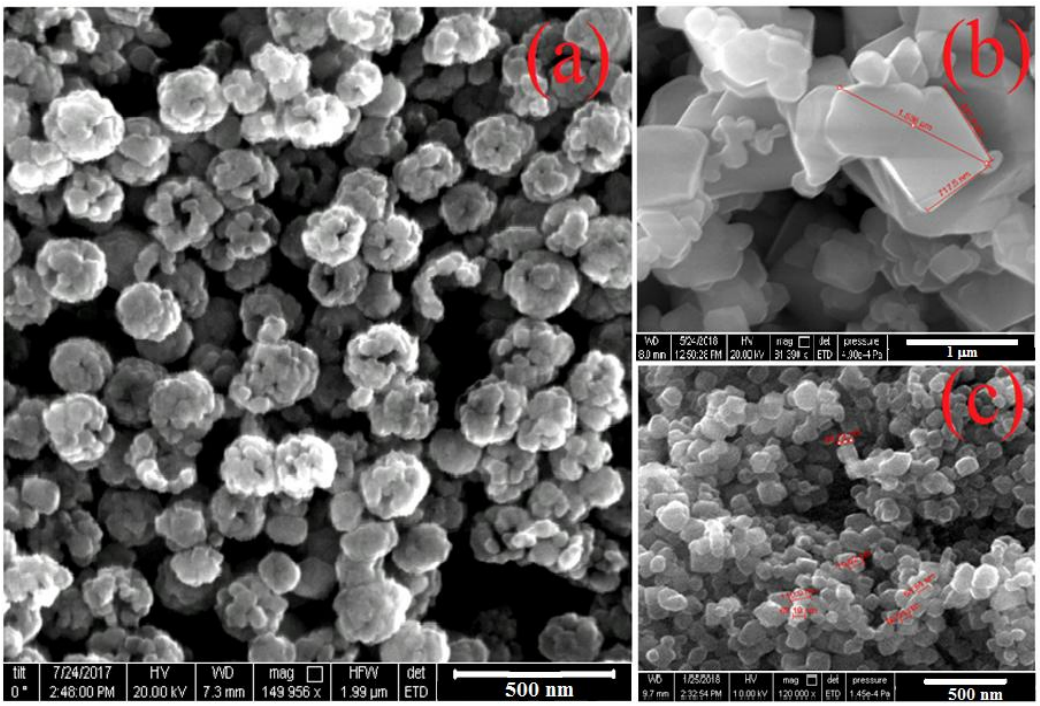

Figure 3.3. FESEM micrographs of the as-prepared (a) NFO NHS, (b) NFO Bulk and (c) NFO NPs

3.4 Magnetic Properties

Figure 3.5 describes *M-H* hysteresis loops of NFO NHS with maximum applied field of 2 kOe at temperature values 100K, 200K, 300K and 400K. At around room temperature (300K), H_C and M_R values of NHS are found to be 122 Oe and 10.5 emu/g that displaying the soft ferrimagnetic nature of NFO. Inset of Fig. 3.5 shows the decay of both H_C and M_R with increasing temperature. The increase in H_C and M_R on lowering the temperature are related with a growth of magnetic anisotropy preventing the alignment of the atomic magnetic moments in an applied field [23]. Further, a comparison between magnetic properties of NFO NHS, NPs and bulk at 300K are depicted in Fig. 3.6(a). H_C and M_S are found to increase from bulk (H_C= 78 Oe, M_S= 48.5 emu/g) to NPs (H_C= 93 Oe, M_S= 58.3 emu/g) to NHS (H_C= 122 Oe, M_S= 63.5 emu/g).

Temperature dependent magnetization curves of NFO samples are measured in presence of 100 Oe field at 10 K interval within the temperature region of 80 K - 400 K during both zero field cooled (ZFC) and field cooled (FC) modes, are shown in Fig. 3.6(b). The minimum separation between ZFC and FC curves of NHS confirms the highest magnetic anisotropy in them. From the morphology of NHS, as it is found as pile of single crystallites in a particular pattern, structural strain may be responsible for the high magnetic anisotropy in NHS.

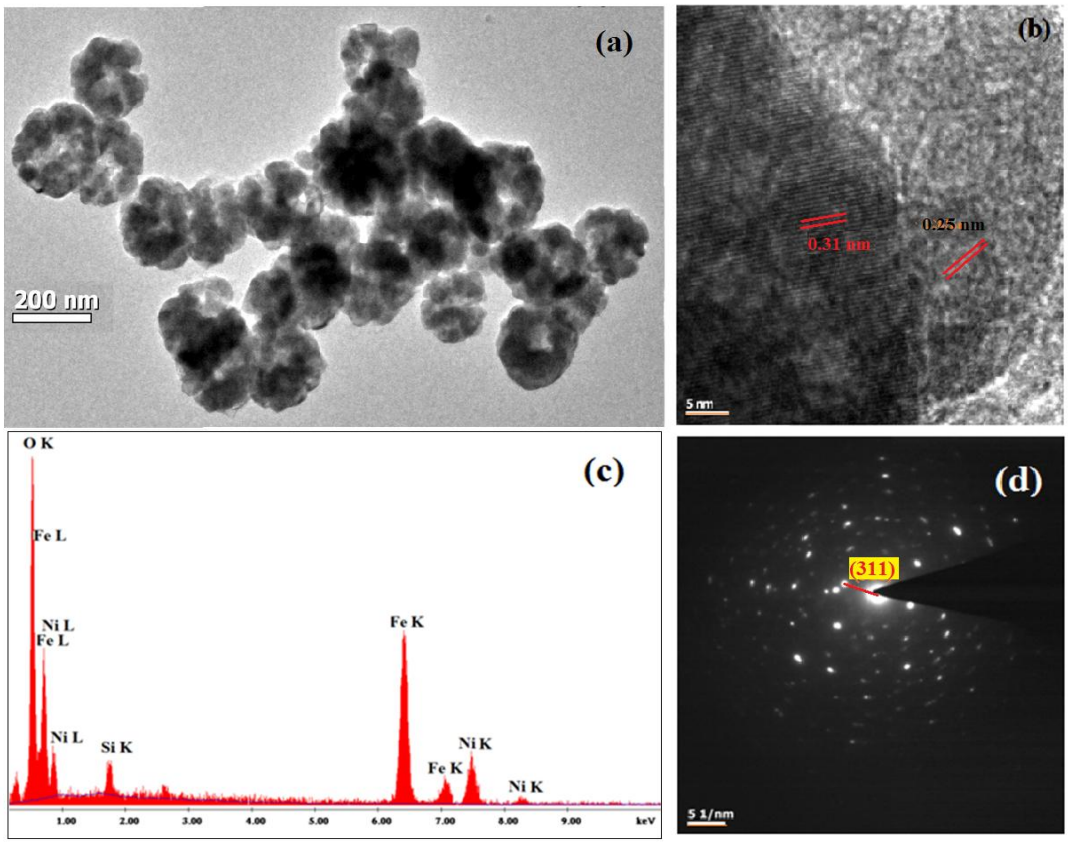

Figure 3.4. (a) TEM micrograph of NFO NHS, (b) HRTEM image showing distance between diffraction planes, (c) EDX (Energy Dispersive X-ray) spectra showing Ni, Fe, O present in NHS, (d) SAED (Selected Area Electron Diffraction) pattern displaying the crystallization of the sample and its lattice parameters

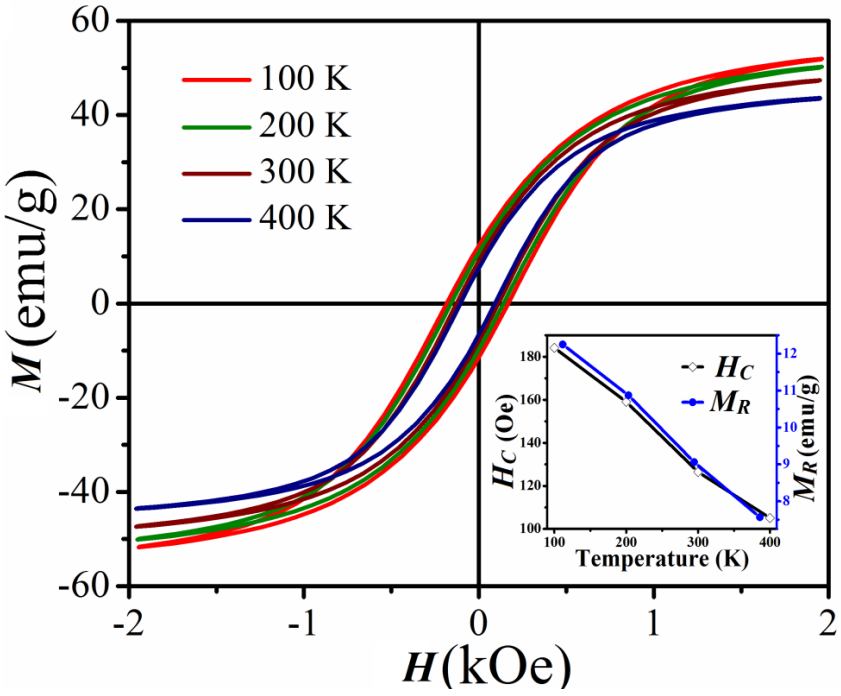

Figure 3.5. *M-H* curves of NFO NHS at 100K, 200K, 300K and 400K; Inset: H_C and remanent magnetization (M_R) vs. temperature plot

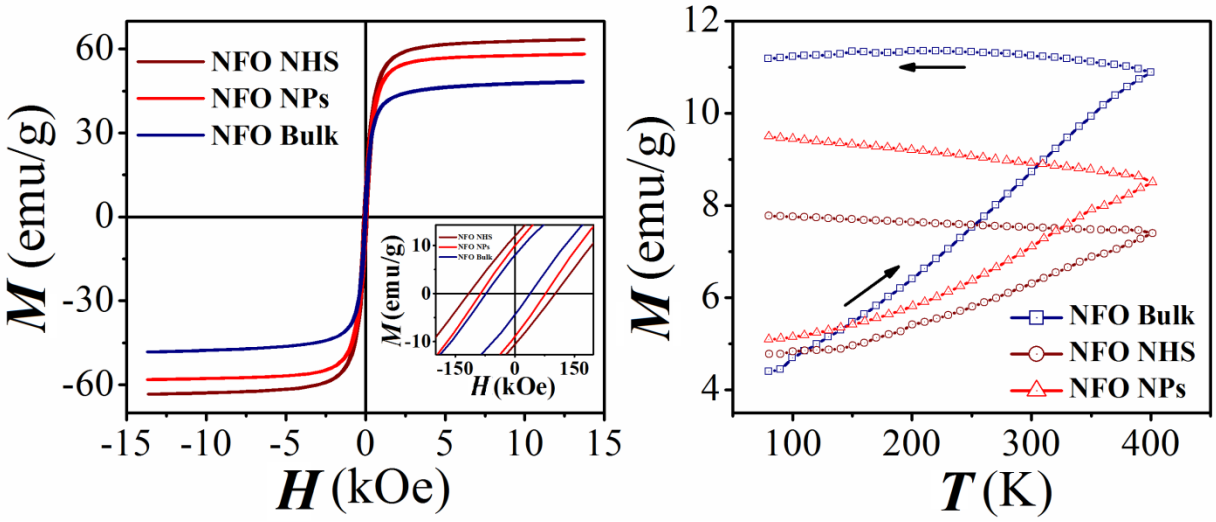

Figure 3.6. (a) Room temperature M-H curves for all the samples and (b) M-T curves under ZFC and FC mode for NFO NHS, Bulk NFO and NFO NPs

Magnetization and coercivity depends on several factors such as magnetic anisotropy, defects, strain, size, synthesis procedure, nature of the surface and interface [24]. The effective anisotropy constant ($K_{eff} = K_V + K_S/6$) of NPs is found to be much higher than that of bulk one [25] due to the inclusion of surface anisotropy (K_S) in addition to the volume anisotropy constant (K_V). As the cationic distribution of NFO at nanoscale is concerned, both the increase in anisotropy and cationic movements are responsible for the increase in H_C, M_R and M_S values of NPs respectively than bulk NFO [26,27]. High temperature needed in solvothermal method to synthesize NHS [15,28,29] and large surface to volume ratio of NHS are reasons behind higher H_C, M_R and M_S values than NPs [12].

3.5 Dielectric Properties

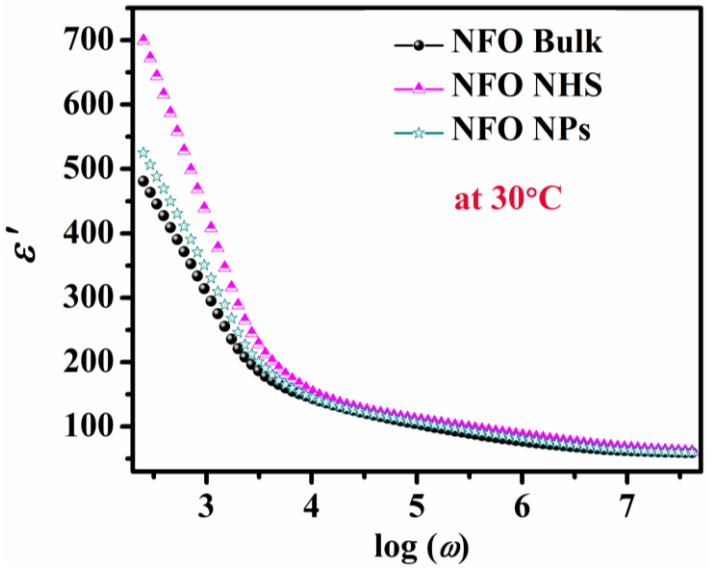

Figure 3.7. Frequency dependence (40 Hz-110 MHz) of ε' for NFO NHS, Bulk and NPs at room temperature

The study of the dielectric properties gives valuable information about the polarization behavior, conduction and relaxation mechanisms of a material. These properties vary with parameters such as frequency, temperature, pressure and also with the orientation, mixture and molecular structure of the sample. The real part of dielectric

constant/ relative permittivity (ε') is related to the polarization while the imaginary part (ε'') is associated with the energy dissipation. High obtained value of ε' indicates their usage in various devices such as in isolators and circulators for microwave communications [17]. Real and imaginary parts of dielectric constant are evaluated from measured impedance ($Z = Z' - iZ''$) – phase (θ) data as [25,26]

$$\varepsilon' = \frac{Z''}{\omega C_0 (Z'^2 + Z''^2)} \quad 3.1$$

$$\varepsilon'' = \frac{Z'}{\omega C_0 (Z'^2 + Z''^2)} \quad 3.2$$

where C_0 is the capacitance of free space and is given by $C_0 = \frac{\epsilon_0 A}{d}$, d, the thickness, A, the surface area and ε_0, the dielectric permittivity of air.

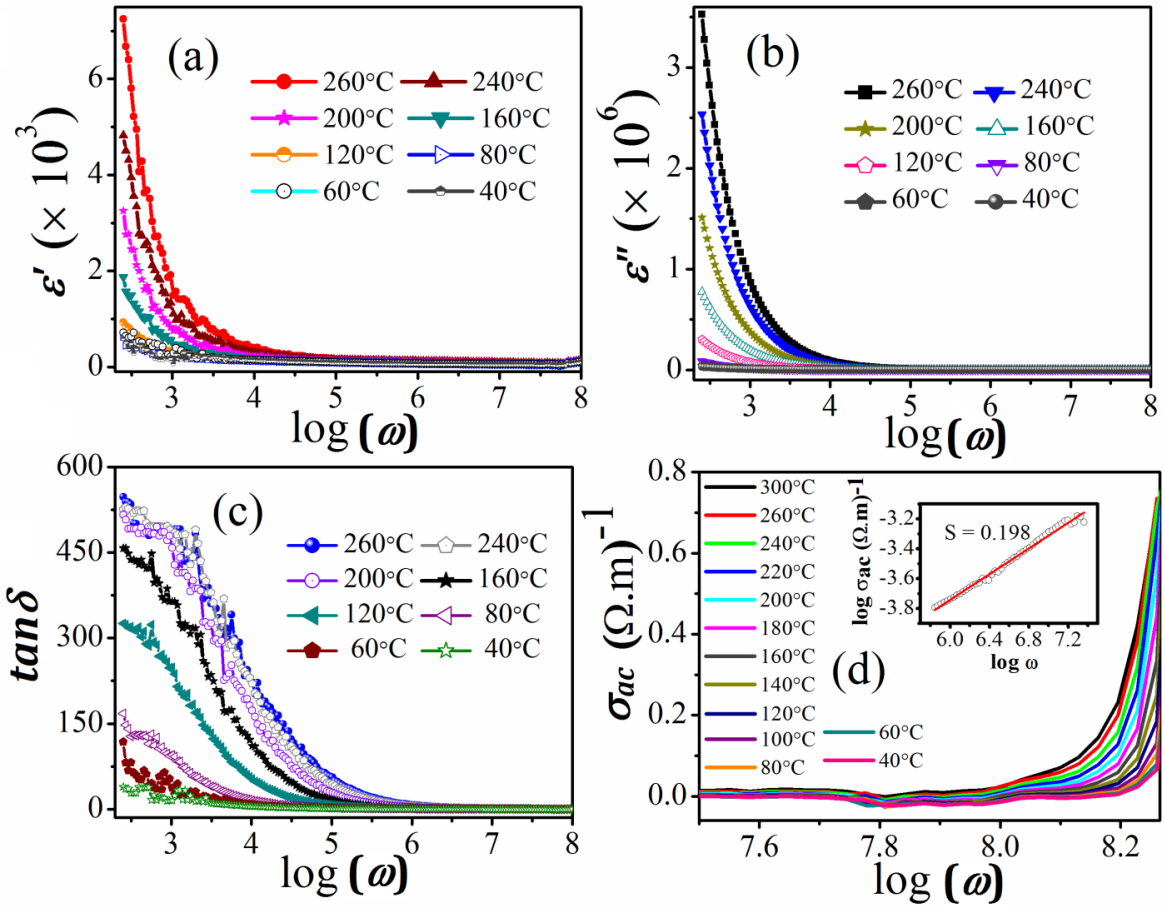

Figure 3.8. Frequency dependence (40 Hz-110 MHz) of (a) real (ε) and (b) imaginary (ε'') values of dielectric constant at different temperatures (30°C to 300°C). Variation of (c)

dielectric loss ($tan\delta$) with frequency and temperature and (d) ac conductivity (σ_{ac}); inset: fitted curve to find s value according to Jonscher's power law

A preliminary frequency dependent ε' study at room temperature, as shown in Fig. 3.7, reveals NFO NHS contains greater value of ε' than its other two counterparts. The inner and outer surface of hollow spheres enhances the total interfacial area for dielectric polarization in NHS which is even higher than that of NPs and hence ε' increases. Therefore, the frequency dependence of dielectric behavior of NFO NHS at different temperature (30^0C - 300^0C) for the frequency region of 40 Hz to 110 MHz is plotted in Fig. 3.8. ε', ε'' and dielectric loss ($tan\,\delta = \varepsilon'/\varepsilon''$) are high at low frequency region for all the temperatures, but as the frequency increases they sharply fall and approach to almost frequency independent nature. It is also observed that the dielectric constant and dielectric loss show a shift towards higher values with enhancing temperature at a particular frequency. Decay of ε' and ε'' with increase in frequency is due to the inability of electric dipoles to comply with variation (i.e. frequency) of applied ac electric field. These dipoles are formed with Fe^{2+}- Fe^{3+} cations present in tetrahedral (A) and octahedral (B) sites respectively in inverse spinel NFO. The contribution of exchanged electrons towards polarization is more prominent than holes because of the larger mobility of electrons [32]. Increase in dielectric constant with temperature is attributed to more number of excited dipoles which try to orient along the field, at higher temperature. This fact increases both space-charge and dipolar polarization in the sample. The value of ε' found for this NHS morphology is higher than that of NFO NPs [31,33] and other ferrites [14,34] and it is comparable to NFO/MWCNTs by Gul et al. [17] and bulk NFO by Ponpandian et al. [35]. The larger interfacial area in NHS may play an important role on the large value of ε'. Generally, dielectric losses occur due to absorption of electrical energy which is utilized for rotations of dipoles of the space charge formed at grain boundary [3,31,36]. The value of $tan\delta$ decreases with increasing frequency and remains unchanged further as the space charge accumulation decays resulting higher ac conduction.

The real part of ac conductivity (σ_{ac}) of the sample was calculated by $\sigma_{ac} = \omega\varepsilon_0\varepsilon''$, where $\omega = 2\pi f$ is the operating angular frequency [34,35]. However σ_{ac} is

attributed to the dielectric relaxation caused by the localized electric charge carriers, which obeys Jonscher's power law:

$$\sigma_{ac}(\omega, T) = \sigma_{dc}(T) + A\omega^{s}(T) \quad 3.3$$

Here, σ_{dc} is the dc conductivity of the material, A is material dependent and s is the temperature dependent parameter, varies within $0 < s < 1$ depending on the mechanism of conduction. Frequency dependence of σ_{ac} at different temperatures is shown in Fig. 3.8(d). It is observed that σ_{ac} starts to increase with increasing frequency above 200 kHz; below that it shows almost frequency independent behavior. From the fitted curve of log σ_{ac} vs. log ω, according to Jonscher's power law, s values are estimated to be ~ 0.198 and ~ 0.351 at 300°C and 100°C respectively, which supports the ac conduction mechanism [27,31,37] for NFO NHS.

Ferrites have cubic close packed oxygen lattice with the cation at octahedral (B) and tetrahedral (A) sites. In ferrites, conduction occurs mostly by the hopping of electrons between cations present on equivalent lattice sites through the following process [15],

$$Ni^{2+} + Fe^{3+} \leftrightarrow Ni^{3+} + Fe^{2+}$$

where both Fe^{3+} and Ni^{2+} ions fill the octahedral sites (B). Thus, conduction occurs as a result of electron transfer between Fe^{3+} and Fe^{2+}, and hole transfer between Ni^{2+} and Ni^{3+}. Moreover, the variation of ε' as well as σ_{ac} with frequency can be explained on the basis of Maxwell-Wagner two layer model for space charge. According to this theory, ferrimagnetic materials are assumed to have conducting larger grains and insulating smaller grain boundaries. When an external electric field is applied, the charge carriers can easily migrate from the grain and get accumulated (space charge) at the resistive grain boundaries. This process can produce large polarization and high ε' at low frequencies. The presence of inertia to the charge movement would cause a relaxation of dipoles to the polarizing field which gets more significant above a sufficiently high frequency (here > 200 kHz). In low frequencies, grain boundaries remain operative whereas conductive grains become more active at higher frequencies, where electron

hopping takes place between Fe^{2+} and Fe^{3+} present in two adjacent B sites (having smaller lattice constant), thereby increasing the hopping conduction and conductivity (σ_{ac}).

The complex impedance spectroscopy represents the electrical processes taking place within the system and the relaxation mechanism happening. No peaks in ε'' vs. log (ω) data (Fig. 3.8(b)) and non-correspondence of dielectric constant nature with Debye dispersion formulae gives hint that here the relaxation is non-Debye type i.e. greater than one ions are responsible in dielectric relaxation [38].

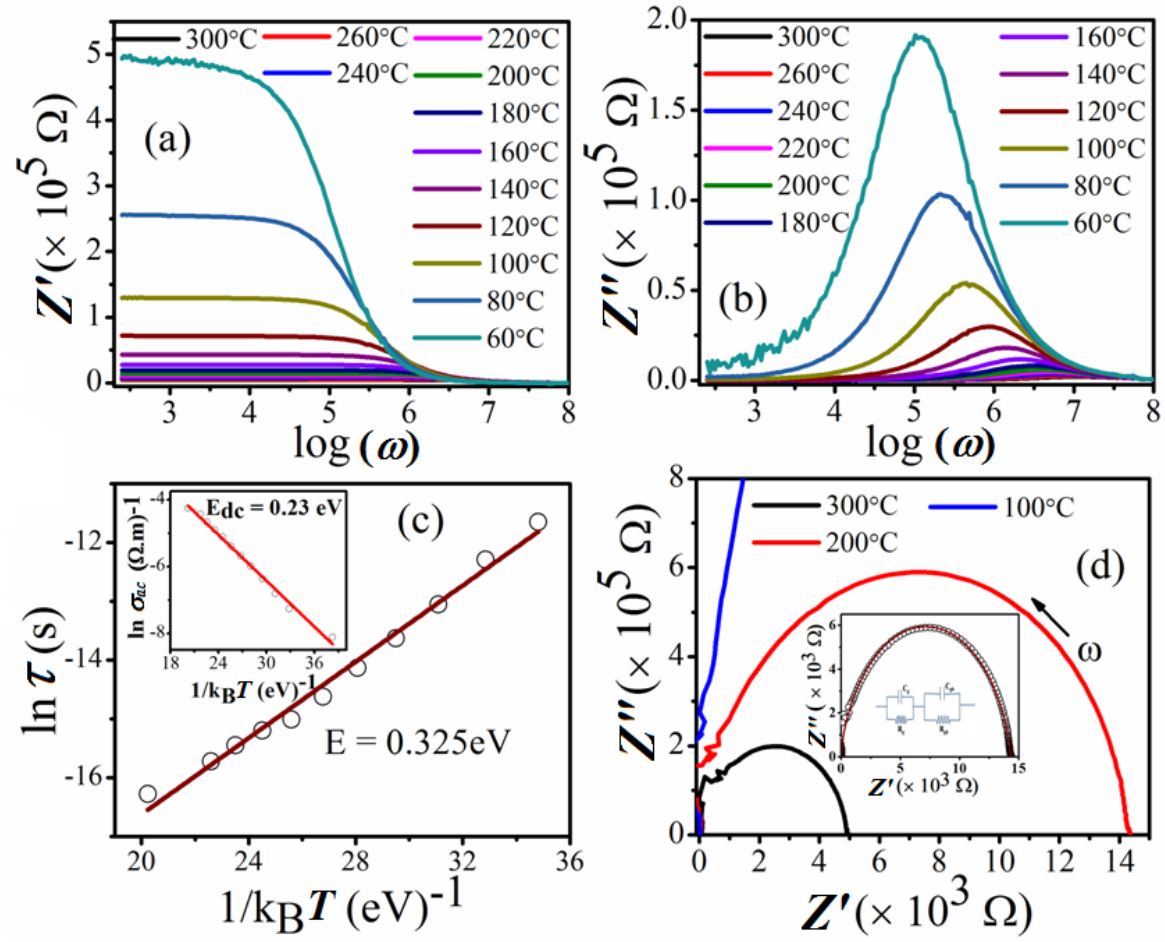

Figure 3.9. Frequency dependent plots of (a) real (Z') and (b) imaginary (Z'') parts of impedance at different temperatures (c) Activation energy (E) calculation from ln τ ($\tau = 1/2\pi f_{max}$) vs. $1/k_B T$ plot; inset: E_{dc} from ln σ_{ac} vs. $1/k_B T$ graph (d) Cole-Cole plot (Z' vs. Z'') for NFO NHS at 100°C, 200°C and 300°C; inset: fitted curve of Cole-Cole plot for NFO NHS at 200°C

by equivalent circuit with grain and grain boundary parameters and Equivalent circuit for dielectric properties of grain and grain boundaries.

Figure 3.9(a) and (b) show the frequency (40Hz - 110MHz) dependence of Z' and Z''at different temperatures for NFO NHS. At a particular temperature, Z'remains constant till a certain frequency showing its dc nature and then after decreasing with the increasing frequency, it becomes constant from ~ 200 kHz which is in agreement with σ_{ac} vs. frequency curves shown in Fig. 3.8(d). Z''vs. log (ω) plot shows a broad peak which shifts to higher frequency with rise in temperature. Both $Z'$and Z''decrease with increase in temperature at a particular frequency. The broadness of these Z''peaks (Fig. 3.9(b)) assures the existence of non-Debye relaxation peaks that would be due to the presence of space–charge relaxation at low frequencies. More precisely, in this frequency region, β-type relaxation (dipolar) arises strongly following Maxwell-Wagner Model [38]. Activation energy (E) for dielectric relaxation (taking it also as thermally activated) is calculated using Arrhenius equation:

$$\tau = \tau_0 \exp\left(\frac{E}{k_B T}\right), \text{where } \tau = \frac{1}{2\pi f_{max}} \qquad 3.4$$

Here τ is dielectric relaxation time which decreases with increase in temperature, k_B is Boltzmann constant, T is temperature and f_{max} is the peak frequency. Frequency at which Z''_{max} obtained is known as the relaxation frequency. The lower value of E (~ 0.325eV) compared to other materials [35,36] suggests faster dipolar relaxation in NFO NHS. Activation energy for dc conduction (E_{dc}) is found by fitting Arrhenius equation of conductivity to ln σ_{ac} vs. $1/k_B T$ plot at low frequency (inset of Fig. 7(c)). E_{dc} (~ 0.23eV) is lower than E and occur at low frequency due to hopping of electrons.

Figure 3.9(d) depicts the Cole–Cole plot (Z' vs. Z'') of NFO NHS at different temperatures. Here, curves at different temperatures consist of depressed semi-circular arc, not centered on real axis, where the contributions from grains (g) and grain boundaries (gb) overlap. At around 200 kHz, a kink present in the plots, emphasize the presence of grain effect along with the grain boundary one. The resistance values for the grain and grain boundary are calculated from the intercepts on the Z'axis, where as

the capacitance values can be calculated from the frequency peaks of the semi-circular arcs. The resistive (R_g, R_{gb}) and capacitive (C_g, C_{gb}) components are obtained by fitting the Cole-Cole plots with the equivalent circuit (shown in inset of Fig. 3.9(d)) in EC-lab software and the values are listed in Table 3.1. At higher frequencies, $>$ 50MHz, possibly ionic conduction is happening through electrode polarization [39] and because of that some unusual response is showing in the plot (near $(Z', Z'') = (0, 0)$).

Table 3.1. R_{gb}, C_{gb}, R_g and C_g values for different temperatures

Operating Temperature	R_{gb} (MΩ)	C_{gb} (pF)	R_g (MΩ)	C_g (pF)
100°C	1.153	81.82	0.143	6.2
200°C	0.143	99.25	0.0458	16.9
300°C	0.049	117	0.0043	22

Electric modulus (M_E), defined as the inverse of relative permittivity, is a powerful tool for analyzing dielectric behavior at relatively high temperatures, where ε usually becomes very high due to electrode polarization and carrier transport. Figure 3.10(a) and (b) shows the variation of real and imaginary parts of M_E with frequency at different temperatures which also support the previous experimental results on dielectric properties. From a very low value ($\sim$ 0), M' increases with increasing frequency (depicted in Fig. 3.10(a)). Each curves for a fixed temperature in Fig. 3.10(b) exhibits broad and asymmetric peaks indicating non-Debye type relaxation which implies broadness of the peaks expresses distribution of relaxation times of carriers. For each curve, the frequency (f_{max}) where the peak is located is on the increasing slope of M', which may suggest two different natures of mobility of charge carriers for before and after the peak. Relaxation peak (M''_{max}) shifts toward higher frequency side as temperature increases like the complex impedance behavior due to larger polarization [15,30].

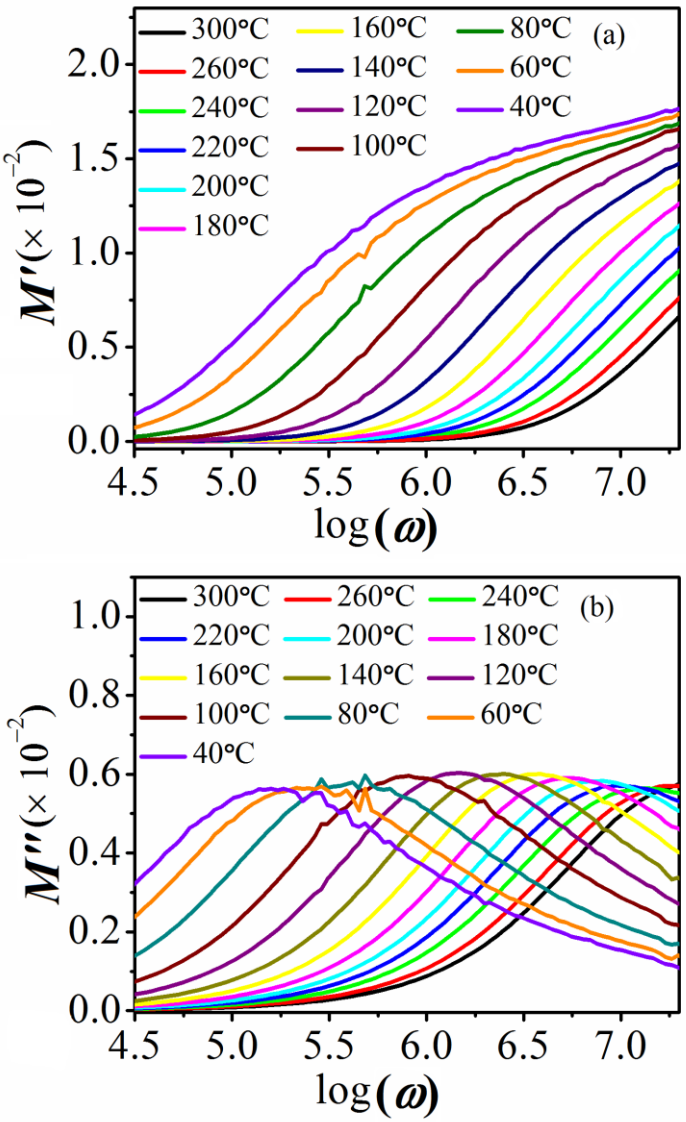

Figure 3.10. (a) Frequency dependent plots of real (M') and (b) imaginary (M'') parts of electric modulus at different temperature

3.6 Conclusion

In summary, we have successfully synthesized crystalline $NiFe_2O_4$ nano-hollow spheres in solvothermal method and reported a detail frequency and temperature dependent study on its magnetic and dielectric nature. The morphological analysis assures the sample to be nano-hollow spheres. Study of magnetic properties shows NFO NHS as soft a ferrimagnetic material having M_S and H_C, 63.5 emu/g and 122 Oe respectively which

are comparatively higher than that of its other morphologies. The variation of ε, Z, $tan\delta$ and σ_{ac} with frequency and temperature are explained in terms of Maxwell-Wagner two-layer model, where NFO are taken as piles of grain and grain boundaries, and hopping of charges at Fe^{3+} to Fe^{2+} as well as Ni^{2+} to Ni^{3+} ions at B (octahedral)-sites. The parameters of conductive grain and resistive grain boundaries are obtained from Cole-Cole plot. The conduction mechanism for NHS is found to be ac type from Jonscher's power law and the activation energy is relatively lower than that of other ferrites. Here dielectric relaxation of charge carriers is found to be of non-Debye type. Lower density, larger surface area and the enhanced dielectric and magnetic properties in this morphology (NHS) of NFO compared to its NPs and bulk counterparts, seems interesting towards its application in high-frequency devices.

References

[1] C. Liu, B. Zou, A. J. Rondinone, and Z. J. Zhang, J. Am. Chem. Soc. 122, 6263 (2000).

[2] K. Khaja Mohaideen and P. A. Joy, Appl. Phys. Lett. 101, 2 (2012).

[3] A. T. Raghavender and K. M. Jadhav, Bull. Mater. Sci. 32, 575 (2009).

[4] C.-Y. Wen, H.-Y. Xie, Z.-L. Zhang, L.-L. Wu, J. Hu, M. Tang, M. Wu, and D.-W. Pang, Nanoscale 8, 12406 (2016).

[5] F. Wang, J. Liu, J. Kong, Z. Zhang, X. Wang, M. Itoh, and K. Machida, J. Mater. Chem. 21, 4314 (2011).

[6] J. S. An, W. J. Han, and H. J. Choi, Colloids Surfaces A Physicochem. Eng. Asp. 535, 16 (2017).

[7] B. Guo, K. Yu, H. Li, H. Song, Y. Zhang, X. Lei, H. Fu, Y. Tan, and Z. Zhu, ACS Appl. Mater. Interfaces 8, 5517 (2016).

[8] Q. Wang, Y. Zhu, J. Xue, X. Zhao, Z. Guo, and C. Wang, ACS Appl. Mater. Interfaces 8, 17226 (2016).

[9] C. C. Li, Q. H. Li, L. B. Chen, and T. H. Wang, ACS Appl. Mater. Interfaces 4, 1233 (2012).

[10] J. W. Yoon, Y. J. Hong, Y. C. Kang, and J. H. Lee, RSC Adv. 4, 16067 (2014).

[11] Z. Yang, Z. Li, Y. Yang, and Z. J. Xu, ACS Appl. Mater. Interfaces 6, 21911 (2014).

[12] S. Talukdar, D. Mandal, and K. Mandal, Chem. Phys. Lett. 672, (2017).

[13] M. Dasari, G. Gajula, R. Hanumantha, A. Chintabathini, S. Kurimella, and B. Somayajula, Process. Appl. Ceram. 11, 7 (2017).

[14] E. E. Tanrıverdi, A. T. Uzumcu, H. Kavas, A. Demir, and A. Baykal, Nano-Micro Lett. 3, 99 (2011).

[15] R. S. Yadav, I. Kuřitka, J. Vilcakova, J. Havlica, J. Masilko, L. Kalina, J. Tkacz, V. Enev, and M. Hajdúchová, J. Phys. Chem. Solids 107, 150 (2017).

[16] K. Vasundhara, S. N. Achary, S. K. Deshpande, P. D. Babu, S. S. Meena, and A. K. Tyagi, J. Appl. Phys. 113, 194101 (2013).

[17] S. A. Soomro, I. H. Gul, M. Z. Khan, H. Naseer, and A. N. Khan, Ceram. Int. 43, 4090 (2017).

[18] R. K. Grubbs, E. L. Venturini, P. G. Clem, J. J. Richardson, B. A. Tuttle, and G. A. Samara, Phys. Rev. B 72, 104111 (2005).

[19] Z. Li, M. Ye, A. Han, and H. Du, J. Mater. Sci. Mater. Electron. 27, 1031 (2016).

[20] A. Hirohata, H. Sukegawa, H. Yanagihara, I. Zutic, T. Seki, S. Mizukami, and R. Swaminathan, IEEE Trans. Magn. 51, 1 (2015).

[21] C. L. Hogan, Rev. Mod. Phys. 25, 253 (1953).

[22] M. Mandal Goswami, Sci. Rep. 6, 35721 (2016).

[23] B. G. Toksha, S. E. Shirsath, S. M. Patange, and K. M. Jadhav, Solid State Commun. 147, 479 (2008).

[24] R. H. Kodama, A. E. Berkowitz, E. J. McNiff, Jr., and S. Foner, Phys. Rev. Lett. 77, 394 (1996).

[25] D. Mandal, M. M. Goswami, and K. Mandal, IEEE Trans. Magn. 54, 1 (2018).

[26] J. Wang, Mater. Sci. Eng. B 127, 81 (2006).

[27] K. C. BABU NAIDU and W. MADHURI, Bull. Mater. Sci. 40, 417 (2017).

[28] F. L. Zabotto, A. J. Gualdi, J. A. Eiras, A. J. A. de Oliveira, and D. Garcia, Mater. Res. 15, 428 (2012).

[29] J. N. P. Neeraja, S. R. Jeya, and R. V Umapathy, J. Supercond. Nov. Magn. (2016).

[30] F. Tian, IEEE Trans. Dielectr. Electr. Insul. 21, 929 (2014).

[31] K. M. Batoo, J. Phys. Chem. Solids 72, 1400 (2011).

[32] C. V. Ramana, Y. D. Kolekar, K. Kamala Bharathi, B. Sinha, and K. Ghosh, J. Appl. Phys. 114, 183907 (2013).

[33] Z. K. Heiba, M. Bakr, M. A. Ahmed, M. A. A. Moussa, and H. H. Hamdeh, J. Alloys Compd. 586, 773 (2014).

[34] K. Ali, A. Bahadur, A. Jabbar, S. Iqbal, and I. Ahmad, J. Magn. Magn. Mater. 434, 30 (2017).

[35] N. Ponpandian, P. Balaya, and A. Narayanasamy, J. Phys. Condens. Matter 14, 3221 (2002).

[36] J. H. Joshi, D. K. Kanchan, M. J. Joshi, H. O. Jethva, and K. D. Parikh, Mater. Res. Bull. 93, 63 (2017).

[37] S. Joshi, M. Kumar, S. Chhoker, G. Srivastava, M. Jewariya, and V. N. Singh, J. Mol. Struct. 1076, 55 (2014).

[38] A. Vassilikou-Dova and I. M. Kalogeras, in *Therm. Anal. Polym.* (John Wiley & Sons, Inc., Hoboken, NJ, USA, 2008), pp. 497–613.

[39] R. Nongjai, S. Khan, K. Asokan, H. Ahmed, and I. Khan, J. Appl. Phys. 112, 84321 (2012).

Chapter 4

$NiFe_2O_4$ Nano Hollow Spheres as an Efficient Microwave Absorber

In this chapter, material properties along with microwave absorption properties are studied in detail for three morphologies (bulk, nanoparticles and nano-hollow spheres (NHS)) of Nickel ferrite in widely used X-band frequency (8 – 12 GHz) range. Incident electromagnetic wave is found to be trapped inside the hollow core of $NiFe_2O_4$ NHS and cause interesting phenomena regarding its microwave absorption.

4.1 Preamble

With the widespread usage of wireless communication devices in recent years, electromagnetic interference (EMI) or wave pollution has become a serious problem to the environment and also to the advances in technology [1–4]. Therefore, EM wave absorbing materials are in need to shield unwanted waves. Moreover, microwave absorbers (MA) are also popular in military and civil applications to avoid information stealth. Within the electromagnetic spectrum, X-band (8-12 GHz) is extensively used in radars and communication networks [5]. In search of light-weight, broad band, low cost, thin and efficient MA, materials such as carbon-based materials, conductive polymers with significant dielectric loss and materials such as ferrites, ultrafine metal powders with large magnetic loss have been broadly used [6–10].

Among the above mentioned materials, ferrites have combined effect of relatively better permittivity (ε) and permeability (μ) which ensures higher impedance matching, broader bandwidth (BW) and higher reflection loss (RL) [2,11]. $NiFe_2O_4$ (NFO) being one of the most significant spinel ferrites due to its specific qualities such as low coercivity (H_C), large saturation magnetization (M_S), high Curie temperature (T_C) and electrical resistivity, is an important candidate as MA [12]. To achieve a light-weight and size efficient yet thermally and chemically stable absorbing material, nano hollow spheres (NHS) of ferrites are found very promising [2,5]. Their high M_S, large surface area, low density, ability to withstand volume changes due to changes in temperature and pressure enable them to be used in wide varieties of applications in the fields of biomedical research [13], high frequency magnetic devices [7], ferro-fluids [14], Hydrogen evolution reaction [15], super capacitors [16] and Li ion battery [17]. Moreover, the inner cavity causes repeated internal reflections and large surface area enhances permittivity as well as dielectric loss and thus increasing their applicability as MA [5,7,18].

During the past decade, a number of researches had been carried out on microwave absorbing materials [3,6,19–21]. Morphology control, chemical doping and composite materials have become a promising strategy to enhance the EM wave

attenuation capability [22–24]. Liu et al. characterized ZnO coated Fe nanocapsules and found an optimal *RL* of −57.1dB at 7.8 GHz [4]. Li et al. [19] and Khan [25] reported microwave absorption (MA) properties of NFO and cobalt ferrite respectively. Che et al. studied the same for Fe_3O_4-TiO_2 hetero-structures to enhance the *RL* and absorption frequency range [26]. EM wave absorption properties of $ZnFe_2O_4$ and Fe_3O_4 NHS were studied by Yang et al. [2] and Liu et al. [7] respectively and an optimal *RL* were found ~ −45 dB for $Zn_{0.6}Fe_{2.4}O_4$ and ~ −42.7 dB for Fe_3O_4.

From our previous work, NFO NHS was found to have improved magnetic and dielectric properties than those of its other morphologies such as NFO nanoparticles (NPs) and bulk NFO [27]. In search of lightweight, broadband and stable microwave absorbing material, here we have presented a comparative morphology dependent study of microwave properties on Nickel Ferrite (NFO). A comparative study of permittivity (ε), permeability (μ), Reflection Loss (*RL*) and Shielding efficiency (*SE*) on NFO nano hollow spheres (NHS) with its nano particles (NPs) and bulk counterpart has been performed for widely used X-Band (8-12 GHz) on composites filled (25 wt% and thickness of 2 mm) with each sample. Interestingly, NFO nano hollow spheres (NHS) are found to be highly efficient material towards microwave attenuation. An optimal *RL* of ~ −59.2 dB is obtained for frequency ~ 11.7 GHz with a broad band-width (*BW*) of ~ (9.18 – 12) GHz having $RL < -10$ dB (absorption > 90%). Hollow cavity of NHS leads to a lower density (~ 3.91 g/cc) as well as multiple internal reflections, which enhances wave absorption. Excellent impedance matching with free space, accompanied by proper dielectric and magnetic loss contributes towards maximization of *RL* for NHS. These properties enhance the potentiality of NFO NHS as an efficient microwave absorbing material suitable in various microwave devices.

4.2 Experimental

4.2.1 Synthesis Procedure

NFO NHS is successfully synthesized by a low cost and template free solvothermal process using oleylamine as capping agent [27,28]. Here Oleylamine micelles control the growth of NHS and Ostwald ripening method is considered as the mechanism for formation of NHS [7,28]. NFO NPs are prepared using the same process except the synthesis time is lessened (15 h) whereas Bulk NFO is synthesized in a wet-chemical combustion method and the as prepared powder sample is annealed at 900 °C for 4h [27].

The detailed chemical synthesis procedure is described in the previous chapter.

4.2.2 Characterizations

The structural phase and crystallite size of as-prepared NFO NHS are studied by powder X-ray diffraction (XRD) using Rikagu MiniFlex II diffractometer equipped with Cu K_α radiation at the scanning rate of 1° per minute in the 2θ range of 20°–80°. A FEI QUANTA FEG 250 field-emission scanning electron microscope (FESEM) (0.2–30 kV) and a FEG high-resolution transmission electron microscope (HRTEM) (80–200 kV) are used to study the size, shape and morphology of NHS. All the relevant magnetic measurements are carried out using a vibrating sample magnetometer (VSM) (Lake Shore). Microwave properties of the samples are measured using an Agilent E8364B Vector Network Analyzer (VNA). For the microwave measurements in the X-band the samples are prepared as, 25 wt% of each powder Nickel ferrite samples are mixed with Epoxy Resin matrix and the mixture is poured and hardened in a precise Teflon mould to construct the final composites in rectangular form with length, a = 22.56 mm, breadth b = 10.24 mm and thickness, d = 2.0 mm. Analysis from 2-port scattering (S)-parameters measured in transmission line technique is performed using Nicholson-Ross-Weir (NRW) algorithm.

4.3 Results and Discussion

4.3.1 Crystallography and Morphology

X-Ray Diffraction (XRD) curve with Rietveld profile refinement is plotted for NFO in the inset of Fig. 4.1. The peak profile and background for NFO sample are described by the Thompson–Cox–Hastings formulation of the pseudo-Voigt function and Chebyshev polynomial for Powder XRD data. Additionally, the scale factors, lattice parameters, oxygen positions, Debye–Waller factors and zero-point offset are refined [29].

Figure 4.2(a) and 4.2(c) represents the Field Emission Scanning Electron Microscope (FESEM) micrographs for NFO NHS and bulk whereas Fig. 4.2(b) and 4.2(d) are the Transmission Electron Microscope (TEM) micrographs for NFO NHS and NPs respectively. From the study of crystallographic phase using XRD and morphological characterization using FESEM and TEM, it is found that NFO NHS has an average size of ~ 228 nm (outer shell width ~ 55 nm) with crystallite size ~ 23.6 nm [27]. XRD pattern confirms the single phase inverse spinel face centered cubic structure of NFO, as reported in the literature (JCPDS file no. 010–0325). The estimated tap density of NFO NHS (~ 3.91 g/cc) is much lower than that of its bulk counterpart (~ 4.78 g/cc) [27], which is favorable to achieve a light-weight MA.

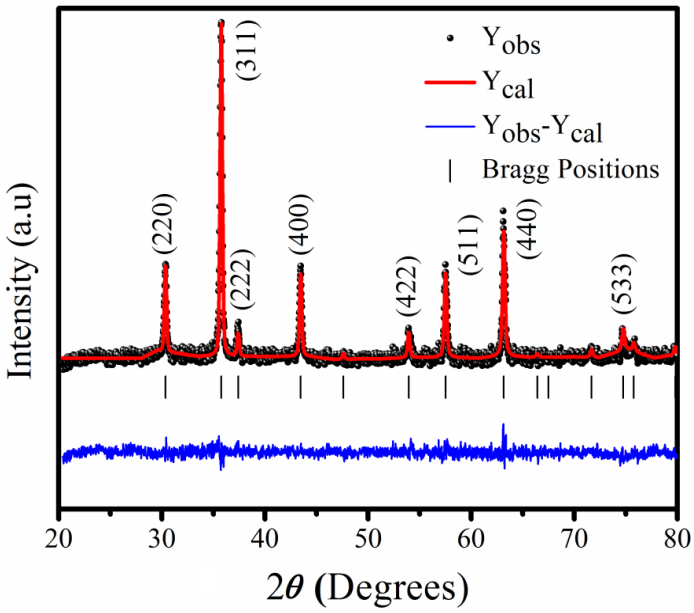

Figure 4.1. X-Ray Diffraction plots of Bulk NFO with Rietveld profile refinement is plotted

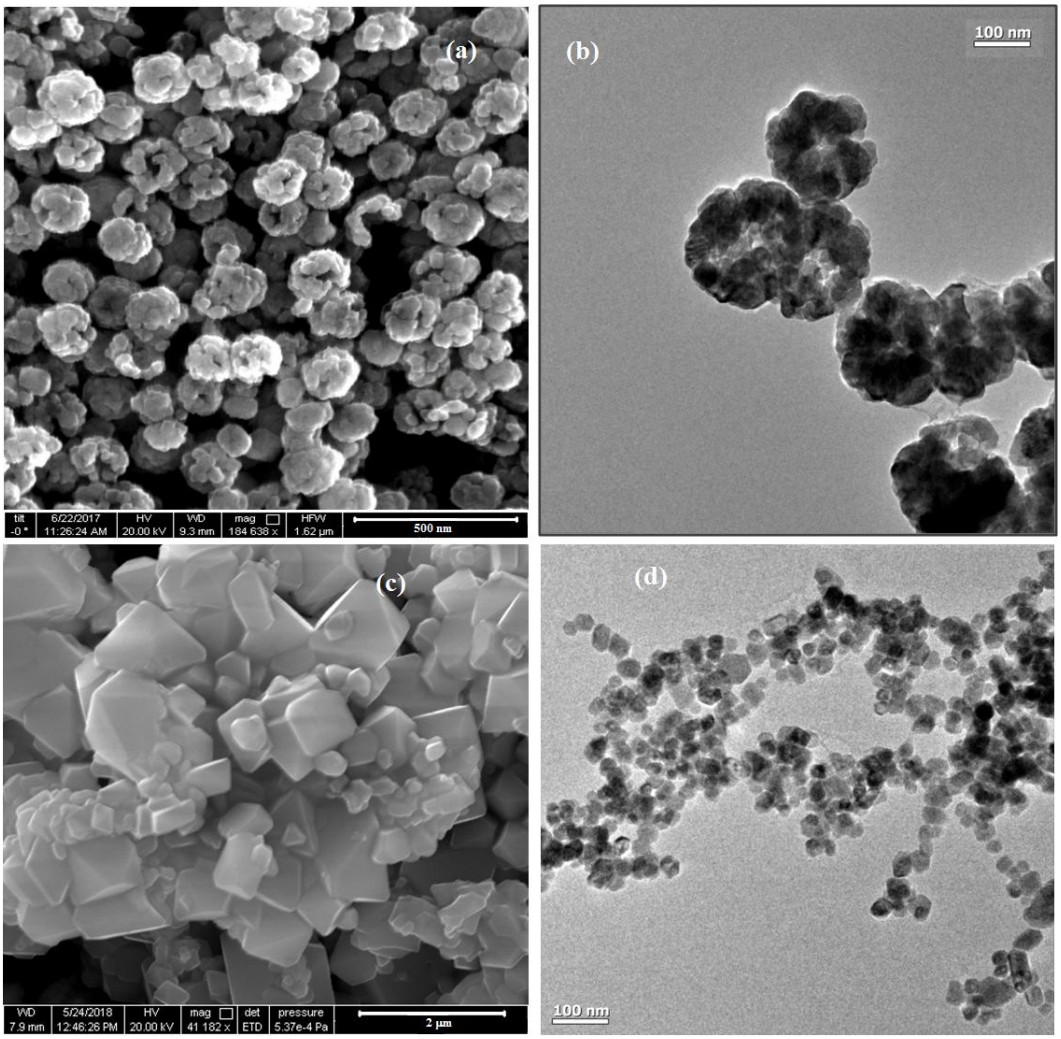

Figure 4.2. FESEM micrographs of the as-prepared (a) NFO NHS, (c) NFO Bulk and TEM micrographs of (b) NFO NHS, (d) NFO NPs; Inset of (b): XRD plot for NFO NHS

4.3.2 Magnetic and Dielectric Properties

Variation of real (ε′) and imaginary (ε'') values of dielectric constant with frequency (f) are shown in Fig. 4.3(a) and 4.3(b). ε' remains almost ~ 1.8 for NFO NHS throughout the frequency region whereas for NFO NPs and bulk, it slightly increases upto 9.6 GHz and then decreases with increasing frequency. It is well-known that ε' is related to polarization of a material and for inverse spinel NFO, dipoles formed with Fe^{2+}-Fe^{3+} cations present in tetrahedral (A) and octahedral (B) sites respectively, are responsible

for the polarization [30]. Larger surface area of NHS leads to higher polarization which enhances ε' and as the dipoles can not comply with increasing frequency, ε' reduces at higher frequency. ε'' as a function of *f*, shows an inverted cusp like behavior. For NHS, the value of ε'' is ~ 0.9 at 8 GHz and ~ 2.6 at 12 GHz with minimum value of ~ 0.43 at 9.81 GHz. Corresponding values of ε'' at the respective frequencies are ~ 1.73, 1.86 and 0.30 for NPs and ~ 1.64, 2.6 and 0.50 for bulk NFO. ε'' is related to energy dissipation of dipoles and according to resistivity, $\rho \sim 1/2\pi f\varepsilon_0\varepsilon''$, lower value of ε'' gives rise to higher resistivity of the material which is an important parameter for MA [4].

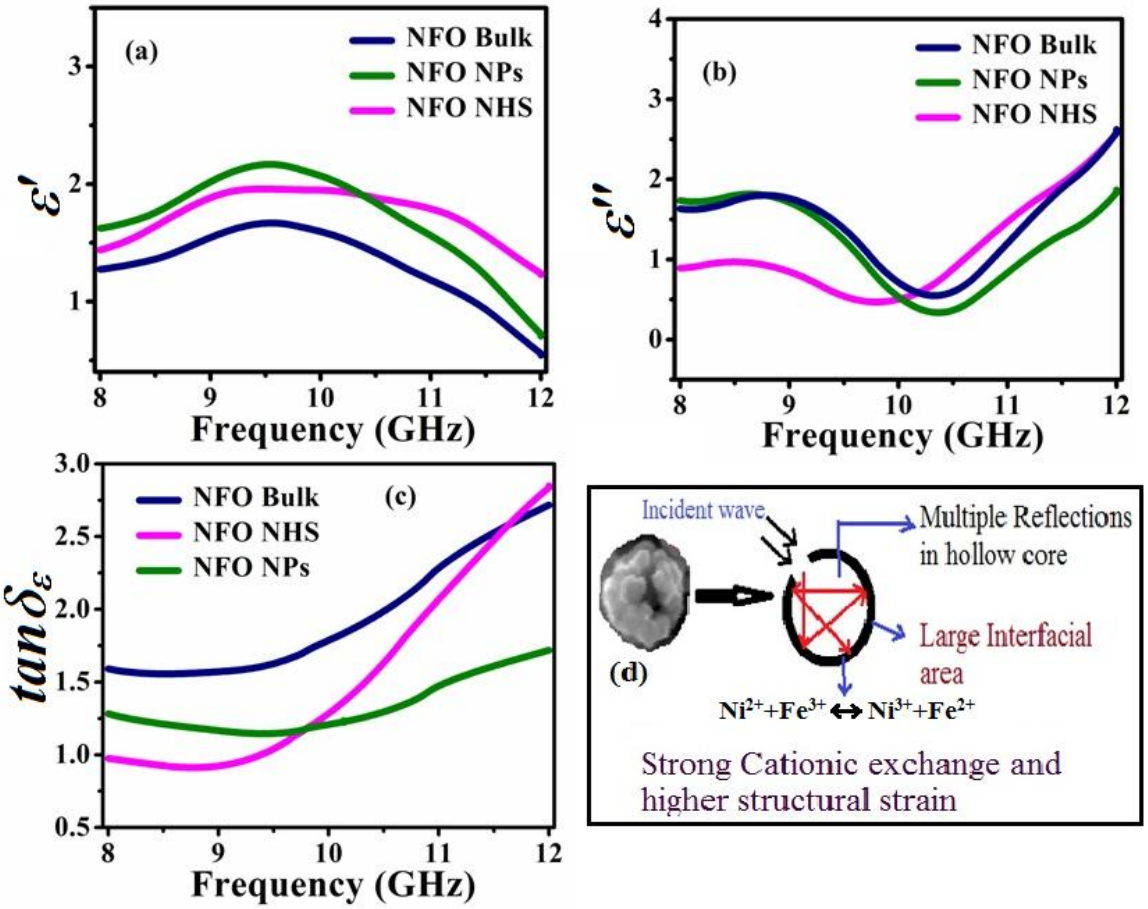

Figure 4.3. Frequency dependence (8-12 GHz) of (a) real (ε'), (b) imaginary (ε'') values of dielectric constant and (c) dielectric loss ($tan\delta_\varepsilon$), (d) A schematic approach showing reasons behind high EM wave absorption for NFO NHS

In Fig. 4.3(c), dielectric loss, defined as $tan\delta_\varepsilon = \varepsilon''/\varepsilon'$, is found to increase with frequency in a stiffer way for NHS than NPs and bulk. In case of NHS, it can be presumed that $tan\delta_\varepsilon$ is not only arising from the movement of dipoles but also owing to multiple reflections in internal hollow core causing $tan\delta_\varepsilon$ to increase sharply. Thus increase in polarization area and combined effect of higher resistivity with dielectric loss in NFO NHS makes it more suitable towards electro-magnetic wave absorbing materials. A schematic approach showing reasons behind high EM wave absorption for NFO NHS is depicted in Fig. 4.3(d).

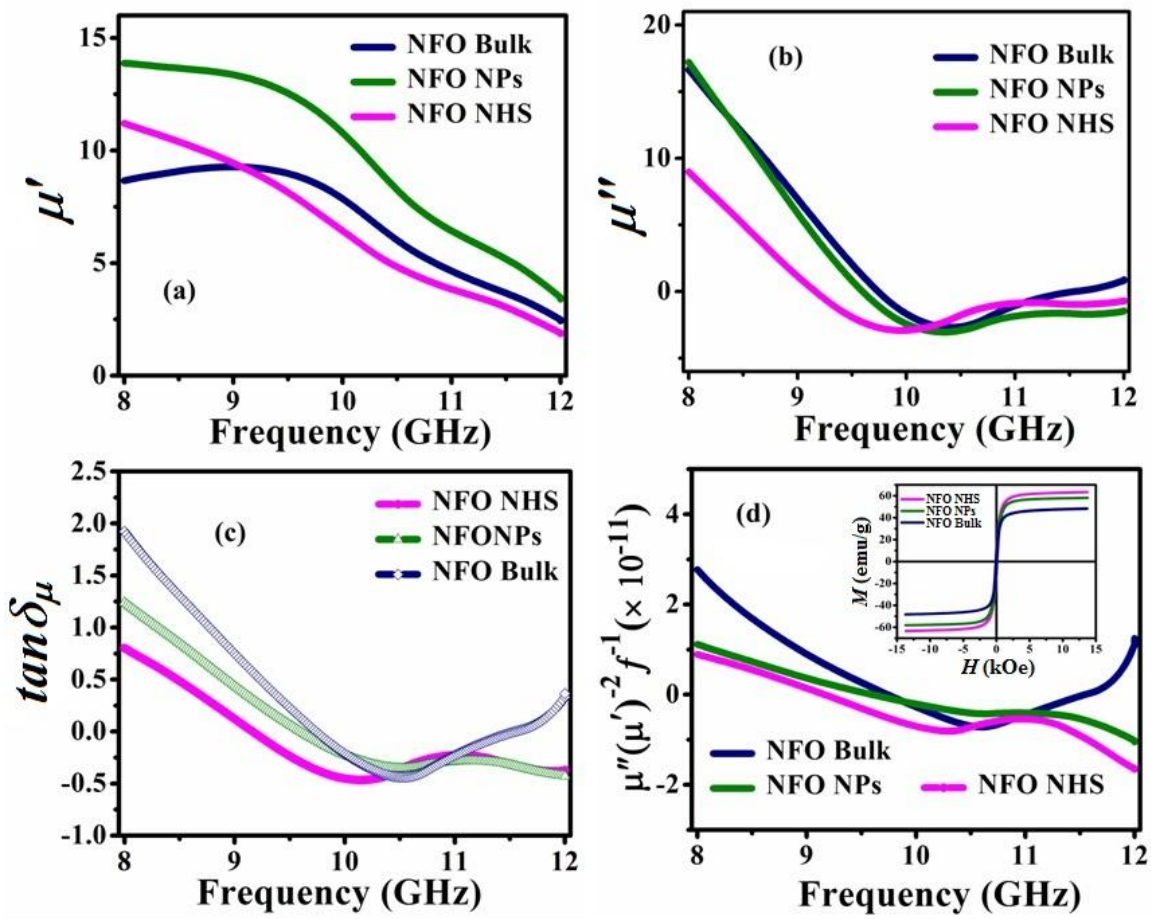

Figure 4.4. Frequency dependence (8-12 GHz) of (a) real (μ'), (b) imaginary (μ'') values of dielectric constant and (c) magnetic loss ($tan\delta_\mu$), and (d) $\mu''(\mu')^{-2}f^{-1}$ versus frequency; inset of (d): *M-H* plots at 300 K for NFO NHS, NPs and Bulk

Variation of real (μ') and imaginary (μ'') parts of permeability with frequency (f) are shown in Fig. 4.4(a), 4.4(b). It is observed that μ' decreases with frequency for all the NFO samples and μ'' becomes almost constant with frequency after decreasing till ~ 10 GHz. From the previous study of magnetic properties of NFO samples (also shown in inset of Fig. 4.4(d)), it was found that at room temperature (~ 300 K) coercivity (H_C) and saturation magnetization (M_S) increase from bulk (H_C= 78 Oe, M_S= 48.5 emu/g) to NPs (H_C = 93 Oe, M_S = 58.3 emu/g) to NHS (H_C = 122 Oe, M_S = 63.5 emu/g) [27]. According to the Landau-Lifshitz-Gilbert (LLG) equation, dynamic magnetic properties of the soft ferrimagnetic materials are strongly related to the parameters like magnetic anisotropy and M_S [2,3,31]. High value of both H_C and anisotropy for NHS restricts μ value from being highest for NHS. Moreover, according to Globus equation, $\mu' \propto (M_S{}^2 D \,/\, K^{1/2})$, where D is the crystallite size and K is the magneto-crystalline anisotropy constant [2]. From the micro-structure of the samples, smaller crystallite size, D, of NHS enhances K which also suppresses μ' [3,4].

From Fig. 4.4(c), magnetic loss tangent, defined as $tan\delta_\mu = \mu''/\mu'$, is found to follow almost the same trend with f, as shown in case of μ'' (Fig. 4.4(b)). In general, dynamic magnetic loss mostly arises from magnetic hysteresis, domain wall resonance, eddy current effects, natural and exchange resonance. Here, the first two contributions can be excluded for NFO samples in $8 - 12$ GHz frequency range [10]. From the natural resonance equation [4], $2\pi f_r = (4\gamma K)/(3\mu_0 M_S)$, where γ is gyromagnetic ratio (~ 2.8 GHz/kOe for ferrites), resonance frequency (f_r) is found ~ 1.8 GHz for NFO NHS which is much lower from X-band regime. Therefore in our concerned frequency region, resonance should not have significant role in magnetic loss. The eddy current loss contribution to the μ'', can be expressed as [32] $\mu'' \sim 2\pi\mu_0\mu'^2(d^2\sigma)f$, d, thickness of the sample, σ, electrical conductivity, μ_0, permeability of free space. According to this equation, if μ'' (or $tan\delta_\mu$) only originates from the eddy current loss, the values of $\mu''(\mu')^{-2}f^{-1}$ will be constant with frequency [33]. Further, to know the probable cause of magnetic loss, nature of $\mu''(\mu')^{-2}f^{-1}$ versus frequency curve is plotted in Fig. 4.4(d). It can be noticed that there are no peaks in the curve and the value remains almost constant in

this frequency region. Therefore, eddy current loss has overpowering contribution in μ'' (or $tan\delta_\mu$) than other causes which may be related to the large size of NFO samples [10].

4.3.3 Microwave Properties

Reflection loss (*RL*) measurement of a sample is a popular way to ensure the importance of the material as microwave absorbers (MA). Here *RL* is calculated following these equations:

$$Z_{in} = Z_0(\frac{\mu_r}{\varepsilon_r})^{1/2} \tanh[j\left(\frac{2\pi df}{c}\right)(\mu_r \varepsilon_r)^{\frac{1}{2}}] \quad 4.1$$

$$RL = -20\log|(Z_{in} - Z_0)/(Z_{in} + Z_0)| \quad 4.2$$

where μ_r $(=\mu'- i\mu'')$ and ε_r $(=\varepsilon'- i\varepsilon'')$ are relative permeability and permittivity of the material, *f*, the frequency of EM wave, c, velocity of light, d, absorber composite thickness, Z_0 and Z_{in} are impedance of free space and input impedance of absorber respectively. These equations are simplified equation for *RL* estimated under metal-backed condition and based on transmission line technique. To acquire knowledge about optimum absorption properties from dielectric and magnetic properties of a sample, the above equations can be implied whereas *RL* vs. *f* curve directly follows S_{11}_short vs. *f* curve while using metal-backed material itself [34].

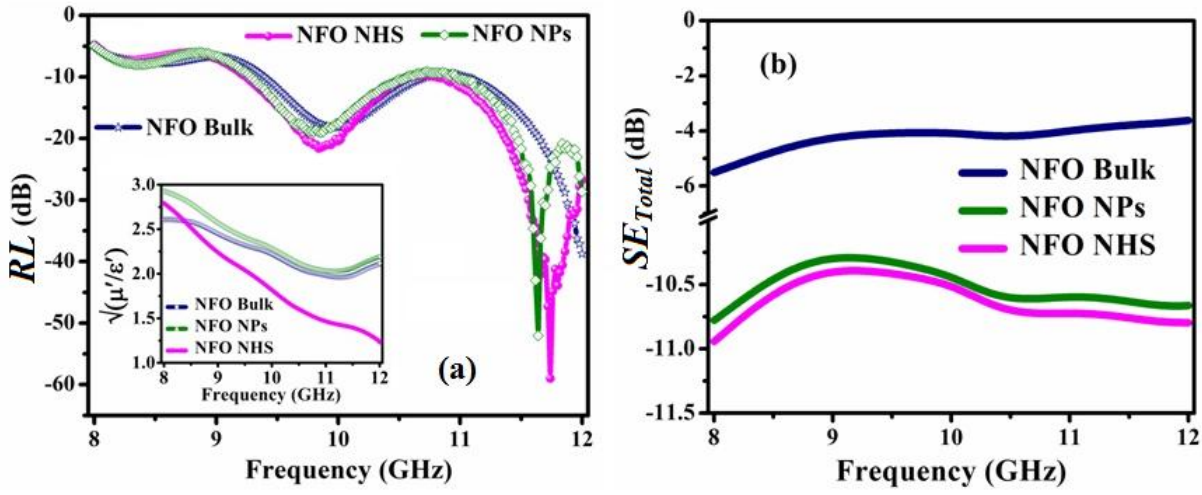

Figure 4.5. (a) Variation of reflection loss (RL) and (b) total shielding efficiency (SE (total)) with frequency (8-12 GHz) for all the samples; Inset of (a): √(μ′/ε′) vs. Frequency

Figure 4.5(a) shows the frequency dependence of *RL* in $8 - 12$ GHz range for all the samples. In this frequency region, two peaks of *RL* are observed for NPs (-19.8 dB at 9.83 GHz and -51.9 dB at 11.6 GHz) and NHS (-22.2 dB at 9.85 GHz and -59.2 dB for 11.7 GHz). For bulk with less surface area the peaks are shifted towards higher frequency probably following the relation $f_{peak} \sim 1/\text{Area}$. Therefore one peak ($-18.2$ dB at 9.96 GHz) is observed and perhaps the second peak moves beyond X-band. The observed value of optimal $RL \sim -59.2$ dB for NFO NHS, is comparable with that from previous researches, -65 dB for octahedral Fe_3O_4/RGO composites [9], -57.1 dB for ZnO coated Fe NPs [4], -42 dB for PANI coated flaked NFO [19], -42.7 dB for hollow magnetite spheres [7] and -45 dB for $Zn_{0.6}Fe_{2.4}O_4$ NHS [2].

Generally, the reason behind *RL* can be attributed to (i) higher transmission of the incident wave which requires better impedance matching and to achieve this, closer values of μ' and ε' is needed to make $\sqrt{(\mu'/\varepsilon')} \sim 1$ (ii) high value of dielectric and magnetic loss [2,10]. To assure the impedance matching, $\sqrt{(\mu'/\varepsilon')}$ vs. frequency (f) curve is plotted (inset of Fig. 4.5(a)), which shows for NHS, $\sqrt{(\mu'/\varepsilon')}$ is decreasing with f, and has a minimum value ~ 1.2. Larger effective surface area in NHS and cationic movement in nanoscale NFO are responsible for higher dielectric loss which is more effective in 10 - 12 GHz frequency region. Moreover, the total internal reflection in the hollow interior of NHS increases the total propagation path of incident microwave, hence absorbing it more [18,33]. For $8 - 10$ GHz frequency regime, magnetic loss is responsible for EM wave attenuation. Moreover, according to the quarter wavelength ($\lambda/4$) model for best matching thickness, $t_m = \frac{c}{4f_m\sqrt{|\varepsilon_r\mu_r|}}$, where t_m and f_m are the optimum thickness of microwave absorption material and the microwave frequency of the minimum RL respectively (for NFO NHS, f_m is 11.7 GHz) [19,35]. For NFO NHS sample, the calculated d_m is found to be ~ 2.3 mm and for microwave measurement, the thicknesses of all the NFO composites are taken around 2 mm. Therefore, around minimum RL frequency, optimal thickness matching is also responsible for strong EM wave absorption. Moreover, from *RL* vs. f curve, it is found that the effective bandwidth ($RL < -10$ dB i.e. absorption $> 90\%$) is $9.18 - 12$ GHz which is highest among the three

morphologies and covers almost the whole X-band. Here, excellent impedance matching with free space, with moderate dielectric and magnetic loss contributes towards optimization of RL and effective bandwidth for NHS.

Further, shielding efficiency (SE) is studied for all the samples in Fig. 4.5(b), which is another evidence for wave absorption properties [18]. Total shielding efficiency is estimated as the sum of the contribution due to reflection (SE_R) and absorption shielding (SE_A) using the equation,

$$SE(total) = (SE_A + SE_R) = -20\log|S_{21}| \quad 4.3$$

where S_{21} is reverse transmission co-efficient. SE_{Total} is ~ -11 dB for NHS which is lowest in comparison with other samples supports the RL study. This increase in RL and SE value in NHS is also correlated to its morphology. Reflections from outer shell as well as multiple internal reflections in the hollow core of porous NHS traps EM wave in it increase the total propagation path in the composite which in turn enhances wave attenuation. NFO NHS with great EM impedance matching and low thickness, synthesis cost, proper amount of loss, high interfacial area, hollow cavity and strong cationic interaction, is an attractive candidate for microwave absorption and also suitable for applications in high-frequency devices.

4.4 Conclusion

In summary, as-synthesized $NiFe_2O_4$ nano hollow spheres exhibit strong EM absorption properties ($RL < -10$ dB) in the 9.1−12 GHz range for an absorber thickness of 2 mm and an optimal RL (− 59.2 dB) at 11.7 GHz. Also a comparative RL and SE study in widely used X-band frequency region is shown for NFO NHS with its nano particle ($RL \sim -51.9$ dB at 11.6 GHz) and bulk ($RL \sim -18.2$ dB at 9.96 GHz) counterpart. Natural or exchange resonance peak is not found in either permittivity or permeability data. The excellent absorption properties are mainly associated with transmission of EM wave because of perfect impedance matching in the microstructure with free space, high dielectric loss arising from polarization in large interfacial area and cationic interaction,

moderate dynamic magnetic loss as well as with the wave attenuation through multiple internal reflections in hollow core of NHS. On the contrary, solid spherical NFO NPs and also NFO Bulk with less effective surface area have lower *RL* and *SE* with respect to NHS in 8−12 GHz. With the hollow interior, NHS has lower density than bulk one, makes it a light weight absorbing filler material. Hence, NFO NHS seems interesting towards its application as mass efficient and broadband microwave absorbing materials.

References

[1] Y. Qing, W. Zhou, F. Luo, and D. Zhu, J. Magn. Magn. Mater. 321, 25 (2009).

[2] Z. Yang, Z. Li, Y. Yang, and Z. J. Xu, ACS Appl. Mater. Interfaces 6, 21911 (2014).

[3] M. Mehdipour and H. Shokrollahi, J. Appl. Phys. 114, 43906 (2013).

[4] X. G. Liu, D. Y. Geng, H. Meng, P. J. Shang, and Z. D. Zhang, Appl. Phys. Lett. 92, 173117 (2008).

[5] M. Han, X. Yin, L. Kong, M. Li, W. Duan, L. Zhang, and L. Cheng, J. Mater. Chem. A 2, 16403 (2014).

[6] Y. Ding, Q. Liao, S. Liu, H. Guo, Y. Sun, G. Zhang, and Y. Zhang, Sci. Rep. 6, 32381 (2016).

[7] F. Wang, J. Liu, J. Kong, Z. Zhang, X. Wang, M. Itoh, and K. Machida, J. Mater. Chem. 21, 4314 (2011).

[8] P. Chen, R. K. Li, Y. Gu, Y. Shi, and R. X. Wu, J. Magn. Magn. Mater. 349, 259 (2014).

[9] Y. Huang, Q. Qi, H. Pan, X. Lei, and X. Liu, J. Mater. Sci. Mater. Electron. 27, 9577 (2016).

[10] W. Zhu, L. Wang, R. Zhao, J. Ren, G. Lu, and Y. Wang, Nanoscale 3, 2862 (2011).

[11] N. N. Ali, R. Al-Qassar Bani Al-Marjeh, Y. Atassi, A. Salloum, A. Malki, and M. Jafarian, J. Magn. Magn. Mater. 453, 53 (2018).

[12] A. T. Raghavender and K. M. Jadhav, Bull. Mater. Sci. 32, 575 (2009).

[13] C.-Y. Wen, H.-Y. Xie, Z.-L. Zhang, L.-L. Wu, J. Hu, M. Tang, M. Wu, and D.-W. Pang, Nanoscale 8, 12406 (2016).

[14] J. S. An, W. J. Han, and H. J. Choi, Colloids Surfaces A Physicochem. Eng. Asp. 535, 16 (2017).

[15] B. Guo, K. Yu, H. Li, H. Song, Y. Zhang, X. Lei, H. Fu, Y. Tan, and Z. Zhu, ACS Appl. Mater. Interfaces 8, 5517 (2016).

[16] Q. Wang, Y. Zhu, J. Xue, X. Zhao, Z. Guo, and C. Wang, ACS Appl. Mater. Interfaces 8, 17226

(2016).

[17] C. C. Li, Q. H. Li, L. B. Chen, and T. H. Wang, ACS Appl. Mater. Interfaces 4, 1233 (2012).

[18] R. Panigrahi and S. K. Srivastava, Sci. Rep. 5, 7638 (2015).

[19] Z. Li, M. Ye, A. Han, and H. Du, J. Mater. Sci. Mater. Electron. 27, 1031 (2016).

[20] L. Wang, Y. Huang, X. Sun, H. Huang, P. Liu, M. Zong, and Y. Wang, Nanoscale 6, 3157 (2014).

[21] S. S. Seyyed Afghahi, M. Jafarian, M. Salehi, and Y. Atassi, J. Magn. Magn. Mater. 421, 340 (2017).

[22] P. Liu, Y. Huang, J. Yan, and Y. Zhao, J. Mater. Chem. C 4, 6362 (2016).

[23] P. Liu, Y. Huang, J. Yan, Y. Yang, and Y. Zhao, ACS Appl. Mater. Interfaces 8, 5536 (2016).

[24] P. Liu, Y. Zhang, J. Yan, Y. Huang, L. Xia, and Z. Guang, Chem. Eng. J. 368, 285 (2019).

[25] K. Khan, J. Supercond. Nov. Magn. 27, 453 (2014).

[26] J. Liu, R. Che, H. Chen, F. Zhang, F. Xia, Q. Wu, and M. Wang, Small 8, 1214 (2012).

[27] D. Mandal, M. Alam, and K. Mandal, Phys. B Condens. Matter 554, 51 (2019).

[28] M. Mandal Goswami, Sci. Rep. 6, 35721 (2016).

[29] J. Hölscher, H. L. Andersen, M. Saura-Múzquiz, P. G. Garbus, and M. Christensen, CrystEngComm 22, 515 (2020).

[30] K. Vasundhara, S. N. Achary, S. K. Deshpande, P. D. Babu, S. S. Meena, and A. K. Tyagi, J. Appl. Phys. 113, 194101 (2013).

[31] T. L. Gilbert, IEEE Trans. Magn. 40, 3443 (2004).

[32] J. Luo, Y. Zuo, P. Shen, Z. Yan, and K. Zhang, RSC Adv. 7, 36433 (2017).

[33] G. Wang, X. Peng, L. Yu, G. Wan, S. Lin, and Y. Qin, J. Mater. Chem. A Mater. Energy Sustain. 3, 2734 (2015).

[34] B. Wang, J. Wei, Y. Yang, T. Wang, and F. Li, J. Magn. Magn. Mater. 323, 1101 (2011).

[35] B. Wang, J. Wei, Y. Yang, T. Wang, and F. Li, J. Magn. Magn. Mater. 323, 1101 (2011).

Chapter 5

Structural, Magnetic and Dielectric Properties of TFe_2O_4 (T= Mn, Fe, Co, Ni, Cu and Zn) Nano-Hollow Spheres

This chapter contains synthesis of nano-hollow spheres of transition metal based spinel ferrites with different divalent cations (TFe_2O_4, T= Mn, Fe, Co, Ni, Cu and Zn) and a thorough comparative investigation of their structural, magnetic and dielectric properties.

5.1 Preamble

Ferrite materials have never-ending interest among the researchers and recently attention on them is significantly enhanced owing to their intensive uses not only as magnetic materials but also in dye degradation [1], energy saving materials [2], ferro-fluids [3,4], bio-medical applications [5] and spintronics [6]. From designing high-frequency devices [7] to meta-material [8] and electro-magnetic wave absorbers [9], strong presence of ferrites are always witnessed due to their significant properties such as high saturation magnetization (M_S), Curie temperature (T_C) and resistivity, better chemical stability, low cost and non-toxicity. Among the various ferrites, those with spinel structures having formula TFe_2O_4 (T= transition metal ion) are found to be more versatile as T can be any of the divalent cations such as T= Mn^{+2}, Fe^{+2}, Co^{+2}, Ni^{+2}, Cu^{+2}, Zn^{+2} etc.

Depending on octahedral site preference energy (OSPE) from crystal field theory, the spinel ferrites can be classified into normal and inverse [10]. The change in cation distribution among tetrahedral (A) and octahedral (B) sites can affect their structural properties which in turn vary their magnetic and dielectric properties [11]. For instance, Ramana et al. [12] and Datt et al. [13] analyzed the variation of dielectric and magnetic properties in $CoFe_2O_4$ from structural modification due to magnetic and non-magnetic cation doping. Hou et al. [14] studied the same theoretically using first principle calculation. Tuning of magnetic and electric properties in Fe_3O_4 nano-structures with domain structure and size was discussed by Sarkar et al. [15]. Though $ZnFe_2O_4$ is supposed to be a normal spinel, with reduction of grain size, their nanoparticles (NPs) are found to transform from normal to inverse as well as from anti-ferromagnetic to ferrimagnetic [10,16]. Cation ordering and exchange interaction calculations for $MnFe_2O_4$ was carefully discussed from theoretical density functional theorem and experimental studies [17–19]. Magnetic and dielectric properties in $CuFe_2O_4$ NPs and bulk $NiFe_2O_4$ were investigated in detail to show their potential in various applications [20–22].

Till date, several morphologies of ferrites such as Nanoparticles (NPs), Nano-rods, Nano-flowers, Nano-hollow spheres (NHSs) and so on are investigated, since nanostructures bear various unique properties than their bulk counterparts. Among them, NHSs are found to show some excellent qualities such as better stability, enhanced magnetic and dielectric properties due to their larger surface area, lower density, size and weight efficiency for their hollow core etc. [23–27]. Moreover the hollow core may act as a nano-container for capturing drugs [28]. The repeated internal reflections in hollow core enhances their applicability as an efficient microwave absorbers [1,9]. By varying the synthesis parameters, this particular morphology of ferrites can be easily tuned to different sizes and shell thicknesses which can also govern their magnetic and electric properties.

From our previous study, NHSs are found to have better M_S and permittivity, appropriate H_C and high reflection loss compared to their NPs and bulk counterparts [9,29]. Therefore, in this present report, detail studies on structural, magnetic and dielectric properties of TFe_2O_4 (T= Mn, Fe, Co, Ni, Cu and Zn) nano-hollow spheres are carried out varying their compositions. The morphological analysis evidences the samples to be NHSs of almost similar sizes. These properties are found to largely depend on different divalent cation placements in the ferrite structures. Coercivity of TFe_2O_4 samples are observed to vary from ~ 576 Oe (T= Co) to ~ 116 Oe (T= Ni) and saturation magnetization, from ~ 73.6 emu/g (T= Fe) to ~ 53.6 emu/g (T= Mn), discussed in terms of anisotropy, super-exchange interaction and crystallite size of the materials. Variation of dielectric properties such as permittivity, dielectric loss and ac conductivity of these NHSs within frequency range 10 Hz -5.5 MHz at ~ 300 K are explained on the basis of Maxwell-Wagner two layer model for space charge and polaron hopping from Fe^{3+} to Fe^{2+} as well as T^{2+} to T^{3+} ions at tetrahedral (A) and octahedral (B) sites. Analysis of dielectric relaxation mechanism ensures it as modified-Debye type and Jonscher's power law displays ac conduction mechanism for TFe_2O_4 NHSs. Cole-Cole plots are fitted with equivalent circuit to understand the effect of resistive grain boundary and conductive grains with frequency. This study on tunable dielectric and magnetic properties with substitution of different cations provides a map

to select an efficient and light-weight material for applications from high-frequency devices to bio-medical field.

5.2 Experimental

5.2.1 Synthesis Procedure

TFe_2O_4 (T= Mn, Fe, Co, Ni, Cu and Zn) NHSs are synthesized by one-pot template-free solvothermal process using oleylamine as capping agent. Precursors, TCl_2, $6H_2O$ and $FeCl_3$, $6H_2O$ are taken in 1:2 molar weight ratios whereas for Fe_3O_4 synthesis, only $FeCl_3$, $6H_2O$ is used. Ethylene Glycol (EG) and Ethyl Alcohol (EtOH) are taken in 2:1 ratio as solvents and Urea as reducing agent. Taking all the components in a 100 ml beaker, 1ml oleylamine is added while stirring it. The clear homogeneous solution, after 30 min of stirring, is heated in a 50 ml Teflon lined stainless steel autoclave at 200°C for 24 h in an oven. Then the as-prepared TFe_2O_4 NHSs are washed by EtOH and distilled water for few times, collected through magnetic separation and dried by heating at 60°C for ~ 30 min. During the reaction, urea helps to precipitate T^{2+} and Fe^{3+} ions from their chloride salts to their corresponding hydroxides and after the heat treatment, TFe_2O_4 phase is developed. For Fe_3O_4, EG partially reduces Fe^{3+} ions to Fe^{2+}. The anticipated mechanism related to the synthesis of NHS is considered as Ostwald ripening which involves a gradual re-crystallization of particles from smaller to larger ones to reduce the surface free energy [30]. With further thermal and pressure treatment, the clusters assembled into hollow spheres with the existence of gas bubbles formed by urea under the effect of oleylamine to ensure maximum stability of the spheres [31].

Chemicals, having purity of at least ~ 98%, were brought from Sigma-Aldrich for the above preparation.

5.2.2 Characterizations

The structural phase and parameters of as-prepared TFe_2O_4 NHSs are studied by powder X-ray diffraction (XRD) using PANalytical X'Pert PRO equipped with Cu K_α radiation (~ 1.54 Å). The FTIR measurements are performed using a JASCO FTIR 6300 spectrometer in transmission mode in the wave number range from 400 to 4000 cm^{-1} to view the vibrational modes of T-O bonds. A FEI QUANTA FEG 250 field-emission scanning electron microscope (FESEM) (0.2-30 kV) and a FEG high-resolution transmission electron microscope (HRTEM) (80-200 kV) are used to study the size and morphology of NHSs. The Energy-dispersive X-ray (EDX) spectrum is recorded for elemental analysis of the NHSs. All the relevant magnetic measurements are carried out using a Vibrating Sample Magnetometer (VSM) (Lake Shore). Frequency dependent dielectric properties of NHSs are measured using NF ZM2376 LCR meter and the powder samples are pelletized using Riken Pressure Gauge with a pressure of 25 MPa.

5.3 Results and Discussions

5.3.1 Structure and Morphology

The XRD plots of TFe_2O_4 [TFO, T= Mn, Fe, Co, Ni, Cu and Zn] NHSs with Rietveld profile refinement using FullProf suite are displayed in Fig. 5.1. The peak shape is described as 'Thompson-Cox-Hastings pseudo-Voigt*Axial divergence asymmetry' formulation whereas scale factors, cell, FWHM, shape parameters and atomic positions with respective occupancies are refined. These patterns confirm the single phase spinel face centered cubic structure within resolution of XRD measurement as reported in the literature (JCPDS file no. 65-1123, 19-0629, 22-1086, 10-0325, 34-0425, and 89-1010 for [T= Mn, Fe, Co, Ni, Cu, and Zn] respectively). Fig. 5.2(a) shows position of the (311) peak and change in peak width due to different cation placement in A and B sites and different crystallite sizes of ferrites respectively. Average crystallite sizes (D) (shown in Fig. 5.2(b)) as well as lattice strains (listed in Table 5.1) are calculated from the XRD peaks using Debye-Scherrer equation, $D = \frac{k.\lambda}{\beta \cos \theta}$, where k is the Scherrer constant (here ~ 0.94), λ, the working wave length, β, the FWHM of the selected peak and θ, the

XRD peak angle. Lattice constant (*a*), estimated from XRD pattern using Bragg's law is plotted in Fig. 5.2(c).

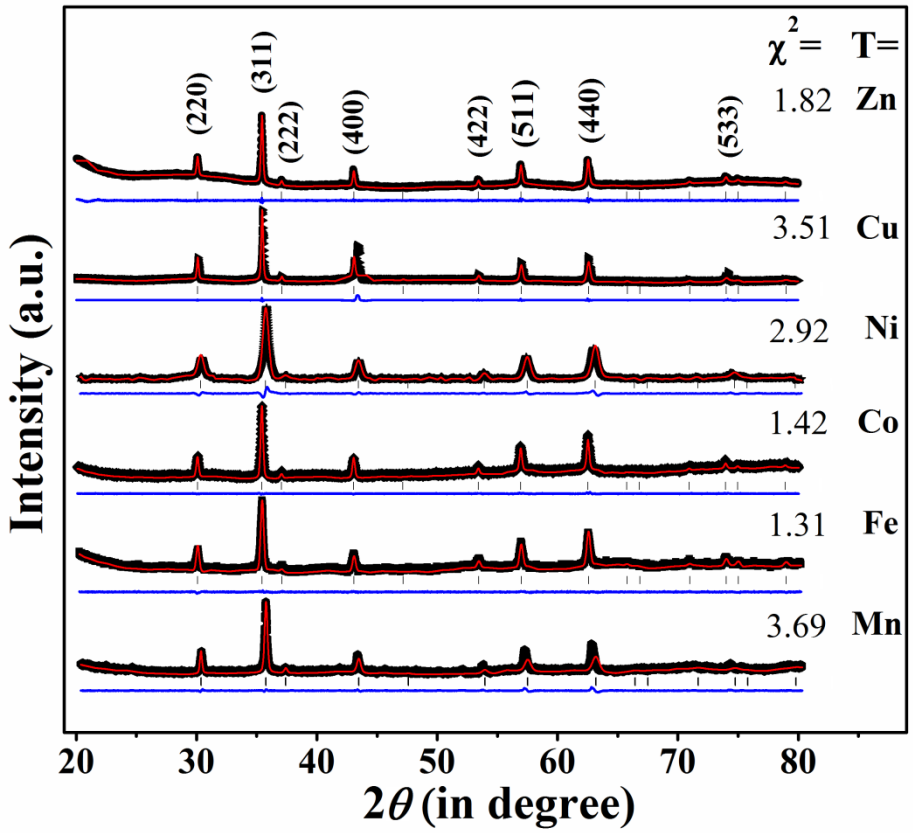

Figure 5.1. X-Ray diffraction plots for all the six sample sets TFe_2O_4 [T= Mn, Fe, Co, Ni, Cu, Zn] nano-hollow spheres

The spinel structure of the ferrite NHSs depends on crystal field stabilization energy (CFSE) of the cations present in the system as well as on their ionic radii [10,32]. The higher value of CFSE of constituent cations decides their preference for higher co-ordination site i.e. B-site and accordingly Fe_3O_4, $CoFe_2O_4$, $NiFe_2O_4$ and $CuFe_2O_4$ are of inverse spinel structure [33]. However, in $ZnFe_2O_4$, Zn^{2+} with d^0 configuration and in $MnFe_2O_4$, both cations Fe^{3+} and Mn^{2+} with states d^5 and similar CFSE, have no specific preference of sites. Therefore $MnFe_2O_4$ and $ZnFe_2O_4$ have possibilities of forming normal, inverse or mixed spinel structure. The (311) peak in Fig. 5.2(a) shifts towards left with the increase in cationic radii (*r*) in B-site, which also indicates enhancement in

lattice constant (plotted in Fig. 5.2(c)). The highest value of '*a*' is ~ 8.393 Å for FeFO (Fe^{2+} with $r = 0.77$ Å) and lowest in MnFO (Mn^{2+} with $r = 0.67$ Å) where '*a*' is ~ 8.343 Å. Crystallite size (*D*) of NHSs significantly depends on the size of nano-hollow spheres (Fig. 6.2(b)). Here ZnFO NHS, with comparatively larger size (~ 314 nm), has $D \sim 47.4$ nm and for NiFO (size ~ 223 nm), *D* is ~ 22.1nm.

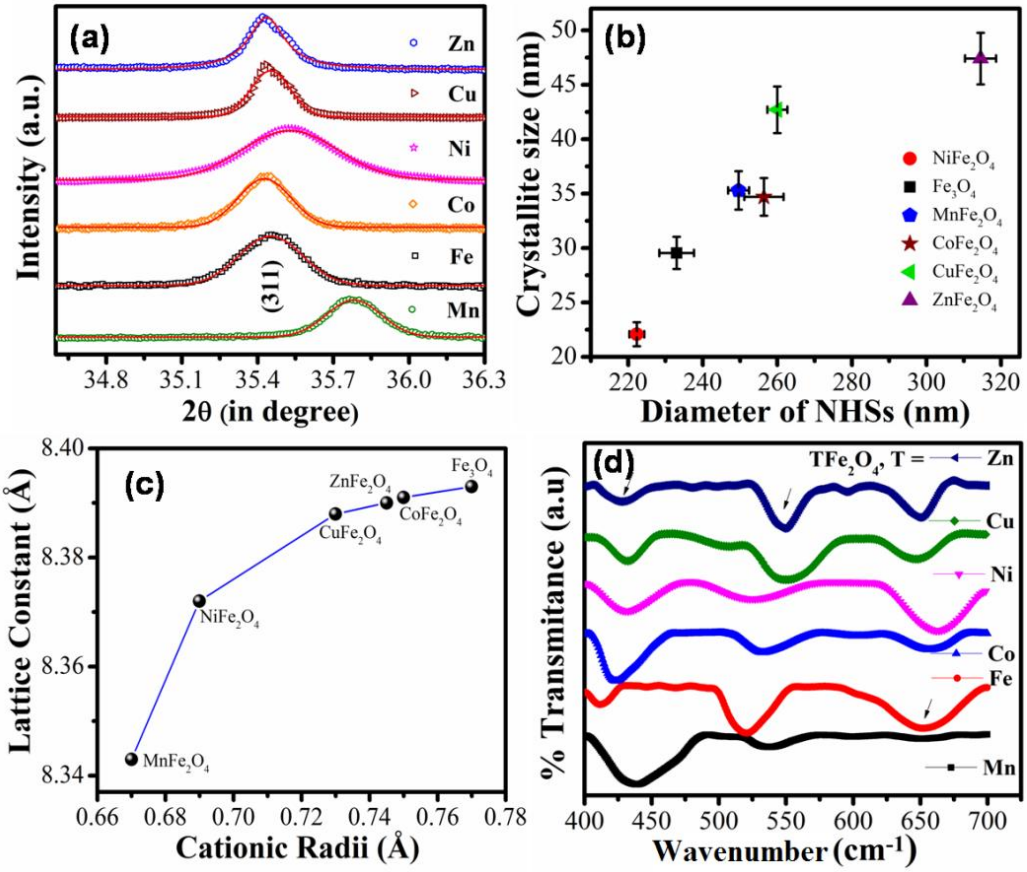

Figure 5.2. (a) Enlarged XRD peak (311) for TFe_2O_4 samples (b) Variation of crystallite size with diameter of NHSs (c) Lattice constant vs. ionic radii of divalent cations (d) FTIR spectra for TFe_2O_4 samples

The FTIR spectra within the range 400-700 cm^{-1} are focused here in Fig. 5.2(d) because the metal-oxygen bond peaks are prominent in this wavelength region. The peaks around ~ 440 cm^{-1}, ~ 535 cm^{-1} and ~ 650 cm^{-1} originate from T-O bond vibrations, Fe-O bond bending in B-site and Fe-O bond stretching from A-site respectively [34]. With

increasing T-O bond length which depends on the ionic radii of T^{2+}, the peaks ~ 440 cm^{-1} are found to (red) shift towards lower wavenumber region [35].

The morphologies of as-prepared ferrite samples, shown in Fig. 5.3, confirm the successful synthesis of TFe_2O_4 NHSs with uniform size distribution (inset: Fig. 5.3). The estimated average diameters and shell thickness of NHSs are respectively (a) 250±3 nm, 71±3 nm for MnFO (b) 233±5 nm, 60±2 nm for FeFO (c) 256±5 nm, 70±3 nm for CoFO (d) 223±2 nm, 55±2 nm for NiFO (e) 260±3 nm, 78±3 nm for CuFO and (f) 314±4 nm, 86±3 nm for ZnFO. Growth and re-crystallization of TFe_2O_4 NHSs depend on the reaction rate which varies with their respective precursor chloride salts, leading to slightly different sizes of NHSs whereas external parameters are kept same during synthesis.

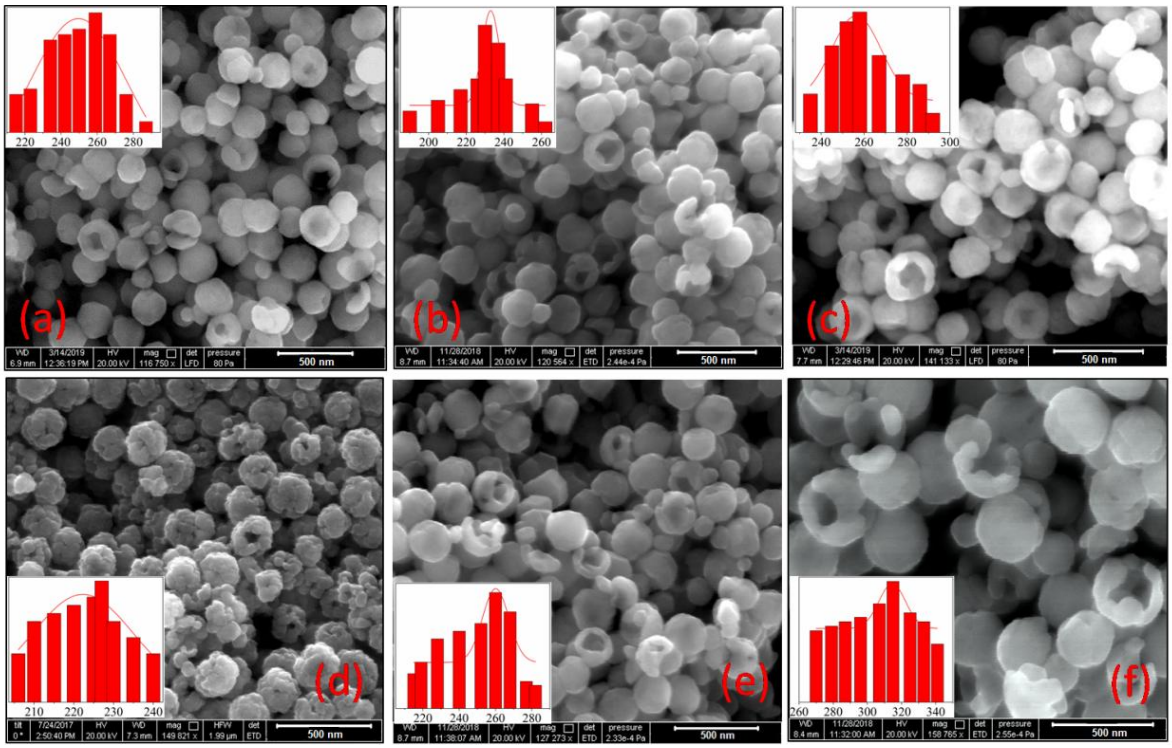

Figure 5.3. FESEM micrographs and corresponding size distribution graphs for all samples T-ferrite (a) T= Mn (b) T= Fe (c) T= Co (d) T= Ni (e) T= Cu (f) T= Zn

The contrast between bright core and dark shells in TEM micrographs (shown in Fig. 5.4(a)-5.4(f)) also confirms the formation of TFe_2O_4 nano-hollow spheres. A

representative EDX spectrum for $MnFe_2O_4$ in Fig. 5.4(g) validates the presence of constituent elements; Mn, Fe, and O in the sample. Single crystalline nature of the sample is observed from bright spots in SAED pattern (inset of Fig. 5.4(g)) and separation between the parallel diffraction planes (0.3 nm for (220) and 0.26 nm for (311) planes) matches well with the XRD results of $MnFe_2O_4$. A line scanned EDX spectrometry is performed across diameter of one NHS, shown by an orange line in Fig. 5.4(h). Fig. 5.4(i)-5.4(k) show the EDX line scanning profile of Mn, Fe, and O, respectively that visualizes the hollow core of size ~ 100 nm and shell width of ~ 70 nm.

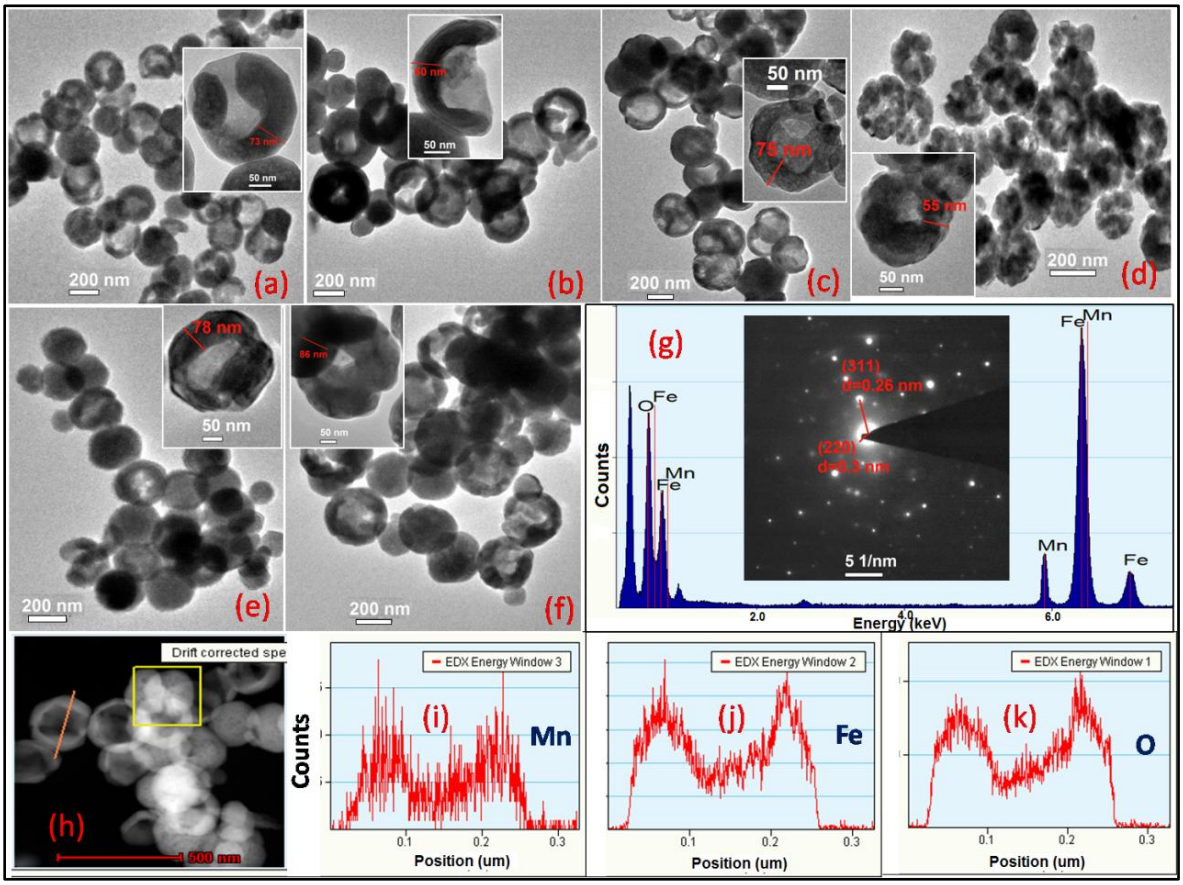

Figure 5.4. TEM micrographs for all T-ferrite NHSs, T= (a) Mn (b) Fe (c) Co (d) Ni (e) Cu and (f) Zn; inset: High magnification TEM micrographs measuring shell widths of NHSs (g) EDX spectra shows components of MnFO; inset: SAED pattern of it showing its crystallinity (h) EDX Line Mapping across the orange line; line mapping spectra shown for (i) Mn (j) Fe (k) O

5.3.2 Magnetic Properties

Magnetization (*M*) vs. Temperature (*T*) studies are performed for NHSs in presence of 100 Oe field within the temperature region of 80 K - 400 K during both zero field cooled (ZFC) and field cooled (FC) mode and are shown in Fig. 5.5. The separation between FC and ZFC curves at low *T* (~ 80 K) is inversely related to magneto-crystalline anisotropy energy barrier [29]. For $CoFe_2O_4$, as this gap is lowest, anisotropy in it is maximum which is consistant with outcomes of Fig. 5.6(a) and 5.6(b). From *M-T* curves, the samples are found to exist in ferrimagnetic region for the studied temperature regime. Moreover, close observation to ZFC *M-T* curves in Fig. 5.5(b), 5.5(e) and 5.5(f) shows that Fe_3O_4, $CuFe_2O_4$ and $ZnFe_2O_4$ NHSs exhibit a phase transition at ~ 110 K, 114 K and 116 K respectively. For Fe_3O_4, it resembles well-known Verwey transition which is normally visible at ~ 120 K for bulk Fe_3O_4 [15]. Verwey like transition is possibly observed due to presence of Fe^{2+} ions caused by cation vacancy in NHSs of $CuFe_2O_4$ and $ZnFe_2O_4$ [36,37].

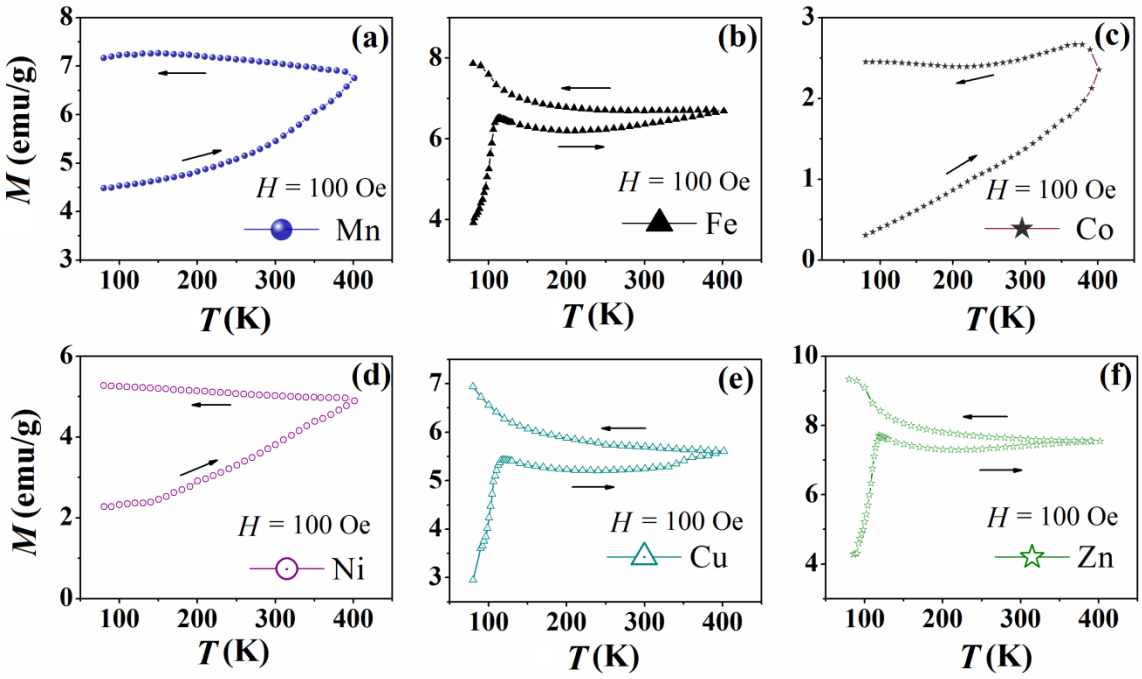

Figure 5.5. *M-T* plots (ZFC an FC) at 100 Oe magnetic field for TFe_2O_4 NHSs; (a) T= Mn (b) T= Fe (c) T= Co (d) T= Ni (e) T= Cu (f) T= Zn

Field dependent magnetization (M vs. H) curves are carried out with a maximum applied field of 14 kOe within temperature range 100 K $\leq T \leq$ 400 K. Fig. 5.6(a) and 5.6(b) illustrate hysteresis loops at 300 K and 100 K respectively. The studied ferrites excluding $CoFe_2O_4$, reveal their soft ferrimagnetic nature. At room temperature (~ 300 K), the maximum value of saturation magnetization (M_S) is obtained for Fe_3O_4 NHS ~ 73.6 emu/g (~ 3.3 μ_B/f.u.) and lowest one for $MnFe_2O_4$ NHS ~ 53.6 emu/g (~ 2.4 μ_B/f.u.). Both coercivity (H_C) and remanent magnetization (M_R) at 300 and 100 K are plotted in the insets of Fig. 5.6(a) and 5.6(b) respectively. Maximum H_C at 300 K is obtained for $CoFe_2O_4$ (~ 576 Oe) whereas $NiFe_2O_4$ shows minimum value (~ 116 Oe). On lowering the temperature from 400 K to 100 K, H_C, M_R and M_S values of NHSs enhance as a result of higher magnetic anisotropy and reduced thermal fluctuation of spins with decreasing temperature. Here several parameters like magnetic anisotropy, domain structure, crystallite size, cation distribution and exchange interaction in microstructure are responsible for varying the magnetic properties of investigated TFe_2O_4 NHSs [15,33,38].

Table 5.1. Lattice strain of TFe_2O_4 NHSs, anisotropy constant (K), Bloch's constant (B) (from Eqn. 5.2), dielectric relaxation time (τ) and spreading factor (α) (from Eqn. 5.6), power factor to frequency (s) (from Eqn. 5.7)

TFe_2O_4 NHSs, T=	Lattice Strain ($\times 10^{-3}$)	K ($\times 10^5$) (J/m^3)	B ($\times 10^{-5}$) (K$^{-3/2}$)	τ ($\times 10^{-4}$) (s)	α	s
Mn	3.6±0.03	1.55±0.02	2.35±0.07	1.3±0.1	0.52±0.06	0.18±0.008
Fe	4.0±0.04	1.39±0.02	2.23±0.06	2.86±0.2	0.43±0.03	0.07±0.002
Co	3.3±0.03	4.52±0.04	0.24±0.01	21±0.2	0.16±0.01	0.1±0.003
Ni	4.6±0.04	1±0.02	1.7±0.1	42.7±0.4	0.02±0.01	0.13±0.007
Cu	2.8±0.03	1.4±0.01	2.32±0.05	22±0.2	0.23±0.03	0.24±0.008
Zn	3.0±0.03	1.34±0.02	2.34±0.07	1.2±0.07	0.52±0.03	0.06±0.003

The magnetic anisotropy for the samples is calculated using the law of approach to saturation is given by

$$M(H) = M_S\left(1 - \frac{0.07619\,K^2}{H^2\,{M_S}^2} - \frac{0.0384\,K^3}{H^3\,{M_S}^3}\right) \quad 5.1$$

where *M(H)*, the magnetization at an applied field of *H*, M_S, the saturation magnetization, and *K*, the cubic magneto-crystalline anisotropy constant (listed in Table 6.1) [13,38].

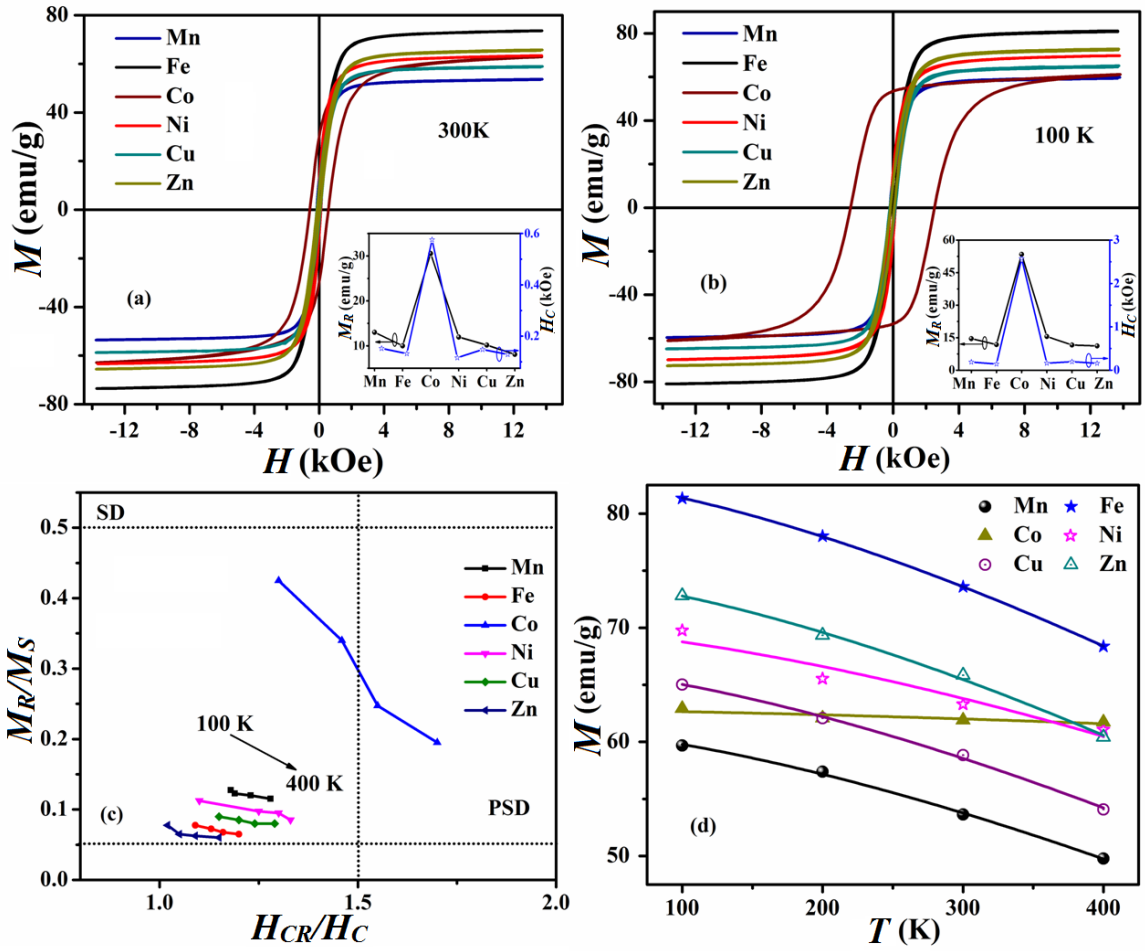

Figure 5.6. *M-H* plots for TFe_2O_4 NHSs in (a) 300 K and (b) 100 K; corresponding insets showing variation of H_C and M_S with Temperature (c) Day Plots and (d) Fitting of Bloch's equation for all ferrite nano-hollow spheres

The highest value of K ($\sim 4.52\times10^5$ J/m^3) in $CoFe_2O_4$ leads to maximum coercivity in it. In Fig. 5.6(c), the possible domain structures of the TFe_2O_4 NHSs are examined in terms of Day plot which is a graphical mapping of M_R/M_S vs. H_{cr}/H_C, where H_{cr} is the field under which M-H loop shows remanence, $M_r = 0.5M_R$. Here the studied materials exist in between single domain (SD) to pseudo single domain (PSD) region for the considered temperature region, which is obvious for TFe_2O_4 NHSs with both small crystallite size (< 50 nm) and shell thickness (< 100 nm). NHSs saturate with magnetic field from SD vortex state through a PSD onion state and the need of higher field to saturate it with lowering temperature, make the curves shift towards SD region from 400 K to 100 K [23,39].

Temperature (T) dependence of M_S is plotted in Fig. 5.6(d) which follows Bloch's law for temperature well below T_C, where B is the Bloch constant (listed in Table 5.1).

$$M_S(T) = M_S(0)(1 - BT^{3/2}) \qquad 5.2$$

For $NiFe_2O_4$ NHS, at low T, there is a deviation from Bloch's law as magnons having larger wavelength than crystallite size ($D \sim 22$ nm for $NiFe_2O_4$) cannot be excited in it. Neel's sub-lattice model for ferrimagnets implies that the metal ions in A and B-sites are coupled ferromagnetically within each sub-lattice and antiferromagnetically between the two sub-lattices and this inter-lattice super-exchange interaction is inversely proportional to Bloch constant. $B \sim 0.24$ ($\times10^{-5}$ K$^{-3/2}$) is found to be lowest for $CoFe_2O_4$ resulting highest exchange interaction and hence higher anisotropy. The obtained value of M_S suggests $MnFe_2O_4$ NHS is possibly in mixed spinel structure [19] and also it has $B \sim 2.34$ ($\times10^{-5}$ K$^{-3/2}$) which can lead to comparatively lower M_S and H_C values in it [40,41].

5.3.3 Dielectric Properties

Dielectric properties of the ferrite NHSs are measured within a frequency (f) range of 10 Hz – 5.5 MHz at room temperature ($\sim$ 300 K) to get acquainted with their polarization, conduction and relaxation mechanism [12,21,29]. Real part of relative dielectric constant (ε'), originating from dipolar, ionic and electronic polarization while

the imaginary part (ε''), associated with the energy dissipation are obtained by measuring complex impedance ($Z= Z'-iZ''$) vs. phase (θ) data [29]. ε' vs. log(ω) [ω $(=2\pi f)$, angular frequency] curves are plotted in Fig. 5.7(a) where ε' is predominantly found to decrease with increasing frequency for the samples.

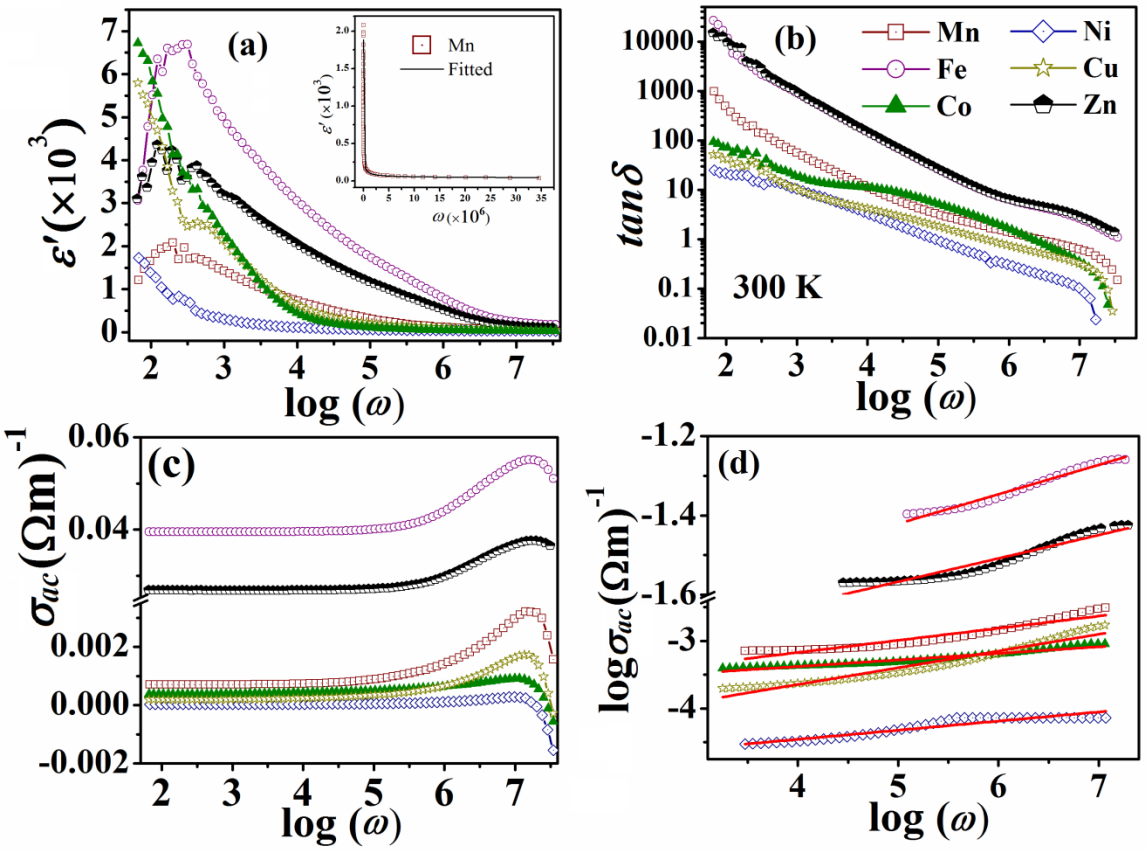

Figure 5.7. (a) Real part of dielectric constant (ε') (b) Dielectric loss tangent ($tan\ \delta$) and (c) Ac conductivity (σ_{ac}), versus frequency from 10 Hz to 5.5 MHz (d) fitting of σ_{ac} with Jonscher's Power law

The dielectric relaxation time (τ) and spreading factor (α) for each ferrite are obtained (listed in Table 5.1) by fitting the ε' *vs.* ω curves with modified Debye's equation,

$$\varepsilon' = \varepsilon'_{\infty} + \frac{(\varepsilon'_0 - \varepsilon'_{\infty})}{(1+(\omega\tau)^{(1-\alpha)})} \qquad 5.6$$

where ε'_{∞} and ε'_0 are the permittivity values at high and at low frequency

respectively [12]. The value of $\alpha \neq 0$ suggests more than one ions participating in this relaxation process resulting the process non-Debye type. Fig. 5.7(b) and 5.7(c) describe the dielectric loss ($tan\,\delta = \frac{\varepsilon''}{\varepsilon'}$), also related to energy dissipation and real part of ac conductivity ($\sigma_{ac} = \omega\varepsilon_0\varepsilon''$) respectively. '$tan\delta$' decays with increasing frequency whereas σ_{ac} remains constant till a specific frequency followed by an enhancement. Though σ_{ac} for the studied ferittes lie in semiconductor region, it tends towards metallic conductivity for Fe_3O_4 and $ZnFe_2O_4$ NHSs. Frequency and temperature as external parameters and internal factors such as microstructure, crystallite size and exchange interaction among cations have significant impact on dielectric properties [42]. The variation of ε', $tan\delta$ as well as σ_{ac} with frequency can be explained on the basis of Maxwell-Wagner (MW) two layer model for space charge and hopping of electrons named as polaron hopping between cations present in A-site and B-site through the following process: $T^{2+} + Fe^{3+} \leftrightarrow T^{3+} + Fe^{2+}$. Since, electron transfer between Fe^{3+} and Fe^{2+} dominates hole transfer between T^{2+} and T^{3+}, Fe^{2+}- Fe^{3+} pair acts as leading dipole.

According to this MW theory, ferrites are constituted with conducting larger grains (g) and insulating thinner grain boundaries (gb). When an external electric field is applied, that dipoles get accumulated (space charge) at the resistive gb producing large polarization and simultaneously high ε' at low frequencies. As $tan\delta$ occurs due to absorption of electrical energy during rotation and vibration of accumulated dipoles at gb, it is also high with higher polarization. Relaxation of dipoles is not possible above a sufficiently high f as dipoles could not comply with field at high f and lags behind. Above a certain frequency, dipoles acquire sufficient energy to cross the barrier potential and electron hopping starts to take place. This characteristic frequency varies inversely with the relaxation time (τ). Fe_3O_4 and $ZnFe_2O_4$ NHSs with comparatively smaller $\tau \sim 10^{-4}$ s can follow the ac electric field till much higher f. From such instance, conductive grain becomes active and σ_{ac} starts to grow.

Maximum ε' arises in $CoFe_2O_4$ at low frequency for higher exchange interaction in it which helps to achieve higher polarization also. On the other hand, minimum ε' is

observed in $NiFe_2O_4$ NHS due to its smaller crystallite size and hence higher gb impedance that causes restriction to movement of dipoles. The hump shown in ε' *vs.* $\log(\omega)$ curve (Fig. 5.7(a)) for Fe_3O_4 and $ZnFe_2O_4$ NHSs can be an effect from change in polarization mechanism that is from ionic to dipolar one. In Fig. 5.7(d), σ_{ac} vs. f plots are fitted with Jonscher's power law:

$$\sigma_{ac}(\omega, T) = \sigma_{dc}(T) + A\omega^{s}(T) \qquad 5.7$$

where, σ_{dc} is the dc conductivity of the material, A, the material dependent parameter and s, the power factor to ω (listed in Table 5.1). For ac mechanism of conduction, s varies within $0 < s < 1$. The lower s value for Fe_3O_4 and $ZnFe_2O_4$ suggests less ac and more dc like conduction and this supports the experimental results in Fig. 5.6.

Figure 5.8 displays the Cole-Cole plots (ρ'' *vs.* ρ'), for the samples fitted with equivalent circuit (Fig. 5.8(f): inset) corresponding to the Maxwell-Wagner grain (g) and grain boundary (gb) model. The arrows in Fig. 6.8 indicate increase in frequency and activation of gb to g effects occur with that.

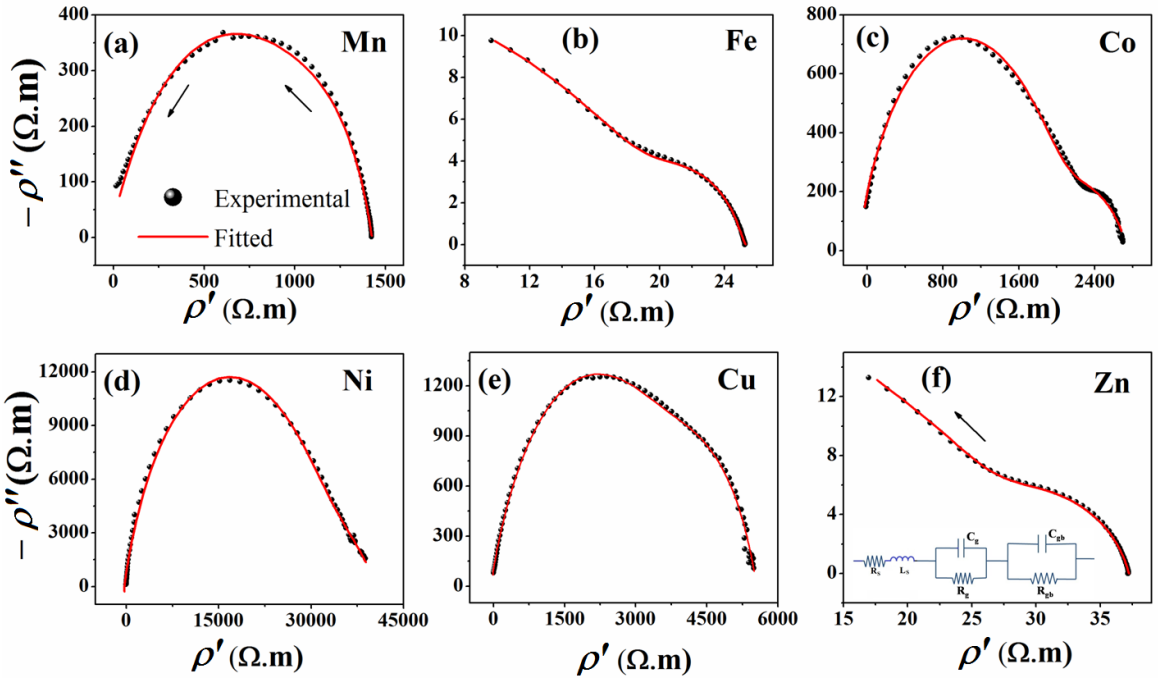

Figure 5.8. Cole-Cole Plots (-ρ''vs. ρ') for all ferrite samples: experimental and fitted; inset of (f): equivalent circuit for fitting

Table 5.2. R_{gb}, C_{gb}, R_g and C_g values for different ferrites

TFe_2O_4 NHSs, T=	R_{gb} (Ω)	C_{gb} (nF)	R_g (Ω)	C_g (μF)
Mn	1143±17.1	137±2	295.4±4.4	0.4±0.006
Fe	99.3±0.8	82.2±0.6	3.5±0.03	0.3±0.002
Co	2164±17	17.4±0.1	728.5±7	10.6±0.1
Ni	29661±216	7.2±0.04	11323±77	2.4±0.02
Cu	3809±26	83.2±0.58	1803±16	1.3±0.01
Zn	18.7±0.1	20.5±0.2	11±0.1	1±0.008

Here, the curves are not proper semi-circular arc and that corresponds to their non-Debye type relaxation of dipoles. The kink in each curve at different frequencies emphasizes the presence of grain effect along with the grain boundary one [43]. The resistive (R_g, R_{gb}) and capacitive (C_g, C_{gb}) components are obtained by fitting the Cole-Cole plots with the circuit in EC-lab software and the values are listed in Table 5.2. The R_S and L_S part of the circuit represents the contributions from leads and electrodes that come up at sufficiently high frequencies (> 5.5 MHz). The high value of grain boundary impedance (R_{gb}) in $NiFe_2O_4$ is the reason behind its low permittivity (Fig. 5.7(a)) whereas for Fe_3O_4 NHS, low value of R_{gb} ensures high ε in it.

5.4 Conclusion

In summary, TFe_2O_4 (T= Mn, Fe, Co, Ni, Cu, and Zn) NHSs are successfully synthesized and a detail study on their structural, magnetic and dielectric properties is presented here. Lattice constants and crystallite sizes are observed to enhance with increase in cationic radii and diameter of NHSs respectively. FTIR spectra depict T-O peaks shift towards lower wavenumber with increase in T^{2+} radii. Maximum H_C is found for $CoFe_2O_4$ NHS (~ 576 Oe) due to its highest magneto-crystalline anisotropy (K ~

4.52×10^5 J/m^3) and super-exchange interaction whereas maximum M_S is obtained for Fe_3O_4 NHS (~ 73.6 emu/g). Day plots describe the studied ferrites belong in pseudo single domain (PSD) to SD region within temperature region 100 K - 400 K. The variation of ε, $tan\delta$ and σ_{ac} with f at ~ 300 K for the ferrites are discussed through Maxwell-Wagner two-layer model and hopping of charges between Fe^{3+} to Fe^{2+} as well as T^{2+} to T^{3+} ions at A and B-sites. Analysis of dielectric relaxation mechanism ensures it as modified-Debye type and Jonscher's power law displays ac conduction mechanism for TFe_2O_4 NHSs. Resistive and capacitive components of conductive grain and resistive grain boundaries are obtained from equivalent circuit fitting over Cole-Cole plots where $NiFe_2O_4$ NHS with smaller crystallite size found to have higher R_{gb} and simultaneously lower ε. This study on TFe_2O_4 NHSs will be highly effective to select a promising material towards diverse applications from high-frequency devices to bio-medical field.

References

[1] S. Talukdar, D. Mandal, and K. Mandal, Chem. Phys. Lett. 672, (2017).

[2] J. Martinek, C. B. Musgrave, and A. W. Weimer, Science (80-.). 341, 540 (2013).

[3] M. H. Sousa, F. A. Tourinho, J. Depeyrot, G. J. da Silva, and M. C. F. L. Lara, J. Phys. Chem. B 105, 1168 (2001).

[4] J. S. An, W. J. Han, and H. J. Choi, Colloids Surfaces A Physicochem. Eng. Asp. 535, 16 (2017).

[5] I. Chakraborty, U. Saha, D. Mandal, S. Mukherjee, N. Joardar, S. P. Sinha Babu, G. Suresh Kumar, and K. Mandal, Phys. Chem. Chem. Phys. 21, 10726 (2019).

[6] M. S. Ansari, M. H. D. Othman, M. O. Ansari, S. Ansari, and M. Z. M. Yusop, J. Alloys Compd. 816, 152532 (2020).

[7] S. Sun, H. Zeng, D. B. Robinson, S. Raoux, P. M. Rice, S. X. Wang, and G. Li, J. Am. Chem. Soc. 126, 273 (2004).

[8] B. Gao, M. M. F. Yuen, and T. T. Ye, Sci. Rep. 7, 45108 (2017).

[9] D. Mandal, A. Gorai, and K. Mandal, J. Magn. Magn. Mater. 485, 43 (2019).

[10] H. L. Andersen, M. Saura-Múzquiz, C. Granados-Miralles, E. Canévet, N. Lock, and M. Christensen, Nanoscale 10, 14902 (2018).

[11] W. B. Cross, L. Afflcck, M. V Kuznetsov, I. P. Parkin, and Q. A. Pankhurst, J. Mater. Chem. 9, 2545 (1999).

[12] C. V. Ramana, Y. D. Kolekar, K. Kamala Bharathi, B. Sinha, and K. Ghosh, J. Appl. Phys. 114, 183907 (2013).

[13] G. Datt and A. C. Abhyankar, J. Appl. Phys. 122, 34102 (2017).

[14] Y. H. Hou, Y. J. Zhao, Z. W. Liu, H. Y. Yu, X. C. Zhong, W. Q. Qiu, D. C. Zeng, and L. S. Wen, J. Phys. D. Appl. Phys. 43, 445003 (2010).

[15] D. Sarkar, M. Mandal, and K. Mandal, J. Appl. Phys. 112, 64318 (2012).

[16] H. Ehrhardt, S. J. Campbell, and M. Hofmann, Scr. Mater. 48, 1141 (2003).

[17] J. R. Huang and C. Cheng, J. Appl. Phys. 113, (2013).

[18] X. Zuo, B. Barbiellini, and C. Vittoria, in *J. Magn. Magn. Mater.* (2004), pp. 306–311.

[19] K. Vamvakidis, M. Katsikini, D. Sakellari, E. C. Paloura, O. Kalogirou, and C. Dendrinou-Samara, Dalt. Trans. 43, 12754 (2014).

[20] V. Manikandan, A. Vanitha, E. R. Kumar, and J. Chandrasekaran, J. Magn. Magn. Mater. 432, 477 (2017).

[21] R. S. Yadav, I. Kuřitka, J. Vilcakova, J. Havlica, J. Masilko, L. Kalina, J. Tkacz, V. Enev, and M. Hajdúchová, J. Phys. Chem. Solids 107, 150 (2017).

[22] R. H. Kodama, A. E. Berkowitz, E. J. McNiff, Jr., and S. Foner, Phys. Rev. Lett. 77, 394 (1996).

[23] Q. Ye, Y. Kozuka, H. Yoshikawa, K. Awaga, S. Bandow, and S. Iijima, Phys. Rev. B 75, 224404 (2007).

[24] Z. Yang, Z. Li, Y. Yang, and Z. J. Xu, ACS Appl. Mater. Interfaces 6, 21911 (2014).

[25] B. Guo, K. Yu, H. Li, H. Song, Y. Zhang, X. Lei, H. Fu, Y. Tan, and Z. Zhu, ACS Appl. Mater. Interfaces 8, 5517 (2016).

[26] Q. Pan, Y. Ding, Z. Yan, Y. Cai, F. Zheng, Y. Huang, H. Wang, and Q. Li, J. Alloys Compd. 821, 153569 (2020).

[27] A. Yan, X. Liu, R. Yi, R. Shi, N. Zhang, and G. Qiu, J. Phys. Chem. C 112, 8558 (2008).

[28] P. Chen, B. Cui, X. Cui, W. Zhao, Y. Bu, and Y. Wang, J. Alloys Compd. 699, 526 (2017).

[29] D. Mandal, M. Alam, and K. Mandal, Phys. B Condens. Matter 554, 51 (2019).

[30] M. Mandal Goswami, Sci. Rep. 6, 35721 (2016).

[31] F. Wang, J. Liu, J. Kong, Z. Zhang, X. Wang, M. Itoh, and K. Machida, J. Mater. Chem. 21, 4314 (2011).

[32] E. Solano, C. Frontera, T. Puig, X. Obradors, S. Ricart, and J. Ros, J. Appl. Crystallogr. 47,

414 (2014).

[33] Z. Szotek, W. M. Temmerman, D. Ködderitzsch, A. Svane, L. Petit, and H. Winter, Phys. Rev. B 74, 174431 (2006).

[34] V. Rathod, A. V Anupama, R. V. Kumar, V. M. Jali, and B. Sahoo, Vib. Spectrosc. (2017).

[35] E. Z. Katsnelson, A. G. Karoza, L. A. Meleshchenko, V. V. Pankov, and B. G. Khavkin, Phys. Status Solidi 141, 599 (1987).

[36] K. Sarkar, R. Mondal, S. Dey, and S. Kumar, Phys. B Phys. Condens. Matter 412015 (2020).

[37] K. L. López Maldonado, L. Vazquez Zubiate, P. de la Presa, J. A. Matutes Aquino, and J. T. Elizalde Galindo, J. Appl. Phys. 115, 17C705 (2014).

[38] D. Mandal, M. M. Goswami, and K. Mandal, IEEE Trans. Magn. 54, 1 (2018).

[39] R. Day, M. Fuller, and V. A. Schmidt, Phys. Earth Planet. Inter. 13, 260 (1977).

[40] L. Patron, G. Marinescu, and I. Mindru, in *Dekker Encycl. Nanosci. Nanotechnology, Second Ed. - Six Vol. Set (Print Version)* (CRC Press, 2008), pp. 1968–1984.

[41] V. B. Barbeta, R. F. Jardim, P. K. Kiyohara, F. B. Effenberger, and L. M. Rossi, J. Appl. Phys. 107, 73913 (2010).

[42] K. M. Batoo and M. S. Ansari, Nanoscale Res. Lett. 7, 1 (2012).

[43] N. Ponpandian, P. Balaya, and A. Narayanasamy, J. Phys. Condens. Matter 14, 3221 (2002).

Chapter 6

Electromagnetic wave attenuation properties of MFe_2O_4 (M = Mn, Fe, Co, Ni, Cu, Zn) Nano-Hollow spheres

Dielectric, magnetic and microwave absorption properties are investigated in detail for transition metal based spinel ferrite (MFe_2O_4, M = Mn, Fe, Co, Ni, Cu and Zn) nano-hollow spheres in frequency range from 1 GHz to 20 GHz. $MnFe_2O_4$ NHS is observed to result in optimum electromagnetic (EM) wave absorption properties and further a thickness and filler concentration dependent study on EM wave absorption is performed in this chapter.

6.1 Preamble

With on-going rapid development of high-frequency communication devices, electromagnetic interference (EMI) or wave pollution is increasing rapidly which not only interrupts smooth operation of electronics but also endangers human health [1–3]. In this scenario, EM wave absorbing materials (EMA) are in serious need to shield the unwanted waves. For their tunable absorption bands, they are widely used in military and civil fields such as stealth technology, anti-radiation sheets and anechoic chambers [4–6]. In comparison to traditional EMA such as carbon-based materials with large dielectric loss and metal powders with significant magnetic loss, ferrites with combination of relatively better permittivity (ε) and permeability (μ) ensures wider bandwidth (BW), higher impedance matching and EM wave absorption [4–7].

Impedance matching, significant dielectric and magnetic loss are the key sources for a material to exhibit large microwave absorption with broad bandwidth [2,8]. Closer values of ε and μ can ensure better matching between impedances of free space and absorber. In addition, high ε and μ values lessen the required thickness (t) of the absorbing material making it size-efficient [9,10]. In this context, oxygen close-packed low-cost spinel ferrites with simple structure are highly suitable as the crucial parameters such as ε, μ and other related properties of these ferrites can be controlled and tuned easily [11–13]. Moreover, C-, X-, and Ku-bands are extensively used in radars and communication networks where ferrites play active roles [4]. Thermal and chemical stability, resistivity, ε and μ values of ferrites largely depend on their microstructure and inherent cations [11,14]. In order to tune the absorption properties, several techniques such as chemical doping, morphology control and hybridization of materials are introduced so far [4,14–17]. For instance; Liu et al. prepared yolk-shell Fe_3O_4@Mesoporus SiO_2 hetero-structures to enhance the reflection loss (RL) and absorption frequency range [17]. Graphene oxide functionalization [4] and Ni doping on $CoFe_2O_4$ [14] were performed to increase its EM attenuation. Size-dependent EMA properties of Fe_3O_4 nano-discs were investigated in order to achieve strong magnetic anisotropy, loss and hence absorption in it [15].

Preference of light-weight and size-efficient EMA materials influences researchers to focus on nano-structures and among those, nano-hollow spheres (NHS) are a new drift [2,18,19]. Though by definition, nanomaterials should have dimension ≤100 nm, NHS with size >100 nm also behave like nano because of their shell thickness less than 100 nm [20]. Their high M_S, large surface to volume ratio, low density, ability to withstand volume changes due to changes in temperature and pressure make them useful in wide varieties of applications [21–23]. Moreover, repeated internal reflections in their inner hollow core increases total path length of EM wave which enables more absorption [18,19,24]. Additionally, lower density of NHSs overcomes the drawbacks in practical usage of ferrites as EMA [2,19]. From our previous morphology dependent EMA study, NHSs are revealed as superior EMA compared to its solid and bulk counterparts [25]. Ferrite NHSs with their simple structure are comparable to other efficient but complex EMA heterostructures in terms of wave absorption properties [4,8,16]. Herein, almost same sized nano-hollow spheres of transition metal-based earth-abundant MFe_2O_4 (M = Mn, Fe, Co, Ni, Cu and Zn) materials are synthesized in facile solvothermal method and their EMA properties within widely-used frequency range of 1 - 20 GHz are examined in-detail. The divalent cation, M^{2+} [M = Mn, Co, Ni, Cu, Zn] substitution in Fe_3O_4 displays a clear enhancement of EM absorption properties compared to traditional magnetite where $MnFe_2O_4$ NHS is found to exhibit an optimal reflection loss (RL) of about −32.7 dB, total shielding efficiency (SE_{Total}) ~ −42 dB and a high attenuation constant (α) ~ 196 Np/m. Significant dielectric and magnetic loss, favorable impedance matching and multiple internal reflections in the hollow core of NHS contribute to enhancement in absorption properties. Interestingly, with increase in filler concentration (in epoxy resin matrix) from 0 wt% to 50 wt%, $MnFe_2O_4$ NHS shows a gradual increase in RL values and an excellent RL of about −45.6 dB at thickness ~ 4.2 mm is obtained for 50 wt% composite with a total effective bandwidth ($RL < -10$ dB i.e. absorption > 90%) of ~ 3.6 GHz. Moreover, analysis of quarter-wavelength model for best matching thickness (t_m) displays a good agreement between experimental and simulated t_m values. The overall results indicate that ferrites in the form of hollow structures are much more efficient than their bulk counterpart and optimized $MnFe_2O_4$

NHS is found to be most suitable for high-frequency applications as an efficient low-cost microwave absorber.

6.2 Experimental

6.2.1 Synthesis Procedure

MFe_2O_4 (M = Mn, Fe, Co, Ni, Cu and Zn) NHSs are synthesized by one-pot template-free solvothermal process using oleylamine as capping agent, as mentioned in Chapter 6 in detail [20,26]. Ostwald ripening is considered as proposed mechanism which involves a gradual growth and re-crystallization of particles to reduce the surface free energy [19,26]. These particles assembled into hollow spheres with soft-templating through the reaction under effect of oleylamine micelles [19,27].

6.2.2 Characterizations

X-ray diffraction (XRD) is carried out by PANalytical X'Pert PRO equipped with Cu K_α radiation to know the parent phase of as-prepared samples. A FEI QUANTA FEG 250 field-emission scanning electron microscope (FESEM) (0.2 - 30 kV) and a FEG high-resolution transmission electron microscope (HRTEM) (80 - 200 kV) are used to obtain the information about size and shape of NHSs. Magnetic measurements are performed using Vibrating Sample Magnetometer (Lake Shore Cryotronics) in a maximum applied field of 14 kOe. Microwave properties of the samples are measured using an Anritsu MS46122B Vector Network Analyzer (VNA) and a coaxial airline (Maury Microwaves-8043S6) within the frequency range of 1 - 20 GHz. The composite samples for microwave measurement are prepared by loading powder samples in different wt% s in Epoxy Resin matrix and molding this mixture precisely. The final composites are in toroidal shape with inner diameter (d) = 1.5 mm, outer d = 3.5 mm. Further analysis of EM wave attenuation parameters from measured 2-port scattering (S)-parameters is performed by polynomial fit model of Nicholson-Ross-Weir (NRW) algorithm based on transmission line technique [28].

6.3 Results and Discussion

6.3.1 Structure and Morphology

The structure and morphology part of MFe_2O_4 (M = Mn, Fe, Co, Ni, Cu, and Zn) NHSs are elaborately described in the previous chapter. Therefore, in the chapter, only brief related information is discussed.

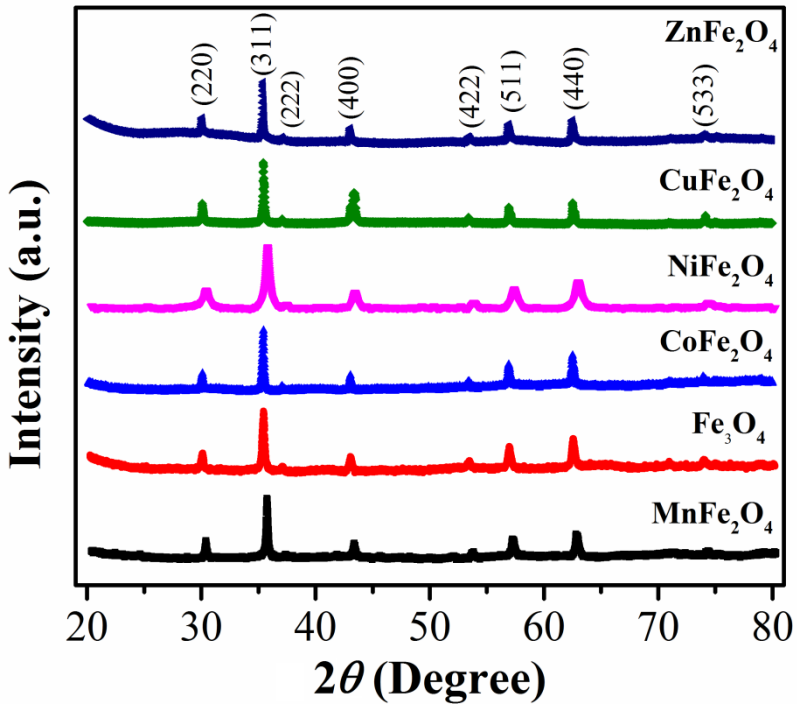

Figure 6.1. X-Ray diffraction plots at ~ 300K for all the six sample sets

X-ray diffraction patterns of all the studied samples, shown in Fig. 6.1, confirm single phase spinel face-centered cubic structure as reported in the literature (JCPDS file no. 65-1123, 19-0629, 22-1086, 10-0325, 34-0425, and 89-1010 for [M = Mn, Fe, Co, Ni, Cu, and Zn] respectively) [2,14,29,30]. Lattice constants (*a*) and crystallite sizes (*D*) for the ferrites are estimated from XRD patterns and listed in Table 7.1. Here, *a* value is found to increase with cationic radii for different cation substitution whereas *D* increases with larger diameters of NHSs.

FESEM and TEM micrographs, displayed in Fig. 6.2, clearly illustrate nano-hollow spheres (NHSs) of MFe_2O_4 with cavity inside. The estimated average diameters and shell thicknesses of NHSs are listed in Table 6.1. NHSs possess lower density than their bulk counterpart due to internal hollow core, hence they are light-weight and much convenient for practical applications [25].

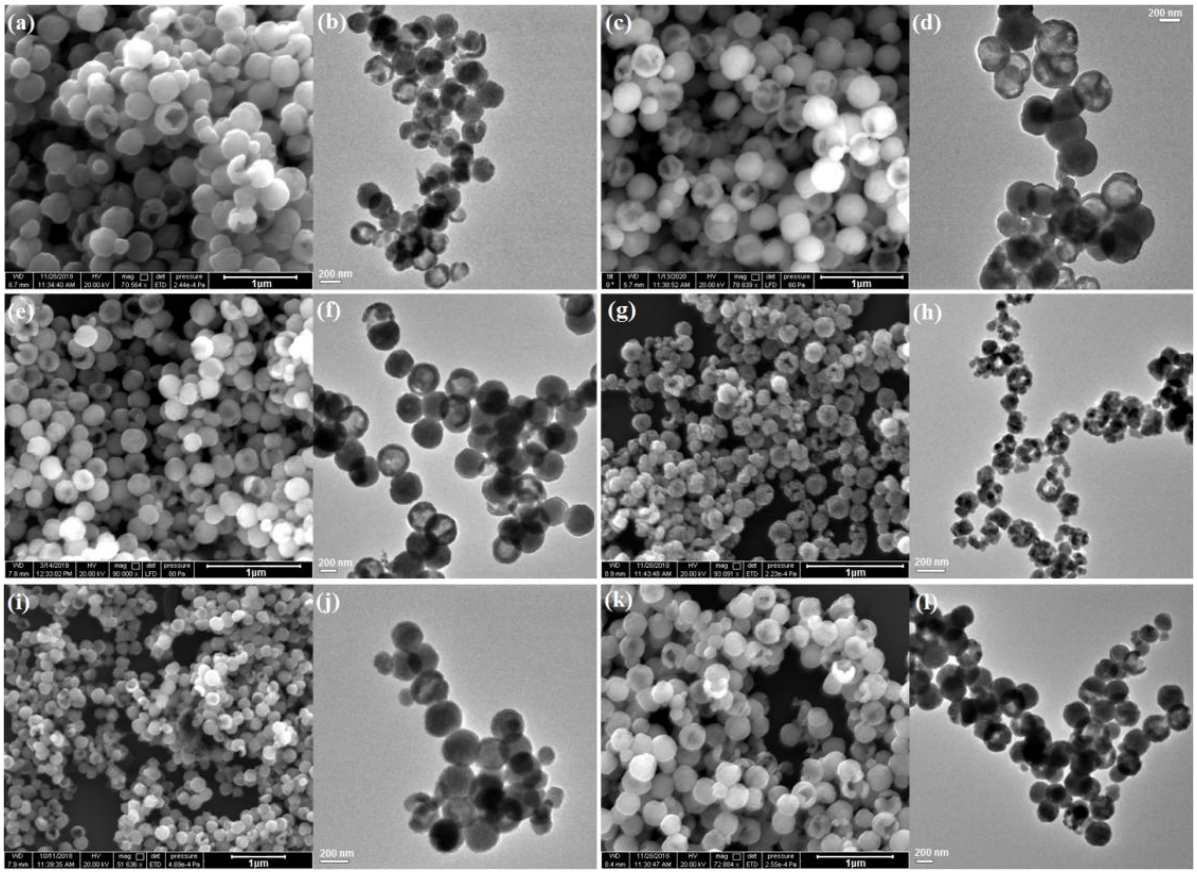

Figure 6.2. FESEM and TEM micrographs of $MnFe_2O_4$ (a), (b); Fe_3O_4 (c), (d); $CoFe_2O_4$ (e), (f); $NiFe_2O_4$ (g), (h); $CuFe_2O_4$ (i), (j) and $ZnFe_2O_4$ (k), (l) respectively

Table 6.1. Cationic radii [30,31], Lattice constants (a), Crystallite sizes (D), Diameters and Shell thicknesses of MFe_2O_4 NHSs

MFe_2O_4 NHSs, M =	Cationic radius (Å)	a (± 1.5%) (Å)	D (± 5%) (nm)	Diameter (± 2%) (nm)	Shell thickness (± 2%) (nm)
Mn	0.66	8.326	35.3	250	70
Fe	0.83	8.397	29.6	235	60
Co	0.745	8.394	34.7	256	70
Ni	0.69	8.343	22.1	223	55
Cu	0.70	8.388	42.7	260	76
Zn	0.74	8.390	47.4	312	85

6.3.2 Dielectric and Magnetic Properties

Real (ε') and imaginary (ε'') parts of relative dielectric constant as a function of frequency (f) for MFe_2O_4 NHSs (20 wt% filled composites) are presented in Fig. 6.3(a) and 6.3(b). ε' is associated with mainly contributions from interfacial and dipolar polarization and at higher frequencies, an additional polarization from shifting of ions [16,32,33]. Maxwell-Wagner grain-grain boundary model for ferrites is applicable in ε' vs. f plots for our investigated materials [7,16]. With increasing f, ε' decreases because the responsible dipole pairs (Fe^{2+}-Fe^{3+} and M^{2+}-M^{3+} in between tetrahedral (A) and octahedral (B) sites) for polarization lags behind the electric field at higher frequencies. The observed peaks at ~ 3 GHz and ~ 18 GHz in ε' vs. f plots suggest presence of dielectric relaxation and resonance respectively [15,16,32]. However, ε'', related to energy dissipation of accumulated charges, increases with f and shows a broad hump at respective frequencies of dielectric relaxation [4,32].

The dielectric loss, defined as $tan\delta_\varepsilon = \varepsilon''/\varepsilon'$, is plotted as a function of frequency in Fig. 6.3(c) which also follows the similar trend as ε'' vs. f curves. The absence of M^{2+}-M^{3+} dipole pair, and the lower impedance value of Fe_3O_4 NHS can be responsible to its lower values of ε' and $tan\delta_\varepsilon$ throughout the studied frequency region [34–36]. The

exterior as well as interior surface of porous NHSs along with their higher surface to volume ratio contributes in enhancing the interfacial area which increases dielectric polarization [18,24]. Thus, larger interfacial area in NHSs increases polarization and hence, amplifies $tan\delta_{\varepsilon}$, which makes NHSs more suitable towards electro-magnetic wave absorbing materials [18,25]. A schematic representation in Fig. 6.3(d) emphasizes the properties of NHSs towards their suitability and effectiveness as microwave absorber.

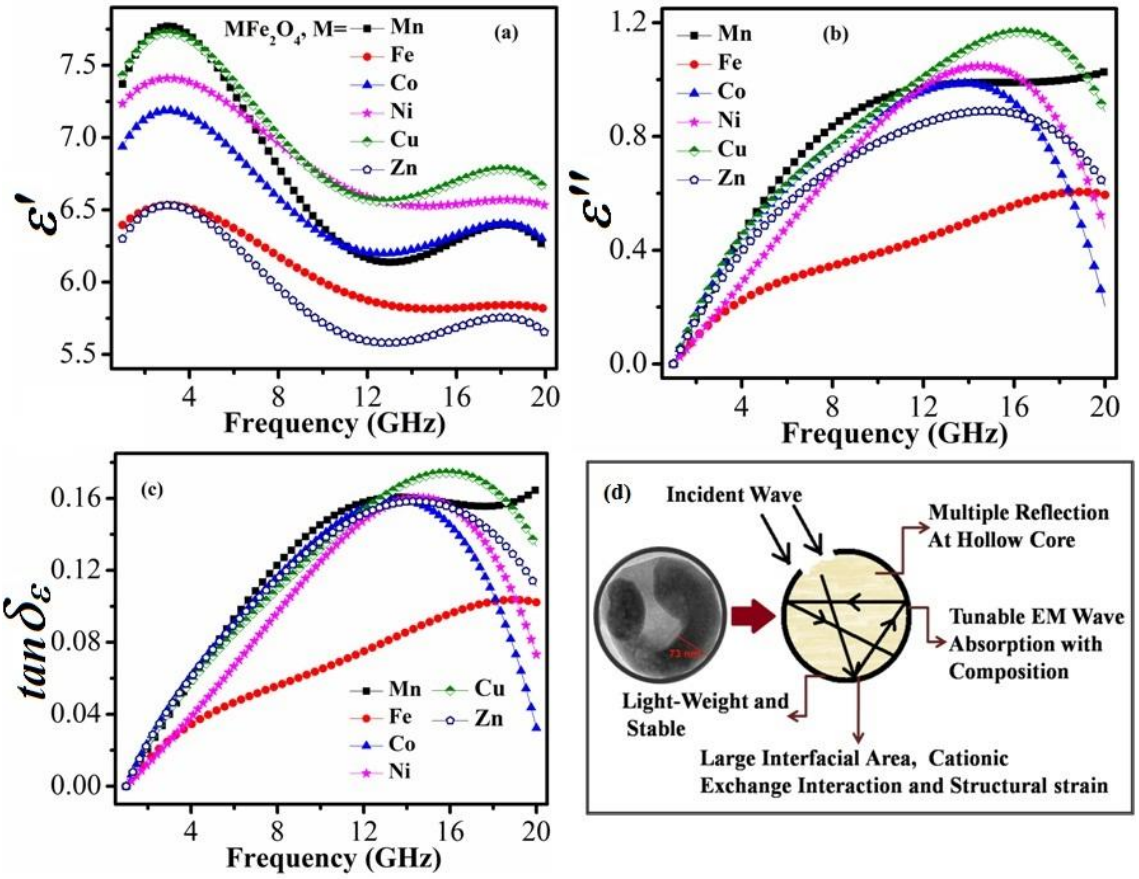

Figure 6.3. Frequency dependence (1 - 20 GHz) of (a) real (ε'), (b) imaginary (ε'') values of dielectric constant and (c) dielectric loss ($tan\delta_{\varepsilon}$), (d) A schematic approach showing effectiveness of NHSs towards EM wave absorption

The variation of real (μ') and imaginary part (μ'') of relative permeability with frequency are plotted in Fig. 6.4(a) and 6.4(b). μ' is observed to decrease up to a certain frequency then it maintains an almost constant value for all MFe_2O_4 NHSs (20 wt% loaded composites), whereas μ'' displays characteristic resonance peaks for all the

samples. Field dependent magnetization curves at 300 K (shown in inset of Fig. 6.4(d)) exhibits that saturation magnetization (M_S) decreases when Fe^{2+} in Fe_3O_4 is replaced with other cations (M = Mn, Co, Ni, Cu, Zn). The estimated coercivity (H_C) and $M_S$values for ferrites are listed in Table 6.2. According to the Landau-Lifshitz-Gilbert (LLG) equation, dynamic magnetic properties of the ferrimagnets are strongly related to the parameters such as magnetic anisotropy and M_S [25,37]. Moreover, Globus equation, $\mu' \propto (M_S{}^2 D / K^{1/2})$, where K is the magneto-crystalline anisotropy constant, ensure highest value of $\mu'$for Fe_3O_4 among other ferrites and lowest for $CoFe_2O_4$ NHS for its maximum H_C and K values [2,25]. Typical morphology of NHSs enhances the surface magnetic anisotropy energy in MFe_2O_4 NHSs than bulk ferrites which is beneficial to achieve higher loss and EM wave absorption in the system [7,15].

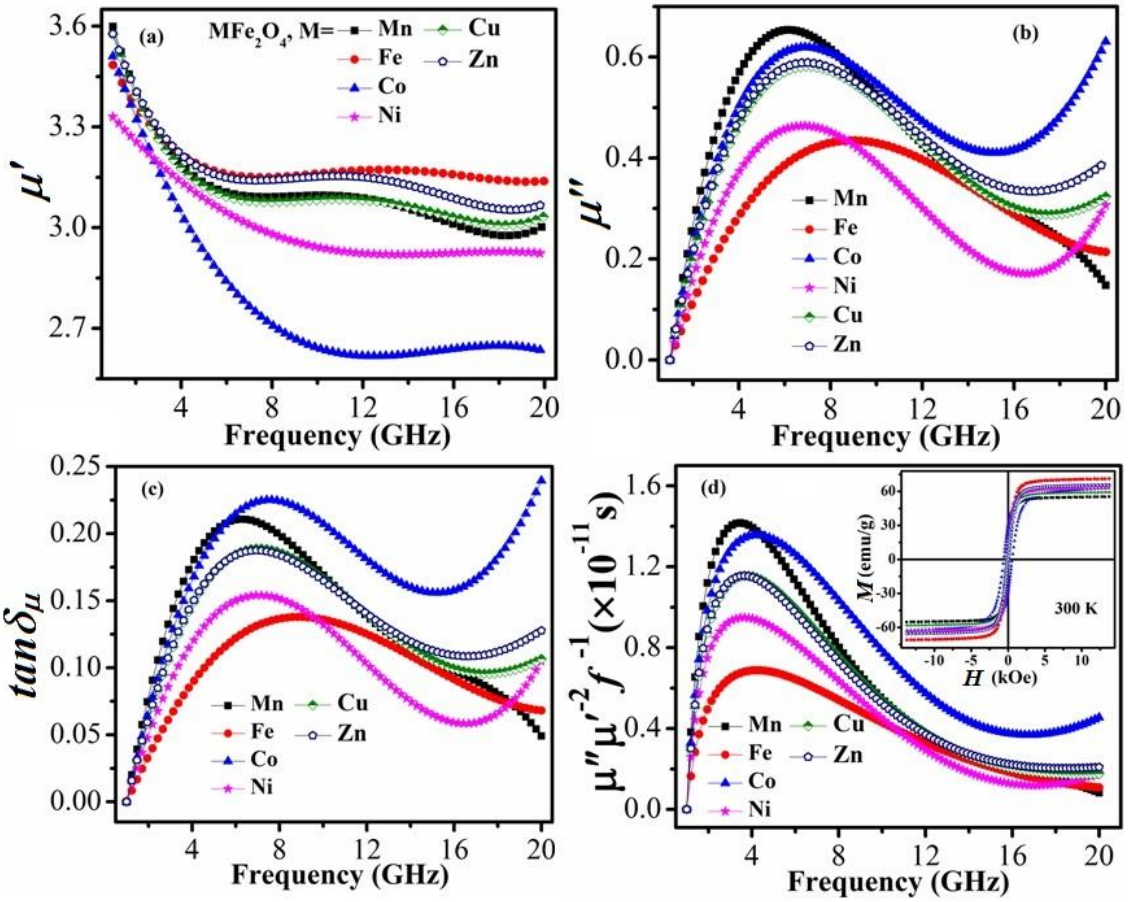

Figure 6.4. Frequency dependence (1 - 20 GHz) of (a) real (μ'), (b) imaginary (μ'') values of permeability and (c) magnetic loss ($tan\delta_\mu$), and (d) $\mu''(\mu')^{-2}f^{-1}$ [inset of (d): M-H plots at 300 K for all samples]

From Fig. 6.4(c), magnetic loss tangent, defined as $tan\delta_\mu = \mu''/\mu'$, is found to follow almost the same nature with f, as shown in case of μ''. In general, dynamic magnetic loss mostly arises from magnetic hysteresis, domain wall resonance, eddy current effects, natural and exchange resonance. Here, due to low field and high frequency ($f > 100$ MHz), first two contributions are less effective for the samples in 1 - 20 GHz frequency range [6,38]. From the natural resonance equation [7,39], $2\pi f_r = (4\gamma K)/(3\mu_0 M_S)$, where γ is gyromagnetic ratio (~ 2.8 GHz/kOe for ferrites), resonance frequency (f_r) is found around ~ 4 to 6 GHz for NHSs which suggests strong EM absorption through magnetic loss at that region. Further, the eddy current loss contribution to μ'', can be expressed as $\mu'' \sim 2\pi\mu_0\mu'^2(d^2\sigma)f$, where d is thickness of the sample (here 4.2 mm), σ, electrical conductivity and μ_0, permeability of free space [25]. According to this equation, if μ'' (or $tan\delta_\mu$) only originates from the eddy current loss, the values of $\mu''(\mu')^{-2}f^{-1}$ will not contain any peak and be constant with frequency [6,9]. In order to know the probable causes of magnetic loss, $\mu''(\mu')^{-2}f^{-1}$ versus frequency curve is plotted in Fig. 6.4(d). It can be noticed that a sharp peak is visible in all the curves around 4 GHz and the value remains almost constant after ~ 10 GHz. Therefore, resonance contributes for magnetic loss at low f, whereas eddy current loss has a significant effect on absorption at higher frequencies.

Table 6.2. Saturation magnetization (M_S) and Coercivity (H_C) values for MFe_2O_4 NHSs

MFe_2O_4 NHSs, M =	M_S (emu/g)	H_C (Oe)
Mn	55.0	152
Fe	71.0	131
Co	61.9	580
Ni	63.3	117
Cu	58.8	148
Zn	65.7	129

6.3.3 Microwave Absorption Properties

To understand EM wave absorption properties of MFe_2O_4 NHSs, frequency dependence of reflection loss (RL) curves for the samples with 20 wt% filler concentration and 4.2

mm thickness (t) are plotted in Fig. 6.5(a). Here, RL is calculated employing these following equations based on transmission line theory [1,6,19],

$$Z_{in} = Z_0(\frac{\mu_r}{\varepsilon_r})^{1/2} \tanh[j\left(\frac{2\pi tf}{c}\right)(\mu_r \varepsilon_r)^{\frac{1}{2}}] \quad 6.1$$

$$RL = 20\log|(Z_{in} - Z_0)/(Z_{in} + Z_0)| \quad 6.2$$

where μ_r $(= \mu' - i\mu'')$ and ε_r $(= \varepsilon' - i\varepsilon'')$ are relative permeability and permittivity of the material, c, the velocity of light, t, absorber composite thickness, Z_0 and Z_{in} are the impedance of free space and input impedance of absorber respectively. Two characteristic RL peaks for all the ferrites around ~ 4 GHz and ~ 12 GHz are witnessed in the examined frequency band. Generally, high RL originates from either (i) higher transmission of the incident wave which requires better impedance matching i.e. $|Z_{in}/Z_0| \sim 1$ or (ii) high value of dielectric and magnetic loss [2,9]. Moreover, total internal reflection in hollow core of NHS traps incident EM wave and increases the total propagation path of it, hence absorbs it in better [18,19,24]. The peaks in RL vs. f curves around 4 and 12 GHz can be attributed to strong magnetic and dielectric losses respectively. An additional intense peak is observed for $MnFe_2O_4$ NHS at ~ 19.3 GHz ($RL_{max} = -32.7$ dB) arising due to proper impedance matching with $|Z_{in}/Z_0|$ nearly equals to 1. To ensure the impedance matching, variation of $|Z_{in}/Z_0|$ is plotted with f in Fig. 6.5(c) which shows a good matching from ~ 10.5 to 14.7 GHz and beyond 18.6 GHz. These frequency bands consisted of $RL < -10$ dB i.e. absorption $> 90\%$ constitute the total effective bandwidth for the samples [40]. Here, Fe_3O_4 NHS with poor matching i.e. $|Z_{in}/Z_0|$ far from 1 displays lowest RL peaks also, as shown in Fig. 6.5(a). Thus, cation substitutions on traditional microwave ferrite Fe_3O_4 can be an effective tool to enhance RL from -6.7 dB to -32.7 dB as well as broaden the total effective bandwidth from 0 GHz to 4.6 GHz.

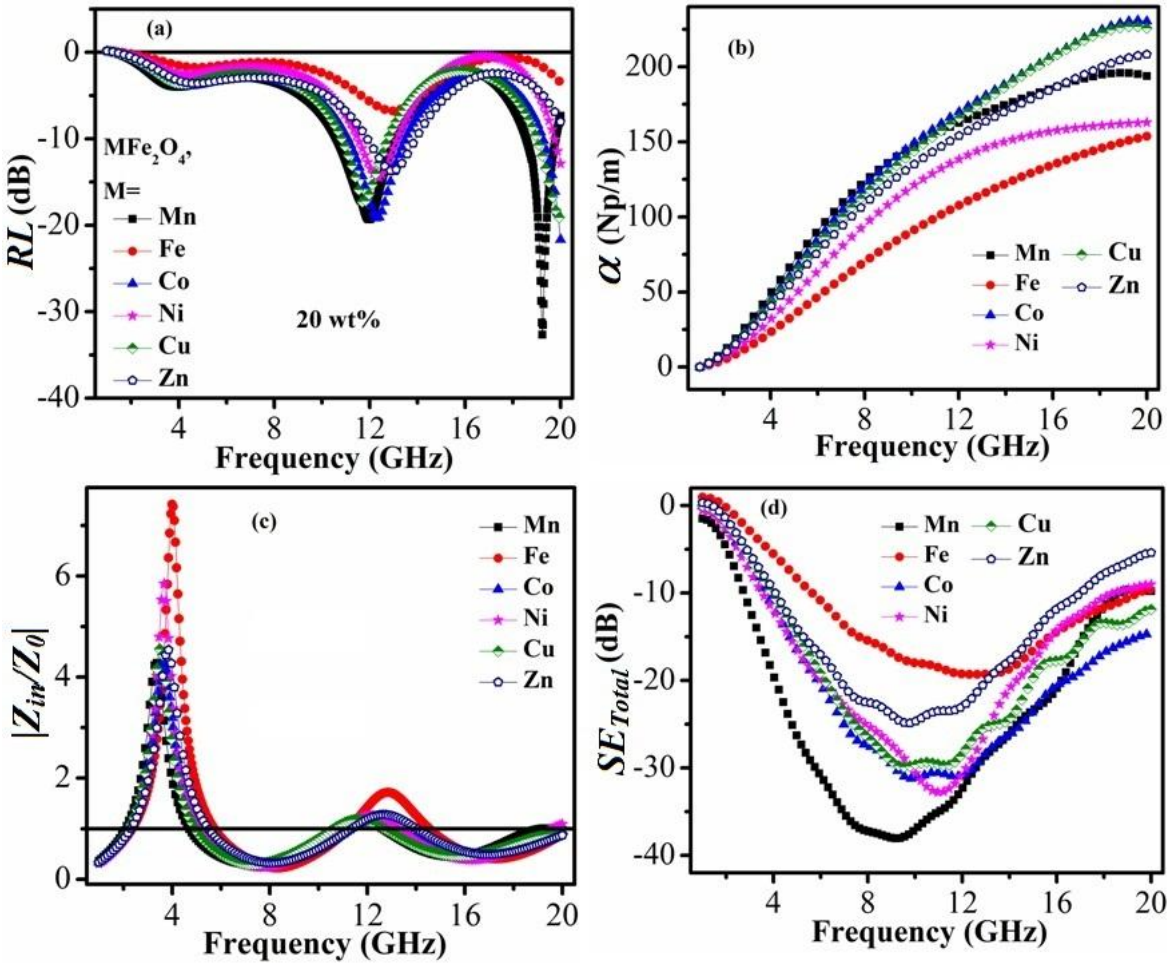

Figure 6.5. Variation of (a) reflection loss (*RL*), (b) attenuation constant (α), (c) $|Z_{in}/Z_0|$ ratio and (d) total shielding efficiency (SE_{Total}) with frequency (1 - 20 GHz) for all the samples

Further, attenuation constants (α) and shielding efficiency (*SE*), associated with microwave loss and transmission through the ferrite/epoxy composites, are estimated for the samples, shown in Fig. 7.5(b) and 7.5(d). Total *SE* (SE_{Total}) is expressed as the sum of the contributions from reflection (SE_R) and absorption shielding (SE_A) obeying the equation [24,25],

$$SE_{Total} = 10\log\left(P_t/P_0\right) = (SE_A + SE_R) = 20\log|S_{21}| \qquad 6.3$$

where, $SE_R\ (dB) = 10 \log\ (1 - R)$, $R = |S_{11}|^2$ and $SE_A\ (dB) = 10 \log[(T/(1 - R)]$, $T = |S_{21}|^2$. In this equation, P_t is the transmitted power, P_0, incident power of EM wave, S_{11} and S_{21}, reflection and reverse-transmission co-efficient respectively.

Attenuation constant (α) is defined as [6,16],

$$\alpha = \frac{\sqrt{2}\pi f}{c}\sqrt{(\mu''\varepsilon'' - \mu'\varepsilon') + \sqrt{(\mu''\varepsilon'' - \mu'\varepsilon')^2 + (\mu''\varepsilon' + \mu'\varepsilon'')^2}} \quad 6.4$$

Here, α is found to increase with frequency and maximum for lossy $CoFe_2O_4$ NHS ($\sim$ 230 Np/m) whereas SE_{Total} is optimum for $MnFe_2O_4$ (-42 dB at $\sim$ 10 GHz) following nature of *RL* curves.

Favorable impedance matching at high f and maximum losses at lower f make $MnFe_2O_4$ NHSs most efficient microwave absorber compared to the other investigated ferrites and hence, filler loading content and thickness dependent study of microwave properties are carried out to assure its practical applications.

Figure 6.6(a) describes *RL* as a function of frequency for $MnFe_2O_4$ NHS for different filler concentration for composite $t = 4.2$ mm. Enhancement of ferrite loading from 0 wt% to 50 wt% in epoxy matrix shows an increase in *RL* from -3.4 dB to -45.6 dB. The ε' and μ' values are also highest for 50 wt% sample (shown in insets of Fig. 7.6(a)). With higher filler content, RL_{max} peak shifts towards lower frequency to maintain thickness matching criteria [38,41]. Moreover, total effective bandwidth as broad as $\sim$ 3.6 GHz obtained for 50 wt% composite represents it as a potential microwave absorber. In addition, composites consisted of epoxy resin matrix and ferrite filler can maintain their stability for high-temperature applications up to 120°C [42]. Frequency dependence of *RL* for 50 wt% sample at different thicknesses is presented in Fig. 6.6(b) and Fig. 6.6(c).

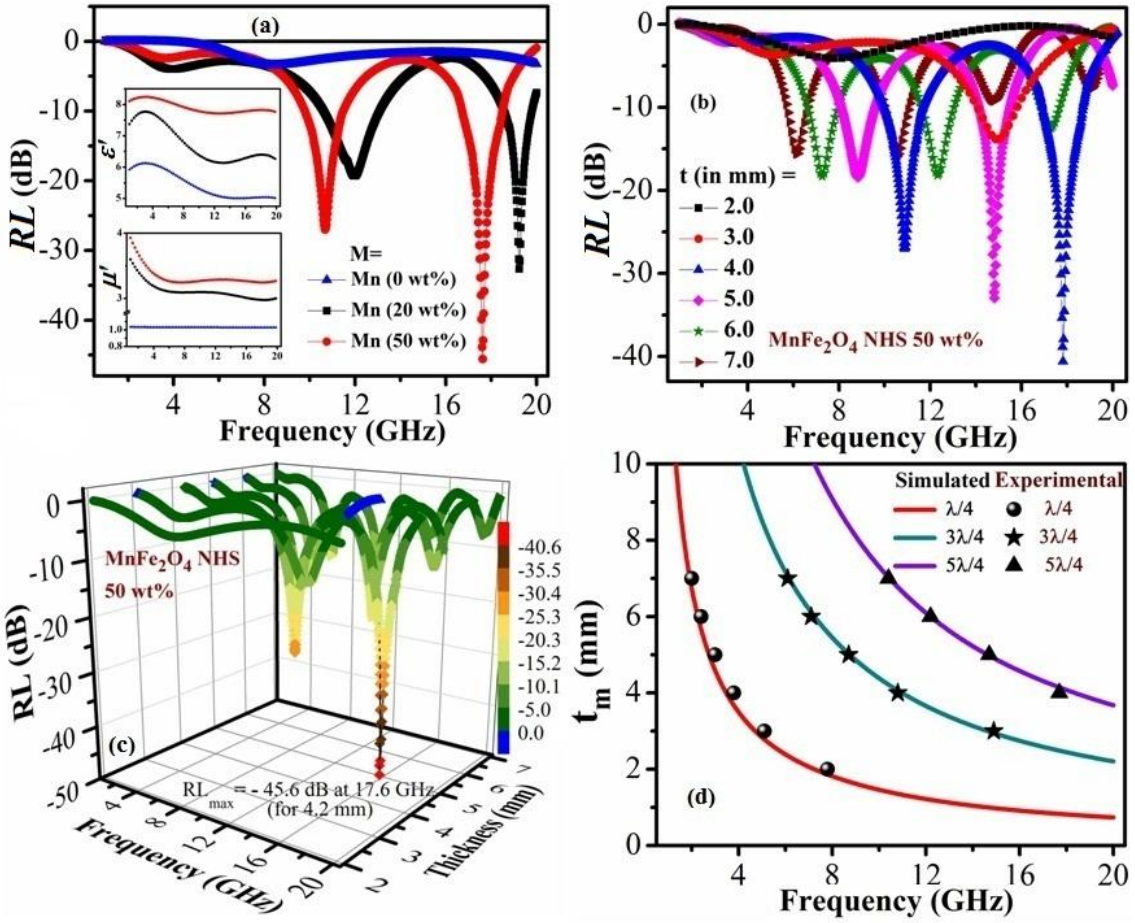

Figure 6.6. Frequency dependence of *RL* varying with (a) filler concentration [Insets: Variation of ε' and μ' with f for composites with 0 wt%, 20 wt% and 50 wt% $MnFe_2O_4$ NHS] and (b) thicknesses (c) 3D representation showing RL_{max} in $MnFe_2O_4$ NHS (50 wt%) and (d) Simulated and experimental matching thicknesses (t_m) with frequency (1 - 20 GHz)

Relation of peak frequency at RL_{max} (f_m) with matching thickness (t_m) can be directly interpreted from quarter wavelength (λ/4) model as,

$$t_m = \frac{nc}{4f_m\sqrt{|\varepsilon_r\mu_r|}} \ (n = 1,3,5,\dots) \qquad 7.5$$

Higher matching modes are visible for higher thicknesses and f_m moves towards lower frequency with increasing t of the samples. A good agreement in experimental and simulated t_m can be noticed in Fig. 6.6(d) which may also provide a guidance for the thickness design required for microwave absorbers [18,38]. The maximum *RL* obtained

here for $MnFe_2O_4$ nano-hollow spheres with 50 wt% filler loading content is comparable to other promising ferrite EMA composites such as $NiFe_2O_4$/r-GO nano particles (~ −42 dB) [16], Fe_3O_4/SiO_2 nanorods (~ −28.6 dB) [7], $CoFe_2O_4$@rGO nano-composites (~ −25.7 dB) [4], Fe_3O_4@TiO_2 microspheres (~ −23 dB) [8], Magnetic graphene@PANI@porous TiO_2 ternary composites (−45.4 dB) [38] etc. Therefore, light-weight $MnFe_2O_4$ NHS (50 wt%) composite is an attractive candidate for microwave absorption and applications in high-frequency devices.

6.4 Conclusion

In summary, electromagnetic wave attenuation properties of as-synthesized low-density MFe_2O_4 [M = Mn, Fe, Co, Ni, Cu, Zn] nano-hollow spheres (20 wt% filled in epoxy resin matrix) are investigated in-detail within widely-used frequency range of 1 - 20 GHz. M^{2+} [M = Mn, Co, Ni, Cu, Zn] substitution in place of Fe^{2+} displays a clear enhancement of microwave absorption properties compared to traditional Fe_3O_4 whereas, $MnFe_2O_4$ NHS is found to exhibit an optimal RL of ~ −32.7 dB, SE_{Total} ~ −42 dB and a high α ~ 196 Np/m. Losses through strong magnetic resonance and dielectric relaxation are responsible for RL peaks of ferrites around ~ 4 GHz and ~ 12 GHz respectively. An additional peak at ~ 19.3 GHz for $MnFe_2O_4$ NHS arises due to favorable impedance matching. Multiple internal reflections in hollow core of NHS are also considered as an influential source to high RL of NHSs. Further, filler loading content and thickness dependent study is carried out on $MnFe_2O_4$ NHS composites and a maximum RL of ~ −45.6 dB at t ~ 4.2 mm with a broad total effective bandwidth ($RL <$ −10 dB) of ~ 3.6 GHz is observed for 50 wt% sample. According to λ/4 model for best matching thickness, experimental t_m is found to agree well with calculated results. Excellent RL and broad BW observed in $MnFe_2O_4$ NHS (50 wt%) makes it a cost-effective promising EMA material towards mass-efficient high-frequency applications.

References

[1] W. Ruan, C. Mu, B. Wang, A. Nie, C. Zhang, X. Du, J. Xiang, F. Wen, and Z. Liu, Nanotechnology 29, 405703 (2018).

[2] Z. Yang, Z. Li, Y. Yang, and Z. J. Xu, ACS Appl. Mater. Interfaces 6, 21911 (2014).

[3] H. M. Yan, M. H. Yan, Y. F. Zhang, T. X. Zhu, L. M. Yu, Y. Liu, T. Maruyama, and X. L. Zhao, J. Appl. Phys. 126, 45101 (2019).

[4] Y. Ding, Q. Liao, S. Liu, H. Guo, Y. Sun, G. Zhang, and Y. Zhang, Sci. Rep. 6, 32381 (2016).

[5] X. Qiu, L. Wang, H. Zhu, Y. Guan, and Q. Zhang, Nanoscale 9, 7408 (2017).

[6] X. Zhou, Z. Jia, A. Feng, S. Qu, X. Wang, X. Liu, B. Wang, and G. Wu, J. Colloid Interface Sci. 575, 130 (2020).

[7] X. Liu, Y. Chen, X. Cui, M. Zeng, R. Yu, and G. S. Wang, J. Mater. Chem. A 3, 12197 (2015).

[8] J. Liu, R. Che, H. Chen, F. Zhang, F. Xia, Q. Wu, and M. Wang, Small 8, 1214 (2012).

[9] Y. Zhang, H. Bin Zhang, X. Wu, Z. Deng, E. Zhou, and Z. Z. Yu, ACS Appl. Nano Mater. 2, 2325 (2019).

[10] L. Wang, Y. Huang, X. Sun, H. Huang, P. Liu, M. Zong, and Y. Wang, Nanoscale 6, 3157 (2014).

[11] M. Pardavi-horvath, J. Magn. Magn. Mater. 216, 171 (2000).

[12] V. G. Harris, A. Geiler, Y. Chen, S. D. Yoon, M. Wu, A. Yang, Z. Chen, P. He, P. V. Parimi, X. Zuo, C. E. Patton, M. Abe, O. Acher, and C. Vittoria, J. Magn. Magn. Mater. 321, 2035 (2009).

[13] M. Amano and Y. Kotsuka, IEEE Trans. Microw. Theory Tech. 51, 238 (2003).

[14] K. Khan, J. Supercond. Nov. Magn. 27, 453 (2014).

[15] Y. Yang, M. Li, Y. Wu, B. Zong, and J. Ding, RSC Adv. 6, 25444 (2016).

[16] J. Z. He, X. X. Wang, Y. L. Zhang, and M. S. Cao, J. Mater. Chem. C 4, 7130 (2016).

[17] J. Liu, W. You, J. Yu, X. Liu, X. Zhang, J. Guo, and R. Che, ACS Appl. Nano Mater. 2, 910 (2019).

[18] M. Han, X. Yin, L. Kong, M. Li, W. Duan, L. Zhang, and L. Cheng, J. Mater. Chem. A 2, 16403 (2014).

[19] F. Wang, J. Liu, J. Kong, Z. Zhang, X. Wang, M. Itoh, and K. Machida, J. Mater. Chem. 21, 4314 (2011).

[20] D. Mandal, M. Alam, and K. Mandal, Phys. B Condens. Matter 554, 51 (2019).

[21] J. S. An, W. J. Han, and H. J. Choi, Colloids Surfaces A Physicochem. Eng. Asp. 535, 16 (2017).

[22] B. Guo, K. Yu, H. Li, H. Song, Y. Zhang, X. Lei, H. Fu, Y. Tan, and Z. Zhu, ACS Appl. Mater. Interfaces 8, 5517 (2016).

[23] I. Chakraborty, U. Saha, D. Mandal, S. Mukherjee, N. Joardar, S. P. Sinha Babu, G. Suresh Kumar, and K. Mandal, Phys. Chem. Chem. Phys. 21, 10726 (2019).

[24] R. Panigrahi and S. K. Srivastava, Sci. Rep. 5, 7638 (2015).

[25] D. Mandal, A. Gorai, and K. Mandal, J. Magn. Magn. Mater. 485, 43 (2019).

[26] M. Mandal Goswami, Sci. Rep. 6, 35721 (2016).

[27] S. F. Soares, T. Fernandes, A. L. Daniel-da-Silva, and T. Trindade, Proc. R. Soc. A Math. Phys. Eng. Sci. 475, 20180677 (2019).

[28] O. Luukkonen, S. I. Maslovski, and S. A. Tretyakov, IEEE Antennas Wirel. Propag. Lett. 10, 1295 (2011).

[29] K. Vamvakidis, M. Katsikini, D. Sakellari, E. C. Paloura, O. Kalogirou, and C. Dendrinou-Samara, Dalt. Trans. 43, 12754 (2014).

[30] D. Thapa, N. Kulkarni, S. N. Mishra, P. L. Paulose, and P. Ayyub, J. Phys. D. Appl. Phys. 43, 195004 (2010).

[31] H. L. Andersen, M. Saura-Múzquiz, C. Granados-Miralles, E. Canévet, N. Lock, and M. Christensen, Nanoscale 10, 14902 (2018).

[32] R. Tang, C. Jiang, W. Qian, J. Jian, X. Zhang, H. Wang, and H. Yang, Sci. Rep. 5, 1 (2015).

[33] S. Thakur, S. C. Katyal, and M. Singh, Appl. Phys. Lett. 91, 262501 (2007).

[34] G. Datt and A. C. Abhyankar, J. Appl. Phys. 122, 34102 (2017).

[35] D. Sarkar, M. Mandal, and K. Mandal, J. Appl. Phys. 112, 64318 (2012).

[36] D. Mandal and K. Mandal, J. Alloys Compd. 851, 1 (2021).

[37] T. L. Gilbert, IEEE Trans. Magn. 40, 3443 (2004).

[38] P. Liu, Y. Huang, J. Yan, and Y. Zhao, J. Mater. Chem. C 4, 6362 (2016).

[39] X. G. Liu, D. Y. Geng, H. Meng, P. J. Shang, and Z. D. Zhang, Appl. Phys. Lett. 92, 173117 (2008).

[40] R. Peymanfar and S. Ghorbanian-Gezaforodi, Nanotechnology 31, 495202 (2020).

[41] X. Li, J. Feng, Y. Du, J. Bai, H. Fan, H. Zhang, Y. Peng, and F. Li, J. Mater. Chem. A 3, 5535 (2015).

[42] H.-I. Hsiang, W.-S. Chen, Y.-L. Chang, F.-C. Hsu, and F.-S. Yen, Am. J. Mater. Sci. 1, 40 (2011).

Chapter 7

Enhancement of Electromagnetic Wave Absorption in $MnFe_2O_4$ Nano-hollow spheres

Following the outcomes of previous chapter, herein dielectric, magnetic and microwave absorption properties are investigated in detail for $MnFe_2O_4$ Nano-hollow spheres (NHS) in the frequency range of 1-20 GHz, through precise modulation of their sizes from 100 nm to 550 nm. Best impedance matching for 450 nm NHS of $MnFe_2O_4$ shows the optimum response in an extremely light-weight composite of the studied material in epoxy resin matrix

7.1 Preamble

Ongoing rapid development of wireless and electronic high-frequency technologies produces severe electromagnetic interference (EMI) or wave pollution to the environment that also extensively threatens the human health [1,2]. To shield unwanted EM waves, light-weight, stable and cost-effective yet efficient EM wave absorbing (EMA) materials are extremely needed [2,3]. EMA materials are also widely used in military and civil fields, such as stealth technology, anechoic chambers and in modern metamaterials [4,5]. In this context, ferrites for their synergistic magnetic and dielectric properties are superior choice over traditional dielectrics like carbon based materials or magnetic ultrafine metal powders [2,4,6]. Moreover, proper tuning of permittivity (ε) and permeability (μ) associated with ferrites, provide favorable impedance matching in it, thus ensuring higher reflection loss (RL) and broader total effective bandwidth (BW) [4,7]. Further, a sufficiently high value of ε and μ is desirable to lessen the required thickness (t) of the absorbing material [8].

In spite of these advantages of ferrites, high density of bulk and solid morphologies of ferrites makes them heavy and thus less usable for practical applications [7,9]. To overcome this drawback, nano-hollow sphere (NHS) morphology of ferrites is a convenient option. NHSs with their internal hollow core are of lower density and this hollow core stimulates multiple internal reflections in it, which enhance total propagation path-length and absorption of EM wave in NHSs [3,7]. In addition, larger surface to volume ratio, porous nature of NHS morphology, presence of both interior and exterior surfaces increase its interfacial area for dielectric polarization enhancing ε values as well as dielectric loss [3,10,11]. On the other side, among low-cost and stable transition metal based ferrites, $MnFe_2O_4$ owns high μ values due to high magnetic moment of its divalent cation [12].

In recent years, researches on microwave absorption properties of ferrites became quite popular [7,13–16]. Morphology control, chemical doping and hybridization of materials are some promising techniques to tune the EM wave attenuation capability [7,17–19]. For instance, size-dependent EMA properties of Fe_3O_4

nano-discs were studied in order to achieve strong EM wave absorption through magnetic losses [13]. Graphene oxide functionalization on $MnFe_2O_4$ [14] and $NiFe_2O_4$ nanoparticles [16] were performed to increase their EM wave attenuation. Yang et al. observed a maximum RL of ~ -45 dB with a broad BW via controlled doping of Zn^{2+} ions on Fe_3O_4 NHSs [7]. In order to obtain light-weight, stable and cost-effective yet efficient electromagnetic (EM) wave absorbing material, here, we investigated EM wave attenuation properties of as-synthesized low-density $MnFe_2O_4$ nano-hollow spheres (NHS) in-detail, varying their sizes [mean diameter (nm) of sample sets = 100, 220, 300, 450 and 550] within a widely-used frequency range of 1 - 20 GHz. In addition to larger interfacial area and magnetic anisotropy of NHSs, multiple reflections in internal hollow core promote better EM wave absorption. Here, tuning of NHS sizes is demonstrated as an effective strategy to achieve excellent microwave absorber and $MnFe_2O_4$ NHS of diameter $\sim$ 450 nm is found to exhibit a maximum reflection loss (RL) of ~ -52.6 dB, total shielding efficiency (SE_{Total}) ~ -39.5 dB and a high attenuation constant (α) $\sim$ 285 Np/m. Significant dielectric and magnetic losses with most favorable impedance matching ($|Z_{in}/Z_0| \sim 1$) for 450 nm NHS are the reasons behind this outcome. Further, a thickness dependent study on 450 nm NHS composites reveals that optimum RL reached ~ -55.4 dB at 9.6 GHz for $t = 5.1$ mm with a broad total effective bandwidth ($RL < -10$ dB i.e. shielding $> 90\%$) of $\sim$ 3.7 GHz. Moreover, analysis from quarter-wavelength model for best matching thickness (t_m) displays a good agreement between experimental and calculated t_m values. This study presents optimized 450 nm $MnFe_2O_4$ NHS at much lower filler concentration (20 wt% in epoxy resin matrix), as a highly promising low-cost and light-weight microwave absorber suitable for practical high-frequency applications.

7.2 Experimental

7.2.1 Synthesis Procedure

MnFe2O4 NHSs are synthesized in a facile one-pot template-free solvothermal process where MnCl2, 6H2O and FeCl3, 6H2O are taken in 1:2 molar weight ratios as

precursors, Ethyl Alcohol (EtOH) and Ethylene Glycol (EG) in 1:2 ratio as solvents and Urea as reducing agent. Taking all the components in a 100 ml beaker, Polyvinylpyrrolidone (PVP) is added while stirring it. PVP, a non-ionic surfactant, plays an important role in controlling size distribution [20] and the amounts of PVP taken here to achieve sample sizes from 100 nm to 550 nm are listed in Table 8.1. The clear homogeneous solution, after 30 min of stirring, is transferred to a 50 ml Teflon-lined stainless steel autoclave and heated at 200°C for 24 h in an oven to obtain NHSs. The as-prepared $MnFe_2O_4$ NHSs are washed by EtOH and distilled water several times, collected through magnetic separation and dried by heating at 60°C for ~ 30 min. Increase in amount of capping agent, PVP, prevents the growth of nano-crystals which results NHSs of smaller diameter. During the reaction, urea helps to precipitate Mn^{2+} and Fe^{3+} ions from chloride salts to its hydroxides and after the heat treatment, $MnFe_2O_4$ phase is developed. The anticipated mechanism related to the synthesis of NHSs is considered as Ostwald ripening which involves a gradual re-crystallization of particles from smaller to bigger ones to reduce their surface free energy [21]. In addition, self-templating with the help of gas bubbles formed by urea, under the effect of PVP ensures controlled formation of stable hollow spheres [11,22].

All the chemicals for above preparation, having analytical grade and purity ≥ 98%, were purchased from Sigma-Aldrich.

7.2.2 Characterizations

X-ray diffraction (XRD) is carried out by PANalytical X'Pert PRO equipped with Cu K_α radiation to know the parent phase of as-prepared samples. A FEI QUANTA FEG 250 field-emission scanning electron microscope (FESEM) (0.2 - 30 kV) and a FEG high-resolution transmission electron microscope (HRTEM) (80 - 200 kV) are used to obtain the information about size and morphology of NHSs. Magnetic measurements are performed using Vibrating Sample Magnetometer (Lake Shore) in a maximum applied field of 14 kOe and at room-temperature (~ 300 K). Microwave properties of the samples are measured using Anritsu MS46122B Vector Network Analyzer (VNA) and coaxial airline (Maury Microwaves 8043S6) within the frequency range of $1 - 20$ GHz.

The composite samples for microwave measurements are prepared by loading 20 wt% powder samples in epoxy resin matrix and molding this mixture properly. The final composites are in toroidal shape with inner diameter (d_{in}) = 1.5 mm, outer diameter (d_{out}) = 3.5 mm and thickness (t) = 5 mm. Each composite sample is properly inserted in port one end of coaxial airline and set-up calibration is performed using TOSLKF50A-20 kit for the measurements. Further analysis from measured 2-port scattering (S)-parameters is executed with polynomial fit model of Nicholson-Ross-Weir (NRW) algorithm based on transmission line technique [23].

7.3 Results and Discussion

7.3.1 Structure and Morphology

XRD patterns of all the samples, displayed in Fig. 7.1(a), confirm single phase spinel face-centered cubic structure as reported in the literature (JCPDS file no. 65-1123). From the enlarged (311) peaks for $MnFe_2O_4$ NHSs shown in Fig. 7.1(b), peak positions are observed to shift towards left with increasing sample sizes while the peak widths become narrower from 0.237˚ to 0.177˚for sizes 100 nm to 550 nm. Average crystallite sizes (D) as well as lattice strains (e) are calculated from the XRD peaks using Williamson–Hall formalism [24] and lattice constant (a) is estimated from XRD pattern using Bragg's law. XRD peaks of each set are fitted following the equation, $\beta_{hkl}\cos\theta = \frac{k\lambda}{D} + 4e\sin\theta$, where k is the Scherrer constant (here ~ 0.94), λ, the working wave length, β_{hkl}, the FWHM of the selected peak and θ, the XRD peak angle. The D, a and e values are summarized in Table 7.1 for respective set of samples where an obvious enhancement in crystallite size and lattice constant with increase in sample size is obtained along with a simultaneous decrease in lattice strain [25].

FESEM micrographs, displayed in Fig. 7.1(c)-7.1(g), clearly illustrate nano-hollow spheres (NHSs) of $MnFe_2O_4$ with inside cavity. The average diameters of NHSs are estimated from size distribution curves (inset of Fig. 7.1(f) is for 450 nm) and these values are listed in Table 7.1 for all the sample sets. Moreover, due to the internal

hollow core, NHSs are of much lower density than their bulk counterpart, therefore they are light-weight and much convenient for practical applications [9].

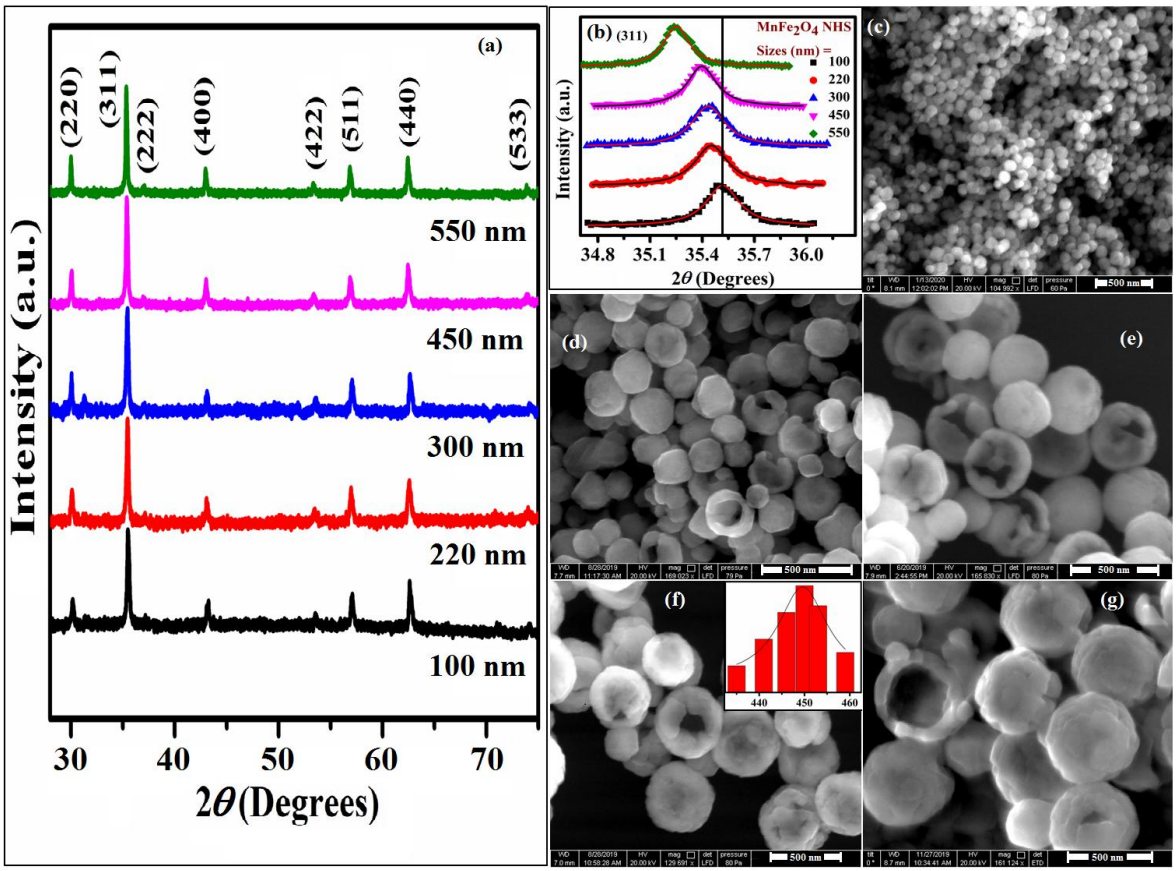

Figure 7.1. (a) X-Ray diffraction plots for all $MnFe_2O_4$ nano-hollow spheres at ~ 300 K, (b) Enlarged XRD peak (311) for $MnFe_2O_4$ samples, FESEM micrographs of MnFO NHSs with sizes (c) 100 nm (d) 220 nm (e) 300 nm (f) 450 nm; inset: corresponding size distribution graph (g) 550 nm

The contrast between bright core and dark shells visible in TEM micrographs, shown in Fig. 7.2(a)-7.2(e), also confirms hollow sphere structures of the samples. The average shell thicknesses obtained from TEM micrographs are listed in Table 7.1. A representative HRTEM micrograph and SAED pattern for 450 nm NHS, presented in Fig. 7.2(f) and Fig. 7.2(g) respectively, displays separation between parallel diffraction planes (0.3 nm for (220), 0.26 nm for (311)) that matches well with the values calculated from XRD data. Furthermore, bright spots in SAED pattern depicts single crystalline nature of the sample and EDX spectra, in Fig. 7.2(h), illustrates constituent

elements present in the sample. A line scanned EDX spectrometry, performed across the diameter of one NHS of ~ 450 nm, is shown by an orange line in Fig. 7.2(i). Fig. 7.2(j)-7.2(l) show the EDX line scanning profile of Mn, Fe, and O, respectively that visualizes the hollow core of size ~ 270 nm and shell width of ~ 90 nm. Here, hollow spheres up to diameter ~ 450 nm will behave like nano as their shell thicknesses are < 100 nm [26].

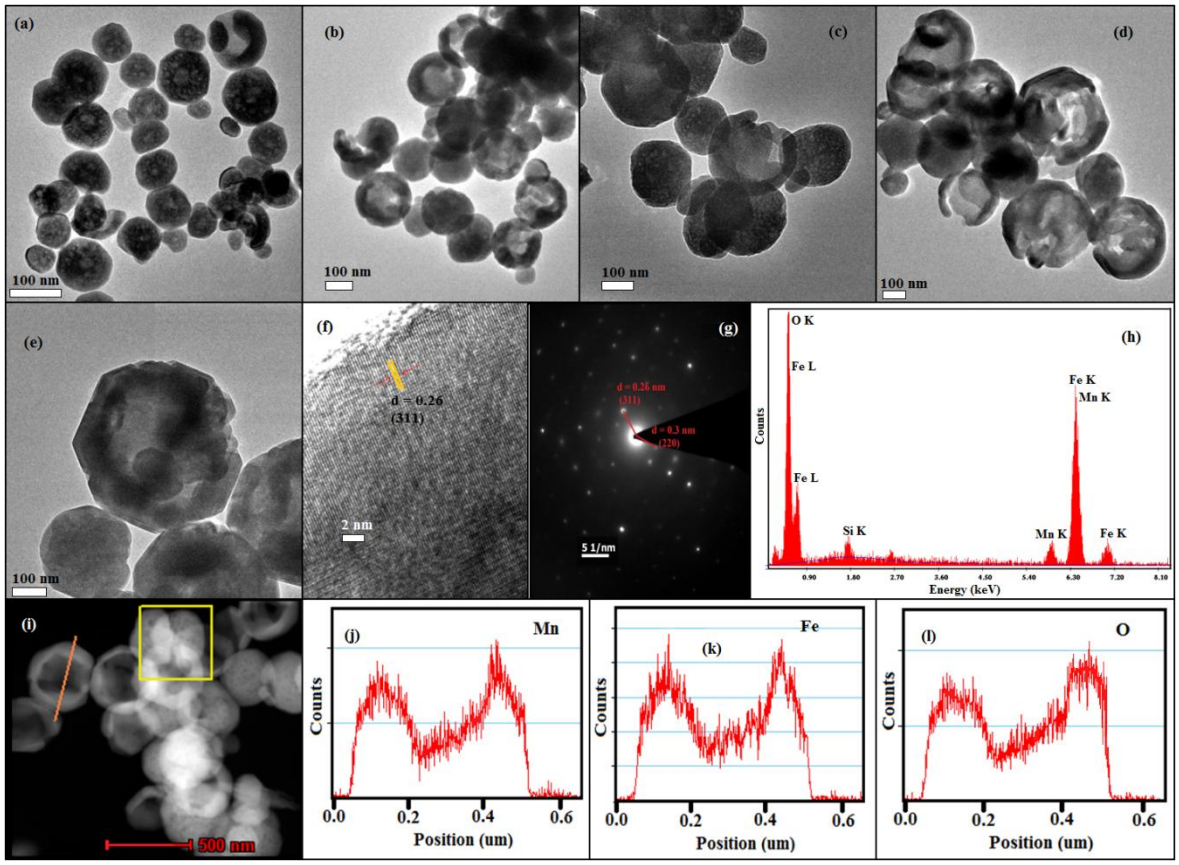

Figure 7.2. TEM micrographs for MnFO NHSs with sizes (a) 100 nm (b) 220 nm (c) 300 nm (d) 450 nm and (e) 550 nm (f) HRTEM micrograph and (g) SAED (Selected Area Electron Diffraction) pattern for 450 nm NHS (h) EDX (Energy Dispersive X-ray) spectra shows components of MnFO (i) EDX Line Mapping across the orange line for 450 nm NHS; line mapping spectra shown for (j) Mn (k) Fe (l) O

Table 7.1. Amount of PVP in chemical reaction, Diameters, Shell thicknesses, Lattice constants (a), Crystallite sizes (D) and Lattice strains (e) of $MnFe_2O_4$ NHSs

Sample Sets	PVP amount (mg)	Diameter (± 2%) (nm)	Shell thickness (± 2%) (nm)	a (± 1.5%) (Å)	D (± 5%) (nm)	e ($\times 10^{-3}$) (± 1%)
Set 1	180	100	29	8.373	36.78	3.2
Set 2	70	220	53	8.387	37.73	3.2
Set 3	55	300	62	8.392	38.05	3.1
Set 4	40	450	86	8.400	42.71	2.8
Set 5	30	550	114	8.411	49.22	2.4

7.3.2 Dielectric and Magnetic Properties

Real (ε') and imaginary (ε'') parts of relative dielectric constant as a function of frequency (f) for $MnFe_2O_4$ NHS samples are plotted in Fig. 7.3(a) and 7.3(b). Here, dielectric constant is originated mainly from the contributions of interfacial and dipolar polarization where the charge carriers and the dipole pairs Fe^{2+}-Fe^{3+} and Mn^{2+}-Mn^{3+} in between tetrahedral (A) and octahedral (B) sites are responsible for this [16,26]. With increasing f, dielectric relaxation occurs as these dipoles can not comply with electric field frequency and lags behind the field [27]. Therefore, ε' decays at high frequencies following Maxwell-Wagner grain-grain boundary model for ferrites [25]. The high-frequency peak observed in Fig. 7.3(a) for the samples at ~ 18 GHz suggests possible presence of dielectric resonance in the system related to atomic polarization [16,28]. Large interfacial area of porous NHSs consisted of its exterior as well as interior surface and higher surface to volume ratio contributes in higher polarization, hence in higher ε [3,10]. Moreover, with increasing size, ε' enhances with increase in interfacial area of NHSs but after a certain size (here, 450 nm), ε' tends to decrease with lowering structural strain in the samples [29,30]. In Fig. 7.3(b), ε'', related to energy dissipation of accumulated charges, increases with NHS sizes and shows a broad hump at frequencies containing dielectric relaxation and resonance f region. Frequency dependence of dielectric loss, defined as $tan\delta_\varepsilon = \varepsilon''/\varepsilon'$, displayed in Fig. 7.3(c), varies with f following similar trend as ε'' vs. f curves. Larger interfacial area in NHSs increases

electric polarization and hence $tan\delta_\varepsilon$, which makes NHSs more suitable towards electro-magnetic wave absorbing materials [3,9].

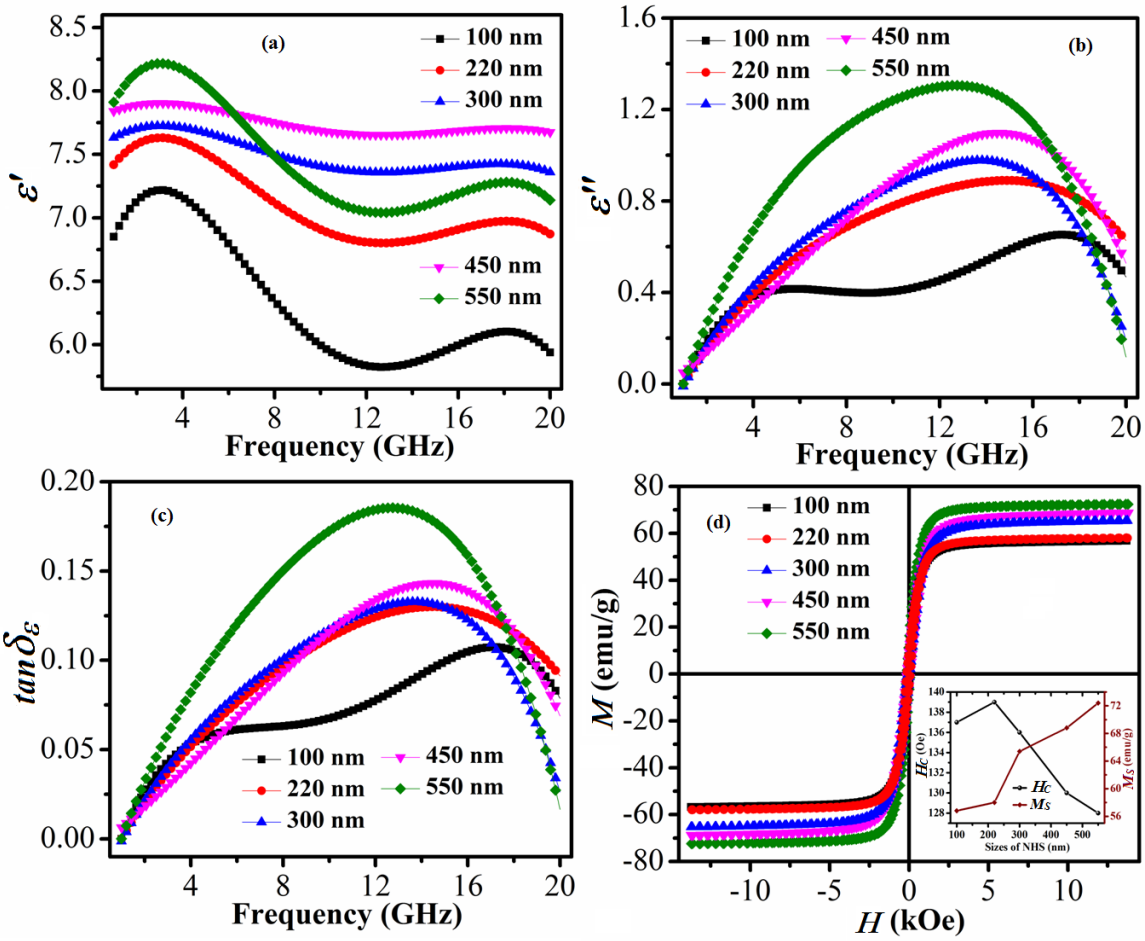

Figure 7.3. Frequency dependence (1 - 20 GHz) of (a) real (ε') (b) imaginary (ε'') values of dielectric constant and (c) dielectric loss ($tan\delta_\varepsilon$) (d) M-H plots at 300 K for all samples [inset of (d): variation of saturation magnetization (M_S) and coercivity (H_C) with NHS sizes]

Field dependent magnetization curves at 300 K, displayed in Fig. 7.3(d), exhibits increase in M_S from 56.2 emu/g to 73.0 emu/g for 100 nm to 550 nm NHSs whereas H_C decreases (shown in inset of Fig. 7.3(d)). NHSs with larger diameter and shell thickness possess larger crystallite sizes (as listed in Table 7.1) and at the same time, lower magnetic anisotropy and lattice strains. Consequently, magnetic spins orient easily along the field direction with increasing sizes to enhance M_S and reduce H_C approaching towards corresponding bulk values of $MnFe_2O_4$ [20].

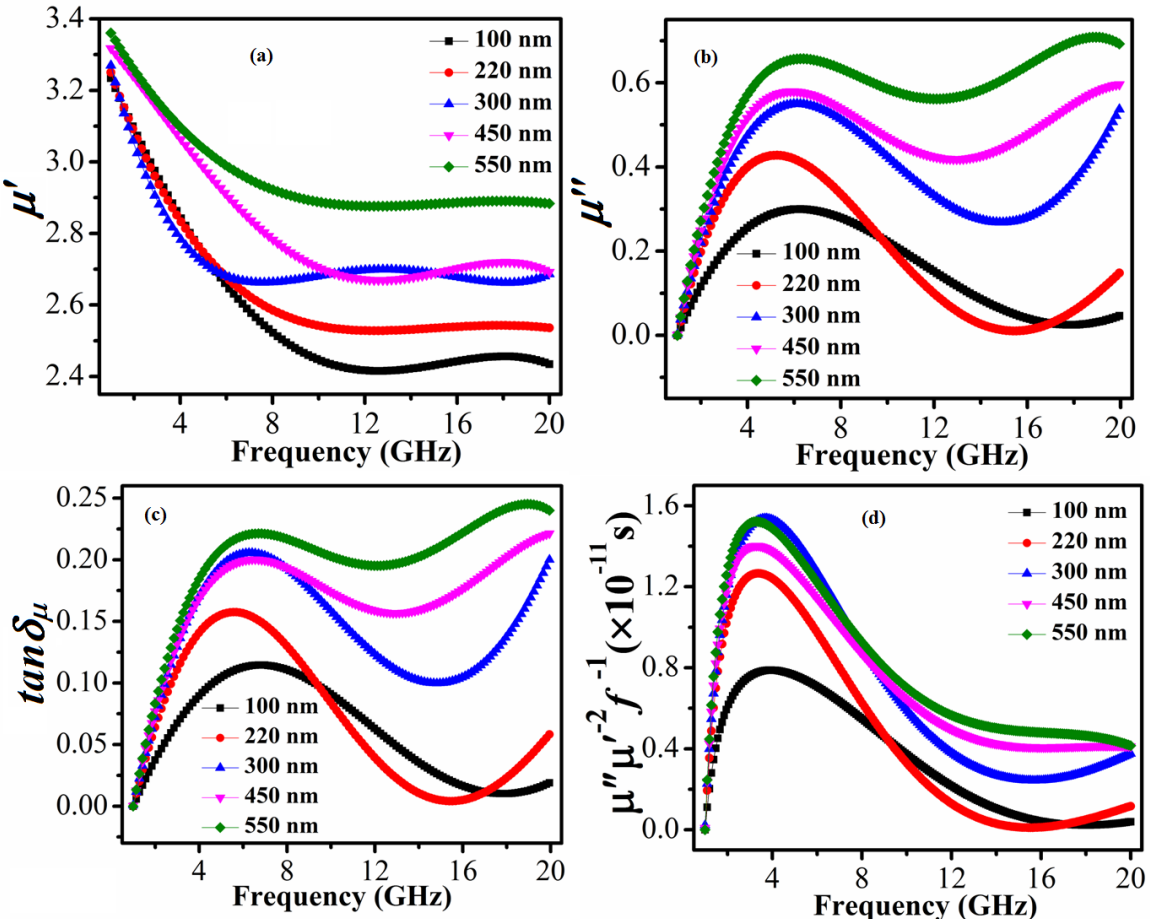

Figure 7.4. Frequency dependence (1 - 20 GHz) of (a) real (μ') (b) imaginary (μ'') values of permeability (c) magnetic loss ($tan\delta_\mu$) and (d) $\mu''(\mu')^{-2}f^{-1}$ value

The real (μ') and imaginary parts (μ'') of relative permeability of all the samples are plotted in Fig. 7.4(a) and 7.4(b) as a function of frequency from 1-20 GHz. μ' values are observed to decrease up to a certain f and then it maintains an almost constant value for all $MnFe_2O_4$ NHSs. μ'' displays characteristic resonance peaks for the samples at around 6 GHz. In case of larger NHSs (here 450 nm and 550 nm), presence of a second magnetic resonance at around 19 GHz is noticed [31]. Dynamic magnetic properties of the ferrimagnets are strongly related to the parameters such as magnetic anisotropy and M_S, according to the Landau-Lifshitz-Gilbert (LLG) equation [9,32]. Moreover, analysis from Globus equation, $\mu' \propto (M_S{}^2 D / K^{1/2})$, where K is the magneto-crystalline anisotropy constant, results in enhancement of μ' with diameter of NHSs and highest value of μ' is obtained for 550 nm NHS [7]. Typical morphology of NHSs raises

their surface magnetic anisotropy constants than bulk ferrites which helps to achieve higher magnetic loss and EM wave absorption in the system [1].

Variations of magnetic loss tangent, defined as $tan\delta_\mu = \mu''/\mu'$, with f and presented in Fig. 7.4(c), follow almost similar nature as μ'' vs. f curves. It is well-known that dynamic magnetic loss mostly arises from magnetic hysteresis, domain wall resonance, eddy current effects, natural and exchange resonance. The first two contributions are less effective for the samples in the high-frequency region and due to presence of low field in this study [18]. From the natural magnetic resonance equation [1,33], $2\pi f_r = (4\gamma K)/(3\mu_0 M_S)$, where γ is gyromagnetic ratio (~ 2.8 GHz/kOe for ferrites), resonance frequency (f_r) is found to be around 4 GHz for $MnFe_2O_4$ NHSs which suggests strong EM absorption through magnetic loss at this region. Furthermore, the eddy current loss contribution to μ'', can be expressed as $\mu'' \sim 2\pi\mu_0\mu'^2(d^2\sigma)f$, where d is the thickness of the sample (here, 5 mm), σ, electrical conductivity and μ_0, the permeability of free space [9,19]. According to this equation, if μ'' (or $tan\delta_\mu$) originates from the eddy current loss, the $\mu''(\mu')^{-2}f^{-1}$ versus f curves will not contain any peak and be constant with frequency [8]. In order to understand the probable sources of magnetic loss, frequency dependence of $\mu''(\mu')^{-2}f^{-1}$ is presented in Fig. 7.4(d). A sharp peak can be noticed for all the curves around 4 GHz and the value remains almost constant after ~ 11 GHz. Hence, contributions in magnetic loss can be attributed to resonance at low f, whereas eddy current loss has a significant role in absorption at higher frequencies.

7.3.3 Microwave Absorption Properties

Frequency dependent reflection loss (RL) curves for $MnFe_2O_4$ NHS composites with 20 wt% filler concentration and 5 mm thickness (t) are plotted in Fig. 7.5(a) to provide insight into their excellent EM wave absorption properties. Here RL is calculated following these equations [3,34]:

$$Z_{in} = Z_0\left(\frac{\mu_r}{\varepsilon_r}\right)^{1/2} \tanh\left[j\left(\frac{2\pi tf}{c}\right)(\mu_r\varepsilon_r)^{\frac{1}{2}}\right] \quad 7.1$$

$$RL = 20\log|(Z_{in} - Z_0)/(Z_{in} + Z_0)| \qquad 7.2$$

where μ_r $(=\mu' - i\mu'')$ and ε_r $(=\varepsilon' - i\varepsilon'')$ are relative permeability and permittivity of the material, c, the velocity of light, t, absorber composite thickness, Z_0 and Z_{in} are the impedance of free space and input impedance of absorber respectively.

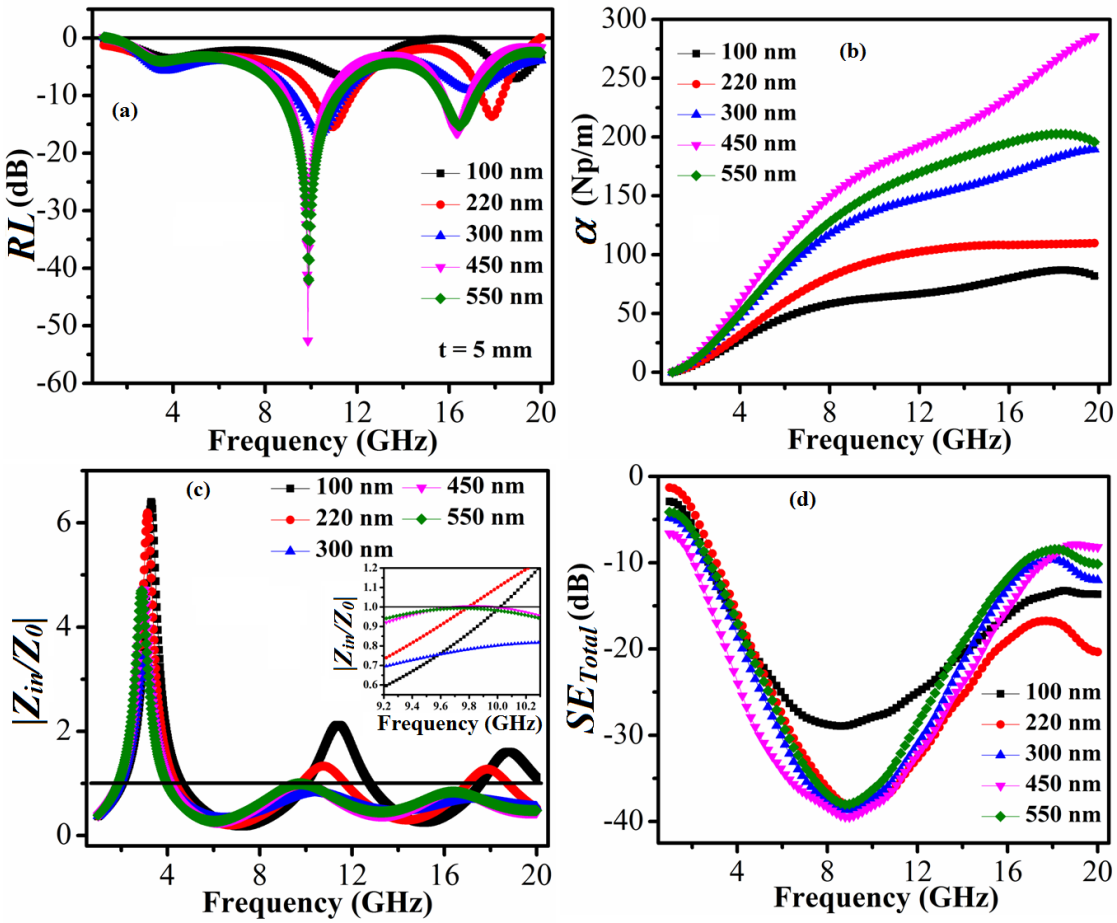

Figure 7.5. Variation of (a) reflection loss (RL) (b) attenuation constant (α) (c) $|Z_{in}/Z_0|$ ratio; inset: magnified plot for $|Z_{in}/Z_0|$ ratio vs. frequency showing $|Z_{in}/Z_0|$ ratio is nearest to 1 for 450 nm NHS and (d) total shielding efficiency (SE_{Total}) with frequency (1 - 20 GHz) for all the samples

Characteristic RL peaks for the samples around 4 GHz, 10 GHz and 17 GHz are witnessed in the examined frequency band where the peak frequencies are shifting towards left with increasing area of NHSs [9,31]. Origin of high RL can be attributed to either (i) higher transmission of the incident wave which requires better impedance

matching i.e. $|Z_{in}/Z_0| \sim 1$ or (ii) high value of dielectric and magnetic loss [7,8]. In addition, total internal reflections in hollow core of NHS traps incident EM wave which increases its total propagation path, hence it gets absorbed in NHS to a greater extent [3,11]. *RL* peaks around 4 and 17 GHz are related to strong magnetic and dielectric losses respectively. The intense peak at ~ 10 GHz for the samples is mostly arising from the impedance matching with $|Z_{in}/Z_0|$ nearly equals to 1 and for 450 nm NHS, due to most favorable matching, *RL* reaches its optimum value ~ −52.6 dB at ~ 10 GHz [8].

To ensure the impedance matching, variation of $|Z_{in}/Z_0|$ is plotted with frequency in Fig. 7.5(c) that shows best matching for the samples is obtained at around 10 GHz which also supports the outcomes from *RL* vs. *f* curves. Moreover, total effective bandwidth (*BW*) [frequency bands with $RL < -10$ dB i.e. absorption > 90%] is found to increase with NHS sizes, from 0 GHz (for 100 nm) to 4.2 GHz (for 550 nm). Thus, size variation of an eminent cost-effective microwave ferrite, $MnFe_2O_4$ in its light-weight NHS morphology is an effective strategy to enhance *RL* from −7.0 dB to −52.6 dB as well as broaden total effective bandwidth. Mn-ferrite NHS of 450 nm diameter having *BW* as broad as ~ 3.6 GHz and highest *RL* achieves maximum efficiency towards its practical applications in high-frequency devices.

Further, attenuation constants (α) and shielding efficiency (*SE*), associated with microwave loss and transmission through the samples, are estimated and shown in Fig. 7.5(b) and 7.5(d) respectively. α is defined in terms of relative permittivity and permeability as [16],

$$\alpha = \frac{\sqrt{2}\pi f}{c}\sqrt{(\mu''\varepsilon'' - \mu'\varepsilon') + \sqrt{(\mu''\varepsilon'' - \mu'\varepsilon')^2 + (\mu''\varepsilon' + \mu'\varepsilon'')^2}} \qquad 7.3$$

Here, α is observed to increase with frequency and also with NHS sizes and it becomes maximum ~ 285 Np/m for 450 nm NHS, whereas for 550 nm sample, with decaying ε' values, EM wave attenuation again decreases. Total *SE* (SE_{Total}) is expressed as the sum of the contributions from reflection (SE_R) and absorption shielding (SE_A) obeying the equation [10],

$$SE_{Total} = (SE_A + SE_R) = 20\log|S_{21}| \quad 7.4$$

where, S_{21} is reverse transmission co-efficient. At ~ 9 GHz a broad peak is visible for all SE_{Total} vs. f curves and a sharp increase in SE_{Total} peaks is noticed from 100 nm to other NHSs with enhanced internal reflections in hollow cores. SE_{Total} is also optimum for 450 nm $MnFe_2O_4$ NHS (− 39.5 dB at ~ 9 GHz) following trend of RL curves.

For a proper thickness design of the ferrite filler/epoxy composites required for practical applications, a thickness modulated study on EM wave absorption is carried out for 450 nm $MnFe_2O_4$ NHS. Figure 7.6(a) describes RL as a function of frequency for different thicknesses from 3 to 6 mm and Fig. 7.6(b) illustrates these results in three-dimension for better visualization. With increasing t, RL rises till 5.1 mm with a maximum RL value of −55.4 dB, then decreases again. This excellent RL_{max} for t = 5.1 mm of 450 nm $MnFe_2O_4$ NHS filler is achieved in midst of widely-used X-band region (at ~ 9.6 GHz) accompanied by a broad BW of ~ 3.7 GHz ($RL < -10$ dB for 8.6-10.8 GHz and 15.2-16.7 GHz regions). Relation of RL peak frequency (f_m) with matching thickness (t_m) can be interpreted from quarter wavelength (λ/4) model as [16,18],

$$t_m = \frac{nc}{4f_m\sqrt{|\varepsilon_r\mu_r|}} \ (n = 1, 3, 5, \dots) \quad 7.5$$

where for odd values of n, reflected waves from two interfaces of the absorber become out of phase. A good agreement between experimental and simulated t_m can be noticed in Fig. 7.6(c) where higher matching modes and hence more peaks are visible for thicker samples and f_m shifts towards lower frequencies with increasing t of the samples [8,18]. A schematic representation in Fig. 7.6(d) summarizes the properties of NHSs which makes them extremely suitable and effective as microwave absorber. In addition, composites consisted of epoxy resin matrix and ferrite filler can remain stable for high-temperature applications also up to 120°C [35]. The maximum RL obtained here is comparable to other promising ferrite based microwave absorbers such as $NiFe_2O_4$/r-GO nano particles (~ −42 dB) [16], Fe_3O_4/SiO_2 nanorods (~ −28.6 dB) [1], $MnFe_2O_4$@rGO nano-composites (~ −29.0 dB) [4], Magnetic graphene@PANI@porous TiO_2 ternary composites (−45.4 dB) [18] etc. Therefore, light-weight 450 nm $MnFe_2O_4$

NHS composite with only 20 wt% loading content is an attractive candidate for microwave absorption and applications in high-frequency devices.

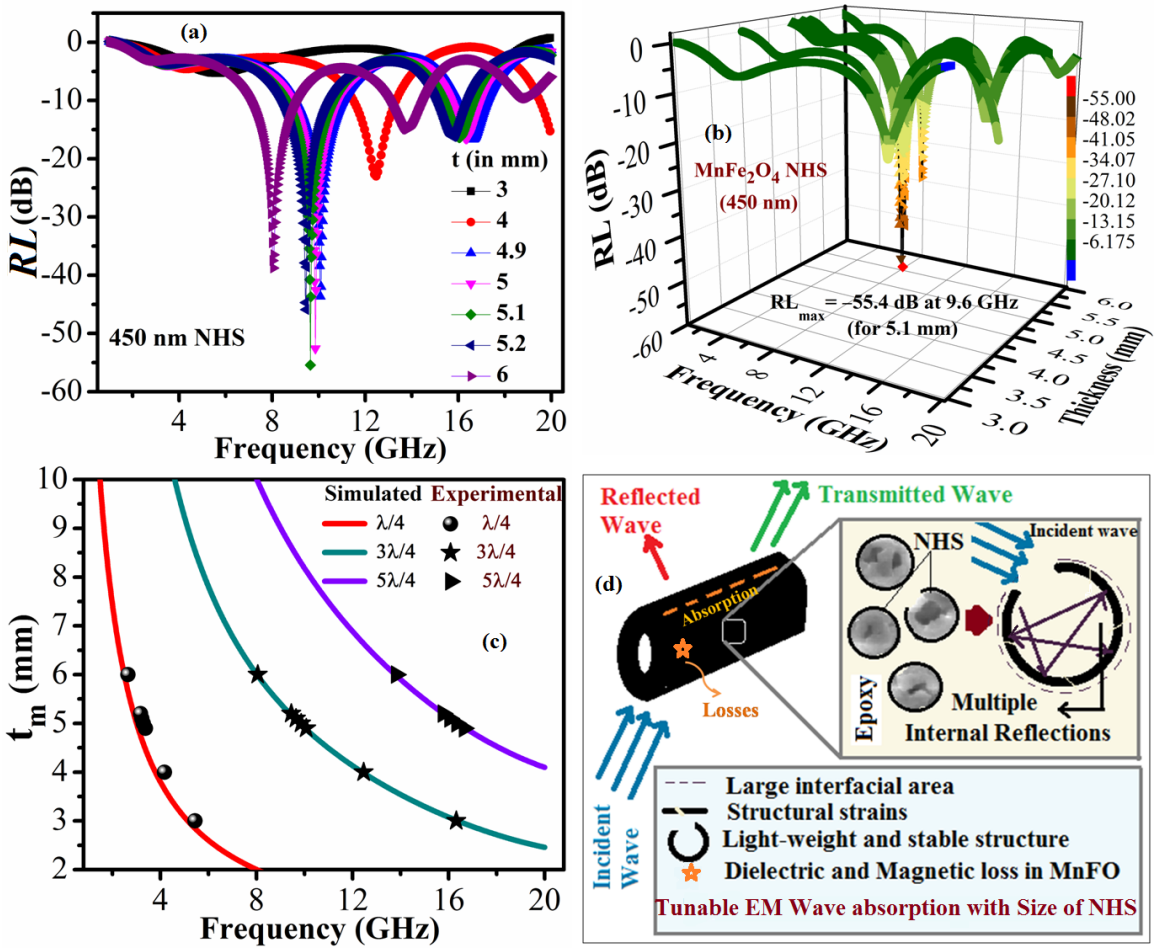

Figure 7.6. Frequency dependence of *RL* varying with (a) thicknesses (b) 3D representation showing RL_{max} in $MnFe_2O_4$ NHS of 450 nm and (c) Simulated and experimental matching thicknesses (t_m) with frequency (1 - 20 GHz) (d) A schematic approach showing toroidal shaped sample and effectiveness of NHSs towards EM wave absorption

7.4 Conclusion

In summary, tuning of EM wave absorption properties within widely-used frequency range of 1 - 20 GHz is performed by varying sizes (diameters in nm = 100, 220, 300, 450 and 550) of as-synthesized $MnFe_2O_4$ nano-hollow spheres (20 wt% filled in epoxy resin matrix). Multiple internal reflections in hollow core of NHS, larger interfacial area

and lower density make this typical morphology superior to its bulk and solid counterparts in terms of efficient and practical EMA materials. Depending on the size and structural properties of NHSs, dielectric and magnetic losses mostly increase from 100 nm to 550 nm NHSs. Intense RL peaks at around 4 GHz, 10 GHz and 17 GHz are related to strong magnetic loss, favorable impedance matching and dielectric loss respectively. Due to the best impedance matching with $|Z_{in}/Z_0|$ nearly equals to 1, $MnFe_2O_4$ NHS of diameter $\sim$ 450 nm is found to exhibit the optimal RL of ~ -52.6 dB, $SE_{Total} \sim -39.5$ dB and a high $\alpha \sim 285$ Np/m. Further, a thickness dependent study on 450 nm NHS composites reveals maximum RL of ~ -55.4 dB at $\sim$ 9.6 GHz for $t = 5.1$ mm with a broad total effective bandwidth ($RL < -10$ dB) of $\sim$ 3.7 GHz. Analysis from $\lambda/4$ model for best matching thickness displays a good agreement in between experimental and calculated t_m values. Therefore, an excellent RL and broad BW observed in 450 nm $MnFe_2O_4$ NHS at much lower filler concentration (20 wt%) illustrates it as a mass-efficient and cost-effective promising EMA material towards various high-frequency applications.

References

[1] X. Liu, Y. Chen, X. Cui, M. Zeng, R. Yu, and G. S. Wang, J. Mater. Chem. A 3, 12197 (2015).

[2] X. Qiu, L. Wang, H. Zhu, Y. Guan, and Q. Zhang, Nanoscale 9, 7408 (2017).

[3] M. Han, X. Yin, L. Kong, M. Li, W. Duan, L. Zhang, and L. Cheng, J. Mater. Chem. A 2, 16403 (2014).

[4] Y. Ding, Q. Liao, S. Liu, H. Guo, Y. Sun, G. Zhang, and Y. Zhang, Sci. Rep. 6, 32381 (2016).

[5] S. Sutradhar, S. Saha, and S. Javed, ACS Appl. Mater. Interfaces 11, 23701 (2019).

[6] L. Quan, F. X. Qin, D. Estevez, W. Lu, H. Wang, and H. X. Peng, J. Phys. D. Appl. Phys. 52, (2019).

[7] Z. Yang, Z. Li, Y. Yang, and Z. J. Xu, ACS Appl. Mater. Interfaces 6, 21911 (2014).

[8] Y. Zhang, H. Bin Zhang, X. Wu, Z. Deng, E. Zhou, and Z. Z. Yu, ACS Appl. Nano Mater. 2, 2325 (2019).

[9] D. Mandal, A. Gorai, and K. Mandal, J. Magn. Magn. Mater. 485, 43 (2019).

[10] R. Panigrahi and S. K. Srivastava, Sci. Rep. 5, 7638 (2015).

[11] F. Wang, J. Liu, J. Kong, Z. Zhang, X. Wang, M. Itoh, and K. Machida, J. Mater. Chem. 21, 4314 (2011).

[12] K. Vamvakidis, M. Katsikini, D. Sakellari, E. C. Paloura, O. Kalogirou, and C. Dendrinou-Samara, Dalt. Trans. 43, 12754 (2014).

[13] Y. Yang, M. Li, Y. Wu, B. Zong, and J. Ding, RSC Adv. 6, 25444 (2016).

[14] X. Zhang, G. Wang, W. Cao, Y. Wei, J. Liang, L. Guo, and M.-S. Cao, ACS Appl. Mater. Interfaces 6, 7471 (2014).

[15] M. Pardavi-horvath, J. Magn. Magn. Mater. 216, 171 (2000).

[16] J. Z. He, X. X. Wang, Y. L. Zhang, and M. S. Cao, J. Mater. Chem. C 4, 7130 (2016).

[17] W. Ruan, C. Mu, B. Wang, A. Nie, C. Zhang, X. Du, J. Xiang, F. Wen, and Z. Liu, Nanotechnology 29, 405703 (2018).

[18] P. Liu, Y. Huang, J. Yan, and Y. Zhao, J. Mater. Chem. C 4, 6362 (2016).

[19] Y. Zhang, X. Zhang, B. Quan, G. Ji, X. Liang, W. Liu, and Y. Du, Nanotechnology 28, (2017).

[20] D. Sarkar, M. Mandal, and K. Mandal, J. Appl. Phys. 112, 64318 (2012).

[21] M. Mandal Goswami, Sci. Rep. 6, 35721 (2016).

[22] S. F. Soares, T. Fernandes, A. L. Daniel-da-Silva, and T. Trindade, Proc. R. Soc. A Math. Phys. Eng. Sci. 475, 20180677 (2019).

[23] O. Luukkonen, S. I. Maslovski, and S. A. Tretyakov, IEEE Antennas Wirel. Propag. Lett. 10, 1295 (2011).

[24] D. Nath, F. Singh, and R. Das, Mater. Chem. Phys. 239, 122021 (2020).

[25] D. Mandal and K. Mandal, J. Alloys Compd. 851, 1 (2021).

[26] D. Mandal, M. Alam, and K. Mandal, Phys. B Condens. Matter 554, 51 (2019).

[27] C. V. Ramana, Y. D. Kolekar, K. Kamala Bharathi, B. Sinha, and K. Ghosh, J. Appl. Phys. 114, 183907 (2013).

[28] R. Tang, C. Jiang, W. Qian, J. Jian, X. Zhang, H. Wang, and H. Yang, Sci. Rep. 5, 1 (2015).

[29] Y. Yang, W. Guo, X. Wang, Z. Wang, J. Qi, and Y. Zhang, Nano Lett. 12, 1919 (2012).

[30] H. Ge, Y. Huang, Y. Hou, H. Xiao, and M. Zhu, RSC Adv. 4, 23344 (2014).

[31] I. Shanenkov, A. Sivkov, A. Ivashutenko, V. Zhuravlev, Q. Guo, L. Li, G. Li, G. Wei, and W. Han, Phys. Chem. Chem. Phys. 19, 19975 (2017).

[32] T. L. Gilbert, IEEE Trans. Magn. 40, 3443 (2004).

[33] X. G. Liu, D. Y. Geng, H. Meng, P. J. Shang, and Z. D. Zhang, Appl. Phys. Lett. 92, 173117 (2008).

[34] X. Li, J. Feng, Y. Du, J. Bai, H. Fan, H. Zhang, Y. Peng, and F. Li, J. Mater. Chem. A 3, 5535 (2015).

[35] H.-I. Hsiang, W.-S. Chen, Y.-L. Chang, F.-C. Hsu, and F.-S. Yen, Am. J. Mater. Sci. 1, 40 (2011).

Chapter 8

Magnetic and Microwave Properties of AOT Functionalized Cobalt-Ferrite Nanoparticles

In this chapter, Dioctyl sodium sulfosuccinate (AOT) functionalized cobalt-ferrite nanoparticles (CFNPs) sets with average sizes from 12 to 22 nm are synthesized and their in-detail magnetic characterizations are performed in search of hard-soft marginal magnet for application in various fields. Further, microwave absorption properties of bare and functionalized CFNPs are performed to observe effect of surface functionalization.

8.1 Preamble

Currently researchers have focused on transition metal oxide (TM) based magnetic nanomaterials for their low cost, low thermal conductivity, physical and chemical stability, unusual optical behavior, electronic and magnetic properties which differ significantly from their bulk counterpart [1–3]. Among all the ferrite materials, the hard magnetic cobalt ferrite (CFO) got popularity due to its high H_C, large M_S and strong anisotropy [4]. These properties of CFNPs make them useful in magnetic recording [5], magneto-optical and magneto-electric devices [6] and also in the field of biomedical research [7] starting from catalysis to drug delivery [1,8] etc.

A magnetic material is expected to show its maximum coercive field when it possesses its single domain size where domain wall movement is no longer possible and magnetization takes place by rotation only [9]. Moreover in nano size range, surface anisotropy, strain induced magnetostriction, inter-particle interaction etc. contribute to intrinsic anisotropy, thereby increasing the coercivity further. On the other hand due to higher thermal fluctuation in nanoscale, thermal demagnetization takes place [10–12]. Therefore, most of the applications of a magnetic nanomaterial require careful control in size to adjust both the single domain behavior and thermal demagnetization.

A number of efforts were made to increase the coercivity in cobalt ferrite by using various synthesis techniques such as mechanical milling, oil-in-water micro-emulsion and surface treatment. Liu et al. [10] reported a high value in coercivity of 5.1 kOe of $CoFe_2O_4$ powder depending on mechanical ball milling time. They explained the reason of high H_C on the basis of high density of defects and high level of strain developed during the milling. A large value of coercivity 9.3 kOe at room temperature is also reported for thin films deposited on SiO_2 single crystal substrate [12]. Further, a very large coercivity 9.47 kOe was found in surface modified CFNPs with crystallite size ~ 20 nm [13]. This large H_C was attributed to the accumulative effect of disordered surface spins, large strain, and surface anisotropy due to oleic acid.

It is well recognized that due to ligand assisted surface modification technique

coercivity of magnetic NPs can be increased to a large value. But those methods are comparatively complicated and change of size of particles by those methods is not so feasible. Recently we reported tuning of magnetic properties of different types of surfactant modified CFNPs where enhancement of coercivity took place due to both the surface modification of CFNPs and induced charge transfer effects [14]. In that study AOT modified CFNPs exhibited the maximum coercivity at some critical size compared to other surface ligands. That work inspires us to make further study on the AOT modified CFNPs in search of TM based permanent magnet.

An in-depth magnetic characterization of Dioctyl sodium sulfosuccinate (AOT) functionalized cobalt-ferrite nanoparticles (CFNPs) with average sizes from 12 to 22 nm, synthesized by co-precipitation of metal precursors are discussed here. The M-H hysteresis loop at room temperature for different particle size reveals that coercivity (Hc) value reaches the maximum (4.1kOe) at a critical size of 17.4 nm. Further, magnetic relaxation (M vs. time) measurements indicate relatively high value of magnetic relaxation time constant (τ) for AOT assisted CFNPs. Therefore, high Hc, significant saturation magnetization (Ms) coupled with high τ ensure the permanent magnetic characteristic of the material which have the potential to replace the expensive rare-earth-transition metal based permanent magnetic materials. On the other hand, materials with comparatively low value of Hc, remanent magnetization (Mr) will be useful for bio-medical applications [15].

8.2 Experimental

8.2.1 Synthesis Procedure

The AOT functionalized CFNPs with controlled size distribution are synthesized by surfactant mediated wet chemical co-precipitation process. A 50 ml aqueous solution of 0.5958 g $CoCl_2$, $6H_2O$ and 1.352 g $FeCl_3$, $6H_2O$ taken in 1:2 molar weight ratios, and also a 4M NaOH solution (50 ml) are prepared. Next, the surfactant solution made up of 2.223 g 0.1 M AOT (Dioctyl Sodium Sulfosuccinate ($C_{20}H_{37}NaO_7S$)) dissolved in ethanol is mixed with the above salt solution and stirred for 30 minutes. This homogeneous

mixture is heated at a constant temperature of 80°C in a 250 ml three-neck flask. Then the preheated sodium hydroxide solution at 40°C is added drop by drop to that solution, keeping the flow rate, stirring speed and temperature constant followed by 1 hour stirring of the solution on hot plate. After the reaction is completed, the whole mixture is left to settle down for 5 hours and then the black precipitate is collected by centrifugation, washed several times by water and dried at room temperature. We varied size of the particles changing the reaction temperature, reagent concentration, stirring speed and reactant addition rate. Thorough control of these reaction parameters allows us to obtain the sets of NPs of sizes 12 to 22 nm with dispersion less than 10%. In case of bare particles the synthesis is done without using the functionalizing material 'AOT' but keeping the other parameters same as taken in case of functionalized particles.

Chemicals, having purity > 98%, are bought from Sigma-Aldrich and Loba Chemic for the above preparation.

8.2.2 Characterizations

The structural phase and crystallite size of as-prepared AOT functionalized $CoFe_2O_4$ are studied by powder X-ray diffraction (XRD) using Rikagu MiniFlex II diffractometer equipped with Cu K_α radiation (at 15 mA and 35 kV) at the scanning rate of 1° per minute in the 2θ range of 20°-80°. A FEI QUANTA FEG 250 field-emission scanning electron microscope (FESEM) (0.2-30 kV) and a FEG transmission electron microscope (TEM) (80-200 kV) are used to investigate the size, shape, morphology of NPs. The Energy-dispersive X-ray (EDX) spectra are recorded for elemental analysis of the AOT-modified CFNPs. FTIR (Fourier transform infrared spectroscopy) is performed on the AOT modified samples by a JASCO FTIR-6300 spectrometer in the range of 500–4000 cm^{-1}. DSC (Differential Scanning Calorimetry) and TGA (Thermal Gravimetric Analysis) measurements are done using Q-2000 unit in the temperature range 300 K to 500 K. All the relevant magnetic measurements are carried out using a Vibrating Sample Magnetometer (Lake Shore).

8.3 Results and Discussion

8.3.1 Crystallography and Morphology

Figure 8.1 shows the X-Ray Diffraction plots of all the AOT functionalized CFNPs indexing the crystal planes present. This graph confirms the inverse spinel face centered cubic structure of CFNPs, as reported in the literature (JCPDS file no. 22–1086). A small peak at approximately 40 degrees, shown in the XRD spectra for some samples ('a', 'b', 'c'), indicates the presence of small amount of residues (NaCl).

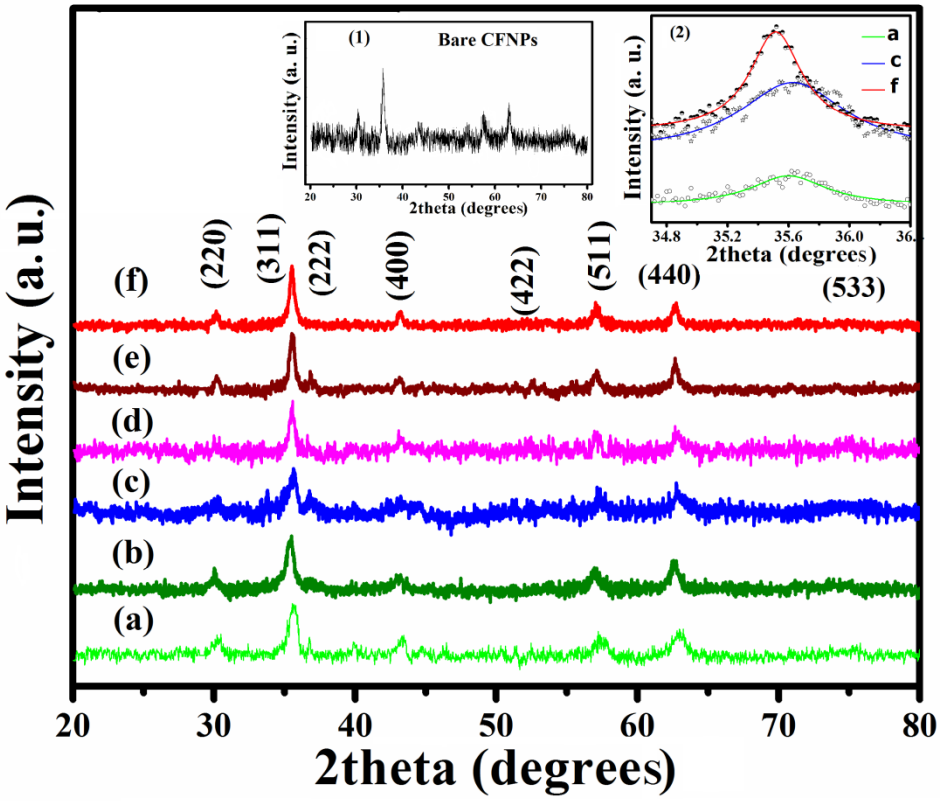

Figure 8.1. X-Ray Diffraction plots of all the AOT functionalized CFNPs with particle sizes (a) 12.5 nm, (b) 13.5 nm, (c) 15.9 nm, (d) 17.4 nm, (e) 20.2 nm and (f) 21.3 nm, Inset 1: XRD plot of bare CFNPs and Inset 2: (311) peak of (a), (c) & (f)

We calculated average crystallite size (D) and lattice strain (e) of the particles from Scherer formula, $D = \frac{k.\lambda}{\beta .\cos\theta}$ and $e = \frac{\beta}{4\tan\theta}$ choosing three peaks from each XRD,

where k is the structural constant (0.94), λ, the working wave length, β, the FWHM of the selected peak in radians and θ, the XRD peak angle in degrees. The inset (1) of Fig. 8.1 shows the XRD plot for uncapped CFNPs. The inset (2) of Fig. 8.1 comparing peak at 35.4°, confirms the increase in particle size from 'a' to 'f' as the peaks getting narrower. Table 8.1 shows the designation of the samples (in the graph) with their sizes and lattice strains.

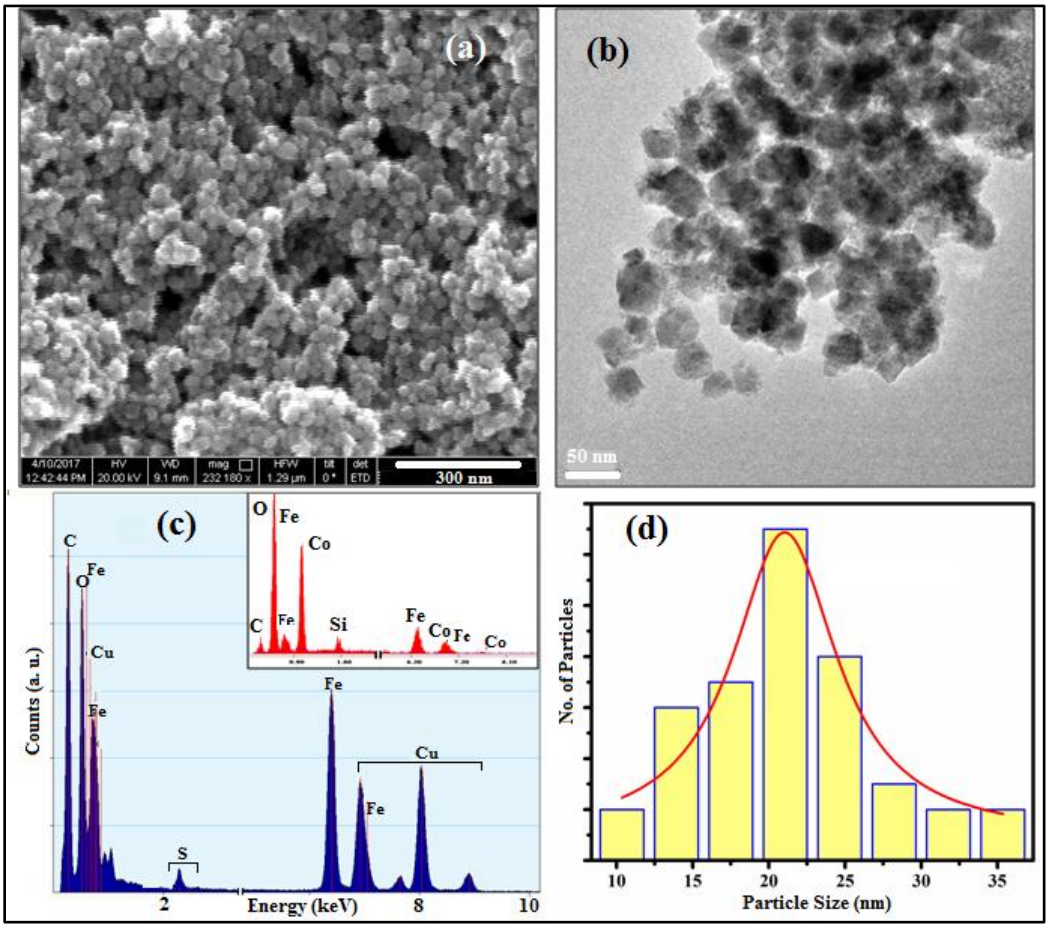

Figure 8.2. (a) FESEM, (b) TEM micrographs of AOT modified $CoFe_2O_4$ NPs (c) EDX spectra showing the composition for both capped and uncapped (inset) CFNPs. (d) Number of particles vs. Particles sizes histogram plot from TEM micrograph showing the relative standard deviation of sample f (21.3 nm)

The particle size and their spherical shape are studied from FESEM and TEM micrographs shown in Fig. 8.2((a) and (b)). Capping is done here with organic molecule

which could not be distinguished with TEM. EDX (Energy Dispersive X-Ray) spectra for both functionalized and bare CFNPs (inset) are also presented in Fig. 8.2(c), which confirms the constituents Fe, Co, O, Na, S, and C present in the AOT modified CFNPs. The 'S' element peak (marked in Fig. 8.2(c)) shown in EDX spectra proves the capping of surfactant, which is not present in the EDX spectra of bare CFNPs. Particle size distribution for sample 'f' is plotted in Fig. 8.2(d) which shows relative standard deviation of ~ 8.4% with an average particle size of 21 nm.

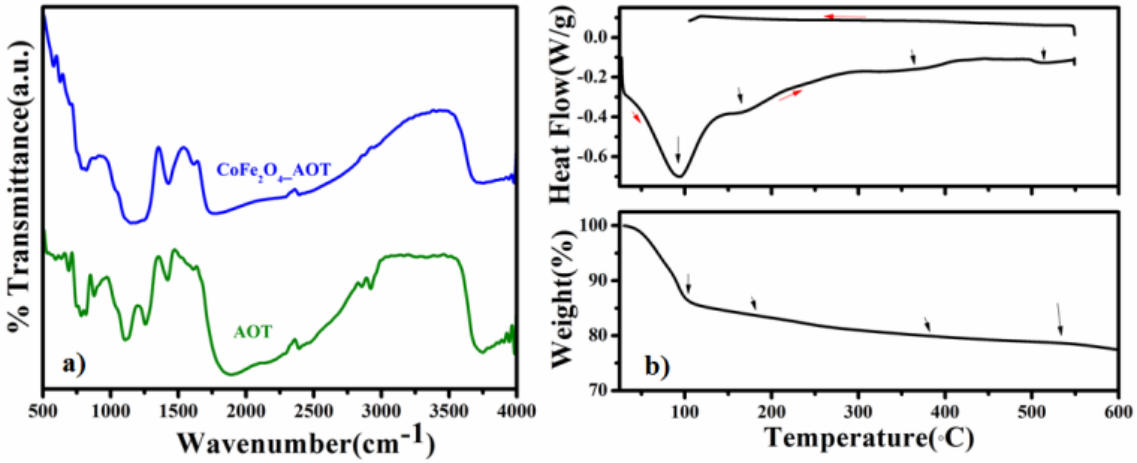

Figure 8.3. (a) FTIR spectra of $CoFe_2O_4$_AOT NPs and of only AOT (b) DSC and TG curve showing peaks at 110˚C, 200˚C, 400˚C, 550˚C

Figure 8.3(a) illustrates the FTIR spectra of AOT modified CFNPs and of only AOT. FTIR spectra can offer information about redistribution of cations between octahedral and tetrahedral sites of the inverse spinel structure in $CoFe_2O_4$ [16]. Analysis on AOT show peaks at 1160 and 1052 cm^{-1} corresponding to asymmetric and symmetric stretch vibrations of the sulfonate (S-O) groups and at 1247 cm^{-1}, which corresponds to the ester stretch (–C(=O)–O–C) [17]. The intense peaks at 2854 and 2924 cm^{-1} correspond to methylene antisymmetric and symmetric vibrational modes in AOT. The suppression or broadening of FTIR peaks of functionalized $CoFe_2O_4$ NPs in comparison to the surfactant implies a serious surface modification of magnetic NPs [14]. However, the peak obtained at 556 cm^{-1} in $CoFe_2O_4$ sample is attributed to Fe-

O or Co-O bond [13]. These comparative studies help to identify the strong coordination of surfactant to NP surface.

Fig. 8.3(b) represents the DSC thermogram of AOT functionalized CFNPs which shows a strong endothermic peak at 110°C due to the evaporation of structural water. The small endothermic peaks near 200˚C, 400˚C, 550˚C are probably associated with the thermal energy released due to the decomposition of ligand molecule. The descending thermogram does not display any peak which confirms the entire decomposition of the strongly attached micelle during ascending half. TGA is performed to show the respective weight losses of AOT modified CFNPs (Fig. 8.3(b)) where thermal energy changes occur.

8.3.2 Size Dependent Magnetic Measurements

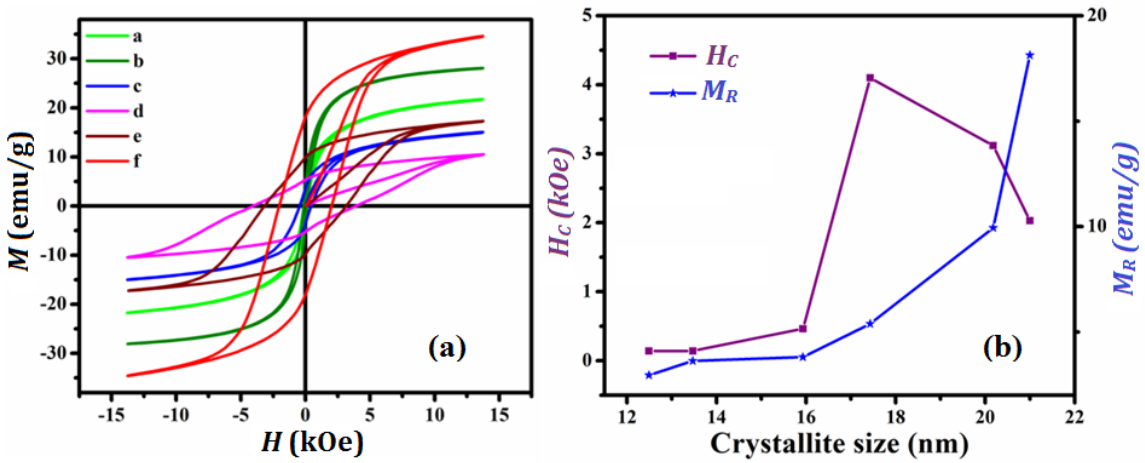

Figure 8.4. (a) M-H curve of all the samples with different particle size, at room temperature 300 K (b) Variation of coercivity and remanent magnetization with crystallite size of particles, at room temperature

Figure 8.4(a) describes *M* - *H* hysteresis loops of all the samples with maximum applied field up to 14 kOe at room temperature. All the loops exhibit the characteristic features of a ferrimagnetic material with sufficiently high H_C values (141 Oe to 4.1 kOe) and M_R values (2.95 emu/g to 18.13 emu/g). A material with a high H_C is suitable for

permanent magnets as these types of materials can prevent them from being easily demagnetized. In addition to high H_C, high M_R is also desirable to increase the energy product required for a permanent magnetic material. The magnetic parameters such as coercivity (H_C), and remanent magnetization (M_R) estimated from the hysteresis loops with their corresponding sizes are listed in Table 8.1 and shown in Fig. 8.4(b).

H_C is found to increase with increasing crystallite size and reaches its maximum value of 4.1 kOe at a size of 17.4 nm, beyond which it reduces. Our reported value of H_C is much higher compared to $H_C \sim 1.2$ kOe achieved by Toksha *et al.* [18] for bare CFNPs of nearly the same size.

Magnetic coercivity depends on several factors such as magnetic anisotropy, defects, strain, size, doping, nature of the surface, and interface as well as inter-particle interaction. Capping of surfactant reduces coagulation and interaction among the particles. Therefore, magnetic anisotropy and interaction of surfactant ligand with NPs are responsible for large coercivity.

Table 8.1. Sample name mentioned in the graph with their corresponding crystallite size, lattice strain, H_C, and M_R

Sample Name	Crystallite Sizes in nm	Lattice Strain	Coercivity (H_C) in kOe	Remanent Magnetization (M_R) in emu/g
a	12.5	0.0095	0.46	2.95
b	13.5	0.0088	0.142	3.63
c	15.9	0.0074	0.143	3.81
d	17.4	0.0066	4.10	5.39
e	20.2	0.0059	3.12	9.94
f	21.3	0.0058	2.03	18.13

The magnetic anisotropy can be calculated using the law of approach (LA) to saturation [19]. Though LA to saturation is applicable to ferromagnetic materials, due to the high magnetization, coercivity and anisotropy of CFNPs, hence it can be applicable here [20–25].

$$M(H) = M_S\left(1 - \frac{0.07619\,K^2}{H^2\,M_S{}^2} - \frac{0.0384\,K^3}{H^3\,M_S{}^3}\right) \quad 8.1$$

where $M(H)$ is the magnetization at an applied field of H, M_S is the saturation magnetization, and K is the cubic magneto-crystalline anisotropy constant. To investigate the effect of AOT surfactant on the CFNPs, we fitted the Eq. 8.1 to the M - H curve (approach to saturation region) of bare CFNPs and AOT modified CFNPs (21.3 nm), as shown in Fig. 8.5.

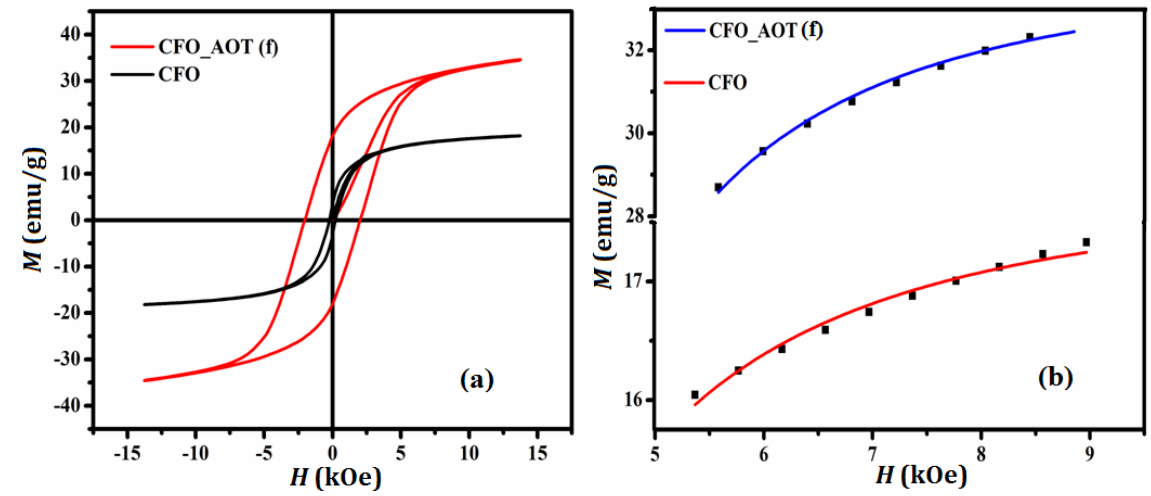

Figure 8.5. (a) M-H hysteresis loops at 300 K for AOT modified CFNPs and bare CFNPs (b) Eq. 1 fitted M-H curves at approach to saturation region

The anisotropy constant (K) of AOT modified CFNPs is found to be ~ 11.9x10^5 J/m^3, which is much higher than that (~ 4.9x10^5 J/m^3) of bare one. Higher value of K is attributed to the surface spin pinning by surfactant molecules. For a spherical particle with diameter D, surface area S, and volume V, the anisotropy energy constant (K) is described by the relation

$$K = K_V + \frac{6}{D}K_S \quad 8.2$$

where K_V and K_S are the bulk and surface anisotropy energy constants, respectively. Using Eq. 3, K_S is estimated to be ~ 3.1x10^5 J/m^3 and ~ 10.1x10^5 J/m^3 for bare and

surface functionalized CFNPs respectively. As K_V is constant for a material, K increases due to the increase in K_S resulting an increase in coercivity.

From the Neel model of the surface magnetic anisotropy [26-27],

$$E_{ij} \propto \frac{L(r_{ij})}{2} \sum_{j=1}^{z_i} (\vec{s}_i . \vec{e}_{ij})^2 \qquad 8.3$$

Where E_{ij} is surface anisotropy energy, $L(r_{ij})$ is pair-anisotropy constant, also can be called K_S, $\vec{s}_i$ and $\vec{e}_{ij}$ are unit vectors along magnetization direction and distance between spin i and j respectively. $L(r_{ij})$ and hence, surface anisotropy increases with the decreasing separation between two neighboring spins at the surface due the adverse break down of local symmetry at the NP surface and hence the lack of attraction in all directions, resulting increase in surface anisotropy and hence increase in coercivity. Bødker et al. [19] reported further enhancement in K when the surface is modified with foreign molecules. Further coercivity is found to increase with increasing chain-length of the surfactant, for example, NPs assisted with TTAB (higher chain-length) shows higher coercivity than those capped with CTAB (shorter chain length) though they have the same π-acceptor head group [14] due to the steric hindrance offered by tail part of the surfactant. Hence, we can anticipate that surface anisotropy as well as the steric hindrance associated with tail part of surfactant may be responsible for such a difference in coercivity. Rakshit et al. [14] have reported that ligands with π-donor head group and large tail group, such as AOT, results in greater M_S and H_C of 3d transition metals in comparison to other ligands stated.

The increase in H_C for particle sizes from 22 to 17 nm (Fig. 8.4(b)) is may be either due to multi domain to single domain transformation or rise of surface anisotropy with decreasing crystallite size. However this multi to single domain shifting is not probable for small particles obtained here, as for CFNPs, single to multi-domain transformation generally occurs after 50 nm. For the smaller particles (from 17 to 12 nm), the anisotropy energy becomes comparable to the thermal energy and H_C decays leading to thermally assisted jumps over the anisotropy barriers [10].

The remanent magnetization increases with increase in particle sizes. M_R is low for smaller particles because of the large value of surface spins in these particles tend to freeze due to strong bonding between surfactant molecules and surface spin. For bigger particles, other parameters such as domain wall alignment, inter-particles interaction etc. plays a role in enhancement of M_R values.

The hysteresis loops at 100 K (H_C ~ 6.7 kOe) and 300 K (H_C ~ 2.03 kOe) as shown in Fig. 8.6(a) indicate the increase in coercivity on lowering temperature. The very large coercivity and low saturation magnetization at 100 K are related with a pronounced growth of magnetic anisotropy inhibiting the alignment of the moment in an applied field [18].

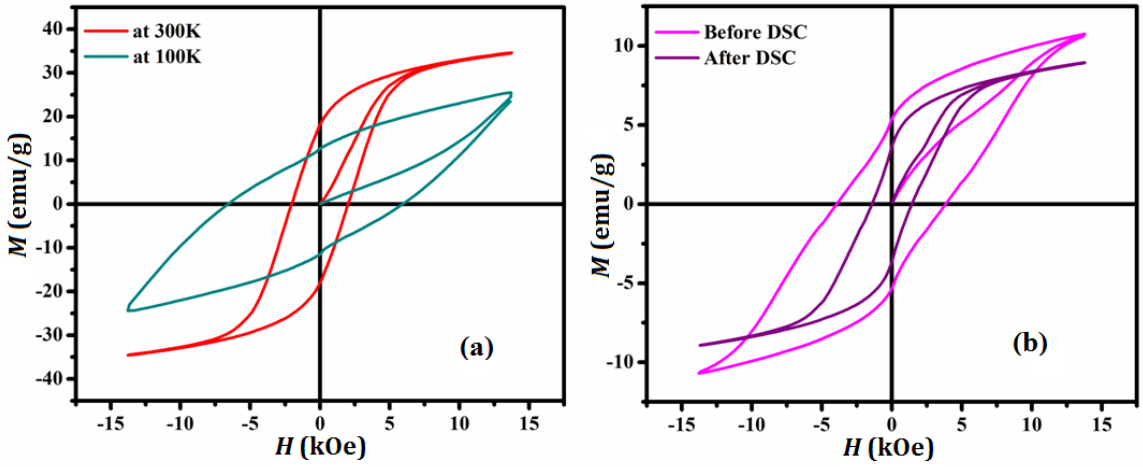

Figure 8.6. (a) M-H curve for sample 'e' at 300 K and 100 K. (b) M-H plot before and after DSC

Before and after DSC, M-H measurements of AOT modified CFNP of size 17.4 nm are performed at room temperature and their H_C values are found to be 4.1 kOe and 1.5 kOe respectively (Fig. 8.6(b)). While performing DSC, beyond 200°C, AOT starts to decompose resulting in lower coercivity. This observation is similar to the result reported previously [28]. From this study we can conclude that micelles on particle surface strongly arrest the surface spins introducing a steric hindrance with restriction in free movement of surface spins of the magnetic nanoparticles.

8.4 Magnetic Relaxation Behavior

To understand the dynamic behavior, the magnetic relaxation property of the samples is measured. The relaxation time constant of the magnetic nanoparticles, τ, characterizes the ability to retain the magnetization after the aligning field is removed. It reflects the influences of Brownian and Neel relaxation. It is found that CFNPs with its surface micelles shows a large value of τ in comparison to bare CFNPs. Figure 8.7 illustrates the magnetic relaxation curves (M vs. time) at different temperatures and sizes after magnetizing the NPs to its saturation value. In this case, non-interacting magnetic CFNPs have probably surface spin-spin relaxation where magnetization decays exponentially with time,

$$M(t) = M_0 e^{-\frac{t}{\tau}} \qquad 8.4$$

where $M(t)$ and M_0 are magnetization of sample at time t and $t = 0$, τ is relaxation time constant.

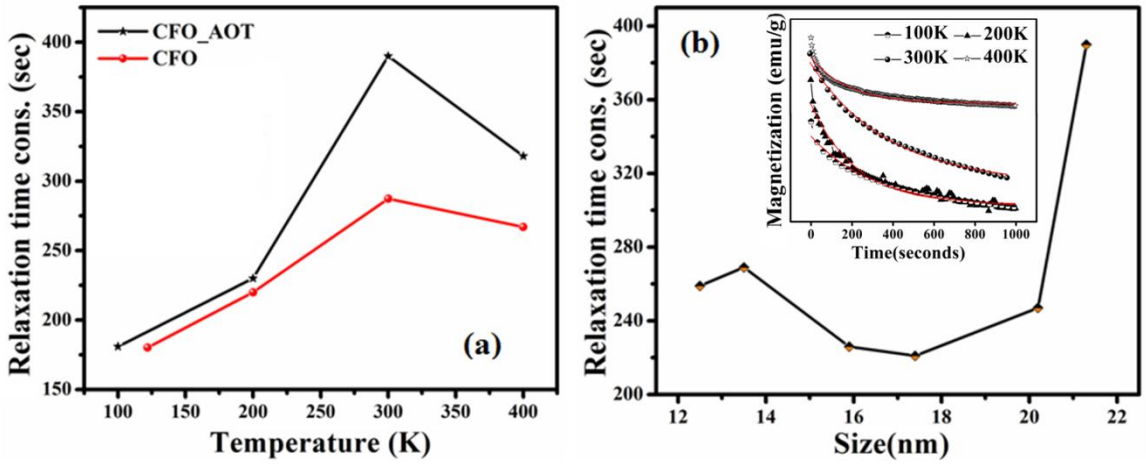

Figure 8.7. (a) Comparison of temperature dependent relaxation time constants of AOT modified CFNPs and uncapped CFNPs (b) τ with different particle sizes (from 12 to 22 nm); Inset: M vs. time plots at different temperatures

Here τ in every case is determined by fitting the Eq. 4 to the experimental data plotted in Fig. 8.7(b) as a function of size. Relaxation time constant (τ) decreases with size up to

17.4 nm, beyond which it increases. As the size and surface area of the particles are increasing, τ increases [29]. Temperature dependence of τ of bare and surface functionalized CFNPs of about 20 nm is plotted in Fig. 8.7(a). Inset picture in 8.7(a) shows the relaxation curves (M vs. t) of functionalized CFNPs at 100 K, 200 K, 300 K, and 400 K after magnetizing the NPs to saturation field. τ becomes maximum at room temperature in both cases. Lowering of τ with the temperature possibly can relate with spin-glass like behavior of the material [30]. The size dependent curve of magnetic relaxation time constant has a similarity with M_S vs. particle size curve. Recently, magnetic relaxation switching (MRS) assays are employed to detect different organisms [31]. Magnetic relaxation measurement in this regard is very important.

8.5 Electromagnetic Wave Absorption Properties

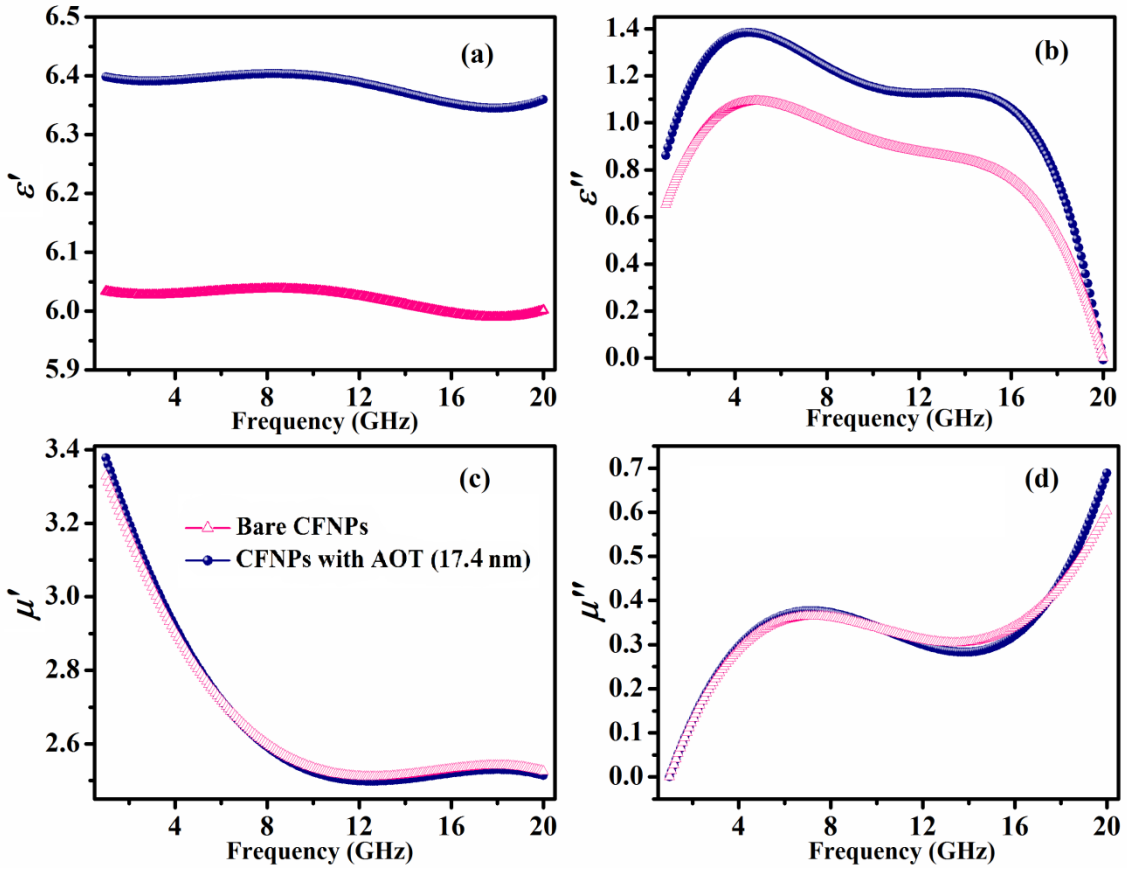

Figure 8.8. Frequency dependence (1 - 20 GHz) of (a) real (ε'), (b) imaginary (ε'') values of dielectric constant (c) real (μ') and (d) imaginary (μ'') values of permeability

To evaluate the effect of AOT surface functionalization on CFNPs for high frequency applications, frequency dependences of permittivity (ε), permeability (μ) and reflection loss (RL) are analyzed for the frequency region 1 – 20 GHz. Figure 8.8(a) shows irrespective of with or without functionalization, real part of permittivity (ε') slightly decreases with increasing frequency similar to the results obtained in previous chapters. Space charge and dipolar polarization mainly contributes to the permittivity and conduction in the sample. A significant enhancement in ε' value is observed for AOT modified CFNPs due to larger effective interfacial area for polarization and charge transfer effect on the surface of NPs [32]. As a result, dielectric loss i.e. imaginary part of permittivity (ε'') is also higher for the surface modified $CoFe_2O_4$ NPs.

Variations of real (μ') and imaginary (μ'') parts of permeability are plotted in Fig. 8.8(c) and 8.8(d). At the studied frequency range, dynamic magnetic parts do not seem to change significantly due to surface functionalization by AOT. For 17.4 nm AOT modified CFNPs, though the saturation magnetization is almost same as bare CFNPs but coercivity value is larger. Now, with low applied magnetic field and at such high frequency, hysteresis loss has lesser contribution to the magnetic loss [33]. Therefore, only a small increase in μ''value is visible here for the AOT modified sample. Though for high power applications, hysteresis loss plays an important role in magnetic loss. Moreover, hard CFNPs remain magnetically stable throughout high frequency region [34].

The frequency dependence of reflection loss (RL) curves for the samples with 20 wt% filler concentration and 4.5 mm thickness (t) are plotted in Fig. 8.9. Here, RL is calculated employing the equations based on transmission line theory, as mentioned in the previous chapter [35]. The enhancement in dielectric and magnetic loss in surface functionalized NPs also improve the EM wave absorption properties of AOT modified CFNPs. The RL value for bare CFNPs is -17.3 dB at 12.9 GHz and for AOT coated CFNPs; it is found much higher, ~ -30 dB at 12.6 GHz. The shift in peak frequency arises from quarter-wavelength model due to increase in the value of permittivity. Therefore,

surface functionalization of ferrite nanoparticles with ionic surfactant like AOT can be considered as an effective tool to enhance electromagnetic interference shielding.

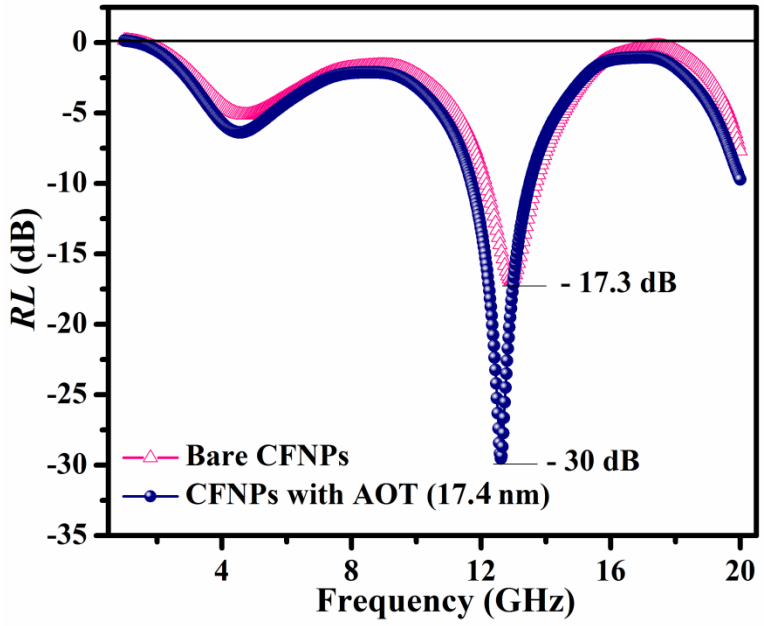

Figure 8.9. Variation of reflection loss (*RL*) with frequency (1 - 20 GHz) for the samples

8.6 Conclusion

In summary, we prepared ferrimagnetic cobalt ferrite ($CoFe_2O_4$) nanoparticles (NPs) ~ (of sizes 12 - 22 nm) by wet chemical method using AOT as a surface assistant. The observed coercivity (H_C) value reaches maximum (4.1 kOe) for a critical size of 17.4 nm, at room temperature. The increase in H_C from 22 nm to 17 nm is due to rise of surface anisotropy with decreasing crystallite size and steric hindrance from the surfactant molecule. For the smaller particles (for 17 nm to 12 nm NPs), the anisotropy energy becomes comparable to thermal fluctuation and therefore H_C reduces with smaller sizes. Here we notice both the remanent magnetization and magnetic relaxation time constant increases with increase of particle size. Samples with low H_C, M_R, M_S values might be useful as soft magnet in many biological purposes such as bio-sensing, hyperthermia, drug delivery, magnetic resonance imaging etc. and high H_C, high relaxation time constant along with sufficient M_R enable this material a possible

replacement for expensive rare-earth transition metal based permanent magnetic material. Among the high-frequency applications, surface functionalization of CFNPs with AOT is found to enhance attenuation of electromagnetic wave pollution and 17.4 nm AOT modified CFNPs can serve as an efficient microwave absorber.

References

[1] C. Liu, B. Zou, A. J. Rondinone, and Z. J. Zhang, J. Am. Chem. Soc. 122, 6263 (2000).

[2] K. Khaja Mohaideen and P. A. Joy, Appl. Phys. Lett. 101, 2 (2012).

[3] A. V. P., A. M. L., E. J. J., R. K., Q. S. T. D., A. christina Fernandez, K. S., and J. Das S., Opt. - Int. J. Light Electron Opt. 127, 9917 (2016).

[4] J. Ding, Y. J. Chen, Y. Shi, and S. Wang, Appl. Phys. Lett. 77, 3621 (2000).

[5] R. Skomski, J. Phys. Condens. Matter 15, R841 (2003).

[6] B. Zhou, Y.-W. Zhang, Y.-J. Yu, C.-S. Liao, C.-H. Yan, L.-Y. Chen, and S.-Y. Wang, Phys. Rev. B 68, 24426 (2003).

[7] S. W. Lee, S. Bae, Y. Takemura, I. B. Shim, T. M. Kim, J. Kim, H. J. Lee, S. Zurn, and C. S. Kim, J. Magn. Magn. Mater. 310, 2868 (2007).

[8] N. Lee and T. Hyeon, Chem. Soc. Rev. 41, 2575 (2012).

[9] A. G. Kolhatkar, A. C. Jamison, D. Litvinov, R. C. Willson, and T. R. Lee, *Tuning the Magnetic Properties of Nanoparticles* (2013).

[10] B. H. Liu, J. Ding, Z. L. Dong, C. B. Boothroyd, J. H. Yin, and J. B. Yi, Phys. Rev. B - Condens. Matter Mater. Phys. 74, 1 (2006).

[11] S. Chakraverty, S. Mitra, K. Mandal, P. M. G. Nambissan, and S. Chattopadhyay, Phys. Rev. B - Condens. Matter Mater. Phys. 71, 1 (2005).

[12] Y. C. Wang, J. Ding, J. B. Yi, B. H. Liu, T. Yu, and Z. X. Shen, Appl. Phys. Lett. 84, 2596 (2004).

[13] M. V Limaye, S. B. Singh, S. K. Date, D. Kothari, V. R. Reddy, A. Gupta, V. Sathe, R. J. Choudhary, and S. K. Kulkarni, J. Phys. Chem. B 113, 9070 (2009).

[14] R. Rakshit, M. Mandal, M. Pal, and K. Mandal, Appl. Phys. Lett. 104, 2 (2014).

[15] A. López-Ortega, E. Lottini, C. D. J. Fernández, and C. Sangregorio, Chem. Mater. 27, 4048 (2015).

[16] K. S. Rao, G. Choudary, K. H. Rao, and C. Sujatha, Procedia Mater. Sci. 10, 19 (2015).

[17] T. Nakanishi, B. Ohtani, and K. Uosaki, J. Phys. Chem. B 102, 1571 (1998).

[18] B. G. Toksha, S. E. Shirsath, S. M. Patange, and K. M. Jadhav, Solid State Commun. 147, 479 (2008).

[19] R. Grossinger, 665, (1981).

[20] N. Ranvah, Y. Melikhov, D. C. Jiles, J. E. Snyder, A. J. Moses, P. I. Williams, and S. H. Song, J. Appl. Phys. 103, 07E506 (2008).

[21] L. Kumar and M. Kar, Ceram. Int. 38, 4771 (2012).

[22] R. Kumar and M. Kar, J. Magn. Magn. Mater. 416, 335 (2016).

[23] L. Kumar, P. Kumar, and M. Kar, J. Mater. Sci. Mater. Electron. 24, 2706 (2013).

[24] L. Kumar, P. Kumar, S. K. Srivastava, and M. Kar, J. Supercond. Nov. Magn. 27, 1677 (2014).

[25] Y. Melikhov, J. E. Snyder, D. C. Jiles, A. P. Ring, J. A. Paulsen, C. C. H. Lo, and K. W. Dennis, J. Appl. Phys. 99, 08R102 (2006).

[26] R. H. Kodama and A. E. Berkowitz, Phys. Rev. B 59, 6321 (1999).

[27] R. Yanes, O. Chubykalo-Fesenko, H. Kachkachi, D. A. Garanin, R. Evans, and R. W. Chantrell, Phys. Rev. B 76, 64416 (2007).

[28] D. Pal, M. Mandal, A. Chaudhuri, B. Das, D. Sarkar, and K. Mandal, J. Appl. Phys. 108, 124317 (2010).

[29] E. M. Markink, 99 (2012).

[30] P. K. Pandey, R. J. Choudhary, and D. M. Phase, Appl. Phys. Lett. 103, (2013).

[31] J. B. Weaver and E. Kuehlert, Med. Phys. 39, 2765 (2012).

[32] J. Liu, R. Che, H. Chen, F. Zhang, F. Xia, Q. Wu, and M. Wang, Small 8, 1214 (2012).

[33] L. Wang, Y. Huang, X. Sun, H. Huang, P. Liu, M. Zong, and Y. Wang, Nanoscale 6, 3157 (2014).

[34] M. Pardavi-horvath, J. Magn. Magn. Mater. 216, 171 (2000).

[35] D. Mandal, A. Gorai, and K. Mandal, J. Magn. Magn. Mater. 485, 43 (2019).

Chapter 9

Conclusion and Future Perspective

The current chapter briefly describes the overall conclusion of the present thesis and scope of future studies related to this field.

9.1 Overall Conclusion of this Thesis

In the present thesis, first of all, the diverse applications of ferrite nanoparticles are revealed through tuning of their sizes, hence their magnetic properties. Among the various applications of ferrites, the concerns related to electromagnetic (EM) wave pollution attracted our attention. To diminish electromagnetic wave interference or thus to enhance EM wave shielding, light-weight, stable, cost-effective yet efficient microwave absorbing material are convenient and preferable options. Therefore, next, we move on to a morphology dependent study on a popular microwave ferrite for high-power applications, Nickel ferrite (NFO). The morphology dependent study shows a promising enhancement in microwave absorption properties in case of NFO nano-hollow spheres (NHS) and multiple internal reflections in their internal hollow core, increase in their interfacial area due to dual surfaces, increase in magnetic anisotropy due to typical morphology of porous NHSs etc. are responsible for this result. Following this outcome, a detailed study on magnetic, dielectric and EM wave absorption properties of earth-abundant transition metal based ferrites is performed which provides a map to select an efficient material for applications from high-frequency devices to bio-medical field as well as shows a clear enhancement of EM wave absorption properties in other investigated ferrites compared to traditional magnetite and $MnFe_2O_4$ NHS is found to exhibit an optimal reflection loss (RL). Further a size dependent study on $MnFe_2O_4$ NHSs shows an optimized 450 nm NHS performs as an excellent microwave absorber at only 20 wt% filler concentration in epoxy resin matrix. Finally, surface modification on ferrite NPs is found to significantly enhance EM wave absorption from -17.3 dB to -30 dB. These overall findings of this journey are summarized below.

We have successfully synthesized crystalline $NiFe_2O_4$ nano-hollow spheres in a facile one-pot solvothermal method and reported a detail frequency and temperature dependent study on its magnetic and dielectric nature. The morphological analysis assures the sample to be nano-hollow spheres. Study of magnetic properties shows NFO NHS as a soft ferrimagnetic material having M_S and H_C, 63.5 emu/g and 122 Oe respectively which are comparatively higher than that of its other morphologies. The

variation of ε, Z, $tan\delta$ and σ_{ac} with frequency and temperature are explained in terms of Maxwell-Wagner two-layer model and hopping of charges at Fe^{3+} to Fe^{2+} as well as Ni^{2+} to Ni^{3+} ions at B (octahedral)-sites. The parameters of conductive grain and resistive grain boundaries are obtained from Cole-Cole plot. The conduction mechanism for NHS is found to be of *ac* type from Jonscher's power law and dielectric relaxation of charge carriers is found to be of non-Debye type. Lower density, larger surface area and the enhanced dielectric and magnetic properties in this morphology (NHS) of NFO compared to its NPs and bulk counterparts, seems interesting towards its application in high-frequency devices.

Focusing on its application, as-synthesized $NiFe_2O_4$ nano hollow spheres are found to exhibit strong EM absorption properties ($RL < -10$ dB) in the $9.1-12$ GHz range for an absorber thickness of 2 mm and an optimal RL ($-$ 59.2 dB) at 11.7 GHz. Also a comparative RL and SE study in widely used X-band frequency region is shown for NFO NHS with its nanoparticle ($RL \sim -51.9$ dB at 11.6 GHz) and bulk ($RL \sim -18.2$ dB at 9.96 GHz) counterpart. Natural or exchange resonance peak is not found in either permittivity or permeability data. The excellent absorption properties are mainly associated with transmission of EM wave because of perfect impedance matching in the microstructure with free space, high dielectric loss arising from interfacial polarization and cationic hopping, moderate dynamic magnetic loss as well as with the wave attenuation through multiple internal reflections in hollow core of NHS. On the contrary, solid spherical NFO NPs and also NFO Bulk with less effective surface area, show lower RL and SE with respect to NHS in $8-12$ GHz. With the hollow interior, NHS has lower density than bulk one, makes it a light weight absorbing filler material. Hence, NFO NHS seems an interesting morphology towards its application as mass efficient and broadband microwave absorbing materials.

Further, TFe_2O_4 (T = Mn, Fe, Co, Ni, Cu and Zn) NHSs are successfully synthesized and a detail study on their structural, magnetic and dielectric properties is presented. Lattice constants and crystallite sizes are observed to enhance with increase in cationic radii and diameter of NHSs respectively. FTIR spectra depict T-O peaks shift

towards lower wavenumber with increase in T^{2+} radii. Maximum H_C is found for $CoFe_2O_4$ NHS (~ 576 Oe) due to its highest magneto-crystalline anisotropy ($K \sim 4.52\times10^5\ J/m^3$) and super-exchange interaction whereas maximum M_S is obtained for Fe_3O_4 NHS (~ 73.6 emu/g). Day plots describe the studied ferrites belong in pseudo single domain (PSD) to SD region within temperature region 100 K - 400 K. The variation of ε, $tan\delta$ and σ_{ac} with f at ~ 300 K for the ferrites are discussed through Maxwell-Wagner two-layer model and hopping of charges between Fe^{3+} to Fe^{2+} as well as T^{2+} to T^{3+} ions at A and B-sites. Analysis of dielectric relaxation mechanism ensures it as modified-Debye type and Jonscher's power law displays ac conduction mechanism for TFe_2O_4 NHSs. Resistive and capacitive components of conductive grain and resistive grain boundaries are obtained from equivalent circuit fitting over Cole-Cole plots where $NiFe_2O_4$ NHS with smaller crystallite size found to have higher R_{gb} and simultaneously lower ε. This study on TFe_2O_4 NHSs will be highly effective to select a promising material towards diverse applications from high-frequency devices to bio-medical field. Moreover, electromagnetic wave attenuation properties of as-synthesized low-density TFe_2O_4 [T = Mn, Fe, Co, Ni, Cu, Zn] nano-hollow spheres (20 wt% filled in epoxy resin matrix) are investigated in-detail within widely-used frequency range of 1 - 20 GHz. T^{2+} [T = Mn, Co, Ni, Cu, Zn] substitution in place of Fe^{2+} displays a clear enhancement of microwave absorption properties compared to traditional Fe_3O_4 whereas, $MnFe_2O_4$ NHS is found to exhibit an optimal RL of ~ −32.7 dB, SE_{Total} ~ −42 dB and a high α ~ 196 Np/m. Losses through strong magnetic resonance and dielectric relaxation are responsible for RL peaks of ferrites around ~ 4 GHz and ~ 12 GHz respectively. An additional peak at ~ 19.3 GHz for $MnFe_2O_4$ NHS arises due to favorable impedance matching. Multiple internal reflections in hollow core of NHS are also considered as an influential source to high RL of NHSs. Further, filler loading content and thickness dependent study is carried out on $MnFe_2O_4$ NHS composites and a maximum RL of ~ −45.6 dB at t ~ 4.2 mm with a broad total effective bandwidth ($RL < -10$ dB) of ~ 3.6 GHz is observed for 50 wt% sample. According to λ/4 model for best matching thickness, experimental t_m is found to agree well with calculated results. Excellent RL and broad BW observed in $MnFe_2O_4$ NHS (50 wt%) makes it a cost-effective promising EMA material towards mass-efficient high-frequency applications.

Therefore, tuning of EM wave absorption properties within widely-used frequency range of 1 - 20 GHz is performed by varying sizes (diameters in nm = 100, 220, 300, 450 and 550) of $MnFe_2O_4$ nano-hollow spheres (20 wt% filled in epoxy resin matrix). Multiple internal reflections in hollow core of NHS, larger interfacial area and lower density make this typical morphology superior to its bulk and solid counterparts in terms of efficient and practical EMA materials. Depending on the size and structural properties of NHSs, dielectric and magnetic losses mostly increase from 100 nm to 550 nm NHSs. Intense RL peaks at around 4 GHz, 10 GHz and 17 GHz are related to strong magnetic loss, favorable impedance matching and dielectric loss respectively. Due to the best impedance matching with $|Z_{in}/Z_0|$ nearly equals to 1, $MnFe_2O_4$ NHS of diameter $\sim$ 450 nm is found to exhibit the optimal RL of ~ -52.6 dB, $SE_{Total} \sim -39.5$ dB and a high $\alpha \sim 285$ Np/m. Further, a thickness dependent study on 450 nm NHS composites reveals maximum RL of ~ -55.4 dB at $\sim$ 9.6 GHz for $t = 5.1$ mm with a broad total effective bandwidth ($RL < -10$ dB) of $\sim$ 3.7 GHz. Analysis from $\lambda/4$ model for best matching thickness displays a good agreement in between experimental and calculated t_m values. Therefore, an excellent RL and broad BW observed in 450 nm $MnFe_2O_4$ NHS at much lower filler concentration (only 20 wt%) illustrates it as a mass-efficient and cost-effective promising EMA material towards various high-frequency applications. Moreover, simpler ways to fabricate ferrite NHS rather than complex heterostructures make NHS more interesting for application purposes. Measurements related to coaxial line consists samples of volume 0.026 cc (considering $t = 5$ mm) whereas measurements in X-band with rectangular waveguide consist samples of volume 0.453 cc (considering $t = 2$ mm).

Furthermore, ferrimagnetic $CoFe_2O_4$ nanoparticles of sizes $\sim 12 - 22$ nm are prepared by wet chemical method using AOT as a surface assistant. The observed H_C value reaches maximum (4.1 kOe) for a critical size of 17.4 nm, at room temperature. The increase in H_C from 22 to 17 nm is due to rise of surface anisotropy with decreasing crystallite size and steric hindrance from the surfactant molecule. For the smaller particles (for 17 to 12 nm NPs), the anisotropy energy becomes comparable to thermal fluctuation and therefore H_C reduces with smaller sizes. It is noticed that both the

remanent magnetization and magnetic relaxation time constant increases with increase of particle size. Samples with low H_C, M_R, M_S values might be useful as soft magnet in many biological purposes such as bio-sensing, hyperthermia, drug delivery, magnetic resonance imaging etc. and high H_C, high relaxation time constant along with sufficient M_R enable this material a possible replacement for expensive rare-earth transition metal based permanent magnetic material. Among the high-frequency applications, surface functionalization of CFNPs with AOT is found to enhance attenuation of electromagnetic wave pollution through increase in dielectric constant and magnetic anisotropy.

9.2 Scope of Future study

We have successfully achieved a light weight, cost-effective, low cost and efficient EM wave absorber in this thesis work. The optimized 450 nm NHS of $MnFe_2O_4$ can be further surface modified with dielectric or magnetic materials. Layering with other material on surface of NHS can enhance the interfacial area for dielectric polarization due to core-shell structure as well as increase magnetic anisotropy due to spins pinning or canting on the intermediate surfaces. Moreover, its dielectric and magnetic properties also can be tuned by choosing proper core and shell material to obtain broad-band EM wave absorption and closer values of permittivity and permeability for better impedance matching. Microwave absorption properties of ferrites can also be enhanced with smartly engineered metamaterials. The frequency selective surface based metamaterials are designed such as their ε or μ values become tunable (even negative) and therefore they find applications in various high-frequency applications. Further, preparation of transparent EM wave shielding materials will be interesting in stealth technology. For high temperature applications of EM wave absorbers their thermal properties should also be studied thoroughly. Thin films or different nanostructures can be investigated to enhance the surface area or to reduce dimensionality of the future absorbers.

The interesting properties of nano-hollow spheres, such as large surface area per volume, low density, inner void space and potential multi-functionality make these

appropriate for several applications apart from microwave absorptions. For instance, the cavity inside NHS can be used as micro- or nano-containers for chemical reactions or carriers for drug delivery. The void space of hollow structures can effectively accommodate the volume change of high-capacity lithium-ion battery anode materials and can provide high specific surface area for charge storage in supercapacitors. Multiple reflection and scattering leads to enhanced light-harvesting capability and superior power conversion efficiency. Ferro-fluid, which is basically immersion of ferrite particles in dense liquid like oil, is a magnetic composite applicable from industrial to biomedical fields. Use of low density nano hollow spheres as loading agent in it can assure higher sustainability of the mixture preventing sedimentation or agglomeration of the fluid. Finally, hollow structures also find scopes in sensing devices, water purification applications etc. Thus, these possible applications open several future scopes for ferrite nano-hollow spheres.